Geocoding and Stereoscopy

of

Synthetic Aperture Radar Images

A Thesis submitted for the degree of

Doctor of Philosophy

in the University of London by

Christine Clark

University College London

July 1991

Abstract

This thesis is concerned with the geocoding of Synthetic Aperture Radar (SAR) images and the use of stereo SAR images. The work was carried out as part of the preparation for the launch of the ERS-1 satellite, due in July 1991, which will carry a SAR sensor.

There are two basic approaches to geocoding: image-to-object and object-to-image. Both of these methods have been analysed and assessed on experimental data, namely SIR-B imagery of Mount Shasta. Each type of geocoding requires the solution of non-linear equations. It has been shown that if the parameters which control the geocoding process are given to a good degree of accuracy, each method can give good results. The effect of inaccuracies in the estimation of these parameters has also been analysed. It was found that there was a predominantly linear response to parameter error in both types of geocoding.

Experimental investigations into the effects of the resampling, inherent in operational geocoding, showed that the statistical properties of the resulting image may be severely corrupted with pixel values of less than zero being obtained. This discovery has subsequently been given theoretical support.

Height can be determined from stereo pairs of images and digital elevation models can thus be produced, aiding both geocoding and topographic mapping. Existing approaches to SAR/SAR stereo all appear to be based on photogrammetric methods. An alternative, analytic approach, believed to be novel, is described and applied to the same Mount Shasta imagery. Using this method, with accurately-known controlling parameters, correspondence with ground data is excellent. However, an analysis of the sensitivity of the approach to inaccuracies in the controlling parameters shows that the method is extremely sensitive to error.

The possibility of combining SAR and optical/infrared imagery for stereometric pur-

poses is also discussed from a theoretical viewpoint.

to Adrian

Contents

List of Figures

List of Tables

Acknowledgements

I would like to thank Professor I. J. Dowman for his supervision and help throughout the course of this work. I would also like to thank Dr. A. F. Clark for his help, especially as a sounding board. My thanks also go to him for introducing me to `Awk` and for his LaTeX expertise. I am grateful for his constant belief in my ability.

Thanks are also due to Joana Fernandes for her help regarding orbits, Francelina Neto for her stereo advise and for acting as my stereo eyes (I cannot see stereo), and James Pearson for his computer systems help. I should also like to thank Dr. A. Sowter, formerly of the GEC-Marconi Research Centre, for his help at the start of this work.

I would like to thank the Science and Engineering Research Council for their financial support in the form of a CASE studentship and to my industrial sponsors, the GEC-Marconi Research Centre.

This document was typeset using Prof. Donald E. Knuth's TeX system and Leslie Lamport's LaTeX macro package, with the text set in the 'Computer Modern' series of fonts, also developed by Donald. E. Knuth. The graphs were produced using `GNUPLOT`, written by Colin Kelley and Thomas Williams.

Chapter 1

Introduction

The concept of Synthetic Aperture Radar (SAR) appears to have originated in the work of Carl Wiley of the Goodyear Aircraft Corporation in the early 1950s. Wiley observed that the along-track co-ordinate of a reflecting object (being linearly transversed by the radar beam) has a one-to-one correspondence with the *instantaneous Doppler shift* of the signal reflected to the radar by the object. He concluded that a frequency analysis of the reflected signals should result in finer along-track resolution than the along-track width of the physical beam would indicate.

SAR has subsequently developed into a mature technology and provides a particularly useful imaging tool. The SAR sensor provides information about a surface by measuring the reflected energy in the microwave region of the electromagnetic spectrum, thereby extending the capability of measuring surface properties. In addition, as it uses its own energy to illuminate the scene and operates at a relatively large wavelength, it can operate at all times, i.e. day or night, and through cloud cover. Thus, it has the unique capability required for continuously monitoring dynamic surface phenomena.

One major difficulty, recognised quite early in the development of SAR, was in the implementation of a physical data processor that could accept wide-band signals from a storage device and carry out the necessary Doppler-frequency analysis at each resolvable slant range. Hence, a large number of arithmetic operations are required in order to generate an image. The first airborne SAR systems used optical processors, though the majority of SAR processors are now digital in nature. However, the development of digital processors for spaceborne SAR systems remains a very active research field.

SAR imaging of the Earth's surface was proven to be practical by the Seasat global ocean-monitoring satellite launched by NASA in June 1978. Although this satellite remained operational only until October 1978, a considerable quantity of SAR imagery was recorded. The Seasat mission demonstrated the usefulness of SAR data from satellites and aircraft for monitoring the Earth's surface, both over land and sea.

Since 1978, the shuttle imaging radars, SIR-A and SIR-B, have provided more data, though SIR-A imagery was optically recorded. The next few years should see a rapid expansion of interest in the field of microwave remote sensing, as SAR images from the European ERS-1, the Canadian RADARSAT, the Japanese JERS-1, and the US SIR-C become routinely available.

In terrestrial remote sensing, the use of SAR has several advantages over instruments operating at optical wavelengths. These include:

- Penetrates clouds, giving night/day and all-weather capabilities.
- The resolution is independent of the distance to the object.
- Provides its own illumination and thus has control over the illumination angle.
- Allows imaging at very shallow angles, giving dramatically different perspective than common vertical photographs.
- Employs wavelengths different from visible and infra-red, and thus provides different information (e.g., surface roughness, dielectric properties, and moisture).
- Has potential to penetrate vegetation, snow, etc..
- Can utilise polarisation effects.
- Can operate simultaneously at several wavelengths, giving a multi-spectral capability.
- Can image ocean waves.
- Can produce overlapping images suitable for stereoscopic viewing.
- Supports shape-from-shading analysis, interferometric operation for 3-D mapping, and analysis of incidence angle signatures of objects.

However, it must be borne in mind that, compared to optical sensors SAR has nominally lower resolution and increased noise (speckle).

1.1 Geocoding

Geocoded Imagery is a term which describes any remotely sensed imagery that has been transformed onto a cartographic projection (e.g., Universal Transverse Mercator, UTM) and is independent of both the sensor and the motion of the satellite platform from which the original raw imagery was collected. It does not imply that terrain effects have been taken into account. In general, the process involves the following operations:

- correction of geometric effects;
- registration to geographic co-ordinate systems;
- resampling to map scale and format without degradation of radiometric quality.

Furthermore, 'Geocoded Imagery' usually indicates that the image is referenced to a cartographic co-ordinate system, while the term *Precision Geocoded Imagery* denotes that the image has been *further* corrected for geometric distortions both due to variations in terrain relief and due to the image formation process. However, the reader should be aware that this terminology is not universally adopted, and confusion occasionally arises. The work in this thesis is primarily concerned with *precision* geocoding.

Geocoded imagery should not, however, be confused with *georeferenced* imagery. Georeferencing is the process of geometrically correcting an image, using ground information, to any map projection, while retaining mission-dependent characteristics such as image framing, orientation and (sometimes) pixel size. Most current ground station processing systems produce mission-dependent, georeferenced image products.

The main advantages of geocoded imagery are:

- data from several different satellites/sensors covering the same area may be combined;
- imagery may be combined with geographically-referenced non-image data;
- adjacent frames of image data may be joined and analysed as one frame.

Hence, geocoding of remotely-sensed imagery allows information that previously had to be analysed separately to be combined and interpreted together, resulting in a more efficient and effective use of the imagery.

The development of digital databases and Geographic Information Systems (GIS) will facilitate the extraction of new thematic information from digital image data, by enabling the comparison of physical parameters measured by one sensor with those measured by another. The geometric relationship between these spatial data must therefore be established. Hence, all datasets must be presented in a common cartographic reference system.

Geocoding of optical/infrared imagery is well known and is implemented in many systems. However, SAR images introduce geometric anomalies which have no counterpart in optical/infrared imagery. Since a number of remote sensing satellites to be launched in the 1990s will carry a SAR, digital image processing and algorithms which facilitate the restitution of the inherent geometric distortions of SAR imagery are urgently required.

[Buchroithner, 1987] reported that, for geological lineament analysis, both geocoded and unrectified imagery should be used. Complimentary evaluation of both is recommended in order to acquire the fullest information on linear features from radar imagery. It is also reported that, in high relief, even geologists experienced in the evaluation of optical/infrared imagery have serious difficulties in carrying out field checks using non-geocoded SAR imagery. Therefore, for effective and time efficient field work, geocoded imagery needs to be available.

However, SAR imagery is affected by a number of radiometric and geometric distortions which, in many applications, complicate or even prevent effective utilisation of the imagery. Hence, great care must be taken in evaluating both geocoded and unrectified SAR imagery alike.

1.2 Stereoscopy

One of the major bases on which the human visual system judges distance is stereoscopy, in which differences between the images recorded by the two eyes allow the brain to estimate relative depths. Stereoscopy is an important topic in many areas of science and engineering. In the computer vision field, it is one of the most effective methods of estimating 3-D shape. In remote sensing, probably the major application is in the production of digital elevation models and topographic maps. However, SAR records its images in a totally different way to the eye; hence, conventional stereoscopy techniques are not applicable to SAR images. Several methods suitable for SAR stereoscopy have been devised; another such technique,

believed to be novel, which is more appropriate for ERS-1 imagery (due to the availability of precise ephemeris data) is presented in this thesis.

1.3 Available Image Data

Despite interest in SAR geocoding and stereoscopy at a number of research establishments throughout the world, suitable data are difficult to obtain. This makes it difficult to assess techniques on a variety of datasets. The work described in this thesis was carried out in preparation for ERS-1 image data. At the start of this work, in April 1988, ERS-1 was due to be launched in late 1989 or early 1990, and hence it was expected that some ERS-1 data would be available to the author. However, at the time of writing, ERS-1 has still to be launched (it is currently expected to be in orbit in July 1991). This has meant that alternative sources of imagery have had to be used.

The work described in this thesis was carried out using SIR-B imagery of Mount Shasta, California, USA, four images of which were available. SIR-B imagery of Egypt and Madagascar were also available, but these were of comparatively flat terrain and hence were not suitable for this type of work, i.e. geocoding and height assessment of a flat terrain would not demonstrate the algorithms sufficiently.

A stereo pair of VARAN-S data of the Aix en Provence area of France was also available. However, it had been shown previously [Quegan *et al.*, 1991] that these data were radiometrically corrupt, causing the images to be bland and with little visible detail. Also no header data accompanied the images, rendering them useless for this work.

A SPOT image of Aix en Provence was available and the German DLR offered to send a Seasat SAR image of this area, thus giving a SPOT/Seasat combination. The request for the Seasat SAR data was sent in late 1989. To date, three images have been received, but *none* of them have been of the requested area. (DLR had stated that, if a user defined a centre latitude and longitude of an area known to be covered by Seasat, then the image could be easily found and sent on to the user. It appears that the header data for the required orbit have been corrupted and so the image has still not been located. So much for ease of data access!)

A stereo pair of Seasat images of Death Valley, California, USA, along with a SPOT scene of the same area, became available at the end of this PhD (March 1991). Unfor-

tunately, the header data of one of the SAR images had been lost at source. The Seasat image which had the header had the least overlap with the SPOT scene; the overlap area was of a high ridge, river valley, and lake. The Seasat SAR image had been acquired in August 1978, and the SPOT scene in June 1987; hence, due to the time and season differences, no ground control points could be reliably obtained from the river or lake. There were a couple of roads on this overlap region, but these had no characteristic points such as road crossings or sharp bends. Matching points on the ridge was also difficult due to SAR foreshortening effects, differing resolutions, and look-angle. No ground control points could be established with any degree of confidence on both of the images and the maps.

Most recently, NASA have released SAR imagery of Venus from the Magellan mission on CD-ROM media. Although of the wrong planet, these data should be usable for both geocoding and stereoscopy. However, the long lead time in obtaining the imagery and the lack of ground data to verify the results means that the use of such data is not feasible for this work.

The Mount Shasta SIR-B imagery used in this study was courtesy of Dr. J-P. Muller. These data had been supplied to him by British Petroleum, originally coming from the Jet Propulsion Laboratory, USA. No documents were supplied describing the images or the header data. The author endeavoured to obtain such information but was told that it was not available. There are various forms of image header depending on from where it was supplied. Hence the author had no header data description.

1.4 Work of this Thesis

One of the objectives at the outset of this study was to define, demonstrate, and perform error analyses of object-to-image and image-to-object geocoding. The other objective was to demonstrate how SAR imagery could be used in stereoscopy and investigate how the resulting procedure responds to errors in the input data. The study was carried out as part of the preparations for the reception of ERS-1 SAR imagery.

The author held a CASE award studentship, the industrial sponsor being the GEC-Marconi Research Centre situated in Great Baddow, Chelmsford, Essex.

For this type of study, analysis of SAR imagery can only be effective if it is built upon a sound understanding of how a SAR image is formed. The author therefore spent a good

deal of time studying SAR image formation. Chapter 2 details the main topics of interest.

Efforts to obtain suitable SAR image data were constantly being made and several sources of image data, unfortunately mostly unsuitable, were investigated.

The different methods of geocoding that were currently being used, or were proposed for the future, were investigated and a decision was made as to the method most suited to this work. A description of geocoding methods is given in Chapter 3. The method chosen for this work was the SAR processor based method, which employs the SAR range and Doppler equations as well as a description of the Earth surface. There are two ways of performing geocoding, namely image-to-object and object-to-image. Algorithms for both these methods were established and are given in detail in Chapter 3. A discrepancy was found between the image-to-object geocoding algorithm defined by the author and that of the German DLR — see Section 3.4.1. The author's definition is correct, as was subsequently confirmed by DLR following numerous communications. The method of SAR processor geocoding requires the solution of two or three non-linear equations (depending on the type of geocoding, i.e. image-to-object or object-to-image). An appropriate, iterative method of solving these equations was found and methods of obtaining a suitable start-point for the iteration were established.

Whole image geocoding necessitates resampling. The author turned her attention to this topic briefly in collaboration with the GEC-Marconi Research Centre. It was established that resampling a single-look image can alter the image statistics — which could have serious consequences on further use of that image. This work is detailed in Section 3.8 and also in a published paper reproduced as Appendix A.

Methods of obtaining position and height information from stereo SAR imagery were investigated. Previous studies have been hampered by the lack of suitable stereo SAR imagery. All the results published so far appear to have been obtained using methods based on photogrammetric approaches. Since ERS-1 will give accurate ephemeris data, the author established an analytic approach which uses the SAR range and Doppler equations and hence relies on the sensor position being known accurately. This approach is detailed in Chapter 4 along with an example of a photogrammetric approach.

Methods of obtaining position and height information using a combination of SAR and optical (or infrared) imagery were also investigated. Again, previous reported work appears to have used methods based on photogrammetric approaches. The author also established a

geometric approach which is based on intersecting a line, representing the optical look-angle, and a sphere representing the SAR emitted pulse. This geometric approach is detailed in Chapter 4 along with an example of a photogrammetric approach. Unfortunately, due to lack of suitable image data (see Section 1.3), it was not possible to demonstrate SAR/optical stereo.

The only suitable image data available for use were the SIR-B data described in Section 1.3. The author spent a considerable amount of time trying to check the validity of the image and header data. Many of the header data were shown to be incorrect. The author had to establish which of the images were usable and evaluate the required input parameters for the geocoding and stereo work. This necessitated modelling the sensor orbit so that the sensor position could be found at any time. This proved to be a surprisingly complicated task, as it requires knowledge of three different reference systems, which are in turn related to different time systems, as well as knowledge of the method of orbital parameter assessment. The SIR-B header data supplied one position and velocity vector for an unspecified time. In Chapter 5, details are given as to how the orbital data were established using only these two vector positions, while Chapter 6 describes how the SIR-B data were validated. It was established that two of the SIR-B images of the Mount Shasta could be used for point, not whole image, analysis.

A computer program `GEOCODE` was written in FORTRAN on a VAX Workstation. This program will perform both image-to-object and object-to-image geocoding. The results of geocoding the SIR-B imagery and the investigations as to how geocoding responds to errors introduced into the main input parameters, namely near-range and Doppler, are reported in Chapter 7. The effects of using different start-points for the iterative method of solving the non-linear equations was also addressed here. This type of analysis into the sensitivity to error of both image-to-object and object-to-image geocoding does not appear to have been reported in the literature.

A program `STEREO` was also written in FORTRAN on a VAX workstation. This program performs the analytic method, devised by the author, of obtaining position and height from stereo SAR. The results of applying this program to the SIR-B imagery are reported in Chapter 8. Again, the effects of introducing errors into the main input parameters were investigated and are reported in this chapter. Iteration start-points were also addressed here.

The objectives at the start of this study have been met, though, due to the lack of suitable image data, these have not been demonstrated as fully as had been hoped at the outset.

1.5 Scope of this Thesis

This thesis is divided into nine chapters. In order to be able to analyse a SAR image it is essential that the SAR processing method is understood. In Chapter 2, the principles of SAR operation, properties, and processing are given. Chapter 3 outlines methods of geocoding and then gives a detailed description of the geocoding technique chosen for use in this study. Error considerations are discussed here, along with the important subject of resampling and radiometric degradation. A section of this Chapter describes the ERS-1 mission and includes the results of an error budget study performed for it.

In Chapter 4, stereoscopy involving SAR imagery is considered. Both SAR/SAR and SAR/optical combinations are outlined in terms of both photogrammetric and analytic methods. Orbit, time, and reference systems are described in Chapter 5; these considerations are essential in this study (but rarely discussed in the literature) so that the sensor position can be predicted accurately at any time. In this study, SIR-B data were used (see Section 1.3). No precise ephemeris data were available and hence had to be calculated from the procedures detailed in Chapter 5.

The available SIR-B data were unfortunately deficient in header data and so detailed preliminary work had to be carried out on the images to see if they were suitable for further study. Chapter 6 describes the methods used to establish this and details how the data needed for the further work were assessed. In Chapter 7, the results of geocoding, both image-to-object and object-to-image, are given. A detailed error analysis was performed and is reported in this chapter. Chapter 8 details the results of a SAR/SAR stereo technique developed for this study. An error analysis of this technique is also reported in this chapter. The conclusions to this work are given in Chapter 9.

Chapter 2

Principles of SAR Imaging and Processing

2.1 Introduction

The SAR image formation process is very complicated, totally unlike that encountered in any conventional optical instrument. In order to gain an appreciation of the meaning of a SAR image, an understanding of this image formation process is essential. The purpose of this Chapter is to give a brief description of the operation of a SAR and the method by which the emitted signal is converted into an image.

This Chapter is not intended to be a definitive text on SAR. Hence, in most of the Chapter, certain simplifying assumptions have been made. In particular, it is assumed that the Earth being illuminated by the SAR is flat. This 'flat Earth' approximation is also assumed in many of the standard texts on the subject, e.g. [Hovanessian, 1980], [Elachi, 1988]. However, it should be noted that, unless specifically stated, a flat Earth has not been assumed in any of the subsequent work described in this thesis.

The Chapter is divided into six sections. The second outlines the fundamental principles on which the instrument is based. The next section discusses the properties of SAR data, including the effects of orbit and atmosphere. Sources of noise in SAR imagery are then considered. Section 2.5 addresses the important topic of SAR processing — an understanding of this is essential for successful analysis of SAR imagery. Finally, types of SAR processor are briefly outlined.

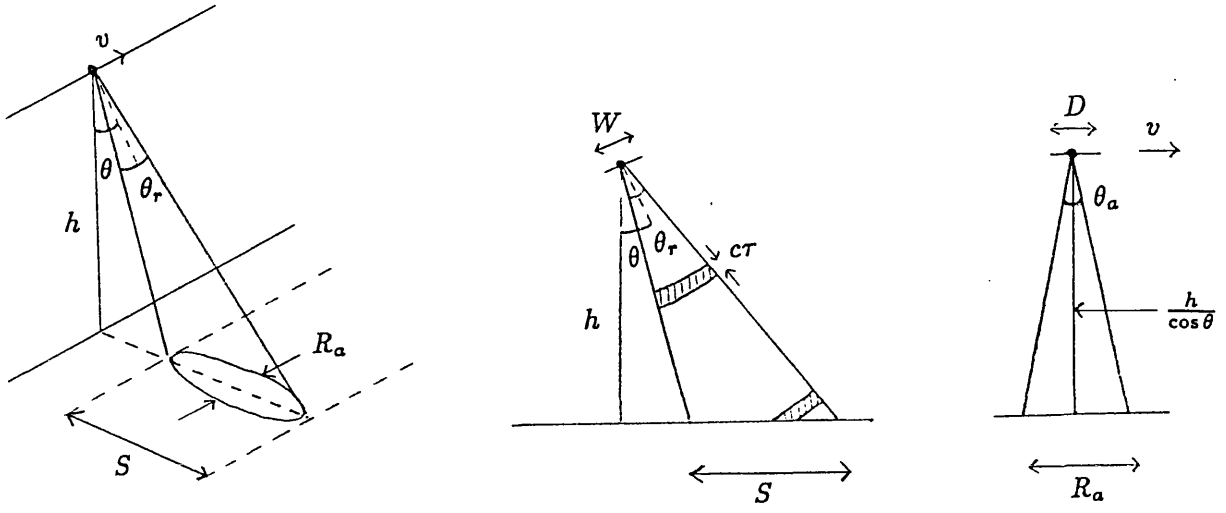

Figure 2.1: Geometry of SAR Imaging. (a) Geometry corresponding to a side looking imaging radar. (b) Geometry in the range plane (perpendicular to the satellite track). (c) Geometry in the azimuth plane. Following [Elachi, 1988]

2.2 Basic Principles

It is assumed that the reader is familiar with the general concepts of frequency and the Doppler effect [Whelan and Hodgson, 1971] and of sampling theory [Bracewell, 1978]. In the synthetic aperture technique, the Doppler information in the returned echo is combined with the time-delay information to generate a high-resolution image of the surface being illuminated by the radar.

The common imaging geometry is illustrated in Figure 2.1. The radar usually looks to one side of the moving platform and perpendicular to its line of motion. It transmits a short pulse of coherent electromagnetic radiation towards the ground. Points equidistant from the radar are thus located on a series of concentric spheres. The intersection of these spheres with the ground, modelled as a flat surface, gives a series of concentric circles centred at the nadir point (see Figure 2.2). The strength of the echoes from each point on the surface is determined by its radar reflectivity (commonly termed *backscatter*). Objects lying on a circle on the ground will produce reflections with a well-defined time delay but different Doppler characteristics. Identical Doppler shifts, but different time delays, are produced by points distributed on co-axial cones, with the flight line as the axis and the

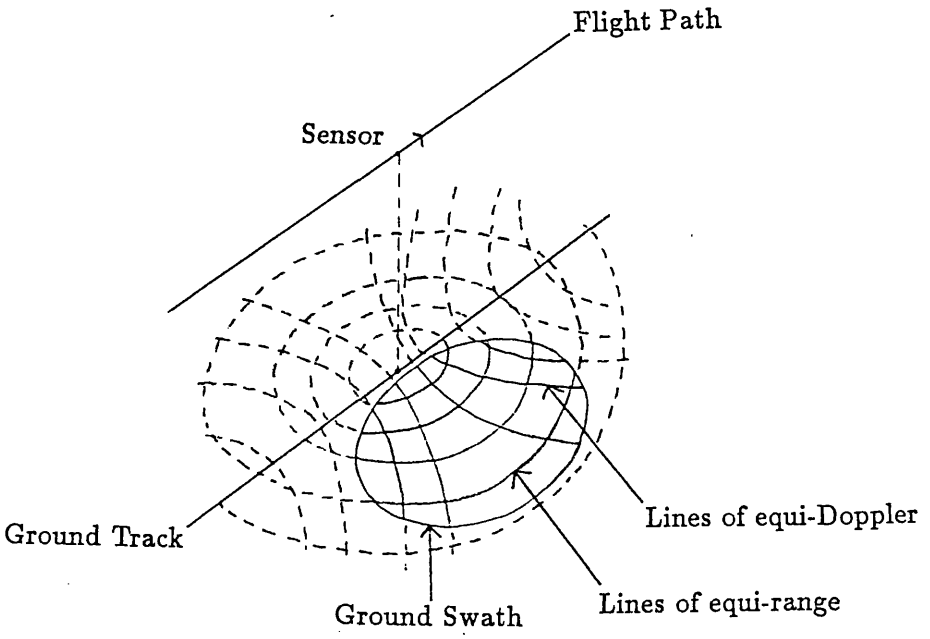

Figure 2.2: Coordinate system for SAR image formation. A set of circles and hyperbolae define the equi-range and equi-Doppler lines respectively. Following [Elachi, 1988].

radar as the apex. The intersection of these cones with the ground generates a family of hyperbolae, as indicated in Figure 2.2. Objects on a specific hyperbola provide equi-Doppler returns. Hence, each point on the surface can be uniquely identified by a specific time delay and specific Doppler.

The basis of SAR image formation is that the forward motion of the platform is used to construct a much longer effective antenna; the movement of the actual antenna allows it to act as a series of elements of a long array. This is illustrated in Figure 2.3. At each position along the track of the platform, the radar transmits a pulse and records the returned echo. To form the long, linear array, the pulse returns from each of the individual elements (i.e., from each position in the echo store) must be combined *coherently*, which means that they are added together after their phases have been synchronised. An appropriate phase correction must therefore be applied to each recorded echo across the whole synthetic aperture. This requires that the phase of each transmitted pulse must be controlled exactly and the echo return referenced to it, usually by means of a local oscillator which must provide phase stability over the entire length of the synthetic aperture. This requirement

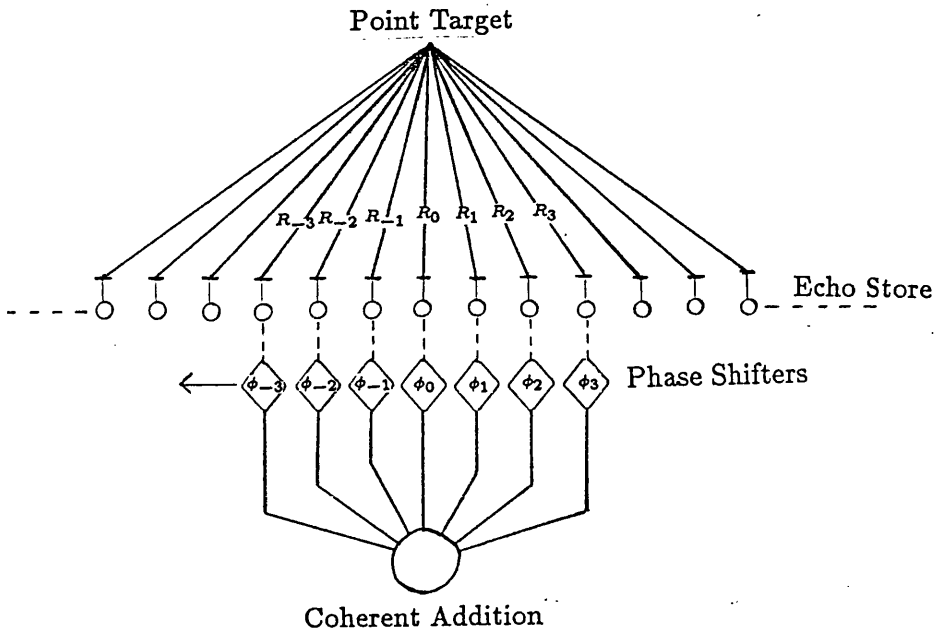

Figure 2.3: Construction of a SAR image of a point target by phase correction.

for coherence is the basic difference between a SAR system and a real-aperture side-looking radar.

The brightness of a specific image pixel is proportional to the echo energy contained in the time-delay and the Doppler return corresponding to the point on the surface being imaged. The resolution of the SAR imager thus depends on the accuracy of measurement of the differential time-delay and differential Doppler (phase) between two neighbouring points on the surface.

The situation is somewhat more complicated in reality. The radar transmits a pulsed signal in order to obtain the time-delay information. To obtain the Doppler information unambiguously, the echoes from many successive pulses are required, using a pulse-repetition frequency (PRF) which meets the Shannon sampling criterion. Thus, as the moving platform passes over a certain region, the received echoes contain complete Doppler and range-change histories for each illuminated point. These histories are then processed to identify uniquely each point on the surface and to generate the image. This is the reason that a large number of operations are required to generate each pixel in the image, a situation that does not arise with optical sensors. SAR processing, as stated in Chapter 1, can be

done either optically or digitally. In this thesis, only digital processing is considered.

One unique feature of SAR is that its resolution is *independent* of the platform altitude. This results from the fact that the image is formed by using the Doppler history and the differential time delays, none of which is a function of the range from the radar to the surface. This unique capability allows the acquisition of high-resolution images from satellites at high altitudes, providing the received echo is above the noise level.

2.2.1 SAR Basic Block Diagram

A simple block diagram of the essential features of a SAR system is shown in Figure 2.4. The transmitter provides high power amplification of the pulse produced in the pulse modulator. The generated pulse travels along a transmission line, through a two-way switch called a duplexer and is radiated out through the antenna. For systems that employ a single antenna for both transmission and reception, the duplexer has to protect the receiver from transmitter leakage. The receiver detects and amplifies the reflected signal. This signal is then mixed with the reference frequency provided by the stable local oscillator down to some intermediate frequency (IF). The stable local oscillator is employed to ensure that each transmitted pulse originating in the pulse modulator has exactly the same phase. The signal is then further amplified at the intermediate frequency stage. It is then further mixed down to zero carrier frequency with the output of an IF oscillator, which is phase-locked to the controlling stable local oscillator.

At the same time, the signal is converted to in-phase (I) and quadrature (Q) format (i.e., in-phase and 90° out of phase). For example, if the received signal is

$$S = A\cos(\omega t + \phi)$$

this is the in-phase part of the signal. The quadrature part of the signal is obtained by applying a phase shift of $\pi/2$, i.e.

$$S_I = A\cos(\omega t' + \phi); S_Q = A\sin(\omega t + \phi).$$

This gives the signal in its complex form, since

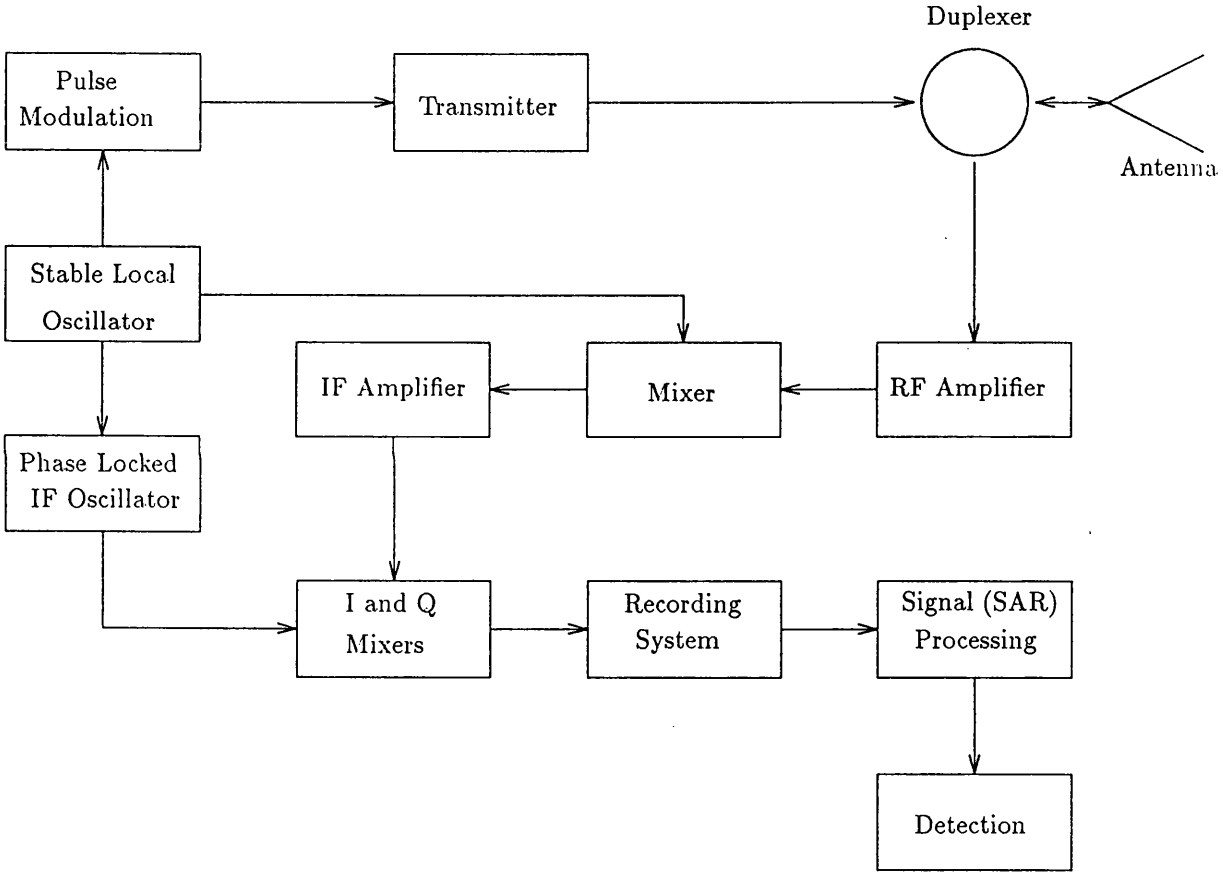

Figure 2.4: Simple SAR block diagram.

$$S_I + iS_Q = A \exp i(\omega t + \phi).$$

There then follows the most complicated part of the SAR, the signal processing, which produces an image for each range and azimuth position. The (coherent) signal processing in the SAR system is usually followed by square-law (power) detection and display of the resulting intensity image. SAR processing will be discussed later in this Chapter.

2.2.2 Resolution of Conventional Radar

A conventional side-looking radar achieves slant-range resolution through the use of pulsing and time delay sorting. If the radar transmits a very short pulse, reflected by a target at slant range R, then the round-trip propagation time between the radar and the target is given by:

$$\Delta T = \frac{2R}{c} \tag{2.1}$$

where c is the propagation speed of the radar wave.

The reflections from targets at different ranges will, naturally, arrive at the receiver with different time delays. If the transmitter pulse is very short, say of duration τ, then the returns from the targets at sufficiently different ranges will be non-overlapping in time. Specifically, the required separation is given by

$$R_s \geq \frac{c\tau}{2}. \tag{2.2}$$

Taking this as a measure of the slant-range resolution, R_r, then

$$R_r \approx \frac{c\tau}{2} \tag{2.3}$$

and the corresponding ground-range resolution is

$$\frac{c\tau}{2\sin\theta}, \tag{2.4}$$

where θ is the look angle.

In a simple pulsed radar, the generation of a pulse of duration τ requires a transmitter bandwidth of the order of

$$B_p \approx \frac{1}{\tau}. \tag{2.5}$$

Preservation of the range resolution $c\tau/2$ requires that the receiver also has a bandwidth of $B_p \approx 1/\tau$. The key to achieving fine range resolution is the use of wide-band radar transmitters and receivers, requiring the use of pulse compression as described in Section 2.5.1. The bandwidth sets the fundamental constraint on range resolution:

$$R_r \approx \frac{c}{2B_p}. \tag{2.6}$$

For example, a radar with a bandwidth of 1 GHz provides a theoretical range resolution of $\approx$ 15 cm.

The along-track or azimuthal cross-section of the antenna pattern has a half-power angular width of β radians. The corresponding along-track beam width at range R is

$$L \approx \beta R. \tag{2.7}$$

If the distance L is accepted as a measure of the along-track resolution R_a of this radar, then the only way to achieve fine resolution at long range is to make β very narrow. However, an antenna aperture with along-track dimension D, operating at its diffraction limit at wavelength λ, yields a half-power angular beam width of [Elachi, 1988]

$$\beta \approx \frac{\lambda}{D}; \tag{2.8}$$

which implies that

$$R_a \approx \frac{\lambda R}{D}. \tag{2.9}$$

To keep R_a small as R increases, D must be increased and/or λ decreased. Either of these options becomes unattractive beyond certain limits. Large-D antennae are incompatible with airborne or spaceborne operation; operation at very short wavelengths

leads to weather limitations due to atmospheric absorption; and finally, construction of a diffraction-limited large antenna can be costly as well as difficult. For example, a radar with $D \approx 10^3\lambda$ realises, at a slant range of $R = 10$ Km, an along-track resolution of $R_a \approx 10$m.

Hence, the potential to achieve fine range resolution appears to be restricted to relatively poor resolution at long operation ranges. The synthetic aperture technique can improve azimuthal resolution to the point where R_a is comparable to R_r.

The concept of the synthetic aperture technique can be explained in two ways, each of which leads to the same result: a synthetic array approach or a Doppler synthesis approach. Let us consider each in turn.

Synthetic Array Approach

Let us assume a radar sensor has an antenna length D and is moving at a velocity v. The antenna main beam footprint on the surface is equal to

$$L = \theta_a h = \frac{\lambda h}{D}. \tag{2.10}$$

As the sensor moves, successive echoes are recorded at points $X_1, X_2, \ldots$ along the flight line (see Figure 2.5). In addition, the target is assumed to be static (or its behaviour known) as each point is recorded.

The echoes are recorded coherently as a function of time and then combined in a processor to synthesize a linear array. The maximum array length that can be achieved is L (see Figure 2.5). The synthesized array will have a beam width of

$$\theta_s = \frac{\lambda}{2L}, \tag{2.11}$$

which is half that for a physical antenna of the same length. This is because the antenna pattern of a conventional radar antenna is determined from the phase shifts due to the one-way path difference between the antenna and the ground. In SAR, however, the synthetic antenna is determined by the phase shift caused by the *two-way* round trip between antenna and the ground. Hence, the synthetic aperture elements are effectively twice as far apart as in the physical aperture case, so the *effective* antenna length is twice L.
Substituting for L gives

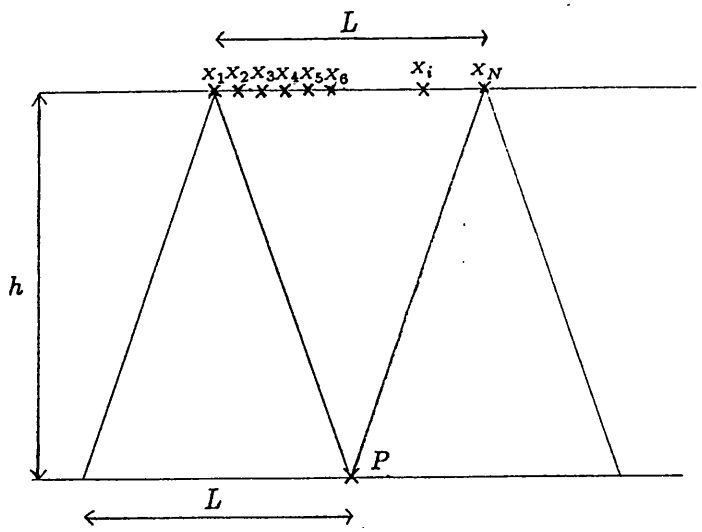

Figure 2.5: Geometry of a synthetic aperture array. Point P is visible from locations X_1 to X_N. The length of the synthetic aperture is equal to the real antenna footprint L. Following [Elachi, 1988]

$$\theta_s = \frac{D}{2h} \tag{2.12}$$

and the resulting array footprint on the ground is

$$R_a = h\theta_s = \frac{D}{2}. \tag{2.13}$$

This corresponds to the finest resolution that can be achieved using the synthetic array. This equation gives the important result that the ultimate azimuth resolution of a SAR is *independent* of the distance between the sensor and the area being imaged. In addition, finer resolution can be achieved with a *smaller* antenna.

Doppler Synthesis Approach

As the radar sensor passes over a target P, the Doppler shift of the echo from P will first be positive (when P enters the beam), then decrease to zero, then become increasingly negative until P exits from the beam (see Figure 2.6). The frequencies of the echo from P cover the region $f_0 \pm f_D$ where

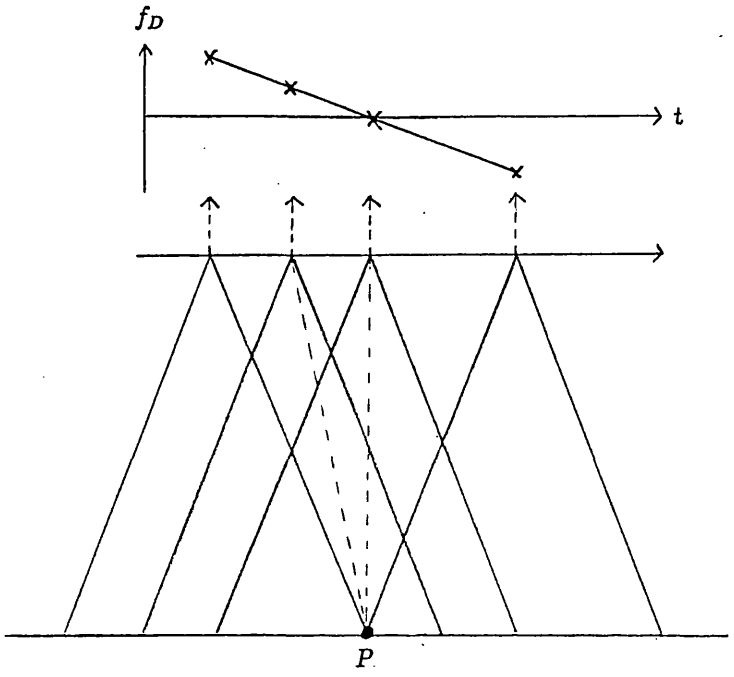

Figure 2.6: Doppler history of a point target. Following [Elachi, 1988]

$$f_D = \frac{2v}{\lambda}\sin\frac{\theta_a}{2} \approx \frac{v\theta_a}{\lambda} = \frac{v}{D} \tag{2.14}$$

and f_0 is the transmitted signal frequency.

If a neighbouring target P′ is positioned at a distance X_a along the azimuth dimension from P, the Doppler history from P′ will be identical to that from P but with a time displacement of $t = X_a/v$. The shortest time displacement that can be measured after processing a signal of spectral bandwidth $B_D = 2f_D$ is

$$t_m = \frac{1}{B_D} = \frac{1}{2f_D} = \frac{D}{2v}. \tag{2.15}$$

The finest possible resolution is then given by

$$X_a = R_a = vt_m = \frac{D}{2}, \tag{2.16}$$

which is the same as that derived using the synthetic array approach.

2.2.3 Stop-Start Approximation

It should be noted that in all (to the author's knowledge) SAR processing, it is assumed that the radar platform is considered as being stationary while a pulse is being transmitted and received, then moving along and stopping again for the next pulse transmission and reception. This is know as the *stop-start approximation*; it can be shown [Barber, 1985] to be valid to a high degree of precision for orbital SARs.

2.2.4 PRF Limits

Ambiguity will result if the PRF is so high that the return signals from two successive transmitted pulses arrive simultaneously at the receiver. This is called *range ambiguity.* Conversely, if the PRF is so low that the return is not sampled at the Nyquist rate, there will be a Doppler or *azimuth ambiguity.*

The upper limit of the PRF is fixed by the range beamwidth, θ_r, of the SAR antenna (see Figure 2.1). In order to avoid having the far edge echo from the current pulse arrive at the receiver at the same time as the near edge echo from the following pulse, we require that

$$T \geq \frac{2X}{c} \tag{2.17}$$

i.e.,

$$T \geq \frac{2h}{c}\frac{\tan\theta}{\cos\theta}\theta_r \tag{2.18}$$

$$= \frac{2\lambda h}{cW}\frac{\sin\theta}{\cos^2\theta} \tag{2.19}$$

or

$$\text{PRF} \leq \frac{cW\cos^2\theta}{2\lambda h\sin\theta}, \tag{2.20}$$

where T is the time between successive pulses, λ is the radar wavelength, W is the antenna width, θ is the look angle, h is the platform height, c is the speed of light, X is the slant range swath and θ_r is the beamwidth. The above equations assume that θ_r is small and

the pulse length is much smaller than T. Curvature of the Earth's surface is neglected.

A lower limit on the PRF is imposed by the requirement that the PRF must equal or exceed the maximum Doppler shift of the return signals. Targets at the centre of the broadside beam will return signals with zero Doppler shift. Targets ahead of broadside centre are characterised by a positive Doppler and those behind by negative Doppler frequencies. If the return of the target is shifted in frequency by an amount equal to the PRF, the receiver will be unable to distinguish the pulsed return signal from that of a target on broadside centre. Thus the PRF has to be sufficiently high to exceed the maximum Doppler shift of targets located at beam edge. The Doppler shift f_D due to a radial velocity v_r is given by

$$f_D = \frac{2v_r f_o}{c} = \frac{2v \sin\psi f_o}{c} \approx \frac{2v\psi}{\lambda} \tag{2.21}$$

where f_o is the radar frequency and $v_r = v \sin\psi \approx v\psi$. The angle to the first null of the transmitted beam is $\psi = \lambda/D$, where D is the antenna length. Thus

$$f_D = \frac{2v}{D} \tag{2.22}$$

and

$$\mathrm{PRF}_{\mathrm{low}} = f_D = \frac{2v}{D}. \tag{2.23}$$

Combining equations 2.23 and 2.20, we obtain

$$\frac{cW \cos^2\theta}{2\lambda h \sin\theta} \geq \mathrm{PRF} \geq \frac{2v}{D} \tag{2.24}$$

which may be written in the form

$$WD \geq \frac{4v\lambda h \sin\theta}{c\cos^2\theta}. \tag{2.25}$$

This condition yields a minimum antenna area (WD) required to avoid ambiguities. The last equation should really only be used in preliminary calculations; in actual design, the curvature of the Earth should also be taken into account.

2.2.5 Focussed and Unfocussed SAR

For a SAR to achieve its full capability, each received echo should be phase-shifted to take into account the fact that the distance between the sensor and target varies across the synthetic aperture. The phase shift needed to be added to the echo received at the $i^{\underline{\text{th}}}$ position along the synthetic aperture order to focus on a point is

$$\phi_{if} = \frac{4\pi}{\lambda}(h - r_i), \tag{2.26}$$

where h is the distance of zero Doppler shift, i.e. the closest range, and r_i is the range.

A synthetic aperture can be constructed over such a short length that no phase correction is necessary — this is called an *unfocussed* synthetic aperture. The signal processing in this case is greatly simplified, since adjustment of the returned pulses is not necessary. Conventionally, no phase correction is performed if the phase changes by less than $\pi/2$. It can be shown [Elachi, 1988] that the best azimuthal resolution available in an unfocussed SAR system is given by

$$R_a \approx \frac{1}{2}(\lambda h)^{\frac{1}{2}}. \tag{2.27}$$

In this case, the resolution *does* depend on the range to the target. The unfocussed aperture is only used in practice for applications where very high resolution in azimuth is not necessary or for short wavelength/range systems.

2.3 Properties of SAR data

In this section, some properties of SAR which have to be accounted for in the sensor or processor are outlined.

2.3.1 Antenna Sidelobes and Integrated Range Ambiguity Noise

The radar signal is transmitted into free space. The antenna characteristics define the gain, shape and width of the beam in which most of the energy is radiated, as well as the amount of energy radiated in the sidelobes. Upon reception, the antenna characteristics also define the amount of energy collected and the directions from which incident radiation is collected. Hence, the antenna acts as a directional filter which allows reception of the

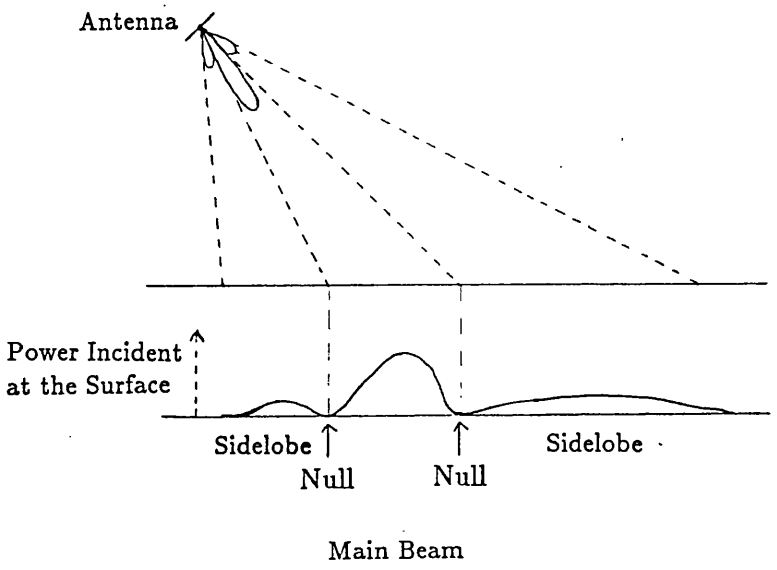

Figure 2.7: Antenna radiation at transmission and the corresponding surface illumination. Following [Elachi, 1988]

energy incident only from specific directions.

Antenna sidelobes (see Figure 2.7) result in the transmission of some energy into, and the reception of energy from, undesirable directions — i.e., from areas other than the swath being imaged. Thus, they can be thought of as a source of 'noise', since the echo of the $N^{\underline{\text{th}}}$ pulse from the main lobe could experience interference from the 'front' sidelobe of the $(N+1)^{\underline{\text{th}}}$ pulse and the 'back' sidelobe of the $(N-1)^{\underline{\text{th}}}$ pulse. Antenna sidelobe noise is commonly called *range ambiguity noise.*

Furthermore, the returned Doppler spectrum is usually not limited to the bandwidth B_D since signals with a larger Doppler shift may be received through the antenna sidelobes. Thus, at the zero offset case, the spectral region $-B_D/2$ to $B_D/2$ contains some signals from the spectral regions around f+PRF, f+2PRF, and so on. The ratio of the total energy from these bands relative to the total energy in the central band is called the *azimuth ambiguity.* A strongly reflective target in the direction of a large sidelobe is indistinguishable from the return through the main lobe and hence will introduce a false target in the direction of the main lobe. This effect is evidenced in SAR imagery where strong targets (e.g., a corner

reflector or radio tower) will show up as a number of bright points at regularly-spaced intervals. The brightest point is the 'true' point target location, other points decreasing in intensity on either side. These points are also known as *ghosts*.

To minimise this range ambiguity noise, the antenna response can be weighted to reduce the level of the sidelobes. Alternatively, a PRF could be used such that the strongest return coming through the sidelobes is not coincident in time with the main lobe echo, and therefore can be eliminated by time gating (see, for example, [Elachi, 1988]). In general, the strongest range ambiguity noise comes through those sidelobes closest to the nadir, as the nadir reflectivity is normally very high.

2.3.2 Range Migration

During integration along the synthetic aperture length, the target range changes by more than the range resolution. During this period, the range between the sensor and the target is

$$r(t) = \sqrt{{r_0}^2 + v^2t^2}, \tag{2.28}$$

where r_0 is the nearest range, v is the sensor velocity and t is the time. (The effect of Earth curvature has again been neglected.) Usually, $vt \ll r_0$; then,

$$r(t) = r_0 + \frac{v^2t^2}{2r_0} \tag{2.29}$$

and the return echo has a phase shift $\phi(t)$ equal to

$$\phi(t) = 2\pi\frac{2r(t)}{\lambda} = \frac{4\pi r_0}{\lambda} + \frac{2\pi v^2t^2}{\lambda r_0}. \tag{2.30}$$

If r_m is the maximum range at the edge of the synthetic aperture, then:

$$r_m = \sqrt{{r_0}^2 + \frac{v^2{T_D}^2}{4}} \approx r_0 + \frac{v^2{T_D}^2}{8r_0} \tag{2.31}$$

where T_D is the time that the target is illuminated, i.e. the dwell time.

The *range curvature*, r_c, is given by:

$$r_c = r_m - r_0 = \frac{v^2 {T_D}^2}{8 r_0}. \tag{2.32}$$

Now

$$vT_D = \frac{r_0 \lambda}{D} = \frac{r_0 \lambda}{2R_a},$$

so that

$$r_c = \frac{r_0 \lambda^2}{32 {R_a}^2}. \tag{2.33}$$

Relative to the slant range resolution R_r,

$$\frac{r_c}{R_r} = \frac{\lambda^2 r_0}{32 {R_a}^2 R_r}. \tag{2.34}$$

For example, in the Seasat SAR system, $R_r = R_a = 7$ m, $\lambda = 0.25$ m and $r_0 = 850$ Km. The range curvature, r_c/R_r, is 4.8; this means that a point moves through 4.8 resolution elements during the formation of the synthetic aperture.

Range walk is the difference in range to a point target from the position at which it enters the beam to that at which it leaves the beam. Range walk is due to orbit eccentricity, attitude errors, squint, Earth rotation and linear velocity of the target. The Earth rotation term depends on latitude, since the Earth's velocity is obviously different at different latitudes. Moreover, the angle between the swath velocity vector and the Earth's surface velocity varies, being equal to the orbit inclination angle at the equator (if the squint is zero) and zero at the poles. Range walk is hence a function of latitude and is not constant in the along-track direction, although it may be considered as constant in a sufficiently small interval. Range walk can be one or two orders of magnitude larger than the range resolution. For Seasat, range walk is normally quoted as 33 range samples. Range curvature and range walk together are known as *range migration* (see Figure 2.8), an effect that must be taken into account during processing.

To summarise, in the case of an orbital SAR, the two components of range migration originate from different causes: range walk is a result of the Earth rotation, non-circular satellite orbit and sensor squint angle, while range curvature is primarily a result of the changing imaging geometry.

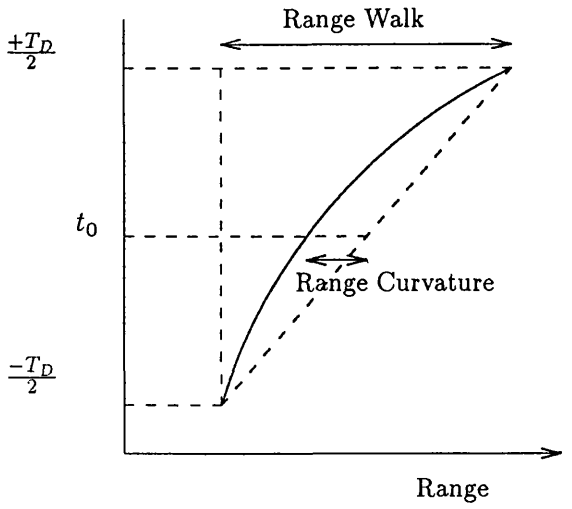

Figure 2.8: Range walk and curvature.

2.3.3 Attitude Errors

A SAR platform may yaw, pitch and/or roll away from its nominal attitude, thereby introducing an error into the antenna beam pointing.

A small roll (rotation about the axis of travel) pointing error does not affect the *location* of the imaged swath. However, the antenna gain pattern weights the echo shape; thus, roll will cause the weighting pattern to be mis-matched and hence introduce an error. If the roll can be detected, a correction may be applied; this is best performed in the processor.

A yaw error (rotation about the vertical axis) is more significant. It will displace the antenna footprint away from the zero Doppler. The Doppler spectrum of the returned echo will be displaced by a frequency δf_y. This can be corrected for in the sensor, by mixing a signal of frequency δf_y with the received echo, or in the processor. As δf_y is a function of look angle, the correction is different for different parts of the swath, making it easier to implement in the processor. After the image has been generated, the image pixel should be re-located to correct for the spatial displacement. This is done in the post-processor.

The effect of a pitch error (rotation about an axis perpendicular to the direction of travel) is similar to that due to a yaw error and results in a Doppler shift of δf_p being added to the return signal. This can be corrected in the processor by adding a constant frequency shift. When both pitch and yaw errors are present then, if each of the errors are known, the correction is straightforward. If they are not known, a clutterlock system

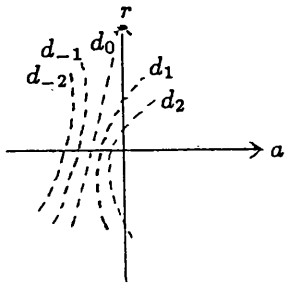

Figure 2.9: Curves of constant Doppler for an orbital SAR in an eccentric orbit for a rotating Earth.

(Section 2.3.7) must be used.

2.3.4 Earth Rotation Effects

As stated in Section 2.3.2, targets on the Earth's surface move with linear velocities that depend on their latitudes. These velocities are maximum at the equator and zero at the poles. The resulting Doppler effects lead to an asymmetry in response (see Figure 2.9). Three methods can be used to compensate for this.

1. Rotate the antenna beam in yaw about the satellite nadir to include the zero Doppler frequency direction. Since the rotation angle varies with latitude, the satellite attitude must be continuously adjusted. This is the method adopted in ERS-1.

2. Continuously adjust the receiver local oscillator frequency with respect to the transmitted frequency to cancel the effect.

3. Subtract the Doppler due the Earth rotation from the received signal during processing. This approach was used in Seasat SAR.

Earth rotation causes range walk effects (see Section 2.3.2). Phase errors can also be caused by the motion of targets on the Earth's surface. Target motion can be resolved into components in the along-track and across-track directions: the along-track component will cause azimuth defocussing, while the across-track component will introduce image shift.

2.3.5 Orbit Eccentricity

Orbit eccentricity causes a rate of change of altitude with time and displaces points imaged in the along-track direction. As with Earth rotation, compensation for altitude variation can be accomplished by rotating the antenna boresight axis in yaw, either by trimming the receiver local oscillator or during processing. It should be noted that, since the orbit perigee will migrate, the orbital position of maximum altitude change rate will necessarily migrate. These orbital effects, ellipticity and attitude errors, are deterministic and can be estimated directly or by analysing the data using clutterlock feedback (Section 2.3.7).

2.3.6 Atmospheric Effects

The ionosphere is composed of layers of free electrons and has a non-unity refractive index. The ionosphere affects phase velocity and hence phase coherence. While random scintillations in amplitude and phase caused by ionosphere irregularities can affect SAR imaging, it is likely that phase scintillations will be more detrimental than amplitude scintillations. The magnitude of phase scintillations can be calculated from time-delay formulations and is expected to have appreciable effect only for systems operating at frequencies lower than 1 GHz.

The presence of rain causes attenuation (and hence loss of signal) and scattering of the transmitted pulse, which can contribute to noise and possibly to range ambiguity.

2.3.7 Clutterlocking/Doppler Tracking

Since spacecraft velocities are high (compared to aircraft), narrow beamwidths are employed in order to reduce the Doppler bandwidth and hence the PRF. Earth rotation and spacecraft attitude variations cause Doppler shifts that are significant relative to the bandwidth and hence this usually necessitates the use of some type of Doppler tracking system. Doppler tracking involves the use of detectors to determine any drift. An error signal is generated and used for re-centering.

2.4 Noise Considerations

There are two sources of noise which will be considered here. The first is *speckle*; the second is thermal noise which will be considered in the *radar equation.*

2.4.1 Speckle

Distributed targets can be modelled as a number of randomly-positioned point scatterers within a resolution cell. Reflections from these scatterers constructively and destructively interfere with one another so that the returned echo is a signal that appears like noise. In the final image, a uniform extended target will be subject to random fluctuations in the pixel intensity. This phenomenon is known as *speckle* and causes SAR images of extended targets to have a somewhat grainy appearance. Hence, it is easy to see how azimuth compression gives no improvement in the signal-to-noise ratio, as discussed in Section 2.4.2. The main consequence of speckle is that a single measure of radar cross-section taken from one resolution cell can be subject to such great statistical fluctuations as to become meaningless. The only solution is to smooth out the variations by averaging over many resolution cells. The number of resolution cells averaged is called the number of *looks*, N. If N_a cells in azimuth and N_r cells in range are averaged, the total number of looks is given by

$$N = N_a N_r. \tag{2.35}$$

Of course, as N increases, the image resolution is proportionally degraded.

One way of describing the radiometric resolution of an image is by the factor [Elachi, 1988]:

$$Q = 10 \log \left(\frac{\sqrt{N} + 1}{\sqrt{N} - 1} \right). \tag{2.36}$$

Higher values of N lead to small values of Q (i.e., better radiometric resolution). However, for $N \geq 25$, a large increase in N gives a comparatively small improvement in Q. Of course, the increase in N should be traded off with the loss of resolution due to averaging. For Seasat imagery, four looks were normally used; for ERS-1, three looks have been proposed.

2.4.2 The Radar Equation

One of the factors that determines the quality of SAR imagery is the signal-to-noise ratio of a pixel in the image. In this section, only thermal noise will be discussed.

Consider, for a moment, a side-looking, real-aperture radar (SLAR) system. The trans-

mitter power P_t is radiated into free space by the SLAR antenna. The least efficient form of antenna is an isotropic one, which radiates power equally in all directions. The power density, P_i, incident on an imaginary sphere of radius R is, in this case,

$$P_i = \frac{P_t}{4\pi R^2}, \tag{2.37}$$

where $4\pi R^2$ is the surface area of a sphere.

Most antennae achieve better performance than the isotropic type and the ability to direct radiated power in the direction of a target is measured in terms of the antenna gain, G. This may be defined as the ratio of the power directed onto the target using the actual antenna to that which would have resulted from an isotropic antenna. The power density, P_d, incident on a target from a directional antenna with gain G is then

$$P_d = \frac{P_t G}{4\pi R^2}. \tag{2.38}$$

Radiated power incident on a target is scattered by it, to some extent, in all directions. A measure of the proportion of the incident power scattered or reflected in the direction of the radar is the radar cross-section, usually denoted as σ; the power density, P_e, of the echo received at the radar from a target of radar cross-section σ would be

$$P_e = \frac{P_t G}{4\pi R^2}\frac{\sigma}{4\pi R^2}. \tag{2.39}$$

The radar cross-section, σ, has units of area and is characteristic of the target on the ground. It can be thought of as a measure of the target's size as 'seen' by the radar.

If the radar antenna receives power over an effective area of A_e, then the total signal, S, received by the radar from a target of cross-section σ at range R is

$$S = \frac{P_t G \sigma A_e}{(4\pi)^2 R^4}. \tag{2.40}$$

Antenna theory gives the relationship between the transmitter gain of the antenna and the effective area of the receiver of the antenna as

$$G = \frac{4\pi A_e}{\lambda^2}; \tag{2.41}$$

hence,

$$S = \frac{P_t G^2 \lambda^2 \sigma}{(4\pi)^3 R^4}. \tag{2.42}$$

Signals received by radars are inevitably contaminated by noise. Noise can arise from random modulations of the radar pulse while propagating through the atmosphere, or due to fluctuations in the receiving circuits. Whatever the cause, noise constitutes a fundamental obstacle to radar designers in measuring the radar cross-section, and much effort has been expended in attempting to improve the signal-to-noise ratio, which is, for a simple SLAR:

$$\frac{S}{N} = \frac{P_t G^2 \lambda^2 \sigma}{(4\pi)^3 R^4 N_o}, \tag{2.43}$$

where N_o is the average noise power, obtained by considering the noise as an unwanted signal on its own.

However, in SAR processing, n received echoes are coherently added, and this leads to a significant change in the form of the expression for the signal-to-noise ratio. Construction of a synthetic aperture of n elements gives an improvement in the gain of the response to a point target by a factor of n^2. To find the appropriate form of the radar equation for the SAR case, we must determine the effect of SAR processing on the noise.

The noise contaminating each return echo can be modelled as a random sequence, N_i, of statistically independent sample values with random amplitude and phase. The noise power is defined as

$$\mathcal{E}[|N_i|^2] = N_o, \tag{2.44}$$

where $\mathcal{E}$ is the expected value. After coherent addition of n of these noise terms during the construction of the synthetic aperture, the noise power is:

$$\mathcal{E}\left[|\sum_{i=1}^{n} N_i|^2\right] = \mathcal{E}\left[\sum_{i=1}^{n} |N_i|^2\right] + 2\mathcal{E}\left[\sum_{i=1}^{n}\sum_{j=1}^{n} N_i^* N_j\right], i \neq j \tag{2.45}$$

$$= nN_o + 2\mathcal{E}\left[\sum_{i=1}^{n}\sum_{j=1}^{n} N_i^* N_j\right], i \neq j. \tag{2.46}$$

Since individual samples of the noise are independent of one another, the second term of

the equation averages to zero. Hence, the noise power after azimuth compression over n elements is just

$$\mathcal{E}\left[\left|\sum_{i=1}^{n} N_i\right|^2\right] = nN_o, \tag{2.47}$$

which is a gain in noise power of n. Thus, the signal-to-noise ratio after SAR processing, for a point source of cross-section σ at range R, is

$$\frac{S}{N} = \frac{P_t G^2 \lambda^2 \sigma n}{(4\pi)^3 R^4 N_o}. \tag{2.48}$$

This improvement in signal-to-noise ratio by a factor of n upon coherent integration is a standard result in radar theory.

The number of elements, n, which comprise the synthetic aperture is

$$n = T_s \times \text{PRF} \tag{2.49}$$

where T_s is the time interval over which the aperture is formed and PRF is the pulse repetition frequency. To obtain a resolution of R_a, an aperture length of

$$L = \frac{\lambda R}{2R_a} \tag{2.50}$$

should be used. T_s is related to L by

$$T_s = \frac{L}{v} = \frac{\lambda R}{2vR_a}, \tag{2.51}$$

so the final form of the SAR radar equation for a point target is

$$\frac{S}{N} = \frac{P_t G^2 \lambda^3 \sigma \text{PRF}}{(4\pi)^3 R^3 N_o 2vR_a}. \tag{2.52}$$

It should be noted that, for a point target in a SAR image, the signal-to-noise ratio *improves* with finer resolution. The form of the SAR radar equation for an extended target can be obtained by substituting $\sigma = \sigma_o R_a R_r$, where σ_o is the mean backscatter cross-section per unit area, in the above equation to give

$$\frac{S}{N} = \frac{P_t G^2 \lambda^3 \sigma_o R_r \mathrm{PRF}}{(4\pi)^3 R^3 N_o 2v}. \tag{2.53}$$

This equation is independent of the along-track resolution R_a, which means that SAR processing to any resolution can be carried out without altering the signal-to-noise ratio for the distributed targets within the final image. In fact, it can be shown [Freeman, 1986] that the signal-to-noise ratio for a distributed target is unchanged by azimuth compression.

Finally, the signal-to-noise ratio must be adjusted to take into account pulse compression, as described in Section 2.5.1. Here, the signal-to-noise ratio is improved by a factor $\tau_p B_p$, where τ_p is the compressed pulse length and B_p is the pulse bandwidth. Hence, the signal-to-noise equation for SAR can be written as

$$\frac{S}{N} = \frac{P_t G^2 \lambda^3 \sigma \mathrm{PRF} \tau_p B_p}{(4\pi)^3 R^3 N_o 2v R_a}. \tag{2.54}$$

2.5 SAR Processing

SAR data processing is performed by correlating the pulse returns with reference functions in the range and azimuth directions. The reference function in the range direction is related to the original pulse structure, while that in the azimuth direction is related to the phase (Doppler) history of the target as it moves through the synthetic aperture.

In the range direction, the reference function is a representation of the transmitted signal chirp, as discussed in Section 2.5.1. The signal processing involved in linear frequency modulation (LFM) compression is known as *matched filtering*, discussed in Section 2.5.2, and maximises the signal-to-noise ratio of the output signals.

In the azimuth direction, the reference function depends on the phase history. From Equation (2.30) we see that

$$\phi(t) = \frac{4\pi r_0}{\lambda} + \frac{2\pi v^2 t^2}{\lambda r_0}, \tag{2.55}$$

which can be written as

$$\phi(t) = \phi_0 + \frac{2\pi v^2 t^2}{\lambda r_0}. \tag{2.56}$$

Hence the phase is quadratic, as shown in Figure 2.10. It should be noted that phase is

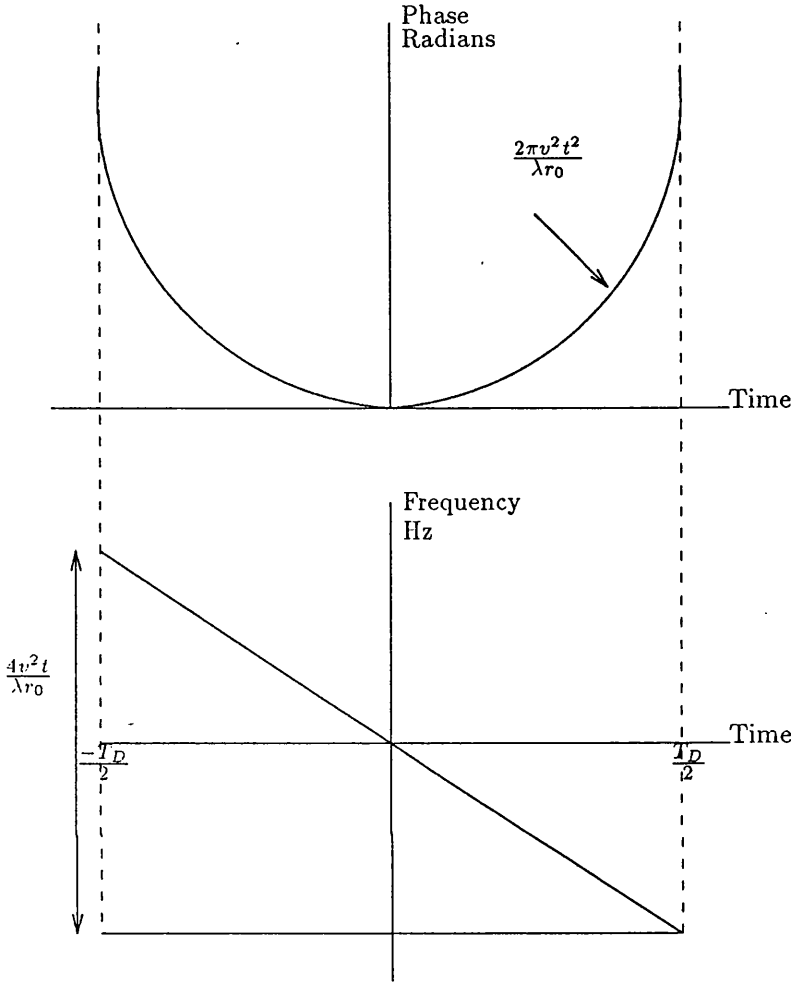

Figure 2.10: Phase and frequency excursions of a single point on the ground as a function of time.

ambiguous over multiples of 2π, so that phases of $\phi, \phi + 2\pi, \phi + 4\pi$ etc.. in the radar signal are indistinguishable.

The rate of change of phase with respect to time is the angular frequency ω:

$$\omega = 2\pi f = \frac{d\phi}{dt} = -\frac{4\pi v^2 t}{\lambda r_0}; \tag{2.57}$$

hence

$$f = -\frac{2v^2 t}{\lambda r_0}. \tag{2.58}$$

The maximum frequency excursion will occur for $t = T_D/2$; hence the two-sided frequency

excursion will be twice this value, as shown in Figure 2.10.

Hence, the process of matching the phases of the echoes can be thought of as a frequency-domain matched filtering process. In this respect, it is very similar to the matched filtering of a chirped pulse in radar pulse compression. Hence, it is often referred to as *azimuth compression* and the characteristic response of a point target in azimuth is often referred to as an *azimuth chirp*.

The propagation velocity of the range pulse is the speed of light, while the azimuth chirp propagates at the forward speed of the platform, v. The range resolution is $c/2B_P$, while in azimuth it is v/B_D. Hence, even though $B_D \ll B_P$, the resolution in both range and azimuth directions can be similar. This difference in frequency modulation due to the range chirp and the azimuth chirp means that they can be decoupled in the received signals.

In order to set up the data in the SAR processor for azimuth compression it is necessary to take samples from each pulse, i.e. to read only the azimuth 'columns'. Unless due care is taken, this process can become inefficient and very time-consuming. Numerous techniques exist for reorganising the data; the most common method used, as it is both simple and efficient, is to transpose the data so that they are stored in column (azimuth) form rather than row (range) form, a process known as *corner-turning*. This transpose operation can itself be carried out in a number of ways, depending on the computer system employed.

2.5.1 Pulse Compression

In Section 2.2.2, it was stated that fine resolution in range could be obtained by transmitting a short sequence of pulses of duration τ — see Equation (2.3). To achieve a slant range of better than 10 m, a pulse of shorter than 67 ns would have to be transmitted. However, in practice, particularly at long range, it is not possible to build a transmitter that provides the high peak power necessary for an adequate signal-to-noise ratio performance over such a short pulse.

The solution to this problem is to use *pulse compression*, in which a long pulse is transmitted such that the average transmitted power

$$P_{av} = P_t \tau_p \mathrm{PRF} \tag{2.59}$$

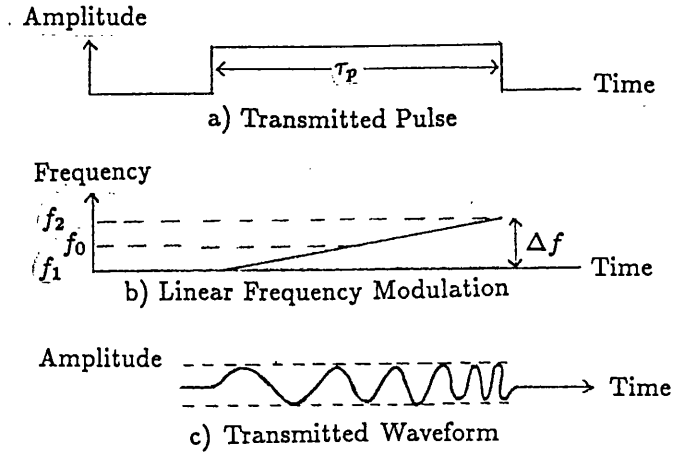

Figure 2.11: Transmitted waveform of an LFM pulse. Following [Hovanessian, 1980]

is kept at a high level, while the peak power, P_t, is lowered. The same amount of energy then impinges on the target, preserving the signal-to-noise ratio. In addition, this offers the high resolution associated with a short pulse because processing of the received signals allows *compression* from low resolution to high resolution.

Many kinds of pulse waveforms have been used in pulse compression; the simplest to understand — and probably the most widely used — is the linear frequency modulated (LFM) pulse, usually known as the *chirp*. It consists of a long pulse, of amplitude A and duration τ_p, over which the frequency is changed linearly as a function of time. This is illustrated in Figure 2.11, in which a rectangular pulse is shown, along with the LFM sweep over the bandwidth B_p from frequencies f_1 to f_2 over a time τ_p. The rate of change of frequency with time is often called the FM slope or the *chirp rate* and may be positive or negative.

When an LFM pulse has been transmitted and the return echo received by the radar, the signals must undergo pulse compression to obtain high resolution. The processing involved is known as *dechirping* and can be considered as the removal of the frequency modulation from the returned echo (see Figure 2.12). This is achieved by applying a time delay that varies linearly with frequency, so that the lowest received frequency f_1 is delayed the longest while the highest received frequency f_2 is not delayed at all. Hence, initially-received low frequencies are made to wait while subsequently-received higher frequencies

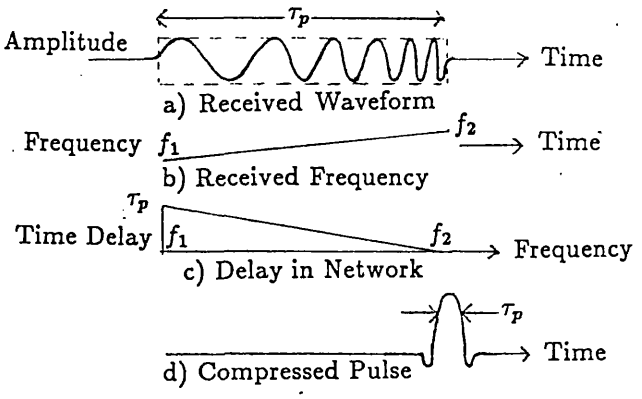

Figure 2.12: Received waveform of the FM pulse and subsequent pulse compression. Following [Hovanessian, 1980]

are delayed by progressively shorter amounts.

Another feature of pulse compression is that the peak power of the pulse is increased by a factor $\approx \tau_p B_p$, which is known as the *time-bandwidth product* of the chirp. In the radar equation for pulse compression, a corresponding improvement in the signal-to-noise ratio of $\tau_p B_p$ occurs.

2.5.2 Matched Filtering

The simplest way to consider matched filtering in LFM pulse compression is as a correlation between the received signal and the reference waveform. The received signal is a combination of the echoes from a large number of point targets in the scene. When this signal is correlated with the reference response corresponding to one pixel in the imaged scene, the output will be maximum when the echo from the targets in that pixel is exactly the reference. All other echoes from the other pixels will not match exactly with the reference, resulting in reduced outputs.

Consider just one pulse of duration τ_p; the transmitted pulse will have the form

$$S_o(t_n) = \exp[2\pi i(f_o t_n + \frac{1}{2}\alpha t_n^2)] \quad \text{for} \quad \frac{-\tau_p}{2} \leq t_n \leq \frac{\tau_p}{2}. \tag{2.60}$$

The received echo of amplitude A from a *point* reflector on the ground will have the form

$$S_i(t_n) = A \exp\left[2\pi i(f_o(t_n - t_D) + \frac{1}{2}\alpha(t_n - t_D)^2\right], \tag{2.61}$$

where f_o is the centre (carrier) frequency of the transmitted chirp, t_n is the time measured from the centre of the pulse, t_D is the round-trip time from the radar to the point and back again, and α is the ratio of the bandwidth to the pulse duration (B_p/τ_p).

Normally, the carrier frequency (f_o) is mixed out. In the correlation that follows, time-symmetric forms of the transmitted and received pulses are used for convenience; hence, the start of transmission occurs at $t_n = -\tau_p/2$ so that $t_n = 0$ coincides with the centre of the transmitted pulse. Correlating the two equations over the values of t_n for $t_D - \tau_p/2$ to $t_D + \tau_p/2$ gives:

$$S(t_D) = \int_{-\frac{\tau_p}{2}}^{\frac{\tau_p}{2}} S_o(t_n) S_i^*(t_n) dt_n \tag{2.62}$$

The reference function usually extends over a time longer than τ_p so as not to affect the integration limits [Elachi, 1988].

$$S(t_D) = A \int_{-\frac{\tau_p}{2}}^{\frac{\tau_p}{2}} \exp[\pi i \alpha t_n^2] \exp[-\pi i \alpha (t_n - t_D)^2] dt_n \tag{2.63}$$

$$= A \exp[-\pi i \alpha t_D^2] \int_{-\frac{\tau_p}{2}}^{\frac{\tau_p}{2}} \exp[2\pi i \alpha t_n t_D] dt_n \tag{2.64}$$

$$= A \exp[-\pi i \alpha t_D^2] \frac{1}{2\pi i \alpha t_D} (\exp[\pi i \alpha t_D \tau_p] - \exp[-\pi i \alpha t_D \tau_p]) \tag{2.65}$$

$$= A \exp[-\pi i \alpha t_D^2] \frac{\sin(\pi \alpha t_D \tau_p)}{\pi \alpha t_D}. \tag{2.66}$$

The output is usually normalised by a factor τ_p to produce a function with a peak value of unity. Therefore,

$$S(t_D) = A \tau_p \exp[-\pi i \alpha t_D^2] \mathrm{sinc}(\alpha t_D \tau_p) \tag{2.67}$$

which is a sinc function of width $1/B_p$, peaking at $t_D = 0$.

If there are two targets, A and B, at the same range but displaced by a distance X, i.e. a time displacement of $\Delta t = X/v$, the matched filter (correlator) output will be

$$\begin{aligned} S(t_D) &= A\tau_p \exp[-\pi i \alpha t_D^2]\mathrm{sinc}(\alpha t_D \tau_p) + \\ & \quad B\tau_p \exp[-\pi i \alpha (t_D - \Delta t)^2]\mathrm{sinc}(\alpha (t_D - \Delta t)\tau_p) \end{aligned} \tag{2.68}$$

which gives two peaks displaced by a time displacement Δt.

For the case in which a scene with a large number of targets is imaged, each pixel has a corresponding reference function, which makes the correlation process very complex computationally. A significant reduction in the number of computations is achieved by using the fact that, when transformed to the frequency domain, correlation becomes multiplication. Thus, the operation may be achieved by taking the Fourier transform of the received signal, multiplying it by the frequency-domain reference function and then performing an inverse transform. If a reference function has N elements, the correlation in the time domain requires of the order of N^2 multiplications. In the case of the fast Fourier transform (FFT) approach, only of the order of $2N \log N + N$ operations are required. Considering that N is usually several thousands, the frequency-domain approach reduces the number of operations required by typically more than two orders of magnitude.

2.5.3 Doppler Blocking

Azimuth compression in the SAR processor relies on the fact that the phase/Doppler history can be modelled precisely. This is, however, not always possible in practice. In spaceborne SARs, the antenna would ideally point at a right angle to the direction of the SAR's velocity relative to the ground, making the beam centre coincident with the zero-Doppler plane. However, this orientation is very difficult to maintain and it is likely that the Doppler characteristics of the beam will vary as the satellite moves in azimuth, although variations from pulse to pulse will normally be slight. For ERS-1, this Doppler frequency variation could be as much as 120 Hz in range and up to 100 Hz in azimuth across an ERS-1 image [Sowter and Smith, 1989].

As stated previously, the Doppler history can be modelled as a linear function of time

and can be written in the form

$$f_D = f_0 + f_1 t, \tag{2.69}$$

where f_D is the Doppler frequency, f_0 is the Doppler centre frequency and f_1 is the Doppler rate.

For practical reasons, it is not possible to determine the Doppler centre frequency, f_0, for every point in the image; so normally f_0 is sampled at given time intervals and applied to small areas of the image. For ERS-1, f_0 will be estimated to an accuracy of 50 Hz. These f_0 values can be interpolated by various means and applied at each position. However, the interpolated f_0 values are only approximations and any error can result in a mis-location of the target.

For ERS-1, *Doppler blocking* will be applied in azimuth compression. Here, the data are divided up to small blocks and each block is processed separately with a fixed f_0. In this case, mismatch of f_0 values between blocks can result in some targets being imaged twice, or some targets not being imaged at all, depending on the type of mismatch. For ERS-1, the block mismatch is expected to be insignificant provided that the yaw steer mechanism functions correctly. However, it is thought that it will be a problem in the X-SAR programme.[1]

2.6 SAR Processors

As stated previously, only digital SAR processors are considered in this report. The design of a SAR processor (both algorithmically and architecturally) comprises essentially two stages. The first stage involves the accurate modelling of the SAR response to both point- and continuous-field targets. This model must allow for the definition of all of the functions needed to reconstruct the image scene from the received signal. Hence, it must include all orbital parameters and required corrections (e.g., planetary motion, attitude drifts, orbital ellipticity, etc.). Where parameters cannot be measured, the required information must be extracted from the data itself, for example by clutterlocking (Section 2.3.7).

The second stage involves the definition of a computationally-efficient mathematical

[1]This is the result of verbal communication with DLR, Germany.

procedure to implement the algorithms. An efficient procedure can lead to major savings in both processing time and processor cost.

Although many types of SAR processors have been developed, the main ones are as follows:

- Correlation
  - Time Domain
  - Frequency Domain
- Phase Array Formation
- Deramp
- Azimuth Surface Acoustic Wave (SAW)

Figure 2.13 shows the essence of the SAR processing procedure. Here, signals returned from the ground for each transmitted pulse are convolved with a range reference function that is a duplicate of the transmitted pulse. This results in range-compressed signals. A corner-turn is then applied so that the signals are 'lined up' for the next convolution. In this step, the range-compressed signals are correlated with the azimuth reference function, namely the modelled Doppler response. The accuracy of the azimuth reference function relies on the precision with which the parameters used to define this function can be found, i.e. how well the clutterlocking etc. works. If the Doppler response is not predictable, e.g. if there is a train in motion on the ground, then the modelled Doppler response of the train will be incorrect and the train will be misplaced on the output image. The result of azimuth convolution is an azimuth-compressed signal that can then be sampled to form part of the output slant range image.

In almost all processors, the range compression is carried out first since it is fairly straightforward. The main complexity and most of the computation is in the azimuth processing. SAR correlation (both range and azimuth) can be carried out in the frequency domain using the fast Fourier transform (FFT) as a means of reducing the number of arithmetic operations (as stated previously). On reception of an echo signal, an FFT is applied (see Figure 2.14); the result is multiplied by the range reference function and an inverse FFT performed. The output range-compressed signal is then input to a corner-turning memory as one row. Successive echoes follow the same route until all the memory

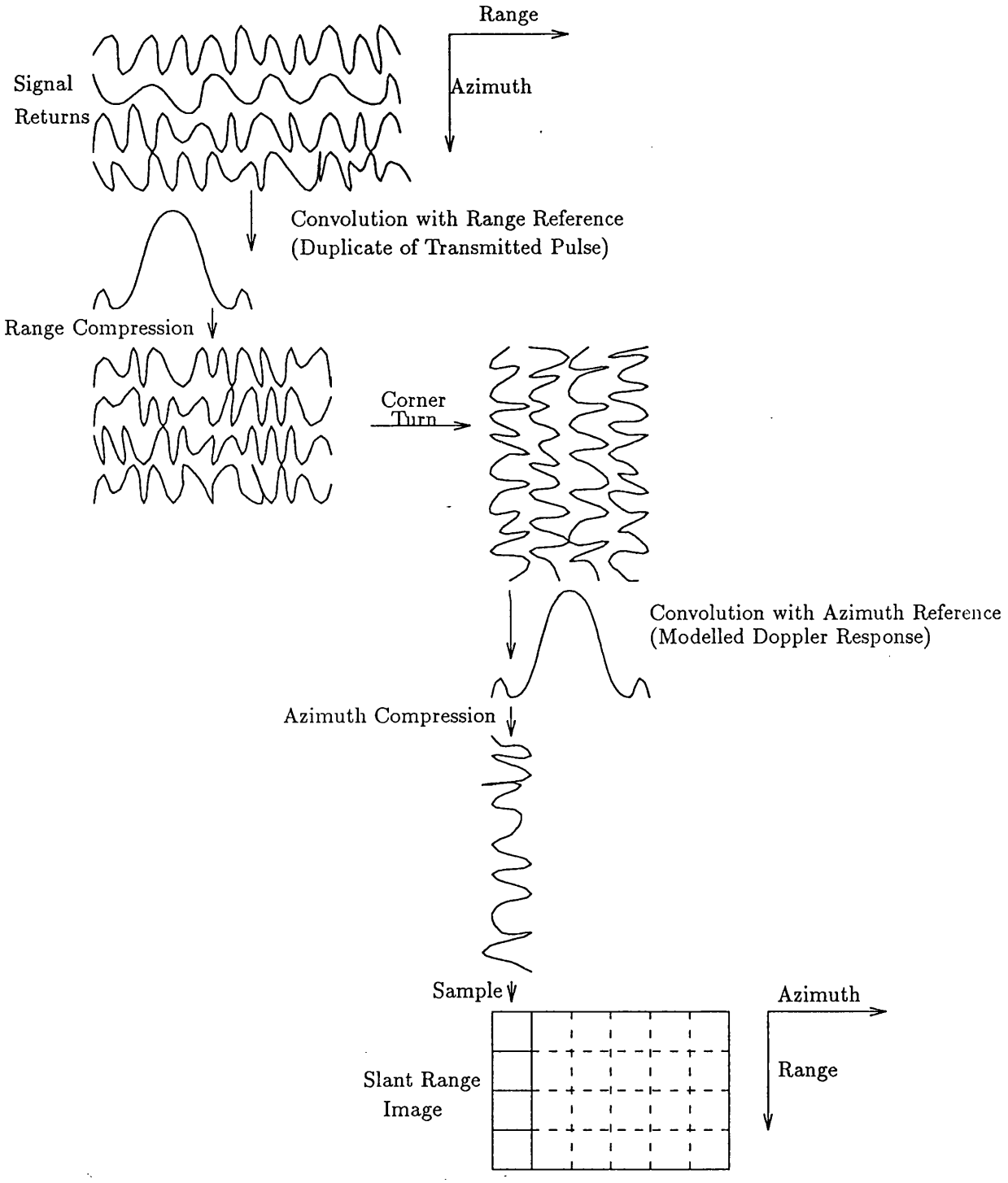

Figure 2.13: Simplified SAR Processing Procedure

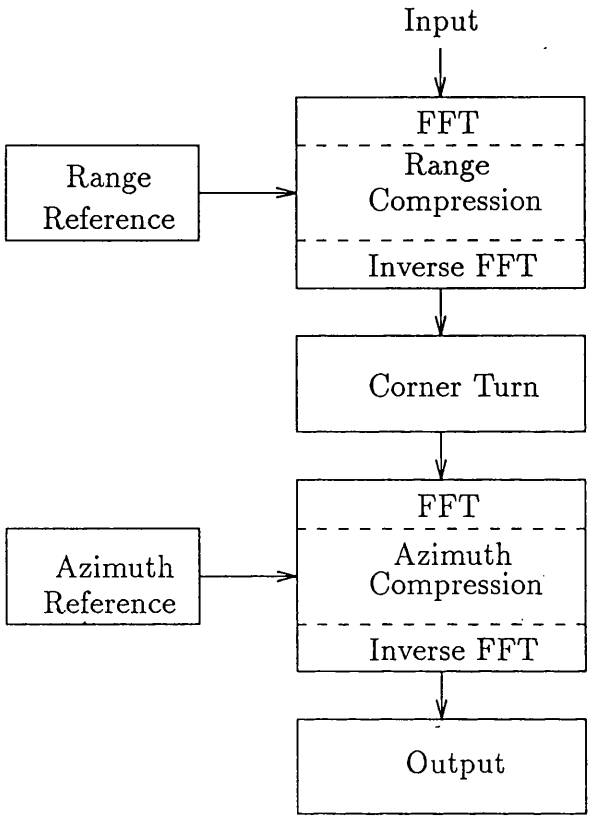

Figure 2.14: Simplified block diagram of a SAR processor using the frequency domain approach.

rows are full (the number of memory rows is equal to the length of the synthetic array). The data are then read, one *column* at a time, and azimuth-correlated using a similar FFT procedure. The output data are then input to a multi-look memory.

It should be noted that any efficient linear transform, not only Fourier, that exhibits the convolution property could also be used — e.g., Hadamard.

2.7 Summary

In this Chapter, the fundamentals of SAR operation and the processing involved to produce a SAR image have both been outlined. Some knowledge of these procedures is essential if the interpretation of SAR images is to be effective. Since SAR image data come in various forms — for example complex or detected, single-look or multi-look, focussed or unfocussed, etc. — one must be able to understand what these terms mean and interpret the image accordingly. Other effects, such as Doppler blocking and ghosting, should also

be considered in image analysis.

SAR image assessment is further complicated by the effect of the terrain relief of an area being imaged. This is known as *geometric distortion* and will be discussed in the next Chapter.

Chapter 3

SAR Geocoding Techniques

3.1 Introduction

This chapter summarises the major techniques for geocoding SAR imagery and gives a detailed description of the type of geocoding chosen for use in this thesis. The following section considers some of the problems that can occur in SAR image interpretation; these have a bearing on the accuracy of the geocoding process. Section 3.3 describes the different types of geocoding algorithms that are used and points out the advantages and disadvantages of each type of algorithm. A short general discussion of geocoding is given in Section 3.3.4. In Section 3.4, a detailed description of the SAR processor based method of geocoding is given. It is this type of geocoding that was chosen as most appropriate for the work of this thesis. There are two basic approaches to this type of geocoding, image-to-object and object-to-image; both are described in this Section. Error considerations of geocoding are addressed in Section 3.5. The ERS-1 satellite is considered in Section 3.6, where the geocoded products of the forthcoming ERS-1 mission are outlined. The results of an error budget study performed for the ERS-1 geocoding project are summarised in Section 3.7, giving a theoretical error for geocoding. Radiometric considerations of geocoding are addressed in Section 3.8. In Section 3.9, the computational aspects of geocoding are addressed.

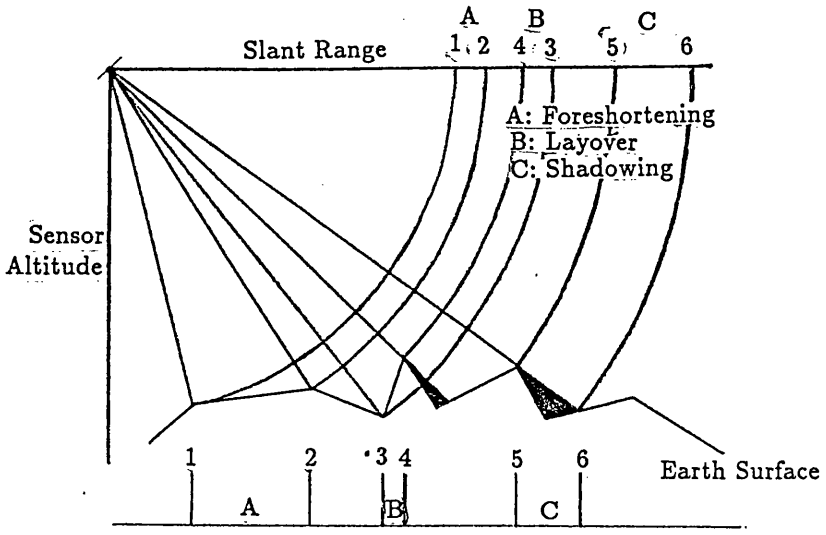

Figure 3.1: Geometric Distortions Due to Terrain Elevation Effects

3.2 SAR Image Considerations

Due to the radar imaging principle (i.e., signal travel-time measurements), terrain relief can introduce significant geometric distortions in the across-track direction, which also results in corrupted radiometric information in the affected part of the SAR image. These distortions are illustrated in Figure 3.1 and can be characterised as follows:

foreshortening in areas where the slope of the terrain is towards the sensor, the distances of adjacent targets are shortened in ground range. This results in a compression of the image signal information in such areas.

layover is the extreme case of foreshortening, where the difference in signal travel-time of adjacent targets is zero or negative. The signal content of these areas is 'folded over'.

shadow when the slope of the terrain is bent away from the sensor and the slope is steeper than the incidence angle of the radar beam, then the respective area does not get direct illumination, and is hence shadowed. No object information is available in the shadow areas.

Foreshortening, layover, and shadow depend heavily on the look angle of the sensor, which is the angle between the line-of-sight and the vertical. As the look angle decreases, the occurrence of layover increases and shadowing decreases. On the other hand, large look angles result in a higher amount of shadow.

Radar primarily senses roughness or geometric characteristics of the surface. However, it also senses the dielectric properties of the material of reflectors. Man-made objects such as bridges, roads, buildings, dams, etc. often cause bright saturated returns (which may also blur parts of the image), or do not appear at all, depending on their orientation relative to the look direction. Some objects, such as smooth water surfaces, reflect the radar pulses away from the sensor like a mirror and therefore normally appear black in the image. Furthermore, the ability of a radar wave to penetrate vegetation, and multiple backscattering of the wave as it passes through the vegetation canopy, results in characteristic, rather bright, responses to forest areas.

The ability to identify objects by examining these radar backscatter properties is significantly reduced by the presence of radar *speckle* (see Chapter 2). This effect in SAR images results from the fact that coherent pulses are reflected from the ground, leading to constructive and destructive interference of echoes within a single resolution cell. A common technique for reducing speckle is to average a number of independent looks. A large number of looks ensures smoother image grey tones and, consequently, easier interpretation — but at the cost of reduced resolution. Experience with Seasat SAR images has shown that three or more looks should be averaged. In the ERS-1 SAR processor, it is intended that three looks will be again averaged. However, speckle cannot be totally eradicated and is expected to remain a significant problem in ERS-1 image analysis.

3.3 Geocoding Algorithms

In general, geocoding algorithms can be divided into three main categories:

1. polynomial methods;
2. parametric methods;
3. SAR processor-based methods.

Let us consider each method in turn.

3.3.1 Polynomial Methods

This approach to geocoding is based on the warping of the SAR image relative to a reference datum, usually a 2-D topographic map, using a polynomial interpolant. It relies on the

identification of a large number of ground control points (GCPs) in the image to allow computation of the polynomial coefficients of the mapping function.

The accuracy of this method is therefore dependent on the accuracy of the location of the GCPs. However, due to the effects discussed in Section 3.2, difficulties exist in locating the GCPs in SAR imagery. This is so even with airborne SAR, as shown with SAR 580 [Dowman, 1984]. Also, a variety of ground features can have similar radar backscatter and be indistinguishable when observed at particular wavelengths and/or look-angles [Blom, 1988]. The availability of GCPs can also be a limiting factor in poorly-mapped areas. Furthermore, the method cannot cope with local distortions, such as those related to varying relief in SAR imagery. Reviews of this method and results can be found in [Leberl, 1990], [Dowman, 1984] and [Diefallah, 1988]

Hence, this method, being fundamentally limited, is usually intended as a back-up for parametric methods, mainly in flat areas. Its main advantage is that it is unrelated to the specific SAR imaging geometry and hence does not rely on the accuracy of the ephemeris data.

3.3.2 Parametric Methods

The parametric approach attempts to model the geometry that existed during data acquisition and has been developed from conventional photogrammetric techniques. The approach can be broadly sub-divided into two alternative methods:

- geocoding using an adjustment of preliminary satellite ephemeris and sensor imaging parameters;
- geocoding based on image simulation.

Neither of these methods take account of the effects of the SAR processor. Let us consider each of them in turn.

Parametric Method using an Adjustment of Preliminary Satellite Ephemeris and Sensor Imaging Parameters

The definition of an analytic sensor model is required to be able to account for topographic effects in the SAR image. Such a model gives a mathematical relationship between a point

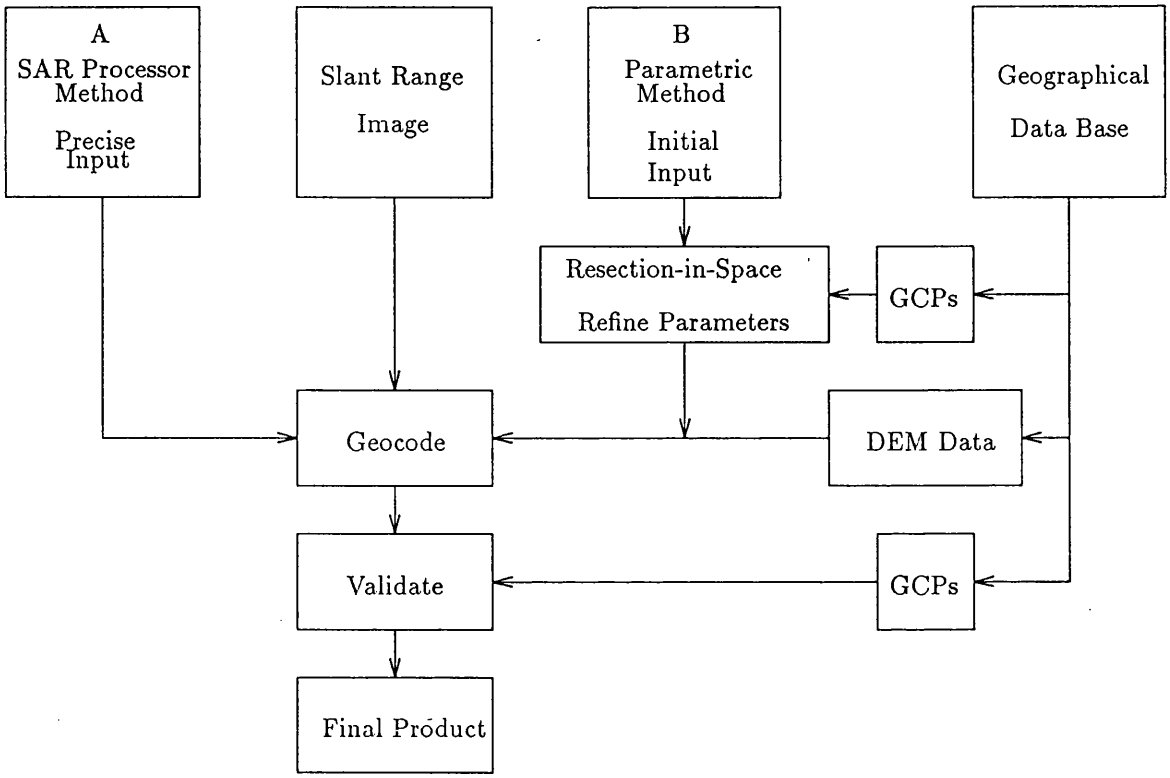

Figure 3.2: Flowchart of Radar Image Geocoding Methods

on the ground (denoted as *object space*) and the corresponding position of the synthetic antenna — and, consequently, the corresponding point in the SAR image (denoted as *image space*). Such geocoding algorithms can be grouped into two categories: those that use an accurate analytic sensor model and those that use approximations as initial values for the parameters, then reconstruct an analytic sensor model by means of GCPs. Figure 3.2 shows flow diagrams of these methods: node A describes the former method and node B the latter. However, in past aircraft and satellite missions, not all the relevant parameters of the sensor model have been received with the required accuracy. Although orbit accuracy for ERS-1 is intended to be less than a metre, the precise orbit may not be available to the radar image post-processor in the required timescale.

To be able to overcome the lack of precise information, the method of node B can be employed: although this is, in principle, the same as the algorithm of node A, an initial resection-in-space refines the parameters of the sensor model. Resection-in-space is a standard photogrammetric technique for images with perspective geometry, permitting the calculation of the parameters of the exterior orientation. This resection-in-space can

be performed using a technique developed for radar imagery known as *bundle adjustment.* This method relies on the availability of at least limited GCPs, which are used to refine the approximately-given orientation parameters using least squares techniques.

The parameters of the analytic sensor model are determined by measuring the image co-ordinates of the GCPs and constructing sets of range and Doppler equations, one for each GCP. The parameters of the sensor model typically include range offset, imaging time, squint, sensor position, and sensor velocity. These non-linear equations are built into 'observation equations' which are then solved for unknowns by an iterative technique. After each iteration, the consistency of the range and Doppler equations is checked using the updated parameters of the sensor model, the process being terminated when the remaining discrepancies fall below a pre-defined limit. The image is transformed into a map reference system using these calculated range and Doppler equations. Terrain effects can be accounted for if a digital elevation model (DEM) is available.

Although the method of node B does not rely on having precise ephemeris data, there still remain a number of disadvantages. Firstly, if the image distortion is due to processor inaccuracies, this method will give erroneous results; moreover there could be convergence problems with very inaccurate preliminary data. Secondly, operator interaction is required. Finally, difficulties can exist in measuring the GCPs. This method is described in more detail in [Raggam, 1987] and [Meier and Nuesch, 1985].

Geocoding Based on Image Simulation

The generation of a simulated (synthetic) radar image using a defined radargrammetric mapping model is called *image simulation.* For this method, a DEM is required. The procedure can be divided into the following main steps [Domik *et al.*, 1984]:

1. generation of a DEM, either from a map or other external sources, or by stereo mapping;
2. verification and improvement, or computation, of sensor position and attitude parameters based on identifiable GCPs (e.g., [Curlander *et al.*, 1989]);
3. creation of a simulated radar image to resemble the given input image;
4. correlation of the real and simulated radar images, either by pointing to homologue features or by automated correlation, thereby creating a grid of tie-points in the

real image to relate to the simulated one and consequently to the object co-ordinate system;

5. using a warping function, correction of the real image to fit over the simulated image;

6. generation of a geometrically rectified real image by assigning the real image grey value associated with the simulated pixel to each DEM grid cell;

7. subtraction of the real image grey values from the simulated image, resulting in a radiometrically corrected output image.

These imply that an extensive software and radar processing system is available.

The projection from the ground points represented by a DEM (a regular grid of heights) into irregularly-spaced image points is called an *object-space* algorithm. An *image-space* algorithm denotes the projection of regularly-sampled image co-ordinates to the ground, where the points become irregularly spaced (see Section 3.8). Simulation of the image geometry can be done using the precise but time-consuming image-space algorithm, or by the fast but inaccurate object-space algorithm [Strobl, 1987] — or by a combination of both algorithms. In the combined method, the ephemeris and attitude parameters of the sensor are estimated using the object-space algorithm. The image-space algorithm is then used to calculate intersection points between the projection circle and the ground.

A model of the registration between the original and simulated radar images must be established. This is normally achieved by the identification of match points, or by auto-correlation, and a polynomial description of the image distortion. In order to obtain an accurate model, every point of the simulated image must contain *all* the obtainable Earth surface information, namely DEM accuracy, DEM resolution, interpolation techniques for intermediate heights, and backscatter models.

Rectification to the map geometry can be done either by using the radargrammetric model again or, more efficiently, by using auxiliary data from the simulation task, combined with the description of the image distortion derived previously. To produce an accurate geocoded product, the equivalent image co-ordinates of each object pixel must be known exactly.

The advantages of this method are that a precise orbit is not required and an additional correction of the radargrammetric model can be performed. Again, however, tie-points have

to be identified and the method is very sensitive to both DEM and tie-point accuracies. The simulation can also be very time-consuming. This method is described in greater detail in [Strobl, 1987], [Domik *et al.*, 1984] and [Naraghi *et al.*, 1983].

Both the parametric methods discussed here are not limited by terrain relief, providing a DEM is available. Operator interaction is required unless automatic GCP determination is possible. Automation of this process has been attempted by several authors [Kiremidjian, 1981], [Guindon, 1985], with varying degrees of success. Using direct resampling, these methods can be faster than the polynomial approach.

3.3.3 SAR Processor-Based Methods

SAR processor-related methods make use of the geometric model used in image formation. The SAR range and Doppler equations, as used in the SAR processor, are employed to locate image pixels in the object space or *vice versa,* as shown by the method of node A in Figure 3.2. This approach was originally developed to map onto a reference surface, neglecting terrain distortions [Curlander, 1984] and has subsequently been extended to incorporate terrain relief using DEMs [Naraghi *et al.*, 1983]. Given precise orbit ephemeris and auxiliary data derived from the SAR processor, this approach does *not* require the use of GCPs. They may, however, be incorporated to refine the parameters in the image geometry model if the orbit and auxiliary data are inaccurate or unavailable [Kwok *et al.*, 1987]. The main difference between this approach and those based on photogrammetric techniques is in the use of the Doppler frequency, as utilised in the SAR processor.

At a particular position in the orbit of a SAR sensor, a point target on the surface of the Earth may be uniquely identified in image space by two parameters: the slant range from sensor to target and the Doppler frequency of the target as measured at the sensor. For geocoding, the basic output of the SAR processor is the slant range image in this image space. Subsequently, the location of a pixel on an Earth model may be obtained by processing these two parameters, along with the Earth model and the satellite orbit, position, and velocity.

The location of an image pixel on the Earth's surface at a particular time may be determined by the solution of three equations:

1. the SAR Doppler equation, defining the conical surface of the beam-centre Doppler frequency;

2. the SAR range equation, defining the distance of the sensor from the target;

3. a model describing the Earth's shape in the locality of the target.

These equations must be derived in a common co-ordinate system, such as the geocentric inertial reference frame, which is often used to express the satellite ephemeris. This method is dependent on the accuracy to which the range and Doppler parameters can be established.

The range equation should account for all timing and instrumental corrections in generating the round-trip delay time. The Doppler frequency may be generated from orbit, attitude, and timing data, although the resulting estimate will contain inaccuracies due to errors in these data. However, a more accurate approach is to estimate the Doppler frequency directly from the signal returns, a technique known as Doppler tracking or clutterlock estimation (see Section 2.3.7), improving image quality. Errors in the linear phase term of the reference function, which is directly related to the beam-centre Doppler frequency, result in a loss of signal power and increased ambiguity levels [Howard, 1987]. In terms of the quality of the resulting geocoded image, this causes a loss of radiometric accuracy and a reduction in image contrast.

The choice of Earth model depends on the required geocoding accuracy and can range from an oblate spheriod, such as WGS84, through a geoid model to a DEM. The co-ordinates of a pixel can be derived using standard transformation routines.

The model may be visualised as the intersection of three surfaces (see Figure 2.2). At a particular time, the range equation describes the surface of a sphere, while the Doppler equation describes the surface of a cone (this reduces to a plane if the beam centre is looking broadside). The intersection of these two surfaces yields a circle, which is intersected with the Earth model to give the pixel position. This method is described in [Howard, 1987], [Curlander, 1982], [Curlander *et al.*, 1987] and [Kwok *et al.*, 1987], and also in [Massonnet, 1987] and [Noack *et al.*, 1987].

Since this method can produce accurate results with minimum ground control, providing the required input data are supplied to a sufficient accuracy, and since for ERS-1 these input data are expected to be routinely supplied to the required accuracy, it was decided that for this research work only SAR-processor-based geocoding would be considered. This type of geocoding is explored in detail in Section 3.4.

3.3.4 Discussion

The choice of geocoding algorithm depends on the accuracy and availability of the input data. An operational SAR image geocoding system should therefore include elements of both SAR processor-related and parametric methods. Parameter refinement will have to utilise GCP data, despite the associated problems of GCP identification in SAR imagery. Resection-in-space may be required to reconstruct or refine parameter subsets. For refinement of orbit data, a simulation of small areas of the image, known as *image chips*, and subsequent matching of the slant range input could be useful.

Precision geocoding requires the availability of a DEM, ideally sampled to the same order of magnitude as the ground resolution of the SAR. At the present time however, there is only limited DEM coverage of the land surface. Therefore, unless a DEM can be obtained for the area under study by some other means, e.g. using stereo pairs of images, for most countries, precision geocoded imagery will not be available. It must also be appreciated that small errors in DEM height can, in areas of steep slope (especially foreshortened slopes near the layover limit), cause large mis-location of geocoded pixels.

SAR imagery is affected by a number of radiometric and geometric distortions which, in many applications, complicate or even prevent effective utilisation of the imagery. Terrain relief causes major radiometric and geometric distortion in radar imagery (see Section 3.2). Although most geometric distortions can be rectified in a precision geocoded image (depending on the accuracy of the DEM employed in the geocoding process), smeared out grey level values in foreshortened and layover regions will remain, hampering object recognition. The superposition of effects like speckle, specular returns, mirror-like reflections, and the dependency of radar response on surface roughness and dielectric constant are together further sources of confusion in the interpretation of radar imagery. However, these effects can have their advantage if they are well understood by the interpreter. It should also be noted that geocoding will degrade radiometric image quality, due to the additional resampling of the image (see Section 3.8).

Therefore, the evaluation of geocoded SAR imagery must be carried out with great care, especially for non-precision geocoding (i.e., no DEM being used), as terrain relief effects will still be present.

3.4 Geocoding Using SAR Processor-Based Methods

There are two types of SAR processor based geocoding:

object-to-image geocoding here a ground position is given and, from this, an image 'location' can be calculated, i.e. $X, Y, Z \rightarrow i, j$

image-to-object geocoding here an image position is given and, from this, a ground 'location' can be calculated, i.e. $i, j \rightarrow X, Y, Z$

Each method requires the solution of two or more non-linear equations, depending on the geocoding type. This is usually carried out using an iterative procedure employing partial derivatives, e.g. the Newton-Raphson method. The equations and derivatives are presented in Section 3.4.1 and Section 3.4.3 for each type of geocoding. Both methods require these data to be in the same reference system; this is usually taken to be the system of the given satellite data, which is nominally an *inertial* system (see Chapter 5). Therefore, *all* data not given in this system must be converted. Also, all the equations given in this section relate to a *slant range* image.

The relationship between the sensor platform, ground location, and frame of reference used in the geocoding procedures described in the following sections is shown in Figure 3.3 where S is the sensor position and P is the point on the ground under consideration.

For both types of geocoding, the relationship between the Doppler, f_{dc}, the image azimuth pixel i (which is related to time), and the image slant-range pixel j must be known. Hence, for a particular (i, j) image position, the Doppler must be assessed by some means, e.g. mathematical equation, look-up table, etc.. The image slant-range pixel j is related to the slant-range R as follows:

$$R = R_0 + m_r(j - 1)$$

where R_0 is the slant-range to the centre of the first pixel in each range line and m_r is the slant-range pixel spacing.

Both the sensor position and velocity are time-dependent vector functions. Since the azimuth is a linear function of time, both vectors describing the sensor orbit may be considered to be functions dependent on azimuth pixel i [Craubner, 1989].

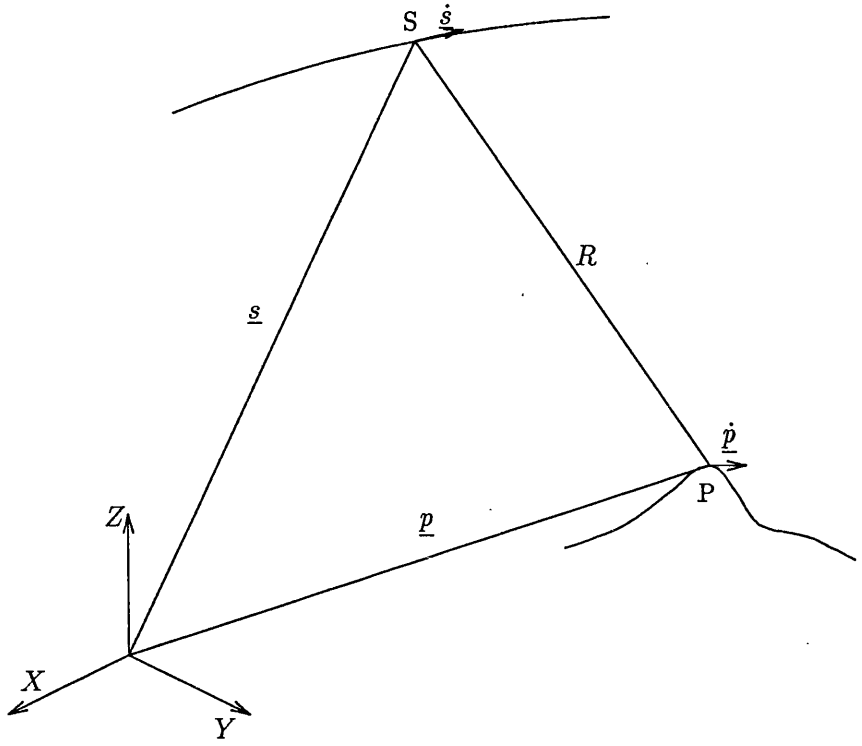

Figure 3.3: Sensor/Ground Geometry

In the following subsections, we shall consider Image-to-Object and Object-to-Image geocoding. In each case, an example of how a start point for the iteration can be found from interpolation will be given.

3.4.1 Image-to-Object Geocoding

The three relations involved are (see Figure 3.4) :

1. Earth model

$$F_1(X,Y,Z) = \frac{X^2+Y^2}{a^2} + \frac{Z^2}{b^2} - 1 = 0 \tag{3.1}$$

2. Doppler Equation

$$F_2(X,Y,Z) = f_{dc} - \frac{2(\underline{\dot{s}} - \underline{\dot{p}}).(\underline{s} - \underline{p})}{\lambda|\underline{s} - \underline{p}|} = 0 \tag{3.2}$$

3. Range Equation

$$F_3(X,Y,Z) = R - |\underline{s} - \underline{p}| = 0 \tag{3.3}$$

where

X, Y, Z are the co-ordinates of an image pixel in an *inertial* system.

a, b are the semi-axes of the Earth ellipsoid.

$\underline{p}$ is the position of a point on the ground $\underline{p} = [X, Y, Z]$.

$\dot{\underline{p}}$ is the velocity of the point, and $\dot{\underline{p}} = \omega \times \underline{p}$.

ω is the Earth rotational velocity $\omega = (0, 0, \frac{2\pi}{24 \text{ hours}})$.

$\underline{s}$ is the sensor position $\underline{s} = [X_s, Y_s, Z_s]$.

$\dot{\underline{s}}$ is the velocity of the sensor along the orbit. $\dot{\underline{s}} = [\dot{X}_s, \dot{Y}_s, \dot{Z}_s]$.

f_{dc} is the Doppler frequency shift.

λ is the radar wavelength.

R is the sensor target slant range.

To solve the three equations, an iterative method must be employed that requires the evaluation of the derivatives of the above equations. The derivatives of the Earth model and Range equations are relatively simple and are:

$$\frac{\partial F_1}{\partial X} = \frac{2X}{a^2}, \quad \frac{\partial F_1}{\partial Y} = \frac{2Y}{a^2}, \quad \frac{\partial F_1}{\partial Z} = \frac{2Z}{b^2}. \tag{3.4}$$

$$\frac{\partial F_3}{\partial X} = \frac{(X_s - X)}{|\underline{s} - \underline{p}|}, \quad \frac{\partial F_3}{\partial Y} = \frac{(Y_s - Y)}{|\underline{s} - \underline{p}|}, \quad \frac{\partial F_3}{\partial Z} = \frac{(Z_s - Z)}{|\underline{s} - \underline{p}|}. \tag{3.5}$$

The derivatives of F_2 are more complicated and some explanation of their derivation is worthwhile. We know that

$$(\underline{s} - \underline{p}) = (X_s - X, Y_s - Y, Z_s - Z)$$

and

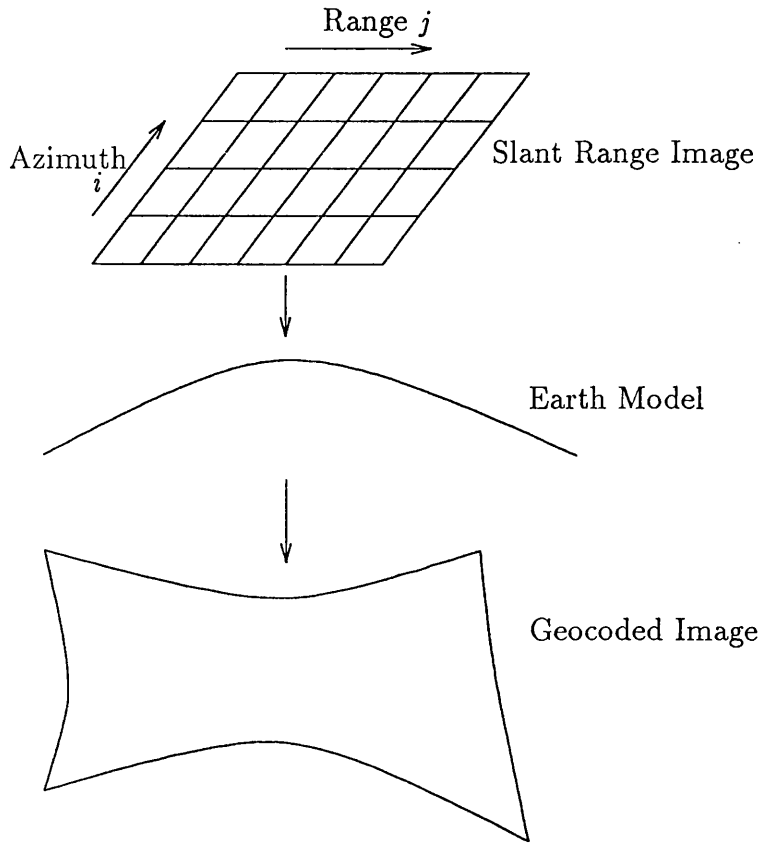

Figure 3.4: Image-to-Object Geocoding — Schematic View

$$(\dot{\underline{s}} - \dot{\underline{p}}) = (\dot{X}_s - \dot{X}, \dot{Y}_s - \dot{Y}, \dot{Z}_s - \dot{Z})$$

Now, $\dot{\underline{p}} = (-\omega Y, \omega X, 0)$. Hence,

$$(\dot{\underline{s}} - \dot{\underline{p}}) = (\dot{X}_s + \omega Y, \dot{Y}_s - \omega X, \dot{Z}_s)$$

Therefore,

$$(\dot{\underline{s}} - \dot{\underline{p}}).(\underline{s} - \underline{p}) = (\dot{X}_s + \omega Y)(X_s - X) + (\dot{Y}_s - \omega X)(Y_s - Y) + \dot{Z}_s(Z_s - Z) = U, \text{say.}$$

Let $|\underline{s} - \underline{p}| = V$, say. Then

$$\frac{\partial V}{\partial X} = -\frac{(X_s - X)}{|\underline{s} - \underline{p}|}, \quad \frac{\partial V}{\partial Y} = -\frac{(Y_s - Y)}{|\underline{s} - \underline{p}|}, \quad \frac{\partial V}{\partial Z} = -\frac{(Z_s - Z)}{|\underline{s} - \underline{p}|} \quad ;$$

and

$$\frac{\partial U}{\partial X} = -(\dot{X}_s + \omega Y) - \omega(Y_s - Y) = -(\dot{X}_s - \dot{X}) - \omega(Y_s - Y);$$

$$\frac{\partial U}{\partial Y} = -(\dot{Y}_s - \omega X) + \omega(X_s - X) = -(\dot{Y}_s - \dot{Y}) + \omega(X_s - X);$$

$$\frac{\partial U}{\partial Z} = -\dot{Z}_s.$$

So,

$$\frac{\partial F_2}{\partial X} = \frac{-2}{\lambda}\left[\frac{-(\dot{X}_s - \dot{X}) - \omega(Y_s - Y)|\underline{s} - \underline{p}|}{|\underline{s} - \underline{p}|^2} - \frac{-(X_s - X)(\dot{\underline{s}} - \dot{\underline{p}}).(\underline{s} - \underline{p})}{|\underline{s} - \underline{p}|^3}\right]$$

$$= \frac{-2}{\lambda}\left[\frac{-(\dot{X}_s - \dot{X}) - \omega(Y_s - Y)}{|\underline{s} - \underline{p}|} - \frac{-(X_s - X)(\dot{\underline{s}} - \dot{\underline{p}}).(\underline{s} - \underline{p})}{|\underline{s} - \underline{p}|^3}\right].$$

Therefore,

$$\frac{\partial F_2}{\partial X} = \frac{2}{\lambda|\underline{s}-\underline{p}|}\left[\frac{-(X_s-X)(\dot{\underline{s}}-\dot{\underline{p}}).(\underline{s}-\underline{p})}{|\underline{s}-\underline{p}|^2} + \omega(Y_s-Y) + (\dot{X}_s-\dot{X})\right]. \tag{3.6}$$

Similarly,

$$\frac{\partial F_2}{\partial Y} = \frac{2}{\lambda|\underline{s}-\underline{p}|}\left[\frac{-(Y_s-Y)(\dot{\underline{s}}-\dot{\underline{p}}).(\underline{s}-\underline{p})}{|\underline{s}-\underline{p}|^2} - \omega(X_s-X) + (\dot{Y}_s-\dot{Y})\right] \tag{3.7}$$

and

$$\frac{\partial F_2}{\partial Z} = \frac{2}{\lambda|\underline{s}-\underline{p}|}\left[\frac{-(Z_s-Z)(\dot{\underline{s}}-\dot{\underline{p}}).(\underline{s}-\underline{p})}{|\underline{s}-\underline{p}|^2} + \dot{Z}_s\right]. \tag{3.8}$$

In [Craubner, 1989], a solution to these equations was found by making the substitution

$$\frac{(\dot{\underline{s}}-\dot{\underline{p}}).(\underline{s}-\underline{p})}{|\underline{s}-\underline{p}|} = \frac{\lambda f_{dc} - F_2}{2}.$$

It was also assumed that $F_2 = 0$, resulting in

$$\frac{(\dot{\underline{s}}-\dot{\underline{p}}).(\underline{s}-\underline{p})}{|\underline{s}-\underline{p}|} = \frac{\lambda f_{dc}}{2}.$$

Iterative numerical techniques are then used to locate roots. However, $F_2 = 0$ is only valid at the *exact* root and hence the substitution should not be made. Although [Craubner, 1989] claims to have successfully geocoded imagery, the inaccuracy introduced by this substitution will certainly make the job of numerically determining the solution to the equations more difficult.

3.4.2 Iteration Start Position: Image-to-Object Geocoding using NEXTPOINT

A start point for the iterative procedure is required. For ERS-1, this could be taken to be any one of the given corner points or the nearest corner point or, more accurately, the bilinear interpolation of the four corner points. Alternatively, the method known as NEXTPOINT, used by the German DLR [Craubner, 1989], could be employed. Here, at least one tiepoint must be known. The NEXTPOINT method considers the Earth as being flat

in the region of interest. Since the purpose of NEXTPOINT is only to generate an iteration start-point, the use of a flat Earth approximation is not unreasonable.

The distance between the existing tiepoint and the point to be found (see Figure 3.5) may be approximated as;

$$\underline{p_{new}} = \underline{p_{old}} + \underline{\Delta g} + \underline{\Delta a},$$

where $\underline{p_{new}}$ is the point to be found, $\underline{p_{old}}$ is the tiepoint position, $\underline{\Delta g}$ is a vector describing the distance between the old and new point in the ground range direction, and $\underline{\Delta a}$ is a vector pointing parallel to the orbit direction.

If a flat Earth is assumed for simplicity, $\underline{\Delta g}$ and $\underline{\Delta a}$ can be calculated as follows (see Figure 3.5):

$$\underline{g} = \underline{p_{old}} - \frac{h\underline{s}}{|\underline{s}|},$$

$$\underline{p_{old}} \cdot \underline{s} = |\underline{p_{old}}||\underline{s}| \cos\phi,$$

$$h = |\underline{p_{old}}| \cos\phi.$$

Therefore,

$$h = \frac{\underline{p_{old}} \cdot \underline{s}}{|\underline{s}|}.$$

Hence,

$$\underline{g} = \underline{p_{old}} - \frac{\underline{p_{old}} \cdot \underline{s}}{|\underline{s}|^2}\underline{s},$$

$$\sin\theta = \frac{|\underline{g}|}{|\underline{s} - \underline{p_{old}}|},$$

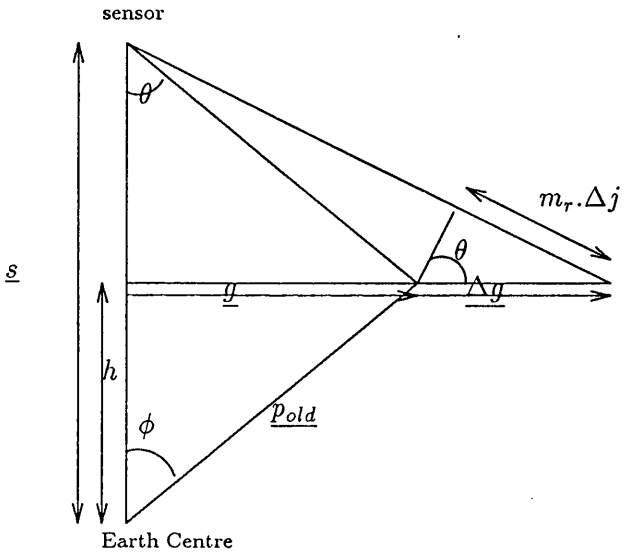

(a) Geometry in Slant-Range Direction

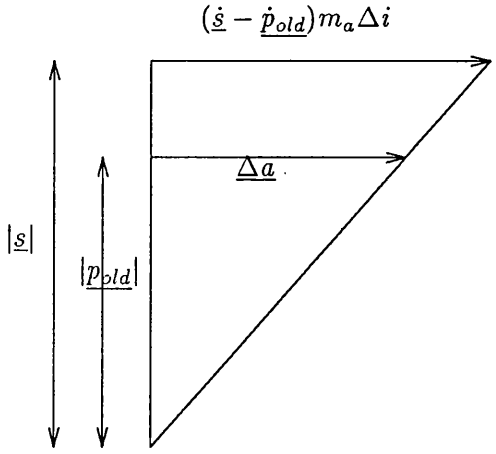

(b) Geometry in Azimuth Direction

Figure 3.5: Iteration Start Position using `NEXTPOINT`

$$\underline{\Delta g} = \frac{m_r \Delta j}{\sin\theta} \frac{\underline{g}}{|\underline{g}|},$$

where $\underline{s}$ is the sensor position, $\underline{g}$ is the ground range between sensor and tiepoint location, m_r is the slant range pixel spacing, θ is the sensor look-angle, and Δj is the number of pixels between the tie point and the new point to be found in range.

The distance $\underline{\Delta a}$ in the azimuth direction is

$$\underline{\Delta a} = \frac{|\underline{p_{old}}|}{|\underline{s}|}(\dot{\underline{s}} - \dot{\underline{p}}_{old}) m_a \Delta i,$$

where $\dot{\underline{s}}$ is the sensor platform velocity, $\dot{\underline{p}}_{old}$ is the tiepoint velocity, m_a is the time between adjacent azimuth samples, and Δi is the number of pixels in azimuth between the tie-point and the new point to be found. The point $\underline{p_{new}}$ can then serve as a starting point for the iteration.

Usually, in this type of geocoding, the image is addressed in a systematic way (i.e., pixel by pixel). Hence, to save on computation for subsequent image points, the starting point for the iteration of the next image point under consideration could be taken to be the result of the last image point. Of course, care must be taken to account for the beginnings of lines.

3.4.3 Object-to-Image Geocoding

Two relations are used in this type of geocoding:

1. Doppler Equation

$$F_1(i,j) = f_{dc} - \frac{2(\dot{\underline{s}} - \dot{\underline{p}}).(\underline{s} - \underline{p})}{\lambda |\underline{s} - \underline{p}|} = 0 \tag{3.9}$$

2. Range Equation

$$F_2(i,j) = R - |\underline{s} - \underline{p}| = 0 \tag{3.10}$$

where

i, j are image pixel co-ordinates.

$\underline{p}$ is the given position on the ground $\underline{p} = [X, Y, Z]$.

X, Y, Z are the co-ordinates of the given ground position given in an *inertial* system.

$\dot{\underline{p}}$ is the velocity of the point, and $\dot{\underline{p}} = \omega \times \underline{p}$.

ω is the Earth rotational velocity, $\omega = (0, 0, \frac{2\pi}{24 \text{ hours}})$.

$\underline{s}$ is the sensor position $\underline{s} = [X_s, Y_s, Z_s]$.

$\dot{\underline{s}}$ is the velocity of the sensor along the orbit $\dot{\underline{s}} = [\dot{X}_s, \dot{Y}_s, \dot{Z}_s]$.

f_{dc} is the Doppler frequency shift.

λ is the radar wavelength.

R is the sensor target slant range.

To solve these equations, an iterative method must be employed which requires the calculation of their derivatives with respect to i and j, the image co-ordinates.

$$\frac{\partial F_1}{\partial i} = \frac{\partial f_{dc}}{\partial i} - \frac{\partial}{\partial i}\left[\frac{2(\dot{\underline{s}} - \dot{\underline{p}}).(\underline{s} - \underline{p})}{\lambda|\underline{s} - \underline{p}|}\right].$$

Let

$$U = (\dot{\underline{s}} - \dot{\underline{p}}).(\underline{s} - \underline{p})$$

$$V = |\underline{s} - \underline{p}|.$$

Then,

$$\frac{\partial U}{\partial i} = \frac{\partial \dot{\underline{s}}}{\partial i}.(\underline{s} - \underline{p}) + \frac{\partial \underline{s}}{\partial i}.(\dot{\underline{s}} - \dot{\underline{p}})$$

$$\frac{\partial V}{\partial i} = \frac{\partial \underline{s}}{\partial i}.\frac{(\underline{s} - \underline{p})}{|\underline{s} - \underline{p}|}.$$

Hence,

$$\frac{\partial F_1}{\partial i} = \frac{\partial f_{dc}}{\partial i} - \frac{2}{\lambda}\left[\frac{(\frac{\partial \dot{\underline{s}}}{\partial i}.(\underline{s}-\underline{p}) + \frac{\partial \underline{s}}{\partial i}.(\dot{\underline{s}}-\dot{\underline{p}}))|\underline{s}-\underline{p}|}{|\underline{s}-\underline{p}|^2} - \frac{\frac{\partial \underline{s}}{\partial i}.(\underline{s}-\underline{p})(\dot{\underline{s}}-\dot{\underline{p}}).(\underline{s}-\underline{p})}{|\underline{s}-\underline{p}|^3}\right].$$

Let $m_t = \frac{\partial i}{\partial t}$, and write

$$\dot{\underline{s}} = \frac{\partial \underline{s}}{\partial t} = \frac{\partial \underline{s}}{\partial i}\frac{\partial i}{\partial t} = m_t \frac{\partial \underline{s}}{\partial i};$$

then

$$\frac{\partial F_1}{\partial i} = \frac{\partial f_{dc}}{\partial i} - \frac{2}{\lambda|\underline{s}-\underline{p}|}\left[m_t \frac{\partial^2 \underline{s}}{\partial i^2}.(\underline{s}-\underline{p}) + \frac{\partial \underline{s}}{\partial i}.(m_t\frac{\partial \underline{s}}{\partial i} - \dot{\underline{p}}) - \frac{\frac{\partial \underline{s}}{\partial i}.(\underline{s}-\underline{p})(m_t\frac{\partial \underline{s}}{\partial i} - \dot{\underline{p}}).(\underline{s}-\underline{p})}{|\underline{s}-\underline{p}|^2}\right] \tag{3.11}$$

$$\frac{\partial F_1}{\partial j} = \frac{\partial f_{dc}}{\partial j} \tag{3.12}$$

Let $R = R_0 + m_r(j-1)$ where R_0 is the slant range to the *centre* of the first pixel in each range line, m_r is the slant range pixel spacing, and j is the range pixel number. Then

$$\frac{\partial F_2}{\partial i} = -\frac{\partial \underline{s}}{\partial i}.\frac{(\underline{s}-\underline{p})}{|\underline{s}-\underline{p}|} \tag{3.13}$$

$$\frac{\partial F_2}{\partial j} = m_r. \tag{3.14}$$

If

$$\underline{s} = \begin{pmatrix} X_s \\ Y_s \\ Z_s \end{pmatrix} = \begin{pmatrix} a_0 + a_1 i + a_2 i^2 + a_3 i^3 \\ b_0 + b_1 i + b_2 i^2 + b_3 i^3 \\ c_0 + c_1 i + c_2 i^2 + c_3 i^3 \end{pmatrix}$$

then

$$\frac{\partial \underline{s}}{\partial i} = \begin{pmatrix} a_1 + 2a_2 i + 3a_3 i^2 \\ b_1 + 2b_2 i + 3b_3 i^2 \\ c_1 + 2c_2 i + 3c_3 i^2 \end{pmatrix}$$

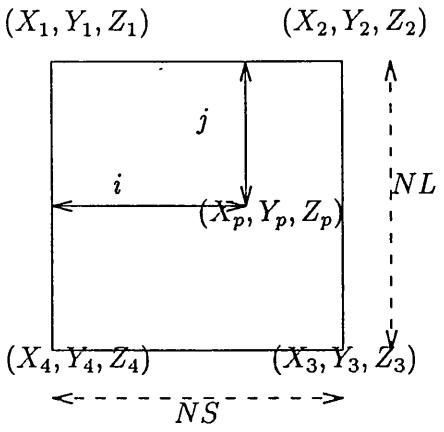

Figure 3.6: Interpolation of i and j from a given position

$$\frac{\partial^2 \underline{s}}{\partial i^2} = \begin{pmatrix} 2a_2 + 6a_3 i \\ 2b_2 + 6b_3 i \\ 2c_2 + 6c_3 i \end{pmatrix}.$$

3.4.4 Iteration Start Position: Object-to-Image Geocoding

A start point for the iterative procedure is required. As mentioned in the last section, for ERS-1 this could be taken to be the i and j values of any one of the corner points or the nearest corner point or, more accurately, the i and j values can be interpolated from the corner points, as shown in Figure 3.6, where:

(X_n, Y_n, Z_n) is the n^{th} corner position.

(X_p, Y_p, Z_p) is the position for which i and j are to be interpolated.

i, j are the image sample and line numbers respectively to be interpolated.

NL is the number of lines in the image.

NS is the number of samples in the image.

Let $f_i = i/NS$ and $f_j = j/NL$; and let

$$\underline{V_{12}} = \begin{pmatrix} X_2 - X_1 \\ Y_2 - Y_1 \\ Z_2 - Z_1 \end{pmatrix}, \quad \underline{V_{1p}} = \begin{pmatrix} X_p - X_1 \\ Y_p - Y_1 \\ Z_p - Z_1 \end{pmatrix}, \quad \text{etc.}$$

Then

$$f_i = \frac{\underline{V_{12}}.\underline{V_{1p}}}{|\underline{V_{12}}|^2}$$

$$f_j = \frac{\underline{V_{14}}.\underline{V_{1p}}}{|\underline{V_{14}}|^2}$$

Also

$$f_i = \frac{\underline{V_{43}}.\underline{V_{4p}}}{|\underline{V_{43}}|^2} = 1 - \frac{\underline{V_{21}}.\underline{V_{2p}}}{|\underline{V_{21}}|^2} = 1 - \frac{\underline{V_{34}}.\underline{V_{3p}}}{|\underline{V_{34}}|^2}$$

$$f_j = \frac{\underline{V_{23}}.\underline{V_{2p}}}{|\underline{V_{23}}|^2} = 1 - \frac{\underline{V_{32}}.\underline{V_{3p}}}{|\underline{V_{32}}|^2} = 1 - \frac{\underline{V_{41}}.\underline{V_{4p}}}{|\underline{V_{41}}|^2}$$

Therefore, start values of i and j can be found from any of the above equations or by taking averages of *all* equations.

3.4.5 Iterative Procedure

The robustness of the geocoding and, still to be described, stereoscopy methods described in this thesis hinges on the accuracy by which the appropriate non-linear equations can be solved. In all the publications seen by this author, *none* address the importance of this step. The solution of non-linear equations is a very difficult task and has long been a significant research topic in the numerical analysis field. It is not appropriate to go into details here.

This author is aware of only two widely used and well-tested libraries containing subroutines for the solution of non-linear equations. One is the British NAG (Numerical Algorithm Group) subroutine library, the other is the American IMSL package; the latter

is not available to the author.

This author has used one of the routines available in the NAG FORTRAN Subroutine Library, namely subroutine C05PBF to find the solution of the given equations. This uses a modification of the Powell hybrid method [Powell, 1970]. The reader is referred to the NAG documentation for further information. The NAG library also contains a subroutine C05ZAF which can be used in conjunction with C05PBF to check the derivatives of the equations. If these subroutines cannot be employed, then a method, such as the Newton-Raphson method for non-linear systems of equations, should be used.

The accuracy with which the iteration start point has to be given depends on the iteration method used and the form of the equations to be solved. The effect of using different start points for the method chosen in this work, as described above, for both geocoding and stereo assessment was investigated. The results are given in Chapters 7 and 8.

3.5 Error Considerations

It is important to note that if, during SAR processing, an incorrect Doppler centre frequency is used, then a target will be assigned to an incorrect output image position. If geocoding is carried out using the *same* incorrect Doppler centre frequency as in the processing, then the target will be located at the correct position. Hence, in this respect, the error is retrievable. However, other errors present in the parameters which define the image geometry model will propagate through to the geocoded position. These errors can be grouped as follows:

slant range errors due to two causes:

- **timing data:** the time of a given pulse return echo is measured to a specific accuracy which converts to a slant range error.
- **linear phase offset:** linear phase differences between the echo and the range compression reference function (such as those caused by drifts in the pulse phase with time) will cause a shift in the output image.

azimuth errors several phenomena can cause azimuth errors:

- **phase drift:** a drift in phase from pulse to pulse will result in a frequency offset that cannot be accounted for in the image geometry model. A constant drift applied

to the whole image will result in a simple time shift to all azimuth time values. However, a drift which varies from pulse to pulse will introduce inaccuracies.

radar frequency drift: a change in the radar frequency from its nominal value will result in a frequency offset. This effect is usually very small.

stop-start approximation: in SAR analysis, it is assumed that a pulse is received at the same time it is transmitted. This leads to a small, positional, azimuth error.

datation errors: these are additional errors of the sensor and satellite due to the time-delay in the transmission of signals from the command centre on the Earth. For ERS-1, there are basically two types of datation error: the AMI timing error, due to sensor operation, and the satellite timing error.

satellite ephemeris introduced by two inaccuracies:

position: along-track positional errors convert into azimuthal positional errors scaled by the ratio of satellite to ground track velocities. Across-track and altitude errors cause range-related positional errors.

velocity: along-track velocity errors have a negligible effect on position. Across-track and altitude velocity errors affect the rate of change of slant range and hence introduce azimuthal position errors.

Earth model assumption errors Positional errors due to the Earth model are a function of the model itself. Errors in the estimation of the target point velocity are usually considered to be negligible and will be considered so in this research. However, the variation of target velocity with height will be discussed in the next Section.

pulse repetition frequency (PRF) errors which occur in the estimation of Doppler frequency. If the error in the Doppler frequency is greater than half the PRF, aliasing may cause the beam to appear to be focussed on a region offset from the true beam direction. Since the slant range walk corrections will then be applied to the wrong part of the beam, this introduces a blurring effect in the image. Such an error for ERS-1 (PRF = 1700 Hz) will result in an error of 0.82 seconds [Howard, 1987]. [Chang and Curlander, 1989] and [Runge and Bamler, 1989] have addressed the problem of PRF ambiguity.

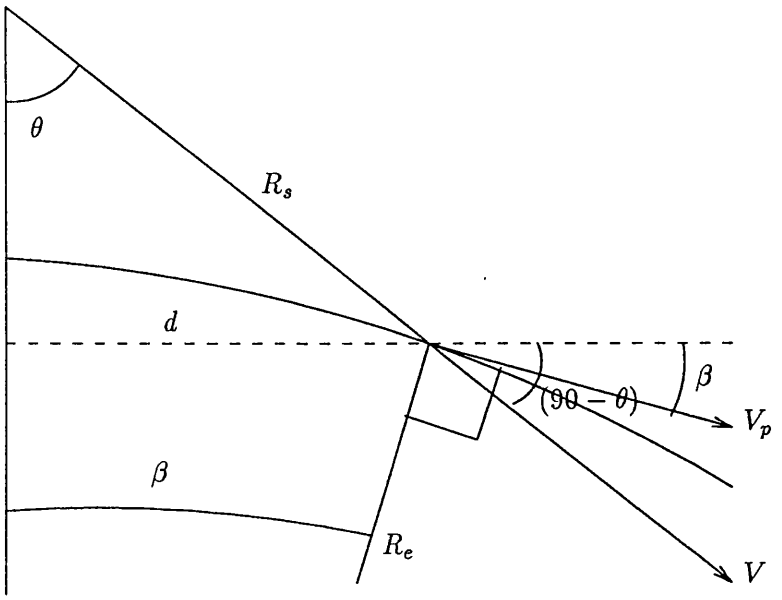

Figure 3.7: Geometry of Satellite and Ground

3.5.1 Variation of Target Velocity with Height

As discussed previously, variations in topography cause distortions such as foreshortening and layover. However, they also affect the radial velocity between the sensor and the target and hence have an influence on the geometry in the azimuth direction. With respect to Figure 3.7,

$$R_e = \frac{a}{(1 - e^2 \sin^2 \phi)^{\frac{1}{2}}}$$

where R_e is the length of the normal to the Earth ellipsoid, a is the semi-major axis, i.e. the equatorial radius, e is the eccentricity, and ϕ is the latitude.

$$V_e = R_e \omega \cos \phi$$

where V_e is the velocity of the Earth at latitude ϕ and ω is the Earth's rotational velocity.

$$V_p = V_e \cos(i - 90)$$

where V_p is the velocity of the Earth along the 'look direction' and i is the orbital inclination

(see Chapter 5).

$$d = R_s \sin\theta$$

where R_s is the slant range from sensor to target, θ is the look angle of the sensor, and d is as shown in Figure 3.7.

$$\beta = \sin^{-1}\left(\frac{d}{R_e}\right)$$

$$V = V_p \cos(90 - \theta - \beta)$$

see Figure 3.7 for β and V.

The radial velocity $V_\perp$ is then given by

$$V_\perp = V_s \sin\chi - V$$

where V_s is the sensor velocity and χ is the squint angle, which is the angle through which the antenna beam points forward (positive squint) or backward (negative squint) of the perpendicular to the flight path.

Let us consider the magnitude of this effect for Seasat at both sea-level and at 1 Km altitude. At sea-level we have, using the WGS84 oblate spheroid to represent the Earth:

$$\begin{aligned} a &= 6378137 \text{ m} \\ e^2 &= 0.00666 \\ \phi &= 46° \\ i &= 108° \\ R_s &= 851855 \text{ m} \\ \theta &= 19.47° \\ \chi &= 0 \end{aligned}$$

and at 1000m in height, $a = 6379137$ m and $\theta = 19.65°$.
then

	Sea-level	At 1 Km Altitude
R_e	6389148.3 m	6390150.0 m
V_e	322.76 m/s	322.81 m/s
V_p	306.96 m/s	307.01 m/s
d	283934.56 m	283934.56 m
β	2.547°	2.547°
V	115.07 m/s	115.98 m/s
$V_\perp$	−115.07 m/s	−115.98 m/s

Hence there is a difference of $\approx$ 1 m/s in target velocity for a height increase of 1000 m. [Meier *et al.*, 1989] has studied this effect in more detail and has shown that there is $\approx$ 1 m/s increase in target velocity for every 1000 m increase in target height. This corresponds, for Seasat, to a 8 Hz Doppler shift. It is thought that this effect will be considered in the German geocoding system.

3.6 The ERS-1 Mission

The European ERS-1 satellite, due to be launched in July 1991, carries the Active Microwave Instrument (AMI), which includes a SAR operating in C-band (5.3 GHz). The image products of ERS-1 will include both geocoded and precision geocoded images, which are the most suitable for land-mapping applications. ERS-1 is expected to acquire nearly 168,000 scenes per year, assuming an average of only 8 minutes data acquisition time per orbit. Of these, 6000 are expected to be processed to give a geocoded product — of which 2000 should be precision geocoded.

These images will be generated on an operational basis by ERS-1 ground processing facilities. It is expected that the ground resolution of the precision product will be 30 m, and a single frame will cover an area of up to 100 × 100 Km. The ERS-1 SAR processor is planned to have interfaces with a system for accurate orbit determination at one end and a post-processing system for precision geocoding at the other.

The available orbit data sets for ERS-1 will be as follows:

1. The *predicted orbit* (from ESOC): very inaccurate, one state vector per orbit.

2. The *restituted orbit* (from ESOC): inaccurate, state vectors at one minute intervals

for the previous 24 hour period calculated during the 5 hours per day of 'off-time', where ERS-1 remains in contact with the ground stations.

3. The *preliminary orbit* (from D-PAF): accurate, state vectors at two minute intervals from one week's worth of data. Available after one week of sensor operation, with an accuracy of ≈ 2 m (radial direction).

4. The *precise orbit* (from D-PAF): very accurate. There will be 2 types of precise orbit covering a four-week period at 30 second intervals. The first type uses a pre-ERS-1 gravity model, the second uses a gravity model derived from ERS-1 orbit analysis which will not be available until some time after the launch date. Routinely, this orbit will be available after 3 to 4 months' delay with an accuracy of less than 1 m (radial direction).

The image quality requirements specified for ERS-1 require that the Doppler frequency be known to within 50 Hz; this is not attainable using only attitude data. It can be achieved using Doppler tracking, but only after the PRF ambiguity has been resolved. Any error in the beam-centre Doppler frequency introduces an error in the assumed slant range and thus into the range walk correction that will be applied during processing. This results in a significant range displacement at the two extrema of the synthetic aperture for a given point target. Range registration of these extrema yields a sufficiently accurate estimate of the Doppler frequency to resolve the PRF ambiguity. This method requires the presence of recognizable features within the image, and hence is only feasible over land. Over ocean and bland landscapes, the ambiguity cannot be resolved in this way. However, since the Doppler frequency of a target varies monotonically over the synthetic aperture, only one absolute estimate is required for the elimination of the error. Furthermore, in ERS-1, the accuracy of the Doppler tracker is 50 Hz and hence it may be used to correct the azimuth pointing to $\pm 0.12°$, a figure which is well within the required azimuth pointing accuracy of $\pm 0.18°$. Hence, it is possible to totally eliminate this source of error. Doppler blocking effects are also said to be negligible [Roth, personal communication]. For ERS-1 the images will be processed to have *zero* Doppler. Hence, the Doppler equations and derivatives given in Section 3.4 can be greatly simplified.

The ERS-1 mission will produce a 'Doppler parameter estimation'; using this and accurately-measured satellite ephemeris data, the SAR processor is expected to produce

geocoded imagery with pixel location accuracies of ≈30 m in range and 150 m in azimuth.

The SAR processor will represent the shape of the Earth as a reference ellipsoid in the geometrical modelling required for the image formation process. It will also perform transformations between reference ellipsoids in order to generate geocoded products with different map projections.

The gross errors in the latitude/longitude indications of the image frame location are expected to be 100 m [Tsilibaris and Tribnig, 1988]. Geocoded SAR images should be suitable for mapping tasks without the need for additional geodetic control. However, since the SAR processor will use a smooth ellipsoid Earth model, terrain relief cannot be considered. This means that the given pixel accuracies will be referable only to the flat terrain case. The look angle of ERS-1 is expected to be around 20° mid-ground swath. Hence, following the earlier discussion of terrain effects in SAR imagery (see Section 3.2), shadow should only occur in rugged mountainous areas. On the other hand, layover will corrupt extended areas in hilly regions.

The geometric correction of such terrain effects using a DEM will be performed by processing subsequent to the SAR processor, resulting finally in the 'precision geocoded' product. For this product, image accuracy figures should also be valid in mountainous regions and are predicted to be of the order of 30 m for ERS-1. It should, however, be remembered that there is limited DEM coverage at present; hence, for most areas, only ellipsoid data will be available to describe the terrain.

Stereo images will be available from ERS-1 using the roll-tilt mode, in which the whole platform will be tilted, thus obtaining different look-angles of the same ground area. Stereo images can also be derived from overlapping adjacent tracks as well as from cross tracks and ascending and descending paths. If the look-angle difference between a pair of images is small they will not offer a stereo capability in the classical sense. However, by evaluating minimum phase differences in the raw radar signals obtained during two different overflights, one can derive terrain height information. This method, called SAR interferometry, presumes at least a small across-track translation between the two spacecraft orbits and suitable alignment of the passes. This technique has been tested using satellite and aircraft imagery and reported, for example, in [Gabriel and Goldstein, 1988] and [Zebker and Goldstein, 1986]. A sensitivity to relief variations of the order of 5 m has been reported.

3σ Accuracy	Position (m)		Velocity (mm/s)	
	Predicted	Restituted	Predicted	Restituted
Radial	30	25	955	40
Along-Track	920	60	29	27
Across-Track	15	15	16	15

Table 3.1: Predicted and Restituted Orbit Accuracy

SOURCE OF ERROR	Slant-Range dR(m)	Azimuth dt(s)
Timing Data	8.99	
Linear Phase Offset	0.19	4.7×10^{-3}
Radar Frequency Drift		6.4×10^{-5}
Stop-Start Approximation		2.8×10^{-3}
Datation Errors		1.5×10^{-2}

Table 3.2: ERS-1 Image Location Error Budget [GEC-Marconi Research Centre and DIBAG, 1989]

3.7 ERS-1 Error Budget

The following error budget is taken from [GEC-Marconi Research Centre and DIBAG, 1989] and more recent work. Since, at present, there are no firm details of the UK ERS-1 SAR processor, the errors associated in SAR processing are taken from [GEC-Marconi Research Centre and DIBAG, 1989]. Here the calculations are based on the Verification Mode Processor, VMP, at ESRIN. All the calculations apply to a *mid-range* image position and should apply to both Object-to-Image and Image-to-Object Geocoding.

Table 3.1 details the component accuracy for the predicted and restituted orbits. In Tables 3.5 and 3.6 the geocoding error for all orbit types are shown. The various types of system error are shown in Table 3.2 and the geocoding inaccuracies resulting from these errors are shown in Tables 3.3 and 3.4. The geocoding errors due to topographic effects are given in Tables 3.7 and 3.8. The final total geocoding errors were calculated by this author and are shown in Tables 3.9 to 3.12.

RANGE ERRORS	Input (m)	Output (m)
Timing Error	8.99	20.95
Linear Phase Offset	0.19	0.44
RMS Error		20.95

Table 3.3: Raw Data Error — Range Errors [GEC-Marconi Research Centre and DIBAG, 1989]

AZIMUTH TIME ERRORS	Input (s)	Output (m)
Linear Phase Offset	4.7×10^{-3}	31.40
Radar Frequency Drift	6.4×10^{-5}	0.43
Stop-Start Approximation	2.8×10^{-3}	18.71
Datation Error	1.5×10^{-2}	100.22
Total Error		150.76

Table 3.4: Raw Data Error — Azimuth Time Errors [GEC-Marconi Research Centre and DIBAG, 1989]

POSITION ERROR	Output (m)			
	Predicted	Restituted	Preliminary	Precise
Radial	71.93	59.91	4.81	2.40
Along-Track	900.67	58.61	1.95	0.98
Cross-Track	13.34	13.33	1.76	0.89
RMS Error	903.64	84.86	5.48	2.74

Table 3.5: ERS-1 Geocoding Errors due to Orbit Position Errors

VELOCITY ERROR	Output (m)			
	Predicted	Restituted	Preliminary	Precise
Radial	81.76	3.40	negligible	negligible
Along-Track	0.11	0.10	negligible	negligible
Cross-Track	0.50	0.47	negligible	negligible
RMS Error	81.76	3.43	negligible	negligible

Table 3.6: ERS-1 Geocoding Errors due to Orbit Velocity Error

TERRAIN HEIGHT ERROR	Input (m)	Output (m)
Local Datum	25	58.84
Total Error		58.84

Table 3.7: Geocoding Error due to Terrain Height Error of 25 m

ELLIPSOID ERROR	Input (m)	Output (m)
Local Datum	10	23.53
Global Datum	10	235.35

Table 3.8: Topographic Height Error — Ellipsoid Corrected Product Error

TOTAL GEOCODING ERROR (m) : Predicted Orbit			
Error Type	Terrain Corrected	Ellipsoid Corrected	
		Local Datum	Global Datum
Range Error	20.95	20.95	20.95
Azimuth Time Error	150.76	150.76	150.76
Orbit Position	903.64	903.64	903.64
Orbit Velocity	81.76	81.76	81.76
Topography	58.84	23.53	235.35
TOTAL	1215.95	1180.64	1392.46

Table 3.9: Total Geocoding Error: Predicted Orbit

TOTAL GEOCODING ERROR (m) : Restituted Orbit			
Error Type	Terrain Corrected	Ellipsoid Corrected	
		Local Datum	Global Datum
Range Error	20.95	20.95	20.95
Azimuth Time Error	150.76	150.76	150.76
Orbit Position	84.86	84.86	84.86
Orbit Velocity	3.43	3.43	3.43
Topography	58.84	23.53	235.35
TOTAL	318.84	283.53	495.35

Table 3.10: Total Geocoding Error: Restituted Orbit

TOTAL GEOCODING ERROR (m) : Preliminary Orbit			
Error Type	Terrain Corrected	Ellipsoid Corrected	
		Local Datum	Global Datum
Range Error	20.95	20.95	20.95
Azimuth Time Error	150.76	150.76	150.76
Orbit Position	5.48	5.48	5.48
Orbit Velocity	0.00	0.00	0.00
Topography	58.84	23.53	235.35
TOTAL	236.03	200.72	412.54

Table 3.11: Total Geocoding Error: Preliminary Orbit

TOTAL GEOCODING ERROR (m) : Precise Orbit			
Error Type	Terrain Corrected	Ellipsoid Corrected	
		Local Datum	Global Datum
Range Error	20.95	20.95	20.95
Azimuth Time Error	150.76	150.76	150.76
Orbit Position	2.74	2.74	2.74
Orbit Velocity	0.00	0.00	0.00
Topography	58.84	23.53	235.35
TOTAL	233.29	197.98	409.80

Table 3.12: Total Geocoding Error: Precise Orbit

From these results it can be seen that the terrain corrected geocoded product should have an error of at best 233 m and at worst 1216 m; the local ellipsoid-corrected geocoded product should have an error of at best 198 m and at worst 1181 m and finally the global ellipsoid-corrected geocoded product should have an error of at best 410 m and at worst 1392 m, depending on the orbital precision available. As can also be seen from these results, the errors of the orbit are rather swamped by the SAR processor errors and topography errors for all but the predicted orbit case. However, it is expected that the errors associated with the SAR processing can be reduced by taking appropriate steps in the processor; also, the terrain height error of 25 m could be rather pessimistic.

3.8 Resampling and Radiometric Considerations

Resampling is a much-utilised procedure for SAR data e.g., to convert between slant range and ground range co-ordinates, to correct geometric effects due to mismatch between range and azimuth pixel sizes, etc. It has always formed a crucial part of geocoding, as it is the link between the geometrically-defined mapping function and the radiometrically-defined image. However, there is at present only a small understanding of the effect of geocoding on image statistics: if the resampling process alters the image statistics, this can severely restrict the further uses of a resampled SAR product.

If the original signal is sampled at the Nyquist rate then the Shannon sampling theorem states that resampling can be carried out with no loss of information if the interpolation kernel is of the form

$$\mathrm{sinc}x = \frac{\sin \pi x}{\pi x},$$

i.e. if a function $f(t)$ has a bandwidth B then it is completely determined by giving its value at a series of points spaced $1/B$ apart; hence, $f(t)$ can be represented as a series given by

$$f(t) = \sum_{n=-\infty}^{\infty} f\left(\frac{n}{B}\right) \frac{\sin \pi(Bt - n)}{\pi(Bt - n)}$$

(see Figure 3.8). In practice, it is difficult to construct a sinc, which has an infinite extent, at all sample data points and hence some simpler form of interpolation is frequently used.

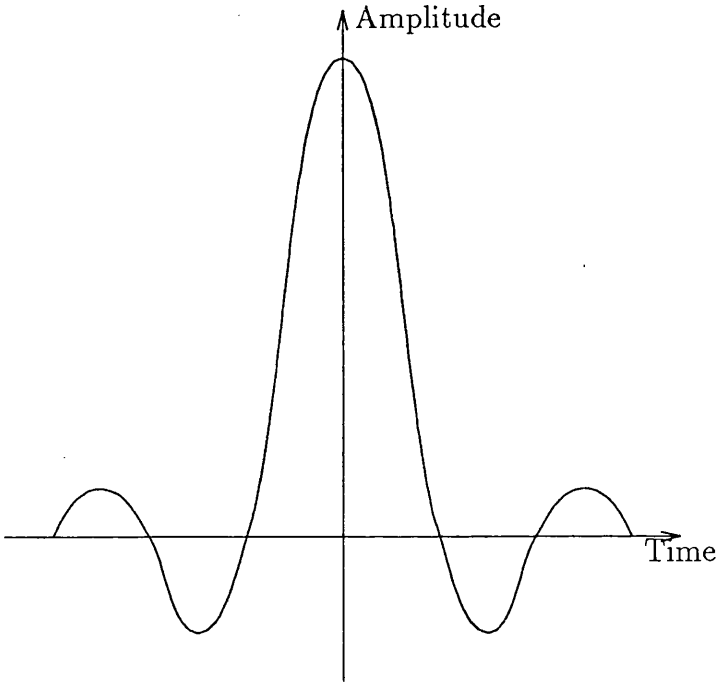

Figure 3.8: Sinc Function

When the data are detected, the bandwidth is doubled. Shannon's sampling theorem still applies to the squared signal. Before detection, SAR data consist of two real values corresponding to the I and Q channels, each containing speckle, which is normally modelled as Gaussian. When the detected image is produced, by finding the sum of the squares of the I and Q channels, then the speckle has an exponential distribution. If an homogeneous region of a detected SAR image is considered, the region has the same mean intensity with the exponentially-distributed speckle superimposed upon it.

Work carried out by the author in conjunction with GEC-Marconi Research Centre (Chelmsford) [1] [Clark *et al.*, 1989] studied the effect of resampling on simulated detected, single-look data, both uncorrelated and correlated. Simulation of the uncorrelated data was provided by simply taking random samples from an exponential distribution to be the pixel values. For the correlated case, an appropriate correlated complex signal was generated; this was sampled at the Nyquist rate and detected, generating pixels at twice the Nyquist rate such that Shannon's sampling theorem would be valid.

Three types of resampling were considered: bilinear, cubic spline and truncated sinc.

[1] The author holds a CASE studentship with MRC.

The results showed that none of these methods successfully preserved the exponential statistics of the original data, the image statistics being distorted and negative values generated (for wholly positive data). This could have serious consequences for further analysis of the resampled data.

Resampling has also been addressed by [Quegan, 1990] from a theoretical viewpoint. Here again only single-look SAR data were considered, but both detected and complex data were examined. This work confirmed that the image statistics were not always preserved. [Quegan, 1990] ventured to suggest that similar results would occur for multi-look data. However, [Laycock, 1990] reports that for detected, multi-look data, this is not the case and the image statistics are preserved.

The radiometric accuracy of a geocoded image can be degraded considerably if the resampling processes are not performed correctly. The correct way to interpolate or resample two-dimensional digital data is with a two-dimensional convolution. In practice however, application of two-dimensional convolution is slow. The large volumes of data must be accessed line-by-line. This becomes even slower when performing image rotation, which requires access to a large portion of the image for one output line (i.e., one must nominally traverse diagonally through the input data; but see below). When the data can be processed in a one-dimensional manner, the number of computations is reduced and the data access problem eased considerably.

[Friedmann, 1981] presents theoretical arguments for validating one-dimensional precision processing of image data from different sensors. It also shows how this processing should be modified from two one-dimensional operations (along and across scan lines) to *three* one-dimensional operations, in order to incorporate image rotation. The basis for this three-pass resampling is best illustrated by a simple rotation through an angle θ (see Figure 3.9). As is well-documented in the literature [Foley *et al.*, 1990, for example], this can be represented by the mapping

$$\begin{pmatrix} x\prime \\ y\prime \end{pmatrix} = \begin{pmatrix} \cos\theta & -\sin\theta \\ \sin\theta & \cos\theta \end{pmatrix} \begin{pmatrix} x \\ y \end{pmatrix}. \tag{3.15}$$

A straightforward implementation of this mapping will rotate an image in a single pass through the data, but at the expense of accessing pixels in the other image in an irregular way. On most computers, and particularly those which use paged virtual memory

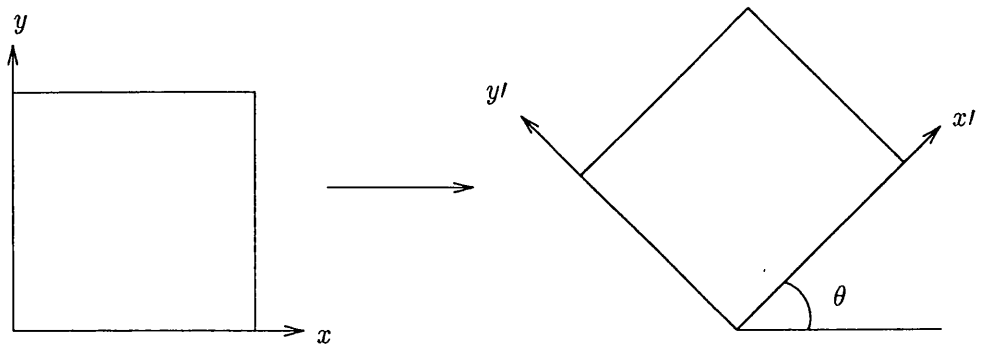

Figure 3.9: Illustration of Image Rotation

(e.g., VAX/VMS and modern versions of Unix), this type of access is particularly inefficient. However, we can decompose the above transform matrix into three:

$$\begin{pmatrix} \cos\theta & -\sin\theta \\ \sin\theta & \cos\theta \end{pmatrix} = \begin{pmatrix} 1 & -\tan\theta/2 \\ 0 & 1 \end{pmatrix} \begin{pmatrix} 1 & 0 \\ \sin\theta & 1 \end{pmatrix} \begin{pmatrix} 1 & -\tan\theta/2 \\ 0 & 1 \end{pmatrix}, \tag{3.16}$$

each of which represents a shear. Although three passes over the image are now required to perform the rotation, each pass involves only one multiplication and one addition per pixel. Furthermore, access to the pixels which comprise the image is more regular, giving a vast speed improvement for images of the size typically obtained from a SAR. Care is obviously required when $\theta \approx 90°$; but here, the image may be first rotated by 90° (which can be performed efficiently using a 'block-swapping' technique) and then rotated through $90° - \theta$. Further discussion of resampling algorithms is given in [Wolberg, 1990].

[Curlander *et al.*, 1987] and [Kwok *et al.*, 1987] also describe how to combine the two resampling passes to rectify the image and the two passes required to rotate the rectified image into geocoded format into three one-dimensional resampling passes. The along-track corrections are applied and the image is over-sampled in the first pass. In the second pass, the across-track corrections are applied and the image is sheared. A final shear then transforms the image onto the desired output grid.

Ideally, geocoding should be performed in object-space, so that ground points are projected into irregularly-spaced image points. This gives a more systematic approach, as each ground position is addressed only once and in a uniform manner. Unfortunately, some methods, e.g. [Curlander *et al.*, 1987] and [Kwok *et al.*, 1987], adopt an image-space

approach, so the ground positions are addressed in an arbitrary manner. Also, each ground position cell will be addressed a different number of times.

3.9 Computational Aspects

The processing time for a Seasat scene of 100 × 100 Km is quoted as being about 7 hours using a ST-100 array processor [Noack *et al.*, 1987]. However, when one takes into account the additional time required for preparation and refinement, a product generation time of about 9 hours is more reasonable. (In 1978, this would have taken about 180 hours of CPU time!) Even so, the mean throughput is only about one high-quality SAR image per working day, or about 240 images per year. As stated in Section 3.6, the processing requirement of ERS-1 is 6000 geocoded scenes per year. Hence, more efficient computer systems for geocoding purposes are needed. Since the geocoding process incorporates additional datasets, such as DEMs, GCPs and other map information, such systems have to incorporate flexible databases and sophisticated access methods. The principal design requirements are:

high precision: the processor has to calculate all parameters to the highest possible accuracy.

high throughput: this implies the use of state-of-the-art hardware technology, e.g. parallel processors. Ideally, image production should be in real time.

high flexibility: a processor should be able to handle data from different bands, polarisations, etc. The processor modules should be designed for easy exchange and modification to accommodate new developments.

efficient man-machine interface: a user-friendly environment is an important practical consideration.

For ERS-1, a mean product time of about half an hour is required. This could be achieved using special hardware; however, hardware that supports real-time processing almost invariably involves low-level programming. For the complex algorithms required, such a system would be fast but rather inflexible. Another possible solution is the use of modern supercomputers such as the Cray-2; however, these machines are very expensive and are

difficult to interface with special peripherals. Yet another solution could be the use of array processors. Descriptions of systems for SAR processing and geocoding are given in [Noack *et al.*, 1987], [Kavanagh *et al.*, 1989] and [Schreier *et al.*, 1988]. SAR processing systems intended for ERS-1 are also described in [Herland, 1989], [Sack *et al.*, 1989] and [Lewis and Wilson, 1989].

3.10 Summary

In this chapter most aspects of SAR geocoding have been addressed. Section 3.2 dealt with image considerations due to terrain, speckle, etc.. Section 3.3 outlined the three main types of geocoding methods and, in Section 3.4, the geocoding method chosen for use in this study, i.e. SAR processor based geocoding for both image-to-object and object-to-image, was discussed in full. The equations were defined and the derivatives needed for their solution, by an iteration procedure, were derived. Examples of how to establish iteration start points were also given. It should be remembered that ERS-1 images will be processed to have *zero* Doppler and hence the Doppler equations and derivatives given in Section 3.4 can be simplified.

In Section 3.5, consideration was given to the types of error that can affect the geocoding process. Since this study was carried out in preparation for the reception of ERS-1 data, the accuracy with which the ERS-1 data can be expected for geocoding (and stereo analysis) was discussed in Section 3.6. The ERS-1 geocoding error budget is summarised in Section 3.7 for comparison with results obtained from this study.

In Section 3.8, the important issue of resampling is addressed, since resampling can alter the statistics of an image — which can then have serious consequences on the further use of the imagery. Finally, a few computational aspects of a geocoding system were considered in Section 3.9. This chapter, therefore, gives a full appreciation of the geocoding process.

Chapter 4

Stereoscopy Using SAR Images

4.1 Introduction

A camera and the human eye record an image in almost the same manner. Hence, if two cameras are located with the same relative geometry as the eyes, a satisfactory stereo model will result. Radar records its image in an entirely different manner; hence, it is not necessary, or even desirable, for the radar to be located so that the view angles correspond to those of the eye or camera. The important consideration is that the resulting radar configurations have parallaxes comparable to those found in optical images. Stereo from optical sensors is well known and documented and will not be discussed here.

Figure 4.1a illustrates the parallax resulting when a feature with height h is imaged by an aerial camera, say. In the radar case (Figure 4.1b) however, the parallax will be different. The image from the radar on the right is analogous to the image from the camera on the left and *vice versa,* so that the placement of the radar images in a stereo-viewer would have to be reversed from that of optical images. This would result in a measured elevation h_r, as shown in Figure 4.1c, which is different from h.

Much of the initial work to aid understanding of the visual aspects of radar stereo was carried out by LaPrade [LaPrade, 1963], [LaPrade, 1972]. LaPrade proposed two permissible radar stereo configurations, shown in Figure 4.2, and these have become the most commonly discussed stereo configurations. Other stereo configurations are shown in Figure 4.3.

It is not possible to achieve SAR stereo using a single flight-line. It is tempting to postulate that two stereo images could be obtained by looking forward (forward squint)

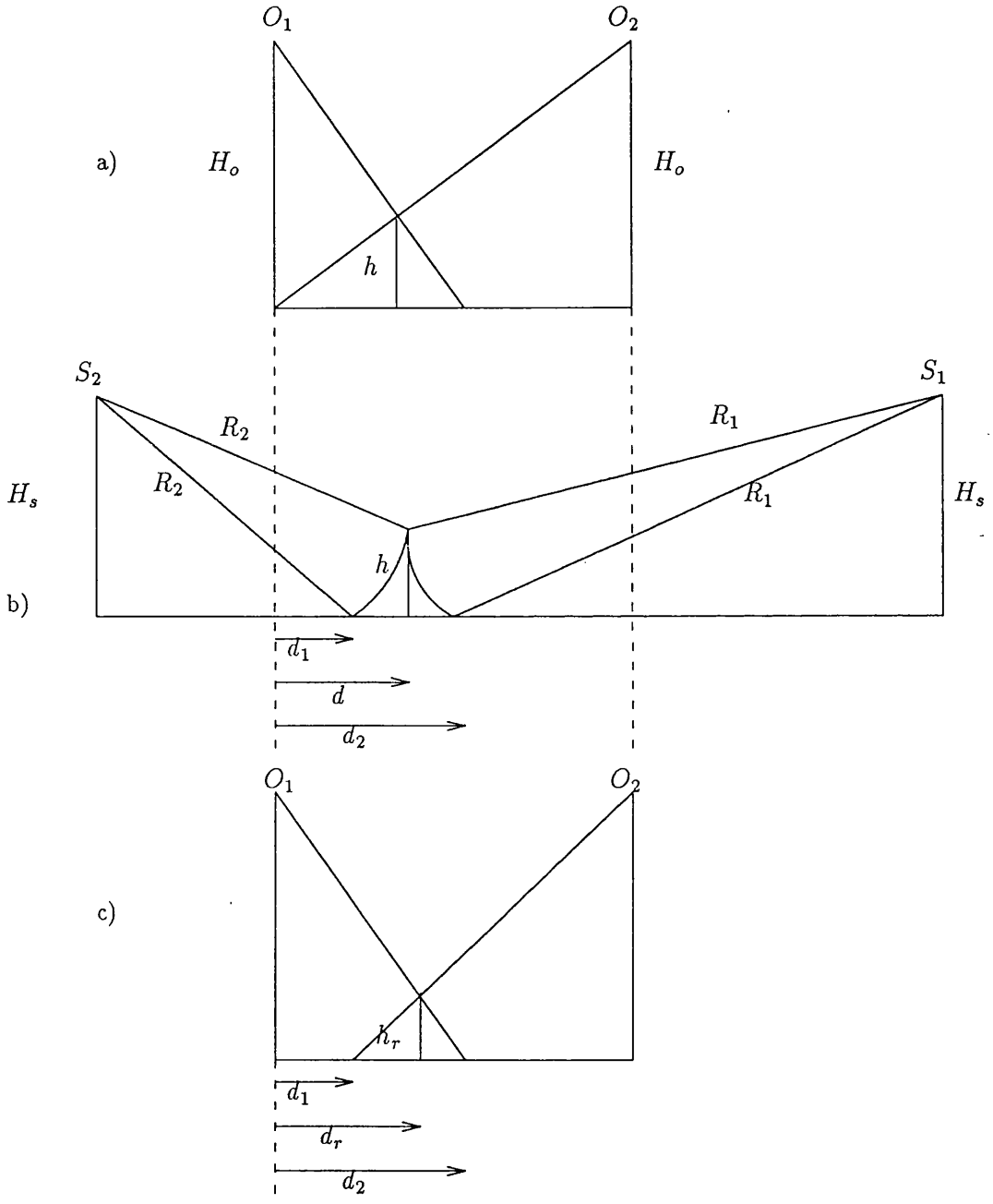

Figure 4.1: Comparison of Optical and Radar Stereo Geometries. Following [LaPrade, 1963]

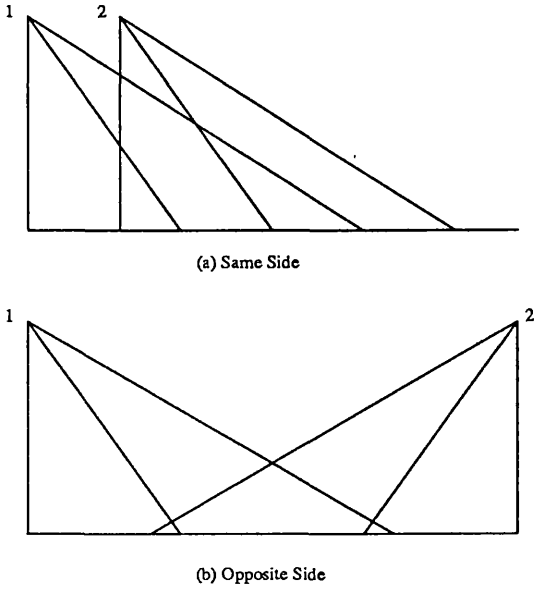

Figure 4.2: Basic Stereo Radar Configurations

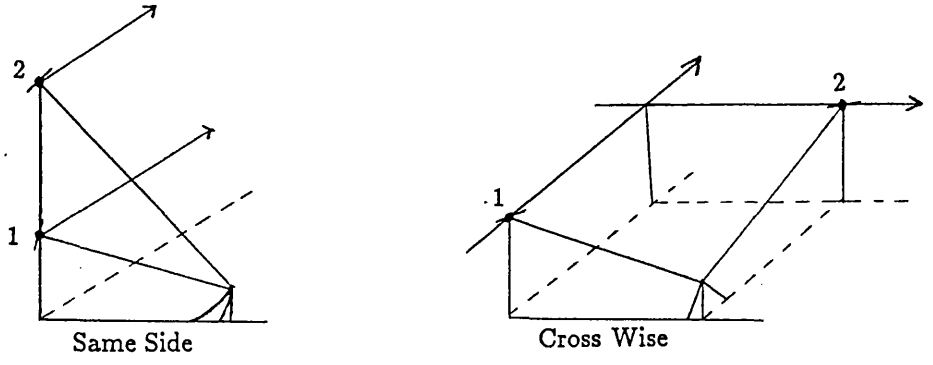

Figure 4.3: Other Stereo Radar Configurations. Following [Leberl, 1979]

and then looking backward (backward squint). However, relief displacements would be of the same magnitude and direction in both cases; as a result, the parallax would be zero.

Numerous authors have examined the height measurement accuracies that could be achieved by radar images if stereoscopic measurements were feasible. Theoretical error propagation studies, e.g. [Leberl, 1979] and [Rosenfield, 1968], indicate that *opposite-side* stereo arrangements are superior to other arrangements, such as *same-side* (Figure 4.2). For an observer to perceive an object in 3-D, the two images of a stereo pair must be sufficiently similar; i.e., image quality, object illumination, tones, and textures must be comparable. This rarely presents a problem with optical images. For example, sun illumination angles do not change drastically in overlapping optical images. However, radar illumination depends on sensor position, so that a radar stereo pair may look like two optical images taken at different times of the day. Furthermore, parallaxes in optical imagery will be excessive only in the most extreme cases; this is not the case for radar imagery.

From radar images with an opposite-side configuration, it can be seen that slopes reflecting strongly in one image are in the radar shadow in the other image. Hence, the impression of stereo cannot be achieved in rugged terrain. Same-side stereo arrangements do not present this problem. However, there are also limits to the successful use of same-side stereo: for some viewing angles, relief displacements and variations in image appearance can be large [Leberl and Raggam, 1982], even with a small stereo base. Furthermore, same-side stereo can be difficult to arrange for a spaceborne sensor due to orbital constraints. The cross-wise configuration (see Figure 4.3) with small angular separations between look directions has been suggested as a reasonable approximation to the most desirable configuration.

Successful radar stereo viewing depends on:

- the stereo arrangement, i.e. the look angles off-nadir, the stereo intersection angles, etc.;
- the ruggedness of the terrain.

In flat or gently rolling areas, stereo presents few problems. In rugged terrain, stereo is possible with same-side geometry and improves with shallow look-angles. For good visual stereo perception, small stereo intersection angles would be preferred. This results in image pairs with little difference in tone and texture but unfortunately little difference in

geometry.

Stereo radar studies, e.g. [Rosenfield, 1968], have been valuable in understanding the implications of different configurations, but the lack of actual stereo SAR imagery of sufficient variation of imaging geometries has prevented a comprehensive evaluation of observer perception and the effect on image analysis. As a result, the required trade-off between geometric accuracy and ease of perception is based on little experimental work. In [Kaupp *et al.*, 1982], [Kaupp *et al.*, 1983], [Welch and Papacharalampos, 1990] and [Pisaruck *et al.*, 1984], computer-simulated radar images were used to investigate spaceborne stereo. Prior to the availability of Seasat and SIR-B image data (pre-1978), few radar stereo results had been reported. Some good results were published by Raytheon and DBA Systems [Leberl, 1990]; however, these were not very representative, as they applied to flat areas with accurately-known control.

Height accuracies of 28 m and 72 m were reported by Leberl [Leberl, 1990] for Seasat data of Los Angeles and SIR-A data of Cephalonia respectively. Leberl and co-workers have also worked extensively with SIR-B stereo imagery [Leberl *et al.*, 1988], [Leberl *et al.*, 1986a], [Leberl *et al.*, 1986b]: here, same-side stereo configurations were employed and height accuracies of up to ± 25 m (1.8 times the range resolution) were reported. A more detailed discussion of these results using the Mount Shasta imagery will be given in Chapter 8. However, for these data, Leberl concluded that the theoretical belief that SAR stereo accuracy would increase with larger intersection angle does not hold. If the terrain under consideration is fairly flat then the theoretical trend is adhered to; but if the terrain is rugged then the theory appears to break down. No explanation for this effect is postulated by Leberl.

Leberl has also looked at a way of employing opposite-side stereo configurations [Fullerton *et al.*, 1986]. Here, one of the images is contrast reversed, i.e. its negative is produced, which is combined with an unaltered second image. Height accuracies of 36 m (twice the pixel resolution) have been quoted.

Hard-copy SAR images can be *viewed* in photogrammetric stereo viewing devices such as a stereo comparator or in an analytical stereo plotting instrument; [Raggam and Leberl, 1984] used a KERN DSR-1. For digital data, the KERN Digital Stereo Plotter could be used and even adapted to deal with SAR imagery.

In Sections 4.2 and 4.3, two methods of obtaining height information from stereo SAR

images are discussed. The first is a photogrammetric approach. All SAR stereo results published so far appear to have been derived using an approach of this type, using hardcopy SAR data in a stereo plotting instrument. In Section 4.3, an alternative, analytic approach is detailed. This approach, developed by the author, employs the range and Doppler equations (as discussed in Chapter 3) for each image. Here, the ground location (X, Y, Z) of a point, which can be identified in each image, can be found. This approach therefore requires sufficient and accurate ephemeris and Doppler data. The accuracy of this approach will depend on the accuracy with which the required parameters are known.

For both approaches, the identification of common points can be done manually or automatically. The manual method is the same as that for photographic images. Automatic matching has proved to be more difficult. Work at University College London has shown that area-based matchers which are successful with SPOT data do not necessarily work well with SAR. [Ramapriyan *et al.*, 1986] and [Thomas *et al.*, 1986] have also studied this topic. [Guindon and Maruyama, 1986] have used simulated data as an aid to matching.

In Sections 4.4 and 4.5, methods of height determination using a combination of optical/infrared and SAR imagery are discussed. In Section 4.4, a photogrammetric approach is addressed. In Section 4.5, a geometric approach is detailed which considers the optical/infrared view as a line joining the sensor to the ground point and the SAR radar pulse as a sphere with a radius equal to the range. The intersection of the sphere and line results in the determination of the ground location (X, Y, Z).

4.2 Radar Height Determination: Photogrammetric Approach

Radar Parallax. The same-side stereo arrangement will be concentrated upon here, as it provides usable stereo pairs for any type of terrain, and is thus more amenable to evaluation. Stereo imagery can be judged by two approaches. The first is described by an *exaggeration factor,* i.e. the flatness perceived by an observer of the three-dimensional model. The vertical scale exaggeration is found for radar by identifying camera positions that would produce the same parallax. The second approach, which will be studied here, considers the amount of parallax for a given object by a specific stereo arrangement. The parallax can be measured from a stereo pair. Figure 4.4 shows the geometry involved for

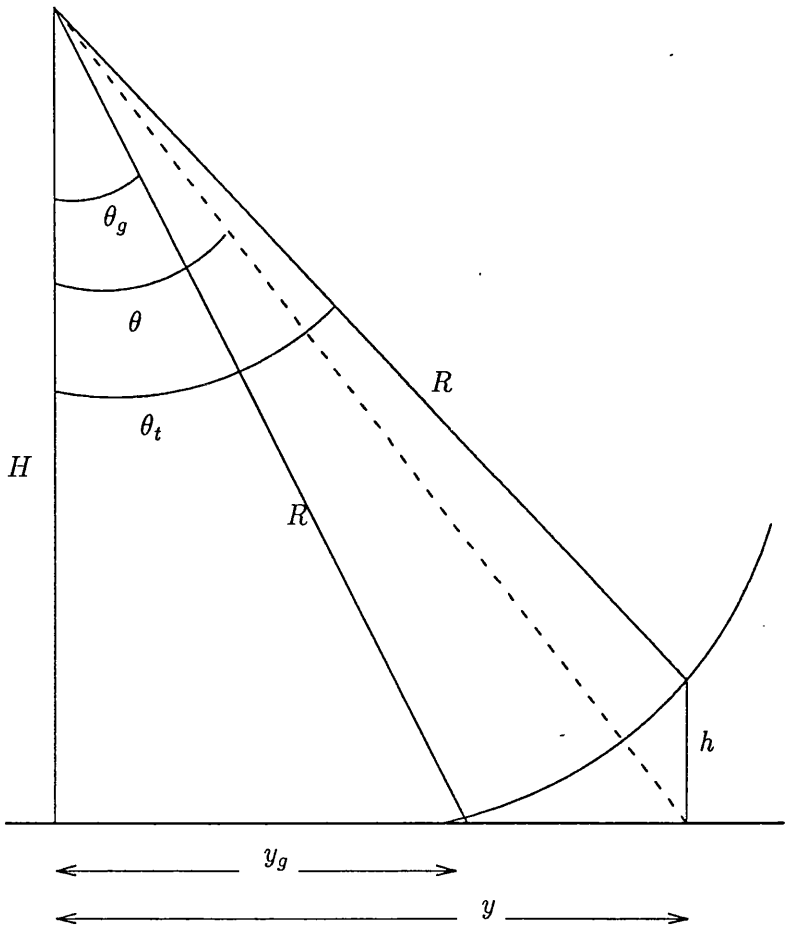

Figure 4.4: Radar Relief Displacement Geometry

radar relief displacements in ground range images. Let us evaluate the relief displacement dp, where $dp = y - y_g$. Now,

$$y = H \tan \theta,$$

$$y_g = H \tan \theta_g,$$

and

$$R = \frac{(H - h)}{\cos \theta_t} = \frac{H}{\cos \theta_g}.$$

Therefore

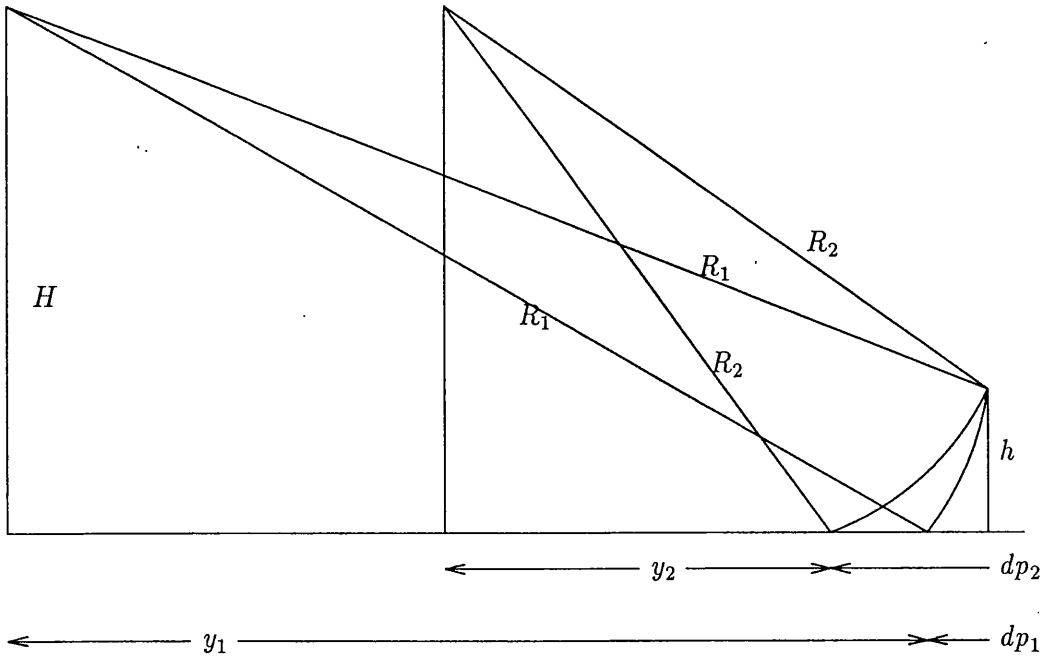

Figure 4.5: Radar Parallax Geometry

$$dp = y - y_g = H\tan\theta - H\tan\theta_g = H(\tan\theta - \tan\theta_g).$$

For same-side stereo, parallax is the difference of the displacements of the two images, as shown in Figure 4.5:

$$\begin{aligned} P = dp_2 - dp_1 &= H(\tan\theta_2 - \tan\theta_{2g}) - H(\tan\theta_1 - \tan\theta_{1g}) \\ &= H((\tan\theta_2 - \tan\theta_1) - (\tan\theta_{2g} - \tan\theta_{1g}). \end{aligned}$$

It should be noted that a given height h will produce a different parallax at different points in the image. For airborne radar, this can be a serious problem. For spaceborne SAR, the angular variation across the range extent of an image is very narrow, making this problem less severe.

Height Determination. Since the imaging geometry of radar differs from that of optical sensors, standard photogrammetric equations cannot be used. A brief development follows

to derive an equation that determines the heights of objects from measurable quantities in a ground-range radar image, thus making it possible to develop accurate topographic maps.

Let Figure 4.5 represent a tower imaged by two radars. In the respective images, the top of the tower would be displaced by an amount dp_1 by the first radar, and the smaller incidence angle of the second would cause a larger displacement dp_2 in the other radar image. Consider expressions for R_1 to the top of the tower and the ground; then

$$R_1^2 = (H - h)^2 + (y_1 + dp_1)^2$$

and

$$R_1^2 = H^2 + y_1^2.$$

Therefore,

$$H^2 + y_1^2 = (H - h)^2 + (y_1 + dp_1)^2$$

and

$$(H - h)^2 = H^2 + y_1^2 - (y_1 + dp_1)^2.$$

Similarly, for R_2,

$$(H - h)^2 = H^2 + y_2^2 - (y_2 + dp_2)^2. \tag{4.1}$$

Equating the $(H - h)^2$ terms,

$$y_1^2 - (y_1 + dp_2)^2 = y_2^2 - (y_2 + dp_2)^2.$$

Now since, $P = dp_2 - dp_1$, then $dp_2 = P + dp_1$; we find, on substituting, that

$$y_1^2 - (y_1 + dp_1)^2 = y_2^2 - (y_2 + P + dp_1)^2.$$

Therefore,

$$y_1^2 - y_2^2 = (y_1 + dp_1)^2 - (y_2 + P + dp_1)^2.$$

Expanding this expression:

$$y_1^2 - y_2^2 = y_1^2 + 2y_1dp_1 + dp_1^2 - y_2^2 - 2y_2P - 2y_2dp_1 - 2Pdp_1 - P^2 - dp_1^2$$

so that

$$0 = 2y_1dp_1 - 2y_2dp_1 - 2Pdp_1 - P^2 - 2y_2P = 2dp_1(y_1 - y_2 - P) - P^2 - 2y_2P.$$

Therefore,

$$dp_1 = \frac{P^2 + 2y_2P}{2(y_1 - y_2 - P)}.$$

Substituting $dp_2 = P + dp_1$ in Equation 4.1, and then using the above expression for dp_1, the height of a feature can then be obtained:

$$(H - h)^2 = H^2 + y_2^2 - \left(y_2 + P + \frac{P^2 + 2y_2P}{2(y_1 - y_2 - P)}\right)^2.$$

Therefore,

$$h = H - \sqrt{H^2 + y_2^2 - \left(y_2 + P + \frac{P^2 + 2y_2P}{2(y_1 - y_2 - P)}\right)^2}. \tag{4.2}$$

Both sensor geometries i.e., altitude H, look-angle, etc., should be known. y_1 and y_2 can be found from the ground-range images along with the parallax P; hence, the height of the object h can be ascertained. [Wu and Lin, 1989] describes work on this topic for SLAR.

However, in practice, the situation described above will, almost certainly, never occur. The two sensors will rarely have perfectly parallel flight-paths with identical attitudes and be at the same altitude. Hence the practical procedure for height assessment is much more complicated than the idealised situation described here.

Leberl [Leberl, 1990] has studied the error analysis of photogrammetric SAR stereo

methods in detail. He divided the errors into two types, *absolute errors* — those of individual point co-ordinates and — *relative errors* — those of co-ordinate differences. The former type was reported to be generally of less importance than the latter. Leberl found large errors with both aircraft and spaceborne radar stereo. He quotes that for aircraft, which generally have relatively large stereo intersection angles, absolute errors in the sensor position or range measurement will result in stereo errors of up to five times larger than this error. For spaceborne SAR, these sensor position errors are magnified to up to 15 times the absolute error. The relative errors are quoted as much larger; for example, for spaceborne SAR stereo, an error in the stereo base of 100 m would result in a height error of 935 m and an across-track error of 988 m. Leberl has, therefore, demonstrated that the photogrammetric approach is very sensitive to error.

Leberl has applied a photogrammetric stereo analysis to the SIR-B imagery of Mount Shasta used in this work. The results obtained by Leberl from the Mount Shasta imagery are discussed in Chapter 8.

4.3 Radar Height Determination: Analytic Approach

If the images are accompanied by sufficient orbit and Doppler information, then the range and Doppler equations, discussed in Section 3.4.1, can be used to determine the co-ordinates of a point that appears in both images. For example, if the two images are denoted as Image 1 and Image 2, then:

$$R_1 = |\underline{s_1} - \underline{p}|$$

$$f_{dc1} = \frac{2(\dot{\underline{s_1}} - \dot{\underline{p}}).(\underline{s_1} - \underline{p})}{\lambda_1 |\underline{s_1} - \underline{p}|}$$

$$R_2 = |\underline{s_2} - \underline{p}|$$

$$f_{dc2} = \frac{2(\dot{\underline{s_2}} - \dot{\underline{p}}).(\underline{s_2} - \underline{p})}{\lambda_2 |\underline{s_2} - \underline{p}|}$$

where

R_1 is the range in Image 1

R_2 is the range in Image 2

f_{dc1} is the Doppler value for Image 1

f_{dc2} is the Doppler value for Image 2

$\underline{s_1}$ is the position of the sensor for Image 1

$\underline{s_2}$ is the position of the sensor for Image 2

$\underline{\dot{s}_1}$ is the velocity of the sensor for Image 1

$\underline{\dot{s}_2}$ is the velocity of the sensor for Image 2

λ_1 is the radar wavelength for Image 1

λ_2 is the radar wavelength for Image 2

$\underline{p}$ is the position of the point on the ground

$\underline{\dot{p}}$ is the velocity of the point

These four equations can be solved, by a similar means to that given in Section 3.4.1, to give the common position $\underline{p}$; i.e., the derivatives are evaluated and used, with these equations, to find a solution via some iterative technique.

It should be noted that the two sets of equations must be in the same co-ordinate system. The work in this study was carried out in a geocentric inertial system. Since the images used in this study were taken at different times, the co-ordinate systems relating to each image will also be different. Therefore, one system must be converted to the other or, alternatively, both converted to a common system. The conversion factor from one system to another is of the form

$$\underline{r} = \begin{pmatrix} \cos(\theta_1 - \theta_2) & \sin(\theta_1 - \theta_2) & 0 \\ -\sin(\theta_1 - \theta_2) & \cos(\theta_1 - \theta_2) & 0 \\ 0 & 0 & 1 \end{pmatrix} \underline{r_0}$$

where θ_1 and θ_2 are the GMSTs (see Chapter 5) of systems 1 and 2 respectively. The signs of θ_1 and θ_2 will depend on the direction of conversion.

This method is obviously dependent on the accuracy with which the required input data can be supplied. In Chapter 8, it is applied to stereo SIR-B imagery of Mount Shasta.

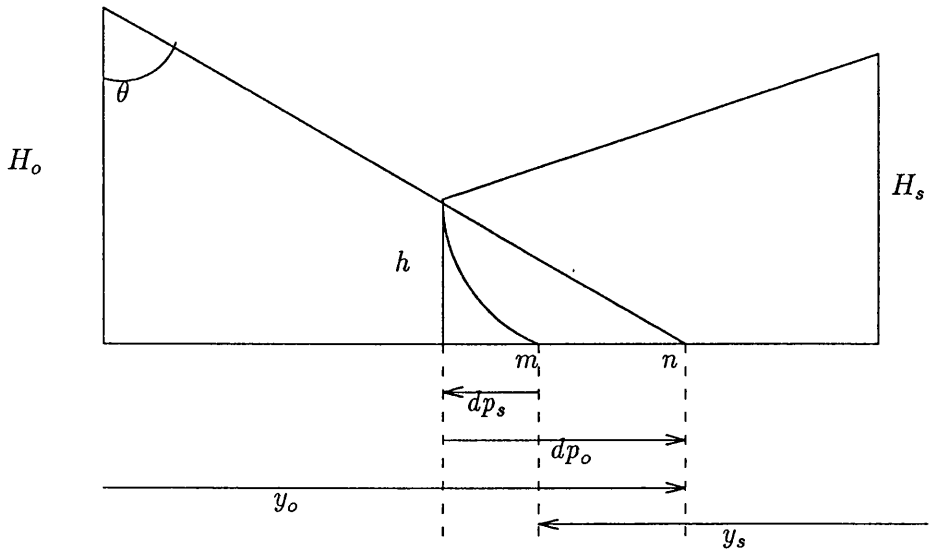

Figure 4.6: Illustration of SAR/Optical Configuration for Height Determination

4.4 SAR/Optical Height Determination: Photogrammetric Approach

SAR has been merged with optical data such as Landsat, e.g. [Bloom *et al.*, 1988], where simplified stereophotogrammetric equations were used to calculate the height of an object above a reference plane from SIR-B and Landsat TM image sets for areas where little or no ground control was available. [Brill, 1987] addresses the same problem for the case when the sensor positions are unknown but matching GCPs have been identified in the SAR and optical images.

A comparison of the imaging geometry of radar and optical sensors is shown in Figure 4.6. The top of an object of elevation h is projected down to position n by the optical sensor. The radar will locate this at m. The base of the object will be located at the correct position by both types of sensor.

If we let dp_s and dp_o be the displacements due the SAR and optical sensors respectively. From the previous discussion on stereo SAR it was shown, Equation 4.1, that

$$(H_s - h)^2 = H_s^2 + y_s^2 - (y_s + dp_s)^2. \tag{4.3}$$

For the optical case,

$$\tan\theta = \frac{y_o}{H_o} = \frac{(y_o - dp_o)}{(H_o - h)},$$

so that

$$dp_o = \frac{hy_o}{H_o}.$$

Now $P = dp_o - dp_s$, so

$$dp_s = dp_o - P = \frac{hy_o}{H_o} - P.$$

Substituting dp_s into Equation 4.3 gives

$$(H_s - h)^2 = H_s^2 + y_s^2 - (y_s + \frac{hy_o}{H_o} - P)^2.$$

Expanding this yields

$$H_s^2 - 2H_s h + h^2 = H_s^2 + y_s^2 - y_s^2 - P^2 - \frac{h^2 y_o^2}{H_o^2} + 2Py_s + \frac{2Phy_o}{H_o} - \frac{2y_s y_o h}{H_o}.$$

Therefore,

$$h^2\left(1 + \frac{y_o^2}{H_o^2}\right) + 2h\left(\frac{y_s y_o}{H_o} - \frac{Py_o}{H_o} - 2H_s\right) - 2Py_s + P^2 = 0$$

This quadratic equation can then be solved for h.

4.5 SAR/Optical Height Determination: Geometric Approach

If, however, there are some auxiliary data available for each image, then the position $\underline{p}$ of a point identified in each image can be found. This is done by considering a 'ray' drawn from the optical sensor to the required position on the ground at a known look angle. The SAR range is considered to be a sphere, with the SAR position at its centre. The intersection of the ray of the optical sensor and the sphere of the SAR will give the required position $\underline{p}$ on

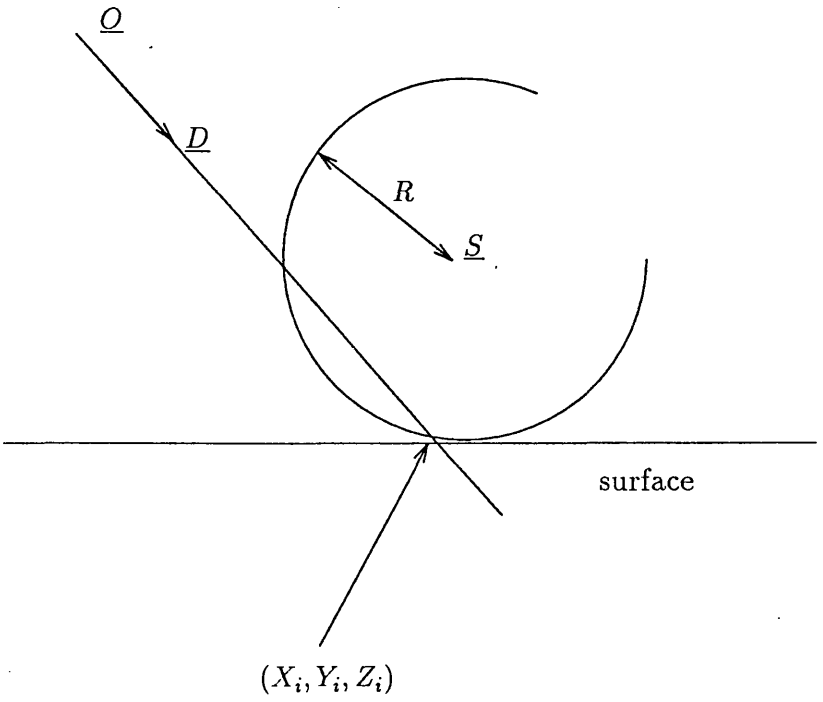

Figure 4.7: Intersection of Line with Sphere

the ground. This is analogous to the intersection of a ray of light with a sphere, a problem which has received significant interest in the context of ray-traced rendering for computer graphics (see [Glassner, 1989], for example).

Consider light being received from the direction $\underline{D}$ at a point $\underline{O}$ by the optical sensor, passing through a sphere of radius R centered at $\underline{S}$, the location of the SAR (Figure 4.7). We can write the path of the ray of light in parametric form as

$$\underline{D}(t) = \underline{O} + t\underline{D}, \quad t > 0 \tag{4.4}$$

and define the surface of the sphere as

$$(X_i - S_x)^2 + (Y_i - S_y)^2 + (Z_i - S_z)^2 = R^2.$$

At the intersection points, we can say

$$(O_x + tD_x - S_x)^2 + (O_y + tD_y - S_y)^2 + (O_z + tD_z - S_z)^2 = R^2.$$

This may be written as a quadratic in t, i.e. as $At^2 + Bt + C = 0$, where the coefficients are given by

$$\begin{aligned} A &= D_x^2 + D_y^2 + D_z^2 \\ B &= 2[D_x(O_x - S_x) + D_y(O_y - S_y) + D_z(O_z - S_z)] \\ C &= (O_x - S_x)^2 + (O_y - S_y)^2 + (O_z - S_z)^2 - R^2 \end{aligned}$$

If we ensure that $\underline{D}$ is normalised, as is normally the case, we will have $A = 1$. This quadratic equation has solutions

$$t_0 = \frac{-B - \sqrt{B^2 - 4AC}}{2A} \tag{4.5}$$

$$t_1 = \frac{-B + \sqrt{B^2 - 4AC}}{2A} \tag{4.6}$$

There are essentially three cases, depending on the sign of the discriminant, $B^2 - 4AC$:

discriminant is negative: the line and sphere do not intersect

discriminant is zero: the line is tangential to the sphere

discriminant is positive: the line and sphere do intersect, and the points of intersection are determined by finding t_0 and t_1 from Equation 4.5 and Equation 4.6, then substituting them back into Equation 4.4.

The steps involved in this procedure are, if we pre-compute as many parameters as possible:

1. calculate A, B and C of the quadratic (8 additions/subtractions, 7 multiplications)
2. calculate the discriminant (1 addition, 2 multiplications, 1 compare)
3. calculate t_0 and determine whether positive (1 subtraction, 1 multiply, 1 square root, 1 compare)
4. possibly calculate t_1 and determine whether positive (1 subtraction, 1 multiply, 1 square root, 1 compare)

5. calculate intersection point (3 additions, 3 multiplications)

It is worth noting that determining t_0 and t_1 by a direct application of Equation 4.5 and Equation 4.6 is not numerically very accurate, particularly for the smaller root when $B^2 \gg 4AC$ [Press *et al.*, 1986]. A better way to compute the roots is via the intermediate result

$$q = \frac{1}{2}\left\{B + \mathrm{sgn}(B)\sqrt{B^2 - 4AC}\right\},$$

whereafter

$$t = \frac{q}{A} \quad \text{or} \quad \frac{C}{q}.$$

To determine which of the two calculated intersection points is correct, the optical sensor is considered. Since the position and look-angle of this sensor is known, a rough vector length can be calculated. All points on the Earth have altitudes of less than 9 Km, so the value of t closest to the roughly-calculated length will give the required solution. Normally, the look-angle of optical spaceborne sensors is relatively small due to the increased atmospheric degradation at large angles (e.g., SPOT is $\pm 27°$).

Chapter 5

Orbit, Time and Reference System Considerations

5.1 Introduction

In the work with the SIR-B data, to be described in Chapters 6, 7 and 8, only one sensor position and velocity vector were given. However, the position of the sensor at some earlier or later time can be predicted if the orbit of the sensor platform can be found. This chapter outlines a procedure for establishing an orbit from only one position and velocity vector. It also details how positions on this orbit can be found for different times. These orbit calculations are carried out in a particular co-ordinate (reference) system known as the *orbital system.* However, the SIR-B data supplied were not given in this system, but in a *geocentric terrestrial system.* In the section on time and reference systems (Section 5.2), the conversions between the reference systems involved in the analysis of SIR-B data will be shown. This can be rather complicated, as the reference systems are associated with particular time systems and conversion from one time system to another can be complex. Again, the time systems and their conversions required for the SIR-B work will be detailed.

5.2 Time and Reference Systems

Three reference systems (shown in Figure 5.1) were considered in this work:

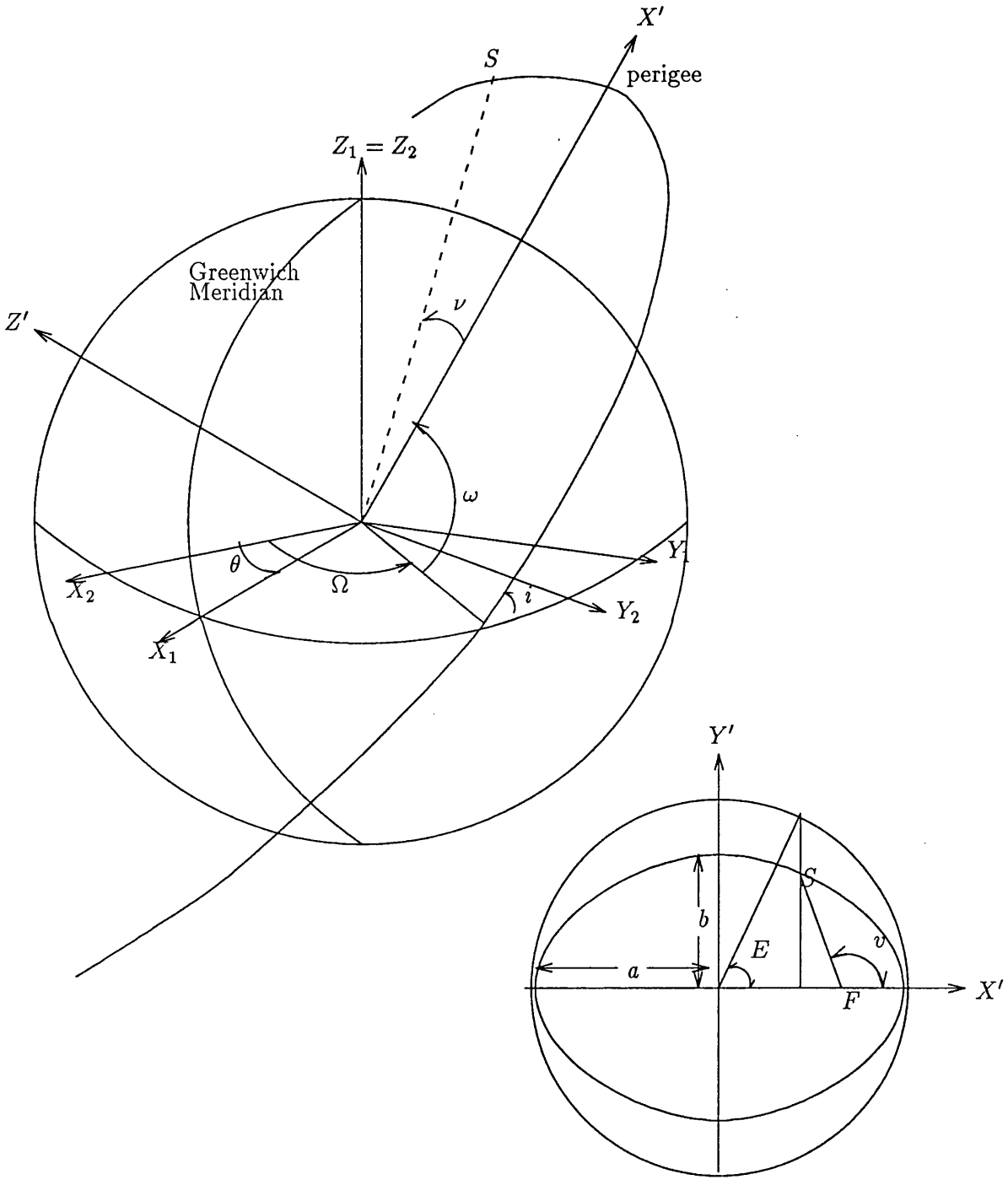

Figure 5.1: Orbital Elements and Reference Systems

$[X', Y', Z']$ is an orbital system with X' pointing to the perigee and perpendicular to the orbital plane.

$[X_2, Y_2, Z_2]$ is a geocentric inertial system, i.e. a system that does not rotate with the Earth. This system is fixed relative to the Sun. The intersection of X_2 with the equator occurs at the vernal equinox.

$[X_1, Y_1, Z_1]$ is a geocentric terrestrial system, i.e. an Earth-fixed system that rotates with the Earth.

Now

$$\begin{pmatrix} X_2 \\ Y_2 \\ Z_2 \end{pmatrix} = R \begin{pmatrix} X' \\ Y' \\ Z' \end{pmatrix}$$

and

$$\begin{pmatrix} X_1 \\ Y_1 \\ Z_1 \end{pmatrix} = R_3(\theta) \begin{pmatrix} X_2 \\ Y_2 \\ Z_2 \end{pmatrix},$$

where R is a rotation matrix to be defined later (see Equation 5.2), R_3 denotes a rotation about the Z axis, and θ is the Greenwich Apparent Sidereal Time or GAST (also known as the hour angle of the vernal equinox). Now

$$\text{GAST} = \text{GMST} + \text{equation of equinox},$$

where GMST is the Greenwich Mean Sidereal Time. The difference between GMST and GAST is small, usually less than one second of time in θ, and is due to nutation effects. The equation of equinox is difficult to calculate and, as it is small, θ was taken to be GMST for this work, i.e. it was assumed that GAST=GMST.

In the SIR-B data, the time of imaging was given with respect to Universal Time (UT; often referred to as Greenwich Mean Time). The conversion from UT to GMST requires the calculation of the Julian Date (JD).. [Hatcher, 1984] describes in detail the JD calculation for all times. The conversion is as follows.

Let A be the year of the common era, reckoned in the usual way with New Year on $1^{\underline{st}}$ January; let M be the month number reckoned from January = 1 through to December = 12; and let the day of the month be represented by D.

$$A' = A - \left\lfloor \frac{12 - M}{10} \right\rfloor$$

$$M' = M - 3 \bmod 12$$

where $\lfloor \cdot \rfloor$ is the operation of taking the integer part.

$$y = \lfloor 365.25(A' + 4712) \rfloor$$

$$d = \lfloor 30.6M' + 0.5 \rfloor$$

$$N = y + d + D + 59$$

$$g = \left\lfloor \left\lfloor \frac{A'}{100} + 1 \right\rfloor \times 0.75 \right\rfloor - 2$$

JD $= N - g - 0.5$ measured from zero hours (midnight), which is what is required. (JD $= N - g$ is measured from *noon*.)

Let T be the given Universal Time in seconds. Then, if

$$t_u = \frac{\text{JD} - 2451545.0}{36525.0}$$

and

$$\alpha_u = 24110.54841 + 8640184.812866 t_u + 9.3104 \times 10^{-2} t_u^2 - 6.2 \times 10^{-6} t_u^3,$$

we have

$$\text{GMST} = \frac{\alpha_u + 1.002737822\ T}{3600.0}.$$

This GMST is in seconds and will be greater than one day. The number of days must be removed and the remainder converted to hours/minutes/seconds.

Let $\underline{r_0}$ and $\underline{v_0}$ be position and velocity vectors respectively (as supplied in the SIR-B header data), defined in a geocentric terrestrial reference system, and let $\underline{r}$ and $\underline{v}$ be the same position and velocity vectors respectively, defined in a geocentric inertial reference system. Then,

$$\underline{r} = \begin{pmatrix} \cos\theta & \sin\theta & 0 \\ -\sin\theta & \cos\theta & 0 \\ 0 & 0 & 1 \end{pmatrix} \underline{r_0}$$

$$\underline{v} = \begin{pmatrix} -\dot{\theta}\sin\theta & \dot{\theta}\cos\theta & 0 \\ -\dot{\theta}\cos\theta & -\dot{\theta}\sin\theta & 0 \\ 0 & 0 & 0 \end{pmatrix} \underline{r_0} + \begin{pmatrix} \cos\theta & \sin\theta & 0 \\ -\sin\theta & \cos\theta & 0 \\ 0 & 0 & 1 \end{pmatrix} \underline{v_0},$$

where $\theta = -\text{GMST}$ and $\dot{\theta} = -2\pi/\text{day}$ radians.

These $\underline{r}$ and $\underline{v}$ can be used in the calculation of orbital parameters and hence new sensor positions can be established using the following procedures.

5.3 Orbits

A satellite orbit is uniquely specified by its orbital elements — see Figure 5.1. The satellite's orbital plane is determined with reference to the equator by two orbital elements, Ω, the right ascension of the ascending node, and i, the orbital inclination (to the equator). These two parameters define not only the orbital plane, but also the sense of the orbital motion. The orientation of the orbit within its plane is specified by the argument of perigee ω. The size and shape of the orbit are given by a, the semi-major axis, and e, the eccentricity, respectively. The timing of the orbit is specified by the time of perigee, τ. These six

parameters $(a, e, \tau, i, \Omega, \omega)$ are usually taken as the orbital elements, though certain variants are possible, and sometimes even essential — as in this case. Here, instead of τ, two other parameters will be used: ν, the true anomaly, and E, the eccentric anomaly [Green, 1985].

5.3.1 Calculation of Orbital Parameters

The material presented in this Section is based on that in [Green, 1985].

Let the satellite's position and velocity vectors at a given time t be $\underline{r} = [X_2, Y_2, Z_2]$ and $\underline{v} = [\dot{X}_2, \dot{Y}_2, \dot{Z}_2]$ respectively. The semi-major axis of the orbit is given by

$$a = \frac{\mu|r|}{2\mu - |r||v|^2}$$

where $\mu = GM = 3.986005 \times 10^{14}$ m^{3}s^{-2}, G is the Universal Gravitational Constant, and M is the mass of the Earth. We also have

$$\underline{h} = \underline{r} \times \underline{v} = \begin{pmatrix} h_1 \\ h_2 \\ h_3 \end{pmatrix},$$

where $\underline{h}$ is the vector angular momentum per unit mass. The other orbital parameters are given by:

$$\Omega = -\tan^{-1}\frac{h_1}{h_2}$$

$$i = \cos^{-1}\frac{h_3}{|h|}$$

$$e = \sqrt{1 - \frac{|h|^2}{\mu a}}$$

$$E = \pm\cos^{-1}\frac{a - |r|}{ae}.$$

The plus sign in the expression for E corresponds to the satellite's outward journey, from

perigee to apogee, when its radial velocity is positive. The sign of the radial velocity is that of the scalar product $\underline{r}.\underline{v}$.

The true anomaly is given by

$$\nu = 2\tan^{-1}\left[\left(\frac{1+e}{1-e}\right)^{\frac{1}{2}}\tan\left(\frac{E}{2}\right)\right]$$

and the argument of perigee by

$$\omega = \pm\cos^{-1}\left(\frac{X\cos\Omega + Y\sin\Omega}{|r|}\right) - \nu,$$

where the plus sign corresponds to positive Z.

Therefore, it has been shown that all the parameters needed to describe the orbit, as described in Section 5.3, can be calculated from *one* satellite position and velocity, $\underline{r}$ and $\underline{v}$.

5.3.2 Calculation of Orbital Position

To calculate the satellite's position at a time $t+\partial t$ from the position at time t, an iterative procedure is required. The mean anomaly, M_t, at time t is given by

$$M_t = E_t - e\sin E_t,$$

where E_t is the value of E at time t (see previous Section). Let M be the mean anomaly at time $t+\partial t$ [Slama *et al.*, 1980]:

$$M = M_t + \partial t\sqrt{\frac{\mu}{a^3}}$$

$$E = M + e\sin E$$

This equation is then solved for E, the value at time $t+\partial t$. For the first iteration, let $E' = M$. Then, for the second iteration, let $E'' = M + e\sin E'$; and so on. The equation is usually solved to adequate accuracy after about five iterations. In terms of the orbital co-ordinate system,

$$\begin{pmatrix} X' \\ Y' \\ Z' \end{pmatrix} = \begin{pmatrix} a(\cos E - e) \\ a\sqrt{1-e^2}\sin E \\ 0 \end{pmatrix}. \tag{5.1}$$

The new position, at time $t + \partial t$, with respect to a geocentric inertial system, is given by

$$\begin{pmatrix} X_2 \\ Y_2 \\ Z_2 \end{pmatrix} = R \begin{pmatrix} X' \\ Y' \\ Z' \end{pmatrix}, \tag{5.2}$$

where R is the rotation matrix given as $R = R_3(-\Omega)R_1(-i)R_3(-\omega)$.[1] Hence,

$$X_2 = a(\cos E - e)(\cos\omega\cos\Omega - \sin\omega\sin\Omega\cos i) - a\sin E\sqrt{1-e^2}(\sin\omega\cos\Omega + \cos\omega\sin\Omega\cos i);$$

$$Y_2 = a(\cos E - e)(\cos\omega\sin\Omega + \sin\omega\cos\Omega\sin i) + a\sin E\sqrt{1-e^2}(\cos\omega\cos\Omega\sin i - \sin\omega\sin\Omega);$$

$$Z_2 = a(\cos E - e)\sin\omega\sin i + a\sin E\sqrt{1-e^2}\cos\omega\sin i.$$

The velocity at the new position is given by

$$\dot{X}_2 = \sqrt{\frac{\mu}{a}}\frac{1}{(1-e\cos E)}((\sin E\sin\omega - \cos E\cos\omega)\sin\Omega\cos i - (\sin E\cos\omega + \cos E\sin\omega)\cos\Omega);$$

$$\dot{Y}_2 = -\sqrt{\frac{\mu}{a}}\frac{1}{(1-e\cos E)}((\sin E\cos\omega + \cos E\sin\omega)\sin\Omega + (\sin E\sin\omega - \cos E\cos\omega)\cos\Omega\cos i);$$

$$\dot{Z}_2 = \sqrt{\frac{\mu}{a}}\frac{1}{(1-e\cos E)}((\sin E\sin\omega - \cos E\cos\omega)\sin i).$$

The position of the satellite at any time in the orbit can hence be calculated using these equations.

[1] R_3 denotes a rotation about the Z axis and R_1 a rotation about the X axis.

5.4 Summary

This chapter has described a procedure for establishing an orbit from only one position and velocity vector and it has shown how positions on this orbit can be found at different times. Conversions between the relevant time and reference systems have also been defined.

As stated in Chapter 3, the geocoding procedure used in this work must be carried out in an inertial reference system. Here the geocentric inertial reference system, as described in this chapter, was used. In operational geocoding systems the orbit will normally be described by a polynomial. For the geocoding work of this study the calculated orbit was similarly represented by a polynomial line fit.

Chapter 6

Assessment of SIR-B Mount Shasta Images

6.1 Introduction

As stated in Section 1.3, the image data used in this study were of Mount Shasta, California, USA, acquired by the Shuttle SIR-B SAR sensor in October 1984. The data were supplied on a tape that also contained images of Egypt and Madagascar. These other images would not be used further for reasons given in Section 1.3. No other information pertaining to these images was available; hence the author had no definition of how these images were stored on the tape or how to extract the header data. There were no documents describing the header data.

In the sections that follow in this Chapter, the author describes how these Mount Shasta images were assessed in order to obtain the information necessary to proceed with the geocoding and stereo studies.

6.2 Preliminary Assessment of Image Data

Nine SIR-B images were supplied on tape. Images 1, 2, 3 and 7 were of the Mt. Shasta area; header data preceded each image. The author was informed that these were slant-range images, and the work proceeded on this basis; however, some checks were made (as detailed in the next section) to see if there were any obvious discrepancies with this assumption. Maps of the area were also obtained.

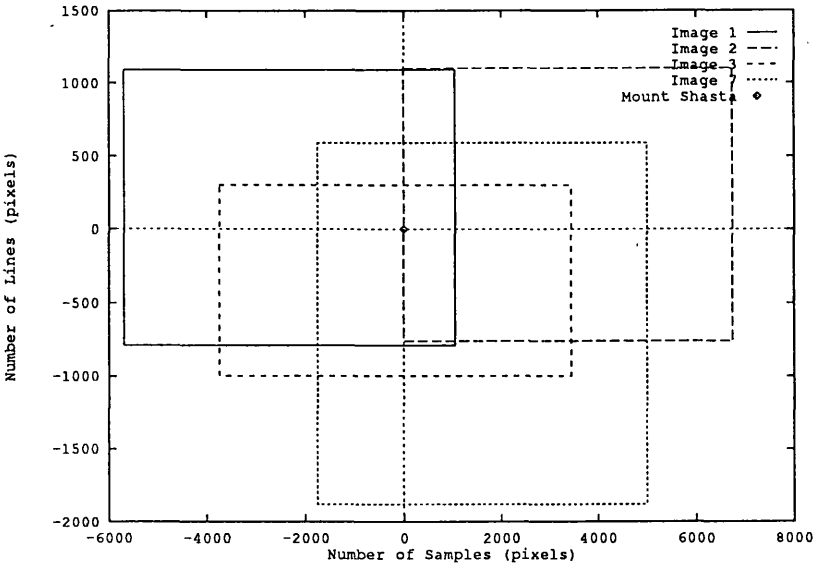

Figure 6.1: Image Extents Relative to Mount Shasta Peak

Image Sizes		
Image No	No of Lines	No of Samples
1	1861	6756
2	1861	6756
3	1308	7184
7	2466	6788

Programs were written to interface to the TAE/BISHOP image processing software package [Perkins *et al.*, 1988] on the VAX so that the images could be handled and viewed; existing software could not handle images of this size. The relative positions of the images with respect to each other and to the peak of Mt. Shasta are shown in Figure 6.1. No maps were available for the area to the east of Mt. Shasta and, since the images of this area appeared fairly feature-free, it was decided that Image 2 should not be studied in detail. The images were observed on the VAX display and an attempt was made to locate the image positions on the maps. This proved to be quite difficult, as the images were of poor contrast and the area away from the actual mountain is quite bland.

The area where the images overlap was extracted and studied in more detail. These image areas are shown in Figures 6.2, 6.3 and 6.4. The header data of Images 1, 2, 3 and 7 are presented in Figures 6.5, 6.6, 6.7, and 6.8. The latitude and longitude values given in

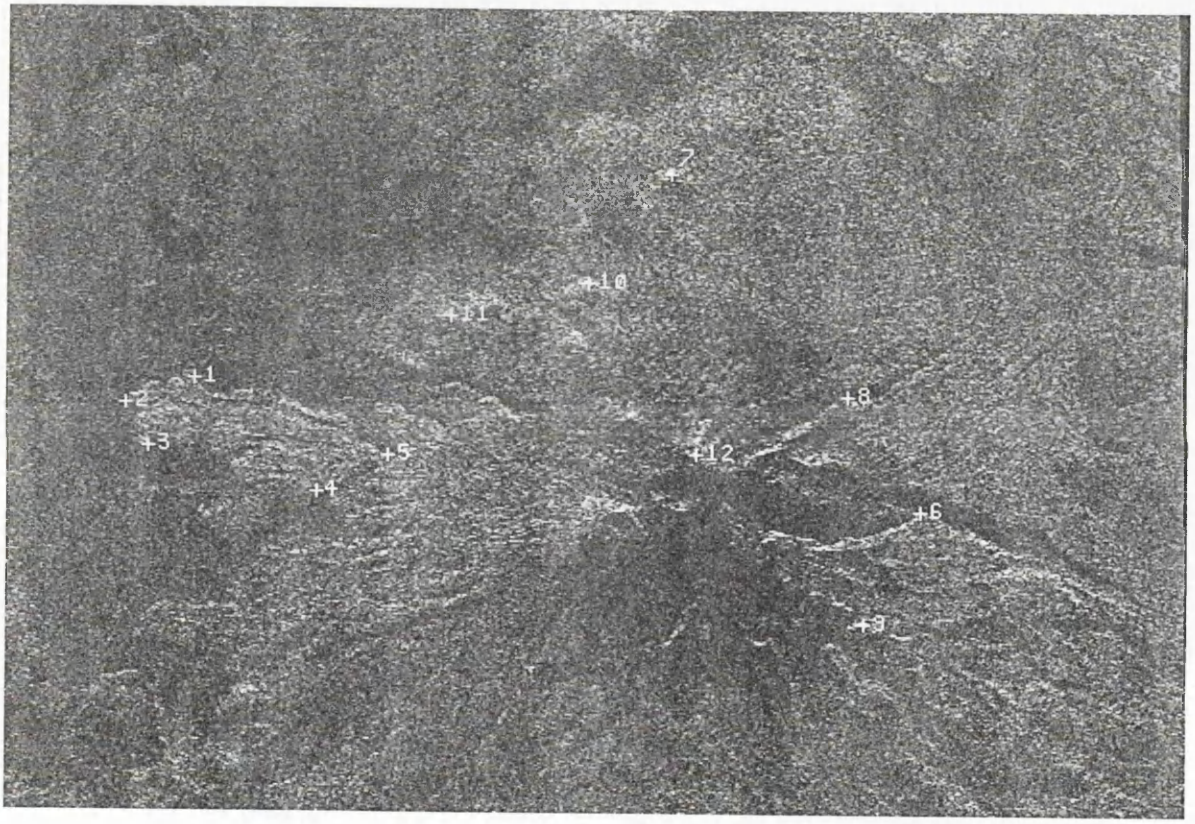

Figure 6.2: Image 1 — Mount Shasta

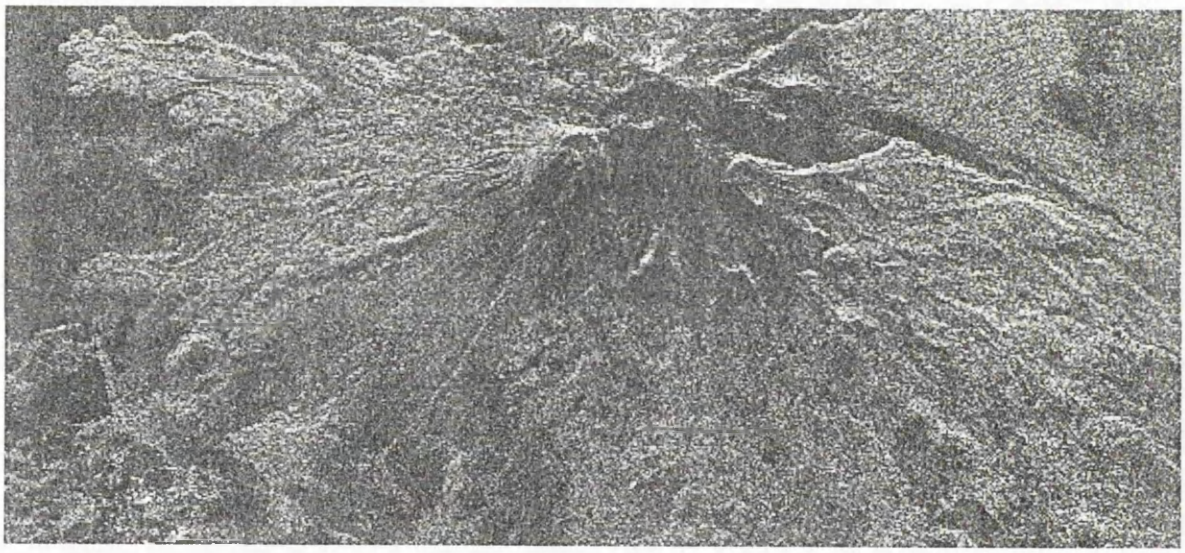

Figure 6.3: Image 3 — Mount Shasta

Figure 6.4: Image 7 — Mount Shasta

```
              NASA JPL SIR-B DIGITALLY CORRELATED SAR IMAGE
                    DATA TAKE AL-087.40  SCENE 001
     CENTER GMT 281/20:52:38.069, 1984     CORR. DATE: 10/18/84
CENTER LAT: 41 DEG (N)              CENTER LONG: 123 DEG (W)
SITE:SHASTA
CENTER RES: 15.7 M (GRND R) X 51.0 M (AZ)     RAW DATA: 5 BPS
PIXEL SIZE = 12.5M     CENTER INCIDENCE ANGLE: 63.8 DEG
TRACK -----> 119.0 DEG (TO TRUE NORTH)
X POSITION: -2346.067 KM, Y POSITION: -4123.520 KM  Z POSITION:  4587.281 KM
X VELOCITY:  3075.009 M/S  Y VELOCITY: -5804.449 M/S Z VELOCITY: -3644.664 M/S
NEAR SLANT RANGE: 432.75 KM
EARTH RADIUS AT TARGET: 6368.88 KM
SHUTTLE ALTITUDE: 231.57 KM
ROLL: 210.0 DEG     YAW:    .0 DEG     PITCH:    .0 DEG
GAIN:  98.60 DB     PRF: 1274.5 HZ     CAL LEVEL: 1     BORE ANGLE:  32.5 DEG
DATA WINDOW POSITION: 44
DATA RATE: 30.4 MHZ
NUMBER OF SAMPLES PER LINE = 6756     TOTAL NUMBER OF LINES = 1676
FD COEFF ACROSS TRACK: FD:A =      .00, FD:B =    18.90, FD:C =  2082.46 HZ
FDDOT COEFF ACROSS TRACK: FR:D =      .00, FR:E =   -16.44,
FR:F =  1058.43 HZ/S  FDDOT COEFF ALONG TRACK: FR:A1 =      .00,
FR:A2 =      .00, FR:A3 =      .00 HZ/S
EARTH RADIUS AT NADIR: 6367.70 KM     AZIMUTH SKEW:   -29 PIXELS
LAT(NE): 42 DEG  1.9 MIN (N)     LON(NE): 122 DEG 54.6 MIN (W)
LAT(NL): 41 DEG 34.8 MIN (N)     LON(NL): 122 DEG 12.3 MIN (W)
LAT(FE): 40 DEG 58.5 MIN (N)     LON(FE): 124 DEG  3.0 MIN (W)
LAT(FL): 40 DEG 23.2 MIN (N)     LON(FL): 123 DEG   .0 MIN (W)
CAL TONE EST:  74.61X DB    BER: -56.82 DB
START TIME: 281/20:52:30     STARTING SAMPLE NO. =    1
SCALE FACTOR:   6.77 DB     FR AZIMUTH INCREMENT FLAG = 0
BLOCKS PER FDDOT AZIMUTH INCREMENT = 27    LINES PER REFERENCE UPDATE =  8
SAMPLES PER SLANT RANGE IMAGE LINE = 3840
NUMBER OF SLANT RANGE IMAGE RECORDS = 1843
SIGNAL TO NOISE RATIO =  4.10X DB    NOISE = 47.08X DB
```

Figure 6.5: Header File for Image 1

```
              NASA JPL SIR-B DIGITALLY CORRELATED SAR IMAGE
                    DATA TAKE AL-087.40  SCENE 002
     CENTER GMT 281/20:52:48.510, 1984     CORR. DATE: 10/18/84
CENTER LAT: 40 DEG (N)              CENTER LONG: 122 DEG (W)
SITE:SHASTA
CENTER RES: 15.7 M (GRND R) X 51.0 M (AZ)   RAW DATA: 5 BPS
PIXEL SIZE = 12.5M     CENTER INCIDENCE ANGLE: 63.8 DEG
TRACK ----> 119.5 DEG (TO TRUE NORTH)
X POSITION: -2313.828 KM   Y POSITION: -4183.836 KM   Z POSITION:  4548.875 KM
X VELOCITY:  3099.752 M/S  Y VELOCITY: -5749.352 M/S  Z VELOCITY: -3710.871 M/S
NEAR SLANT RANGE: 432.75 KM
EARTH RADIUS AT TARGET: 6369.05 KM
SHUTTLE ALTITUDE: 231.39 KM
ROLL: 210.0 DEG     YAW:    .0 DEG     PITCH:    .0 DEG
GAIN:  98.60 DB     PRF: 1274.5 HZ     CAL LEVEL: 1     BORE ANGLE:  32.5 DEG
DATA WINDOW POSITION: 44
DATA RATE: 30.4 MHZ
NUMBER OF SAMPLES PER LINE = 6756     TOTAL NUMBER OF LINES = 1676
FD COEFF ACROSS TRACK: FD:A =      .00, FD:B =    18.90, FD:C =  2082.46 HZ
FDDOT COEFF ACROSS TRACK: FR:D =      .00, FR:E =   -16.44,
FR:F =  1058.43 HZ/S  FDDOT COEFF ALONG TRACK: FR:A1 =      .00,
FR:A2 =      .00, FR:A3 =      .00 HZ/S
EARTH RADIUS AT NADIR: 6367.88 KM     AZIMUTH SKEW:   -29 PIXELS
LAT(NE): 41 DEG 35.6 MIN (N)     LON(NE): 122 DEG 13.5 MIN (W)
LAT(NL): 41 DEG  8.2 MIN (N)     LON(NL): 121 DEG 31.7 MIN (W)
LAT(FE): 40 DEG 32.7 MIN (N)     LON(FE): 123 DEG 22.3 MIN (W)
LAT(FL): 40 DEG 43.0 MIN (N)     LON(FL): 122 DEG   .0 MIN (W)
CAL TONE EST:  74.56X DB    BER: -56.82 DB
START TIME: 281/20:52:40     STARTING SAMPLE NO. =    1
SCALE FACTOR:   6.40 DB     FR AZIMUTH INCREMENT FLAG = 0
BLOCKS PER FDDOT AZIMUTH INCREMENT = 18    LINES PER REFERENCE UPDATE =  8
SAMPLES PER SLANT RANGE IMAGE LINE = 3840
NUMBER OF SLANT RANGE IMAGE RECORDS = 1843
SIGNAL TO NOISE RATIO =  4.36X DB    NOISE = 47.09X DB
```

Figure 6.6: Header File for Image 2

```
                NASA JPL SIR-B DIGITALLY CORRELATED SAR IMAGE
                      DATA TAKE AL-055.40  SCENE 004
     CENTER GMT 282/20:35:46.737, 1984     CORR. DATE: 11/06/84
CENTER LAT: 41 DEG (N)              CENTER LONG: 121 DEG (W)
SITE:SHASTA
CENTER RES: 17.4 M (GRND R) X 23.1 M (AZ)   RAW DATA: 5 BPS
PIXEL SIZE = 12.5M     CENTER INCIDENCE ANGLE: 53.8 DEG
TRACK ----> 120.4 DEG (TO TRUE NORTH)
X POSITION: -2369.790 KM   Y POSITION: -4217.070 KM  Z POSITION:  4491.145 KM
X VELOCITY:  2994.816 M/S  Y VELOCITY: -5740.648 M/S Z VELOCITY: -3807.380 M/S
NEAR SLANT RANGE: 375.27 KM
EARTH RADIUS AT TARGET: 6368.94 KM
SHUTTLE ALTITUDE: 232.60 KM
ROLL:  90.0 DEG      YAW:    .0 DEG      PITCH:    .0 DEG
GAIN:  95.40 DB      PRF: 1824.1 HZ      CAL LEVEL: 1      BORE ANGLE:  38.8 DEG
DATA WINDOW POSITION: 37
DATA RATE: 30.4 MHZ
NUMBER OF SAMPLES PER LINE = 7184      TOTAL NUMBER OF LINES = 1109
FD COEFF ACROSS TRACK: FD:A =      .00, FD:B =    36.89, FD:C =  1355.30 HZ
FDDOT COEFF ACROSS TRACK: FR:D =      .00, FR:E =   -32.37,
FR:F =  1236.00 HZ/S  FDDOT COEFF ALONG TRACK: FR:A1 =      .00,
FR:A2 =      .00, FR:A3 =      .00 HZ/S
EARTH RADIUS AT NADIR: 6368.14 KM     AZIMUTH SKEW:   -31 PIXELS
LAT(NE): 41 DEG 26.5 MIN (N)     LON(NE): 122 DEG  7.8 MIN (W)
LAT(NL): 40 DEG 52.0 MIN (N)     LON(NL): 121 DEG 17.5 MIN (W)
LAT(FE): 41 DEG 21.0 MIN (N)     LON(FE): 122 DEG 14.5 MIN (W)
LAT(FL): 40 DEG 24.1 MIN (N)     LON(FL): 121 DEG   .0 MIN (W)
CAL TONE EST:  72.37X DB    BER: -99.99 DB
START TIME: 282/20:35:39     STARTING SAMPLE NO. =    1
SCALE FACTOR:2601.85 DB     FR AZIMUTH INCREMENT FLAG = 0
BLOCKS PER FDDOT AZIMUTH INCREMENT = 25    LINES PER REFERENCE UPDATE =  8
SAMPLES PER SLANT RANGE IMAGE LINE = 5632
NUMBER OF SLANT RANGE IMAGE RECORDS = 1134
SIGNAL TO NOISE RATIO =  5.99X DB    NOISE = 44.42X DB
```

Figure 6.7: Header File for Image 3

```
                NASA JPL SIR-B DIGITALLY CORRELATED SAR IMAGE
                     DATA TAKE AL-087.40  SCENE 002

    CENTER GMT 284/20: 2:19.394, 1984     CORR. DATE: 10/18/84
CENTER LAT: 41 DEG (N)              CENTER LONG: 122 DEG (W)
SITE:SHASTA
CENTER RES: 28.4 M (GRND R) X 20.5 M (AZ)   RAW DATA: 5 BPS
PIXEL SIZE = 12.5M     CENTER INCIDENCE ANGLE: 29.7 DEG
TRACK ----> 121.6 DEG (TO TRUE NORTH)
X POSITION: -2531.382 KM   Y POSITION: -4203.996 KM   Z POSITION:  4410.418 KM
X VELOCITY:  2744.062 M/S  Y VELOCITY: -5784.742 M/S  Z VELOCITY: -3932.488 M/S
NEAR SLANT RANGE: 256.12 KM
EARTH RADIUS AT TARGET: 6368.86 KM
SHUTTLE ALTITUDE: 229.48 KM
ROLL: 210.0 DEG     YAW:    .0 DEG     PITCH:    .0 DEG
GAIN:  86.67 DB     PRF: 1539.8 HZ     CAL LEVEL: 1     BORE ANGLE:  46.5 DEG
DATA WINDOW POSITION: 41
DATA RATE: 30.4 MHZ
NUMBER OF SAMPLES PER LINE = 6788     TOTAL NUMBER OF LINES = 2281
FD COEFF ACROSS TRACK: FD:A =      .00, FD:B =   123.69, FD:C =  1135.97 HZ
FDDOT COEFF ACROSS TRACK: FR:D =      .00, FR:E =   -63.57,
FR:F =  1817.64 HZ/S  FDDOT COEFF ALONG TRACK: FR:A1 =      .00,
FR:A2 =      .00, FR:A3 =      .00 HZ/S
EARTH RADIUS AT NADIR: 6368.48 KM     AZIMUTH SKEW:   -52 PIXELS
LAT(NE): 41 DEG 41.4 MIN (N)     LON(NE): 122 DEG 21.2 MIN (W)
LAT(NL): 41 DEG  8.7 MIN (N)     LON(NL): 121 DEG 36.8 MIN (W)
LAT(FE): 41 DEG 30.1 MIN (N)     LON(FE): 122 DEG 35.6 MIN (W)
LAT(FL): 40 DEG 51.2 MIN (N)     LON(FL): 121 DEG   .0 MIN (W)
CAL TONE EST:  63.47X DB    BER: -54.32 DB
START TIME: 284/20: 2:12     STARTING SAMPLE NO. =    1
SCALE FACTOR:   9.59 DB     FR AZIMUTH INCREMENT FLAG = 0
BLOCKS PER FDDOT AZIMUTH INCREMENT = 21    LINES PER REFERENCE UPDATE =  8
SAMPLES PER SLANT RANGE IMAGE LINE = 4608
NUMBER OF SLANT RANGE IMAGE RECORDS = 1441
SIGNAL TO NOISE RATIO = 10.98X DB    NOISE = 35.49X DB
```

Figure 6.8: Header File for Image 7

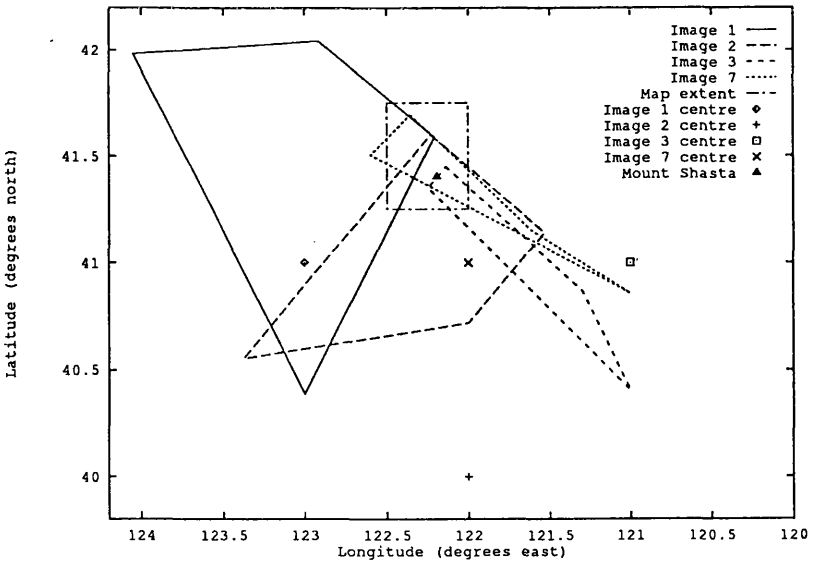

Figure 6.9: Given Latitude and Longitude Extents for the Four Images of Mount Shasta

the header were checked and the results are summarised in Figure 6.9. Here, the available map extent of the area which covers *most* of Images 1, 2, 3 and 7 is shown, along with the position of the centre of the peak. The latitude and longitude extents given in the header data are plotted along with the latitude and longitude values of the image centres. It can be seen that *all* the latitude and longitude values given in the header data are nonsense.

Consider the *centre resolution* and *centre incidence angle* given in the header data:

Image No	Centre Resolution	Centre Incidence Angle
1	15.7m (grnd R) × 51.0m (AZ)	63.8°
3	17.4m (grnd R) × 23.1m (AZ)	53.8°
7	28.4m (grnd R) × 20.5m (AZ)	29.7°

From these ground ranges and angles, an average slant range resolution of ≈14 m is obtained.

The co-ordinate system in which the X, Y and Z position and velocities are given is not defined, but the length of the X, Y, Z vector agrees with the sum of the *shuttle altitude* and the *earth radius at nadir*, indicating that the X, Y, Z origin is at the centre of the earth, i.e. the co-ordinates are in a geocentric terrestrial co-ordinate system, and that the data are consistent.

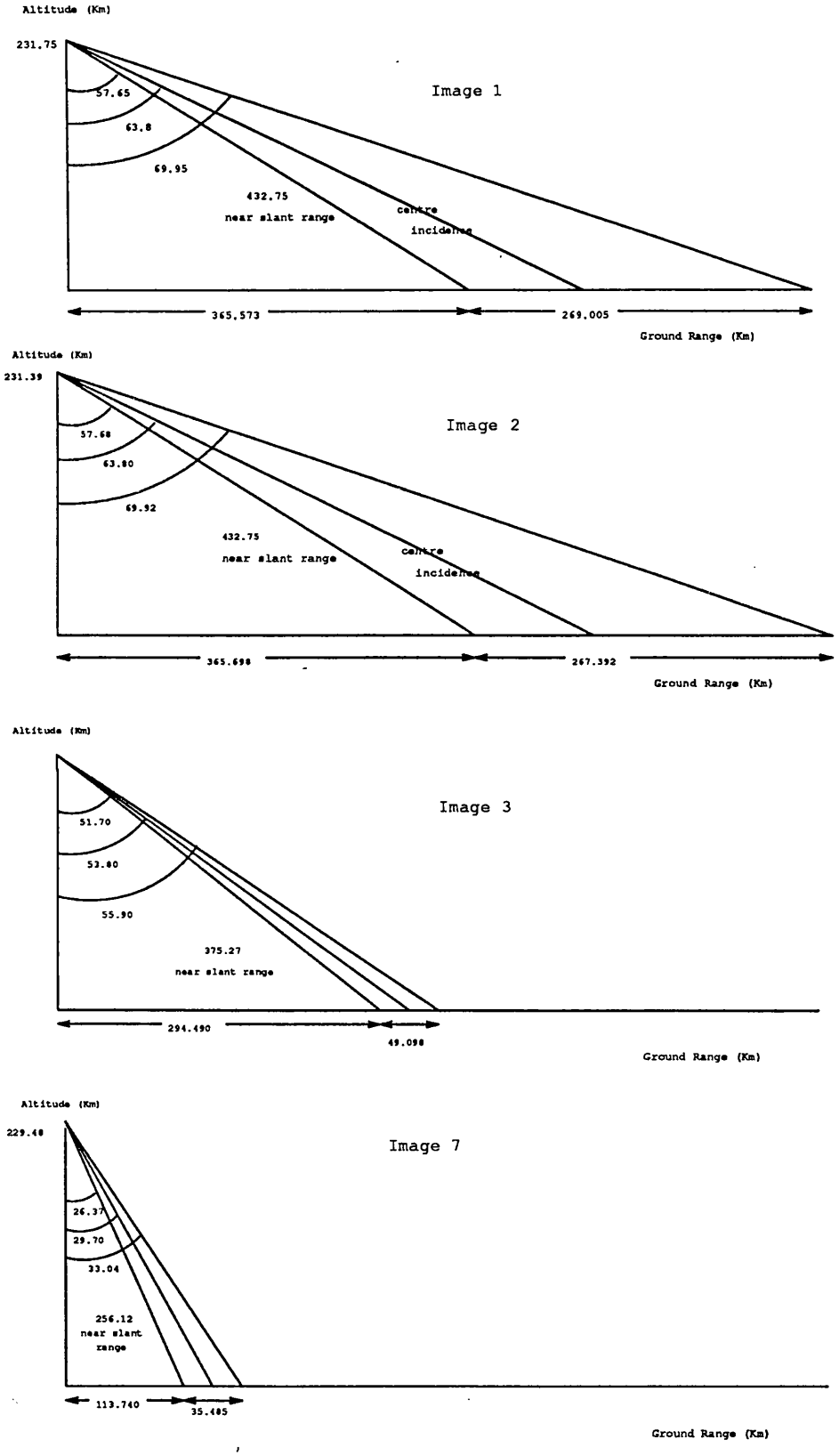

Figure 6.10: Illustrations of the Swath Extents Noted in the Headers of the Four Mount Shasta Images

Using the given *altitude*, *near-slant-range* and *centre incidence angle* values, an attempt was made to roughly assess the range extent of the images. For this assessment only, the Earth was approximated as being flat.

The result of this assessment is shown in Figure 6.10. From the map study, the range extents were measured to be approximately 17, 17, 12 and 23 Km respectively for Images 1, 2, 3 and 7. The range extents of Figure 6.10 are obviously nonsense, being considerably bigger than the map-derived measurements, indicating that one or more of the values given are incorrect.

From the map, the position of the peak of Mt. Shasta was found. Then, using the given position of the satellite and the position of the peak, the slant range between the two was calculated. These values were then compared with the given *near-slant-ranges.* The results are:

Image	Given Near Slant Range (Km)	Slant Range to Peak (Km)
1	432.75	445.799
2	432.75	438.532
3	375.27	380.888
7	256.12	258.481

It can be seen that these are fairly reasonable.

The *track (to the north)* is given in the header data as 119.0°, 120.4° and 121.6° respectively for Images 1, 3 and 7. From the assessed positions of these images on the map, the track appears to lie between 130°–140°. However, assuming that the sensor velocity is correct, the track angle, θ_t, can be calculated from the given velocity vector using

$$\theta_t = 90 + \frac{\dot{Z}}{\sqrt{\dot{X}^2 + \dot{Y}^2}}.$$

Hence,

Track Angle θ_t (degrees)		
Image	Calculated	Given in Header Data
1	119.024	119.000
2	119.602	119.500
3	120.522	120.400
7	121.558	121.600

This indicates that the given velocity vector is probably correct. It also shows that the visual inspection of the track was inaccurate, demonstrating the difficulty of fixing the images relative to maps.

Other data are either undefined or cannot be checked with available information. Most of these remaining data are fairly consistent between the images, apart from the given *roll*, which is 210° in Images 1, 2 and 7 but only 90° in Image 3, and the *scale factor*, which is given as less than 10 dB in Images 1, 2 and 7 but 2601.85 dB in Image 3.

6.3 Detailed Analysis

The preliminary study had shown that most of the image header data could not be trusted. It did indicate that the sensor position and velocity were probably correct, along with the near-slant-range, track, and altitude. However, the time for which the position and velocity vectors are quoted was unknown. A *start time* and a *centre image time* was given in the header but, of course, these cannot be substantiated. It was therefore decided that some points in the images that could be identified on the maps should be found. As previously stated, identifying such points was quite difficult, due to the poor quality and bland nature of the images. Only the areas of images 1, 3 and 7 shown in Figures 6.2 to 6.4, i.e. the overlap regions, were employed in this detailed analysis. However, twelve ground control points (GCPs), were located in Image 1 and 7, the positions of which are shown in Figure 6.2. Unfortunately, as Image 3 has a narrower ground swath, only nine of these GCPs were covered by it (GCPs 7, 10 and 11 are not covered). The GCPs were chosen, as far as possible, to cover the extent of the image portions under study and give a spread of terrain height. The lava 'arm' on which GCPs 1 to 5 are located is very distinctive but it was felt that 5 GCPs here was sufficient. The bends in gullies identified by GCPs 6 and 8

GCP	Geodetic Co-ordinates			Geocentric Co-ordinates (m)		
No	lat (d.ms)	long (d.ms)	height (m)	X	Y	Z
1	41.3058784	122.1708955	1170.432	−2555136.02	−4044040.94	4206419.22
2	41.3110946	122.1816119	1072.896	−2556280.74	−4042936.74	4206635.56
3	41.3035473	122.1844328	1121.664	−2557240.96	−4043231.12	4205848.28
4	41.2816649	122.1724179	1511.808	−2557341.87	−4046870.65	4202897.92
5	41.2805473	122.1533582	1731.264	−2555381.28	−4048573.48	4202784.82
6	41.2232027	122.0823731	1950.720	−2550647.88	−4059793.99	4195213.90
7	41.2838919	122.0814328	1877.568	−2546448.50	−4053520.15	4203655.07
8	41.2419459	122.0811642	2316.480	−2549389.81	−4058319.56	4197943.07
9	41.2140449	122.1042089	2535.936	−2554164.68	−4059344.29	4194406.08
10	41.2756629	122.1039403	2316.480	−2549934.31	−4052738.04	4202967.83
11	41.2903370	122.1259104	1950.720	−2551805.25	−4049624.09	4204268.83
12	41.2358200	122.1137200	4316.578	−2554463.47	−4057413.72	4198773.62
$a = 6378137.0$ m, $e = 0.08161$						

Table 6.1: Ground Control Points

were also fairly easy to establish. Elsewhere the task was difficult and GCPs could only be reliably identified in small areas where there was a change in height, giving a bright but foreshortened region.

The co-ordinates of these GCPs are given in Table 6.1 in both geodetic and geocentric systems. The image positions of the GCPs in terms of sample (azimuth position) and line (slant range position) numbers are given in Table 6.2.

For a slant-range image, a plot of slant-range against image line number should give a straight line because the pixel spacing in slant-range will be constant. The intercept on the slant-range axis gives a value of the near-slant-range and the gradient of the line gives a value for the slant-range pixel spacing.

As a first approximation, it was assumed that the given sensor position was constant across the whole image. The slant-range and look-angle (incidence angle) were then calculated for each GCP. These slant-ranges were plotted against line number and a straight line was obtained. This is consistent with a slant-range image. A least-squares line fit was then applied. In all cases, the resulting near-slant-range was not very close to the near-slant-range given in the header. Furthermore, the look-angles calculated for each GCP were quite different from the given centre incidence angle — especially for Image 1. These slant-range and look-angle results are shown in the second column of Tables 6.4 to 6.9, where they are labelled *constant*. The gradient and intercept of the plotted data are shown in the lines labelled *constant* in Tables 6.11, 6.12, and 6.13.

GCP No	Image 1		Image 3		Image 7	
	Sample	Line	Sample	Line	Sample	Line
1	4723	766	2697	38	743	629
2	4597	818	2577	103	624	703
3	4607	906	2597	193	649	790
4	4950	1028	2977	273	992	829
5	5101	927	3097	193	1132	720
6	6217	1042	4269	278	2255	741
7	5696	339			1685	69
8	6056	808	4089	38	2080	475
9	6098	1263	4153	493	2157	930
10	5510	566			1534	276
11	5230	640			1233	398
12	5741	923	3777	138	1793	440

Table 6.2: Image Position of Ground Control Points

In an attempt to improve these results, it was assumed that the sensor position was given firstly for the start of the image and, secondly, at the centre of the image (the end of the image was thought to be unlikely). It was further assumed that the sensor was travelling at a constant velocity. Using the values given in the header data, the time of imaging one sample (azimuth) pixel was calculated from the start time and image centre time. Values of 2.389×10^{-3}, 2.154×10^{-3} and 2.179×10^{-3} seconds were obtained for Images 1, 3 and 7 respectively. (Assuming a pixel spacing of 12.5 m, a velocity of $\approx$ 6.0 Km/second is obtained, which is reasonable). The position of each GCP in terms of *time* was calculated with respect to the assumed *start-time*, i.e. start or centre of the image (Table 6.3).

Again, the slant-ranges and look-angles were calculated for each GCP. Plots of the slant-range against line position were made and found to be linear. The near-range and range pixel spacing were assessed. The results for this part of the study are shown in Tables 6.4 to 6.13 in the columns or lines entitled *start* and *centre*. Here, the *centre* values are nearest to the given header near-ranges.

As a final and more accurate attempt at assessment, it was decided that, using the given sensor position and velocity, the orbit of the sensor platform should be established and the sensor position at each GCP calculated. Again, the calculations would be made assuming that the initial sensor position was defined at both the start and centre of the images. The procedure for the assessment of the sensor platform orbit and the subsequent calculation of sensor positions associated with each GCP is described in Chapter 5. Again, the slant-

Timings (seconds)						
GCP No	Image 1		Image 3		Image 7	
	Start	Centre	Start	Centre	Start	Centre
1	11.28179	3.21320	5.80921	−1.92783	1.61866	−5.77653
2	10.98081	2.91219	5.55074	−2.18631	1.35942	−6.03583
3	11.00470	2.93608	5.59382	−2.14323	1.41388	−5.98136
4	11.82402	3.75551	6.41232	−1.32471	2.16112	−5.23396
5	12.18472	4.11625	6.67079	−1.06623	2.46612	−4.92890
6	14.85050	6.78237	9.19523	1.45826	4.91263	−2.48188
7	13.60599	5.53770			3.67086	−3.72391
8	14.46592	6.39774	8.80751	1.07054	4.53138	−2.86321
9	14.56624	6.49808	8.94537	1.20839	4.69913	−2.69542
10	13.16169	5.09335			3.34190	−4.05294
11	12.49286	4.42443			2.68615	−4.70882
12	13.71348	5.64521	8.13548	0.39849	3.90614	−3.48858

Table 6.3: Times of Imaging Ground Control Points

ranges and look-angles were calculated for each GCP. Plots of the slant-range against line position were made and found to be linear. The near-range and range pixel spacing were assessed. These results are shown in Tables 6.4 to 6.13 in columns or lines labelled *orbit start* and *orbit centre*. The orbital parameters are given in Table 6.10 for each image.

From Tables 6.11 to 6.13 it can be seen that the *start* and *centre* results are very similar to the *orbit start* and *orbit centre* results. The results which are closest to the given near-slant-ranges are given for the *centre* or *orbit centre* calculations. In Images 1 and 7, the closest result is for the *centre* results, which differ by 0.865 Km and 0.283 Km respectively from the given values. However, the smallest goodness-of-fit error in the calculated values are for the *orbit centre* calculations. In Image 3, the best single result, which is 3.751 Km from the given value, is found from the *orbit centre* calculations, but here the smallest goodness-of-fit error is for the *centre* calculations.

GCP 9 is fairly central in the images and the calculated look-angles from the *orbit centre* configuration are $\approx$ 57.6°, 52.0° and 29.3° for Images 1, 3 and 7 respectively. These can be compared with the values of 63.8°, 53.8° and 29.7° given in the header data. In [Leberl *et al.*, 1986b], these angles were said to be 57°, 51° and 28° for the whole images respectively, supporting the work described in this section. However, Tables 6.11 to 6.13 show that there can be large goodness-of-fit errors in the gradients, indicating uncertainty in the slant-range pixel spacing.

All these calculations had been carried out primarily to establish for which image posi-

Image 1: Calculated Slant Range (Km) from GCPs					
GCP No	Constant	Start	Centre	Orbit Start	Orbit Centre
1	441.681	442.561	440.273	442.217	440.244
2	442.238	443.148	440.978	442.822	440.954
3	443.319	444.205	442.046	443.879	442.021
4	445.267	445.991	443.573	445.616	443.534
5	444.147	444.727	442.229	444.328	442.182
6	446.801	446.438	443.164	445.850	443.039
7	438.431	438.687	435.650	438.186	435.565
8	444.044	443.812	440.648	443.252	440.536
9	449.192	448.919	445.763	448.356	445.649
10	440.759	441.012	438.218	440.545	438.147
11	441.007	441.521	438.900	441.100	438.845
12	445.799	445.662	442.850	445.163	442.763

Table 6.4: Image 1: Calculated Slant Range (Km) from GCPs

Image 1: Calculated Look-Angle (degrees) from GCPs					
GCP No	Constant	Start	Centre	Orbit Start	Orbit Centre
1	57.074	57.057	56.963	57.113	56.967
2	57.100	57.090	57.001	57.142	57.005
3	57.187	57.174	57.088	57.227	57.092
4	57.388	57.352	57.256	57.413	57.262
5	57.340	57.287	57.189	57.352	57.196
6	57.567	57.403	57.276	57.499	57.297
7	56.941	56.840	56.711	56.922	56.725
8	57.422	57.273	57.148	57.364	57.166
9	57.823	57.671	57.553	57.763	57.572
10	57.180	57.087	56.975	57.163	56.986
11	57.142	57.080	56.973	57.149	56.982
12	57.842	57.714	57.612	57.797	57.626

Table 6.5: Image 1: Calculated Look-Angle (degrees) from GCPs

Image 3: Calculated Slant Range (Km) from GCPs					
GCP No	Constant	Start	Centre	Orbit Start	Orbit Centre
1	381.262	390.717	379.184	390.615	379.174
2	382.161	391.226	379.789	391.133	379.776
3	383.082	392.187	380.767	392.093	380.754
4	383.705	393.966	382.309	393.844	382.304
5	382.082	392.645	380.978	392.513	380.975
6	380.816	394.507	382.188	394.259	382.180
8	378.715	392.002	379.740	391.773	379.736
9	383.309	396.617	384.448	396.384	384.443
12	380.888	393.204	381.272	393.010	381.271

Table 6.6: Image 3: Calculated Slant Range (Km) from GCPs

Image 3: Calculated Look-Angle (degrees) from GCPs					
GCP No	Constant	Start	Centre	Orbit Start	Orbit Centre
1	51.426	52.393	51.196	52.409	51.197
2	51.505	52.430	51.243	52.444	51.245
3	51.614	52.536	51.360	52.550	51.362
4	51.755	52.778	51.604	52.797	51.605
5	51.621	52.683	51.501	52.703	51.502
6	51.531	52.882	51.677	52.921	51.678
8	51.368	52.700	51.479	52.736	51.480
9	51.908	53.196	52.027	53.233	52.027
12	51.975	53.182	52.016	53.213	52.016

Table 6.7: Image 3: Calculated Look-Angle (degrees) from GCPs

Image 7: Calculated Slant Range (Km) from GCPs					
GCP No	Constant	Start	Centre	Orbit Start	Orbit Centre
1	260.318	261.769	259.758	261.758	259.628
2	260.935	262.168	260.281	262.160	260.139
3	261.463	262.738	260.830	262.730	260.691
4	261.585	263.439	261.258	263.419	261.152
5	260.468	262.525	260.292	262.500	260.198
6	259.766	263.138	260.046	263.041	260.022
7	256.166	259.050	256.259	258.994	256.205
8	258.247	261.465	258.516	261.382	258.484
9	260.968	264.235	261.239	264.146	261.212
10	257.408	260.049	257.476	260.003	257.412
11	258.351	260.569	258.252	260.539	258.165
12	258.481	261.326	258.744	261.265	258.697

Table 6.8: Image 7: Calculated Slant Range (Km) from GCPs

Image 7: Calculated Look-Angle (degrees) from GCPs					
GCP No	Constant	Start	Centre	Orbit Start	Orbit Centre
1	28.317	28.867	28.044	28.868	28.057
2	28.513	28.976	28.200	28.977	28.215
3	28.738	29.212	28.439	29.213	28.453
4	28.962	29.637	28.796	29.639	28.808
5	28.633	29.393	28.529	29.395	28.539
6	28.474	29.689	28.576	29.697	28.578
7	26.969	28.111	26.988	28.115	26.993
8	28.037	29.230	28.134	29.237	28.137
9	29.193	30.334	29.287	30.342	29.290
10	27.690	28.704	27.693	28.708	27.700
11	27.898	28.747	27.825	28.750	27.833
12	29.026	30.047	29.110	30.053	29.115

Table 6.9: Image 7: Calculated Look-Angle (degrees) from GCPs

Orbital Parameters			
Parameter	Image 1	Image 3	Image 7
a (Mega m)	6.59646984	6.59772422	6.59579339
Ω (rad)	1.20573738	1.12271893	0.95677888
i (rad)	0.99468213	0.99472364	0.99473254
e	0.00042812	0.00051673	0.00065257
E (rad)	3.07382782	2.66596664	2.10212464
ω (rad)	−0.90943201	−0.47105555	0.11644464

Table 6.10: Orbital Parameters for Images 1, 3 and 7

Image 1		
Calculation	Gradient (m)	Intercept (Km)
Header Given		432.750
Constant	11.724 ± 1.163	433.760 ± 1.009
Start	11.367 ± 0.943	434.227 ± 0.818
Centre	11.387 ± 0.341	431.885 ± 0.295
Orbit Start	11.177 ± 0.341	434.105 ± 0.295
Orbit Centre	11.111 ± 0.278	431.840 ± 0.241

Table 6.11: Image 1: Near Slant Range and Range Pixel Spacing

Image 3		
Calculation	Gradient (m)	Intercept (Km)
Header Given		375.270
Constant	6.763 ± 3.211	380.467 ± 0.758
Start	11.963 ± 1.553	390.686 ± 0.367
Centre	11.113 ± 0.937	379.029 ± 0.221
Orbit Start	11.786 ± 1.518	390.559 ± 0.358
Orbit Centre	11.118 ± 1.047	379.021 ± 0.247

Table 6.12: Image 3: Near Slant Range and Range Pixel Spacing

Image 7		
Calculation	Gradient (m)	Intercept (Km)
Header Given		256.120
Constant	8.803 ± 3.258	255.216 ± 0.206
Start	5.753 ± 0.325	258.516 ± 0.206
Centre	6.129 ± 0.248	255.837 ± 0.157
Orbit Start	5.766 ± 0.311	258.464 ± 0.197
Orbit Centre	6.087 ± 0.162	255.783 ± 0.103

Table 6.13: Image 7: Near Slant Range and Range Pixel Spacing

tion the sensor position and velocity had been quoted. In this respect, the work was rather inconclusive. If the given near-slant-range was to be taken as correct, then, for Images 1 and 7, the sensor position was given near to, but not at, the centre of the images. For Image 3, the best results were obtained for an assumed centre position — but here the results were a long way from the given value. All the plots of slant-range against line number were found to be linear, indicating that the images are slant-range in nature.

From these results, it was decided that, in further work, the slant-ranges would be calculated using the *orbit centre* assumption, i.e. the given sensor position would be assumed to be associated with the centre of the image and the sensor position for any other time would be calculated from the orbit of the sensor platform; also, the near-slant-range would be taken to be that calculated on this basis. Therefore, the near-slant-ranges would be taken to be 431.840, 379.021 and 255.783 Km respectively for Images 1, 3 and 7 (as shown in the last line of Tables 6.11, 6.12 and 6.13).

For further investigation, the slant-range pixel spacings were calculated for each GCP in each image. These results are shown in Table 6.14. As can be seen from these range pixel spacing results, the mean value is, as expected, very similar to the gradient values given in Tables 6.11 to 6.13 for the appropriate *orbit centre*. However, the variation of values of 10.8–11.8, 4.0–18.8 and 5.7–6.6 Km for Images 1, 3 and 7 respectively is large. Image 3 results are especially widespread. These findings are, of course, indicated by the standard deviation (SD) of the results. Appropriate centre ground range pixel spacings were calculated from the mean slant-range values using the appropriate centre incidence angles calculated previously.

In an attempt to ascertain the azimuth pixel spacing, pairs of GCP points were considered. Where possible, pairs of similar height and line number were chosen in order to minimise terrain effects. Unfortunately, only two such pairs could be used for Image 3. The separation of the GCP pairs was measured from the map and the line and sample number differences were calculated. A look-angle was needed for each pair so that the ground-range distance between the GCP pairs could be calculated. An average of the appropriate two values was used. The range pixel spacing was taken to be the mean values shown in Table 6.14 for each image. The assessed azimuth pixel spacings for each GCP pair are shown in Tables 6.15, 6.16 and 6.17, along with an average value.

For Images 1 and 7, the spread of results was large. The two results for Image 3 cannot

Slant Range Pixel Spacing (m)			
GCP No	Image 1	Image 3	Image 7
1	10.971	4.026	6.113
2	11.142	7.330	6.196
3	11.237	8.979	6.213
4	11.375	12.026	6.476
5	11.156	10.124	6.132
6	10.748	11.363	5.721
7	10.988		6.116
8	10.762	18.816	5.686
9	10.933	10.998	5.838
10	11.143		5.902
11	10.945		5.985
12	11.834	16.304	6.623
Mean	11.103	11.107	6.083
SD	0.295	4.434	0.281
Approximate Centre Ground Range (m)			
	13.221	14.095	12.430

Table 6.14: Slant Range Pixel Spacing

Image 1: Azimuth Pixel Spacing (m)						
GCPs	GCP Separation (m)	Samples	Lines	Range Res. (m)	Angle (deg)	Azimuth Res. (m)
5-3	6433	494	21	11.103	57.144	13.010
6-4	16458	1267	14	11.103	57.280	12.989
8-9	6030	42	455	11.103	57.369	14.611
6-7	11325	521	703	11.103	57.011	12.388
6-11	13666	987	402	11.103	57.140	12.757
7-11	6652	466	301	11.103	56.853	11.419
8-10	7529	546	242	11.103	57.076	12.481
1-3	2326	116	140	11.103	57.030	12.120
Ignore 8-9 Result						
					Mean	12.407
					SD	0.585

Table 6.15: Image 1: Azimuth Pixel Spacing

Image 3: Azimuth Pixel Spacing (m)						
GCPs	GCP Separation (m)	Samples	Lines	Range Res. (m)	Angle (deg)	Azimuth Res. (m)
5-3	6433	500	0			12.866
6-4	16458	1292	5	11.107	51.520	12.738
					Mean	12.802
					SD	0.091

Table 6.16: Image 3: Azimuth Pixel Spacing

Image 7: Azimuth Pixel Spacing (m)						
GCPs	GCP Separation (m)	Samples	Lines	Range Res. (m)	Angle (deg)	Azimuth Res. (m)
5-3	6433	483	70	6.083	28.496	13.190
6-4	16458	1263	88	6.083	28.643	13.001
8-9	6030	77	455	6.083	28.714	23.132
6-7	11325	570	672	6.083	27.786	12.573
6-11	13666	1022	343	6.083	28.206	12.655
7-11	6652	452	329	6.083	27.413	11.140
8-10	7529	546	199	6.083	27.919	12.951
1-3	2326	94	161	6.083	28.255	11.310
Ignore 8-9 Result						
					Mean	12.403
					SD	0.833

Table 6.17: Image 7: Azimuth Pixel Spacing

be deemed to be statistically significant. For Images 1 and 7, the range and azimuth pixel spacing calculations show that either there is some distortion in the images of an unknown type or the GCPs have been inaccurately identified on the map and/or image. As the results do not seem to be systematic in any way, there are probably both types of error present. Nevertheless, it was felt that further work could proceed with these images.

For Image 3, the large spread of range pixel spacing results indicates that there must be some considerable image distortion, the cause of which would be impossible to ascertain from the information available. It was therefore decided that no further work would be carried out using this image.

For work on geocoding or stereo to proceed, some Doppler frequency data were required. Some values relating to the Doppler are included in the header files, but no information regarding their meaning was available to the author. It was therefore decided that the Doppler frequency at each GCP in Images 1 and 7 should be calculated using the Doppler equation

$$f_{dc} = \frac{2(\dot{\underline{s}} - \dot{\underline{p}}).(\underline{s} - \underline{p})}{\lambda|\underline{s} - \underline{p}|}$$

which is defined in Chapter 3. $\dot{\underline{s}}$ and $\underline{s}$ were calculated previously for each GCP using orbital parameters. $\dot{\underline{p}}$ and $\underline{p}$ are the known position and velocity of the GCPs (in the correct geocentric inertial reference system). The wavelength, λ, was given in the header.

The results of this assessment are shown in Table 6.18 and plots of the calculated f_{dc}

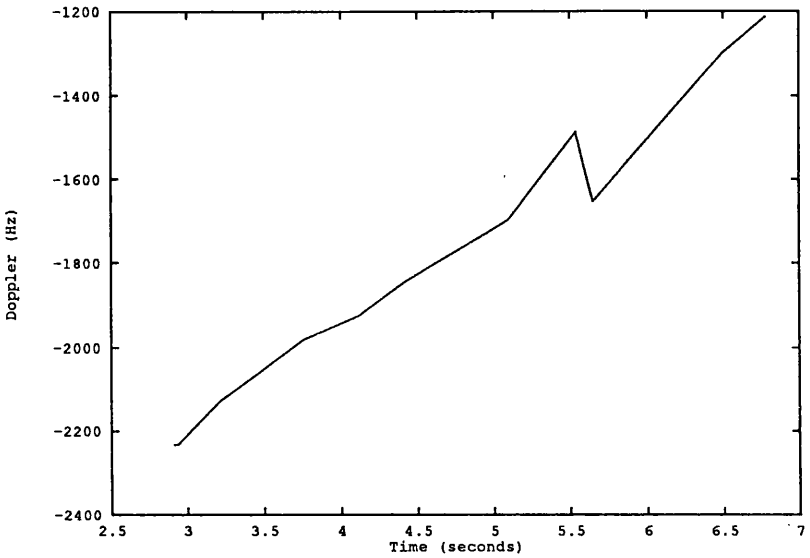

Figure 6.11: Variation of Doppler with Azimuth for Image 1

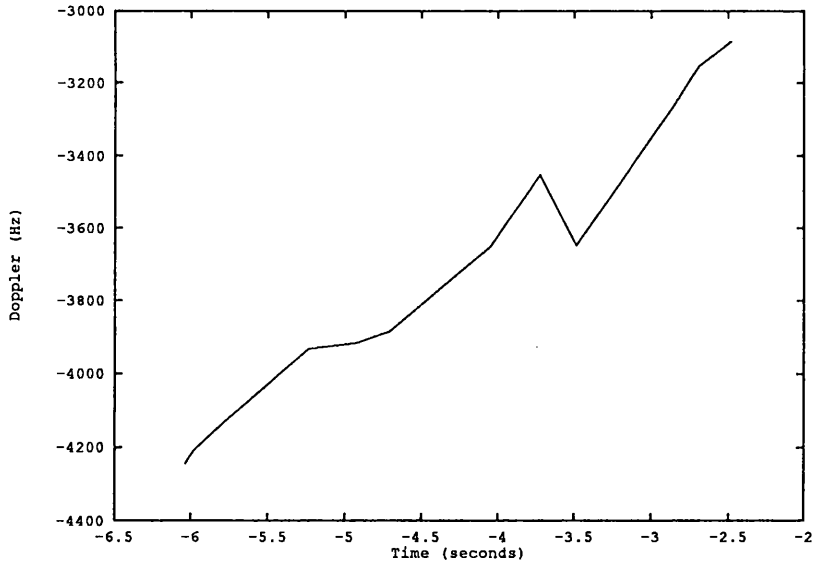

Figure 6.12: Variation of Doppler with Azimuth for Image 7

	Image 1			Image 7		
GCP No	Sample	Line	Doppler Frequency	Sample	Line	Doppler Frequency
1	4723	766	−2128.372	743	629	−4129.959
2	4597	818	−2232.417	624	703	−4243.449
3	4607	906	−2233.510	649	790	−4208.246
4	4950	1028	−1981.169	992	829	−3931.353
5	5101	927	−1925.619	1132	720	−3916.197
6	6217	1042	−1212.372	2255	741	−3085.751
7	5696	339	−1487.191	1685	69	−3451.741
8	6056	808	−1337.627	2080	475	−3267.168
9	6098	1263	−1298.693	2157	930	−3154.719
10	5510	566	−1697.672	1534	276	−3651.105
11	5230	640	−1843.056	1233	398	−3884.600
12	5741	923	−1652.919	1793	440	−3647.605

Table 6.18: Doppler Frequencies (Hz)

against sample number (azimuth position, which is related to time) are shown in Figures 6.11 and 6.12 for Images 1 and 7 respectively. These plots show a Doppler variation of $\approx$ 300 Hz/second; this is very large and would not normally be expected. This may indicate that some timing error is associated with the data (e.g., an effect of PRF errors—see Section 3.5), or perhaps that the zero squint assumption is incorrect. The difference between the Doppler frequencies of the two images is also very large.

However, whether these values are correct or not is largely irrelevant to this work, as only these values will be consistent with the values of sensor and GCP position calculated previously. If these values are not accepted, *no* work can continue. As stated previously, if a target is processed with an incorrect Doppler centre frequency (and the above calculations were intended to identify the Doppler centre frequency used in the processing) and then geocoded using the same incorrect Doppler centre frequency, the target will be imaged to the correct location.

The plots shown in Figures 6.11 and 6.12 could, with some imagination, be approximated by straight lines. However, after some investigation, it was felt that a cubic spline fit would be more appropriate for these particular sets of data. Indeed, this fit was very good, with errors of less than 0.004 Hz for any given point.

From Table 6.18 it can be seen that GCPs of similar sample number, but different line number, have very similar Doppler frequency values (e.g., GCPs 2 and 3), indicating that the Doppler frequency variation with range is small compared to that of the variation in

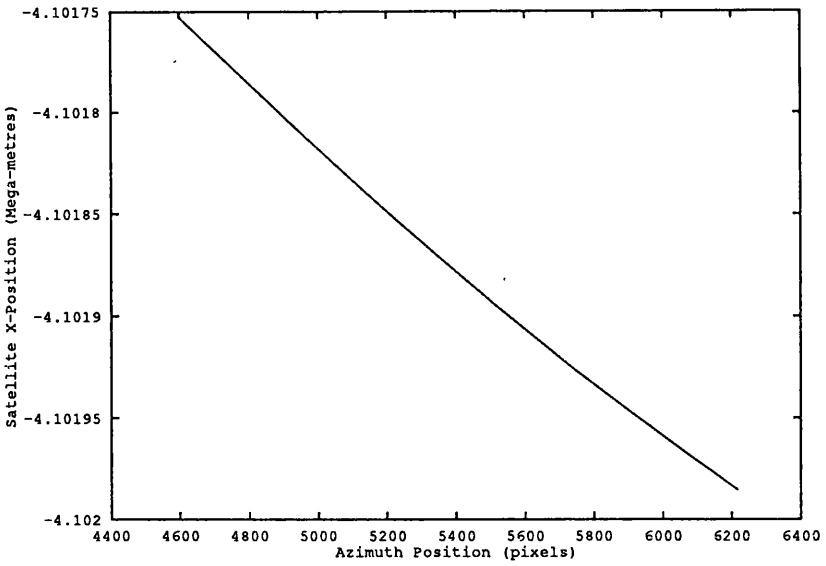

Figure 6.13: Variation of Satellite x-Position with Time for Image 1

azimuth. Hence, it is assumed here that the Doppler frequency does not vary in the range direction. The plots also indicate that this would seem to be a fairly good assumption — but it should be noted that the 'peak' in the data for both images corresponds to the GCP with the lowest line number. Elsewhere, however, there does not appear to be any correlation with line number. As there are insufficient data to investigate this point further, it was assumed that the rate of change of Doppler with respect to line number, $\partial f_{dc}/\partial j$ in Section 3.4.3, should be set to zero. The rate of change of Doppler with respect to sample number, $\partial f_{dc}/\partial i$ in Section 3.4.3, was difficult to assess from these data and would be inaccurate by any method. It was therefore decided that this rate of change would be calculated locally from the slope at the local point and its two nearest neighbours.

For the object-to-image geocoding procedure, the satellite position $\underline{s}$ is defined in terms of a polynomial. Here, as shown in Section 3.4.1, it is defined with respect to azimuth pixels (which are related to time). For image-to-object geocoding, the satellite position and velocity could be calculated from the orbit; however, for an operational system, such calculations for each pixel would be computationally expensive. Hence, in this work, for both types of geocoding, the satellite position, velocity, and acceleration were assessed from a polynomial description, which is discussed in the following paragraph.

Figures 6.13, 6.14 and 6.15 show plots of the X, Y and Z components of the satellite position for each GCP with respect to azimuth pixel for Image 1. Similarly, Figures 6.16,

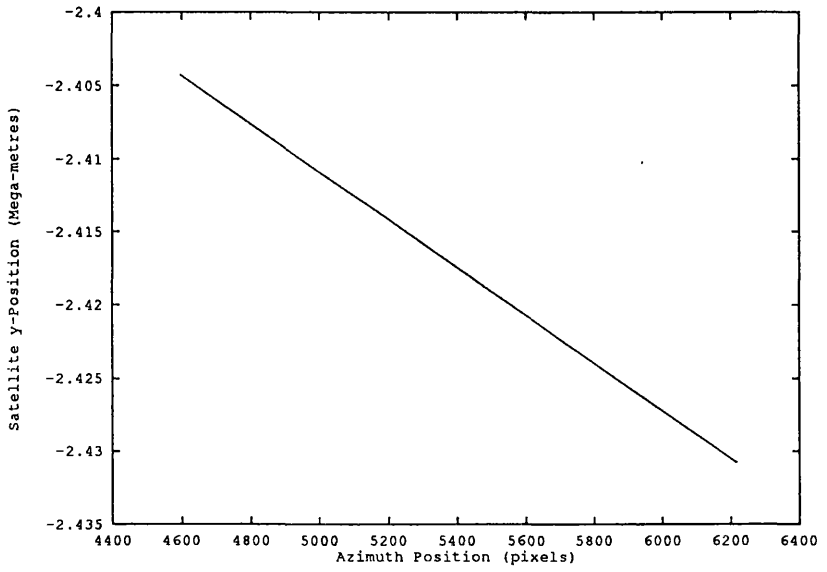

Figure 6.14: Variation of Satellite y-Position with Time for Image 1

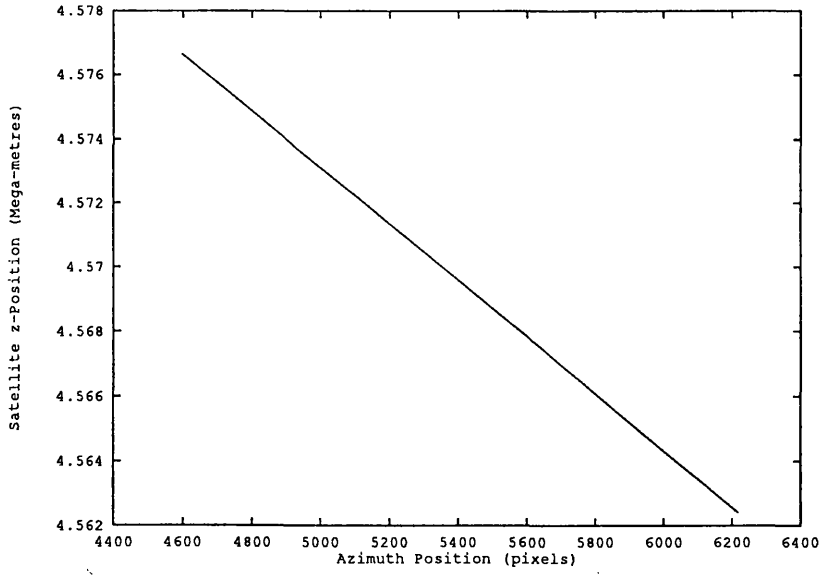

Figure 6.15: Variation of Satellite z-Position with Time for Image 1

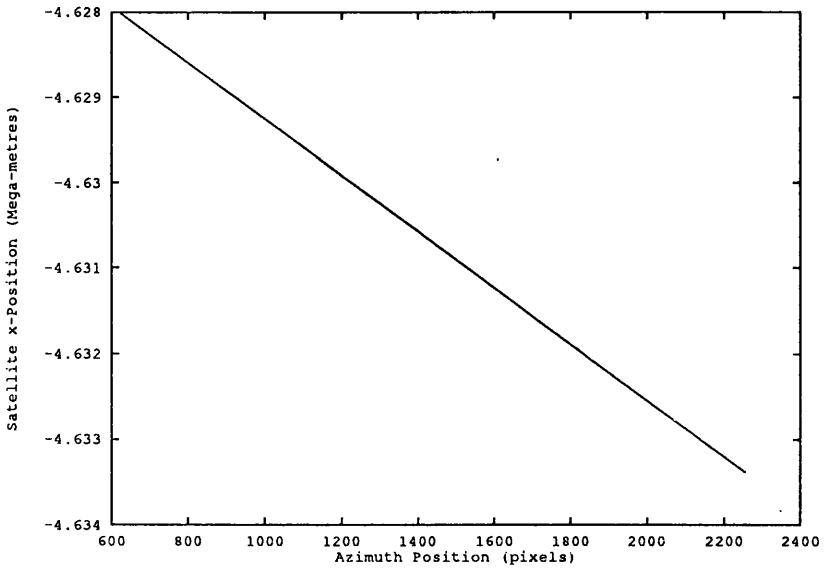

Figure 6.16: Variation of Satellite x-Position with Time for Image 7

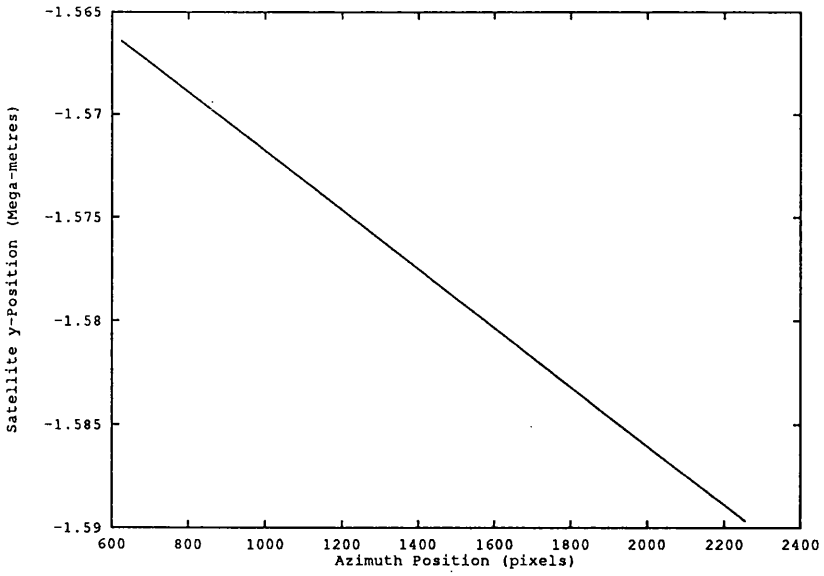

Figure 6.17: Variation of Satellite y-Position with Time for Image 7

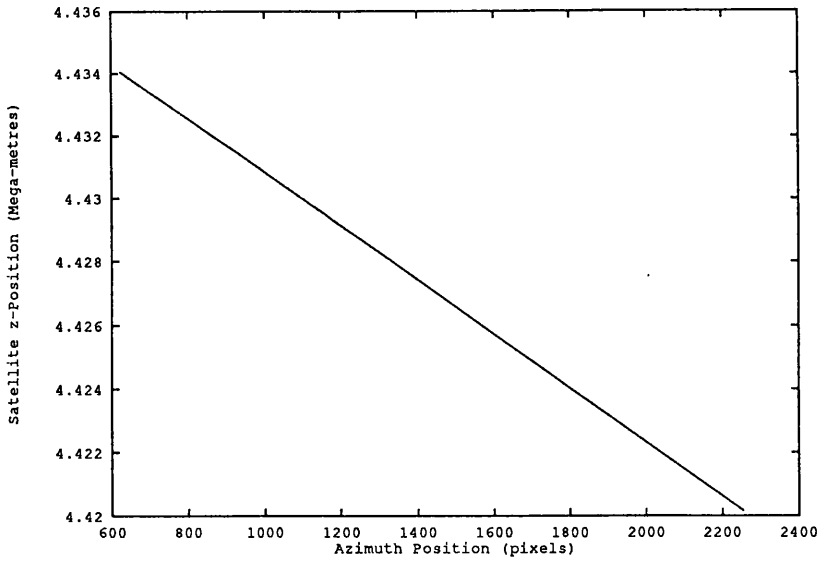

Figure 6.18: Variation of Satellite z-Position with Time for Image 7

Satellite Position: Image 1		
Component	Gradient (Km/s/I)	Intercept (Km/s)
X_s	$-1.543 \times 10^{-4} \pm 8.905 \times 10^{-4}$	-4101.040 ± 4.815
Y_s	$-1.634 \times 10^{-2} \pm 8.905 \times 10^{-4}$	-2329.150 ± 4.815
Z_s	$-8.780 \times 10^{-3} \pm 1.259 \times 10^{-3}$	4617.007 ± 6.810

Table 6.19: Image 1: Satellite Position

6.17 and 6.18 show the same components for Image 7. These data give good linear fits. Tables 6.19 and 6.20 show the gradient and intercept of these lines. The satellite position is, therefore, defined in terms of $a_0 + a_1 i$. Hence, $\partial \underline{s}/\partial i$ (velocity) is a constant and $\partial^2 \underline{s}/\partial i^2$ (acceleration) is *zero*. Other fits were tried but these did not give such a good description. A linear fit was also found by [Chew, 1990] using Seasat satellite data.

All the required inputs for geocoding or SAR stereo work were now established. The work of the next two chapters is to show that geocoding and stereo can be carried out and to investigate how inaccuracies in the individual parameters affect the results of calculations.

Satellite Position: Image 7		
Component	Gradient (Km/s/I)	Intercept (Km/s)
X_s	$-3.289 \times 10^{-3} \pm 8.865 \times 10^{-4}$	-4625.970 ± 1.345
Y_s	$-1.426 \times 10^{-2} \pm 3.134 \times 10^{-4}$	-1557.516 ± 0.475
Z_s	$-8.509 \times 10^{-3} \pm 0.000$	4439.355 ± 0.000

Table 6.20: Image 7: Satellite Position

However, the analysis of the image data in this Chapter has shown that there are many uncertainties — e.g., the Doppler rate was excessive, the azimuth pixel spacing has a large uncertainty, etc.. Nevertheless, for the chosen GCPs, the assessed data (e.g., $\underline{s}$, $\underline{\dot{s}}$, $\underline{p}$, $\underline{\dot{p}}$, R, and f_{dc}) are consistent and should, providing the algorithms are correct, result in the correct location. Although it has been assumed (and the checks carried out support the assumption) that the images are slant-range, from the assessed near-slant range, slant-range pixel spacing, and line number of a given GCP, the correct slant-range will always result, even if this assumption should be incorrect. Hence, a simulated image is effectively being created for each GCP.

It was therefore decided that only the chosen GCP positions should be analysed further. Even if the image data had been "good", whole image geocoding and stereoscopy would be rather pointless, as no valid error analysis could be carried out away from the GCPs and height data were only available at the GCPs.

It could be argued that it is "cheating" to use values calculated from GCPs and sample/line numbers to find the position of the GCPs and sample/line numbers. With these sets of data, one has little choice. As the principal aim of the work was to demonstrate that the geocoding and SAR stereo algorithms are correct, and to investigate how individual parameters affect the overall results, it was felt that using this calculated data in no way invalidates the work.

6.4 Summary

The work described in this chapter has shown that some of the header data supplied with the SIR-B images of Mount Shasta were corrupt. Using GCPs, the data required for the geocoding and stereo analyses to proceed were gradually acquired from careful checking and the establishment of the sensor orbit. The work has shown that Image 3 has considerable distortion and was therefore discarded from further study. Images 1 and 7 also appear to be distorted, though to a much smaller extent.

This work has shown that geocoding and stereo can proceed using these data but, for the reasons described previously, it was decided that only point, and not whole image, analysis would be of value.

Chapter 7

Geocoding Using SIR-B Mount Shasta Imagery

7.1 Introduction

The algorithms of Chapter 3 were coded, along with the required calculation of sensor platform position and velocity, co-ordinate conversion, Doppler estimation, etc.. The resulting program `GEOCODE` performs either object-to-image or image-to-object geocoding.

To test the geocoding techniques described in the previous chapter, two types of input parameter sets have been used: the first of these was as accurate as could be achieved for each point (*exact* data), while the second used *average* values. The first set is intended to provide indications as to the ultimate accuracy of the techniques, while the second gives insight into the operational performance; however, it is expected that operational parameter sets will be somewhat *more* accurate than the average values used here.

In the tables of results in the following sections, ΔX, ΔY and ΔZ are the differences between the calculated GCP positions found from image-to-object geocoding and the positions given in Table 6.1. Similarly, ΔI and ΔJ are the differences between the calculated sample and line positions found from object-to-image geocoding and those given in Table 6.2. In both cases, the root-mean-square (RMS) value (i.e., the square root of the sum of the squares of the component differences) is also provided.

For both types of geocoding, an initial tie-point to be used as a start-point for the iteration procedure was required. GCP 2 was used, as the author had found that this point

the easiest to identify on the images and map.[1] Other start-points were also investigated.

A practical error analysis into the sensitivity of both image-to-object and object-to-image geocoding does not appear to have been reported in the literature.

7.2 Image-to-Object Geocoding

Here, the algorithms of Section 3.4.1 were employed. This method requires an Earth model to be defined. In order to see how well this type of geocoding can be performed, the individually-calculated range pixel spacings for each GCP were employed. Also, to eliminate mis-location due to height, the local ellipsoid Earth model was taken to be an individually-calculated sphere that takes into account the height of each GCP. Using this input, which will be referred to as *exact data*, the results of this type of geocoding are shown in Tables 7.1 and 7.2 for Images 1 and 7 respectively.

7.2.1 Image-to-Object Geocoding: Exact Data Analysis

On the whole, it was found that if a point has a relatively small error in one component then it will have relatively small errors in the other components, and hence have a relatively small RMS error. The only 'non-exact' input data used in this part of the study were the satellite position and velocity, which are calculated from the linear fit described in the previous Chapter, and the Doppler data described by a cubic spline fit. However, for this type of geocoding the Doppler error was less than 0.004 Hz which will be seen from later work on introduced Doppler error to be negligible.

Tables 7.3 and 7.4 show the differences between the 'correct' satellite positions and velocities, calculated from orbital parameters, and the assessed values for each GCP and Image. A comparison of these results and the results obtained from this type of geocoding show that there is a direct correlation between the sizes of these RMS errors for both images. The correlation between the error in the satellite position and the geocoding RMS error is almost exact for Image 1; for Image 7 the correlation is fairly weak. The correlation between the error in the satellite velocity and the geocoding RMS error results is almost exact for Image 7; for Image 1 this correlation is weak. Hence, the satellite position appears to be the main source of error in the geocoding results for Image 1 but not for Image 7.

[1]The author recognises that this could be a delusion on her part.

Geocoding: Image-to-Object (m)				
Exact Input: Image 1				
GCP No	Δ X	Δ Y	Δ Z	RMS Error
1	−245.835	443.774	277.457	578.232
2	−281.623	511.208	320.178	665.702
3	−278.619	506.341	317.358	659.337
4	−183.145	323.303	200.339	422.141
5	−140.510	242.849	149.109	317.730
6	159.666	−342.461	−230.234	442.471
7	19.967	−73.659	−56.541	94.980
8	119.853	−258.538	−173.915	333.846
9	128.127	−279.479	−188.801	360.792
10	−27.315	24.638	8.665	37.792
11	−104.407	173.607	104.742	228.059
12	28.355	−97.580	−74.062	125.742

Table 7.1: Image 1 Image-to-Object Geocoding: Exact Input

Indeed, the positional errors for Image 1 are much larger than those of Image 7. The main source of error in the results of Image 7 appears to be the satellite velocity error. The magnitude of the velocity errors of each image are, however, comparable. These satellite error effects do not appear to be predictable; for example, consider point 10: in Image 1 there is a positional error of 13.787 m and a velocity error of 6.171 m/s; in Image 7 these errors are 6.352 m and 2.628 m/s respectively. It might be expected that Image 7 would give better geocoding results; however, this is not the case. The RMS geocoding error in Image 1 is 37.793 m and in Image 7 it is 89.983 m. Similar effects can be seen for points 6, 7, 8, 9 and 12.

As stated previously, the results shown in Tables 7.1 and 7.2 employed a start-point of GCP 2. Tables 7.5 and 7.6 show the errors produced from this type of geocoding using the same *exact* input but using start-points of GCPs 1, 9 and 12, which have varying height and image position. From these tables, it can be seen that the pattern of results is the same; i.e., for Image 1, GCP 10 gives the best results throughout and GCP 2 the worst, etc.. The variation of results between these start-points is fairly small. For Image 1, the largest RMS difference between the results for the individual GCPs obtained for different start-points is 13.2 m. For Image 7, there is more variation between the results for the individual GCPs obtained for different start-points; the largest RMS difference here is 62.4 m but the differences generally are small.

For Image 1, the worst start-point is GCP 9 for all but two cases (points 10 and 12,

Geocoding: Image-to-Object (m)				
Exact Input: Image 7				
GCP No	Δ X	Δ Y	Δ Z	RMS Error
1	−186.497	300.909	176.049	395.374
2	−215.063	356.546	211.983	467.241
3	−210.352	344.540	203.358	452.007
4	−130.357	182.794	97.141	244.628
5	−92.108	118.709	58.723	161.320
6	240.665	−396.937	−258.177	515.851
7	56.368	−136.197	−96.604	176.237
8	162.228	−316.483	−206.288	411.138
9	156.249	−352.925	−244.321	456.796
10	6.710	−66.974	−59.719	89.983
11	−65.152	72.197	30.379	101.883
12	−72.958	−195.715	−227.131	308.570

Table 7.2: Image 7 Image-to-Object Geocoding: Exact Input

Error in Satellite Position (m)				
GCP No	ΔX	ΔY	ΔZ	RMS
Image 1				
1	4.606	−19.999	−2.224	20.643
2	2.874	−22.329	−5.557	23.189
3	3.030	−22.131	−5.273	22.951
4	6.429	−16.467	2.278	17.823
5	6.714	−14.687	4.253	16.700
6	−14.133	−15.141	6.680	21.763
7	0.632	−11.977	4.038	12.655
8	8.629	−13.612	−5.318	16.971
9	−9.984	−13.951	−3.372	17.483
10	3.768	−12.081	5.472	13.787
11	6.372	−13.525	5.294	15.860
12	−0.295	−12.012	3.481	12.510
Image 7				
1	−3.643	−1.207	−0.742	3.909
2	−6.547	−2.138	−3.053	8.129
3	−5.908	1.961	−2.515	6.714
4	1.035	0.276	2.752	2.953
5	2.837	0.832	3.919	4.909
6	4.351	2.070	7.418	8.845
7	4.109	1.055	2.925	5.153
8	−0.706	0.782	−3.216	3.384
9	−2.187	1.277	4.974	5.582
10	4.688	1.309	4.082	6.352
11	3.766	1.112	4.402	5.899
12	3.265	0.711	1.700	3.749

Table 7.3: Error in Satellite Position as Assessed from Line Fit

Error in Satellite Velocity (m/s)				
GCP No	ΔX	ΔY	ΔZ	RMS
Image 1				
1	−4.902	−7.329	10.069	13.384
2	−6.614	−8.333	11.980	16.022
3	−6.478	−8.254	11.828	15.811
4	−1.817	−5.518	7.323	9.348
5	0.235	−4.312	4.341	6.123
6	15.403	4.643	−12.547	20.402
7	8.322	0.454	−4.668	9.553
8	13.215	3.347	−10.113	16.974
9	13.786	3.685	−10.748	17.865
10	5.794	−1.038	−1.853	6.171
11	1.989	−3.280	2.387	4.518
12	8.934	0.815	−5.350	10.445
Image 7				
1	−10.369	−3.335	8.100	13.574
2	−12.035	−3.899	9.696	15.939
3	−11.685	−3.781	9.361	15.442
4	−6.884	−2.153	4.763	8.644
5	−4.924	−1.488	2.888	5.899
6	10.804	3.884	−12.139	16.708
7	2.819	1.150	−4.516	5.446
8	8.352	3.043	−9.799	13.230
9	9.431	3.413	−10.829	14.760
10	0.705	0.429	−2.495	2.628
11	−3.510	−1.007	1.535	3.961
12	4.332	1.667	5.961	7.555

Table 7.4: Error in Satellite Velocity as Assessed from Line Fit

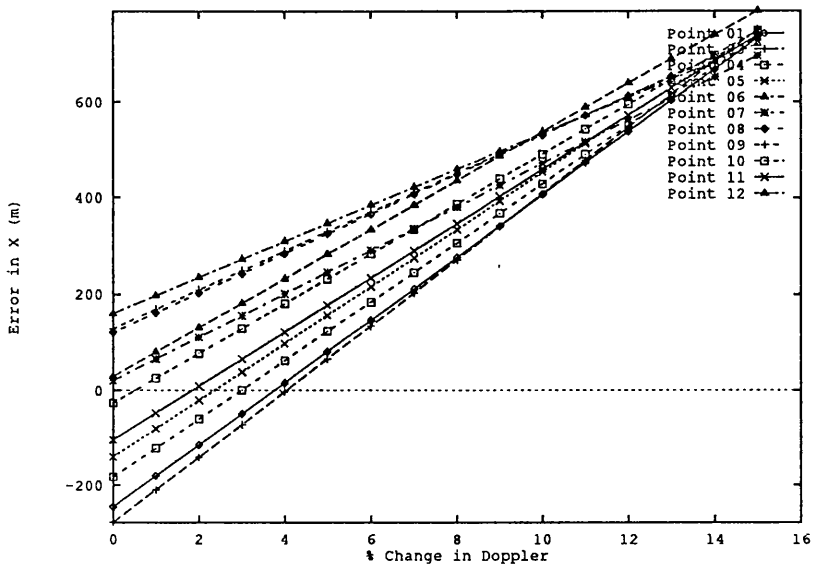

Figure 7.1: Dependence of x-Component of Result on Percentage Error in Doppler for Image 1

where the start-point of GCP 2 is the worst). The best start-point is variable: five points have GCP 2, four have GCP 12, two have GCP 1, and one (point 12) has GCP 9. For Image 7, the worst start-points are GCP 12 (for nine points) and GCP 9 (for three points). The best start-points are GCP 1 (for six points), GCP 2 (for four points) and GCP 9 (for two points, 1 and 12). It should be noted that in *no* case does a start-point of a GCP give the best result for itself; it can, however, give the worst result. There does not seem to be any logical reasoning to these best/worst start-point results, i.e. they do not seem to be correlated to a point/start-point position, height or satellite position/velocity error.

In these results, the component which gives the largest absolute error is usually ΔY. In Table 7.3, it can be seen that, for Image 1, the ΔY error component is always largest. However, for Image 7 this is *not* the case: here it is nominally the smallest error. Therefore, the satellite position error cannot be responsible for the larger ΔY error component in this type of geocoding.

The next part of the study was to ascertain how this type of geocoding is affected by the error in the two most important input data parameters, namely the Doppler and the near-range values.

Geocoding: Image-to-Object (m)				
Exact Input Image 1; Various Start-Points				
GCP No	Δ X	Δ Y	Δ Z	RMS Error
Start-Point 1				
1	−244.270	443.521	278.022	577.646
2	−281.112	511.247	320.478	665.660
3	−278.164	506.461	317.705	659.405
4	−180.409	323.251	201.693	421.567
5	−137.279	242.486	150.424	316.658
6	169.391	−344.331	−227.025	445.867
7	27.056	−74.807	−53.994	96.143
8	128.375	−260.201	−171.125	336.851
9	137.131	−280.972	−185.605	363.592
10	−22.209	23.949	10.630	34.348
11	−100.387	172.912	106.148	226.370
12	33.795	−97.516	−71.225	125.397
Start-Point 9				
1	−269.999	445.398	266.628	585.123
2	−314.992	515.283	306.916	677.447
3	−312.766	511.543	304.744	672.583
4	−198.128	328.668	197.677	431.687
5	−150.736	245.252	146.120	322.833
6	202.820	−347.741	−213.166	455.521
7	43.384	−75.134	−45.980	98.191
8	154.258	−263.101	−160.632	344.703
9	166.062	−282.802	−172.572	370.586
10	−20.428	25.404	12.882	35.052
11	−106.967	173.327	103.176	228.319
12	36.155	−90.478	−63.441	116.268
Start-Point 12				
1	−264.486	439.394	263.977	576.805
2	−305.577	507.306	304.418	665.888
3	−302.604	502.953	302.045	660.123
4	−193.580	321.797	193.648	422.523
5	−147.057	240.300	143.464	316.151
6	180.769	−345.417	−222.131	448.701
7	34.703	−75.298	−50.493	97.075
8	140.606	−261.219	−165.739	339.816
9	151.015	−281.234	−178.704	365.832
10	−18.070	23.252	12.135	31.850
11	−104.466	170.531	101.938	224.467
12	56.315	−93.511	−56.101	122.731

Table 7.5: Image 1 Geocoding Image-to-Object: Exact Data for various Start-Points

Geocoding: Image-to-Object (m)				
Exact Input Image 7; Various Start-Points				
GCP No	Δ X	Δ Y	Δ Z	RMS Error
Start-Point 1				
1	−185.185	300.798	176.699	394.963
2	−214.407	356.536	212.350	467.098
3	−209.080	344.517	204.068	451.719
4	−126.086	182.939	99.734	243.539
5	−88.539	118.537	60.610	159.887
6	212.955	−398.099	−254.532	518.285
7	60.632	−136.664	−94.603	176.927
8	168.661	−317.509	−203.581	413.163
9	165.660	−353.841	−239.796	458.420
10	10.545	−67.457	−57.981	89.574
11	−62.541	71.926	31.618	100.421
12	−61.720	−195.221	−220.209	300.687
Start-Point 9				
1	−236.194	303.072	149.558	412.320
2	−273.290	359.990	181.807	487.169
3	−260.764	348.213	177.891	469.995
4	−143.335	188.724	95.347	255.446
5	−109.681	120.981	50.791	171.015
6	244.197	−401.649	−239.986	527.776
7	57.467	−136.713	−96.471	176.917
8	191.332	−320.418	−193.344	420.306
9	217.140	−355.622	−211.944	467.479
10	10.019	−67.726	−58.547	90.083
11	−86.470	72.655	18.561	114.457
12	−3.430	−186.161	−178.103	257.659
Start-Point 12				
1	−332.129	293.141	85.062	451.084
2	−368.454	348.702	116.465	520.495
3	−354.876	337.119	113.334	502.425
4	−221.671	178.631	40.757	287.590
5	−181.061	113.492	2.701	213.707
6	136.220	−404.171	−304.354	523.967
7	−27.087	−141.962	−149.994	208.291
8	115.256	−322.245	−238.741	417.281
9	144.034	−356.705	−254.927	461.489
10	−40.807	−71.111	−90.931	122.435
11	−146.885	66.966	−21.514	162.857
12	108.649	−186.121	−113.755	243.692

Table 7.6: Image 7 Geocoding Image-to-Object: Exact Data for various Start-Points

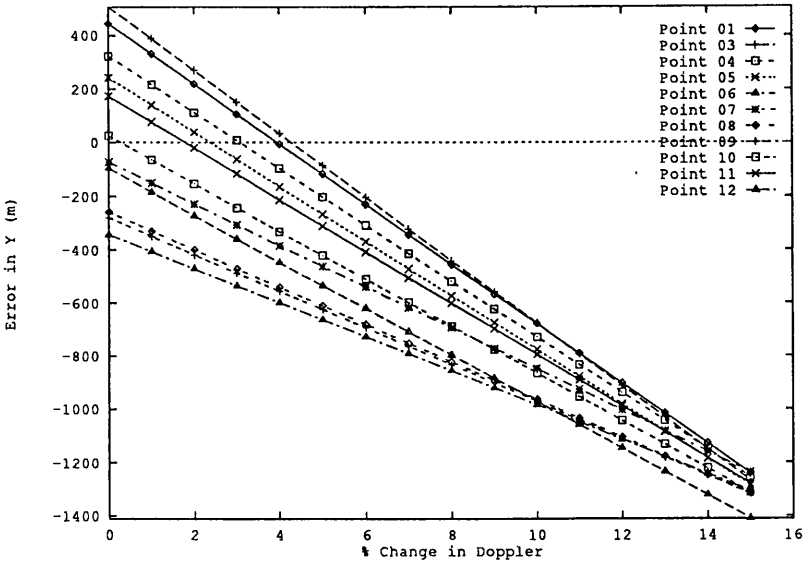

Figure 7.2: Dependence of y-Component of Result on Percentage Error in Doppler for Image 1

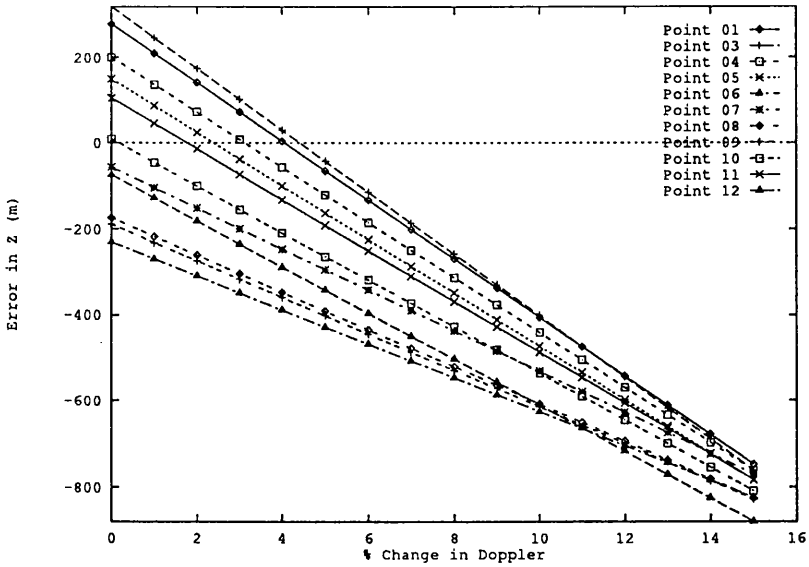

Figure 7.3: Dependence of z-Component of Result on Percentage Error in Doppler for Image 1

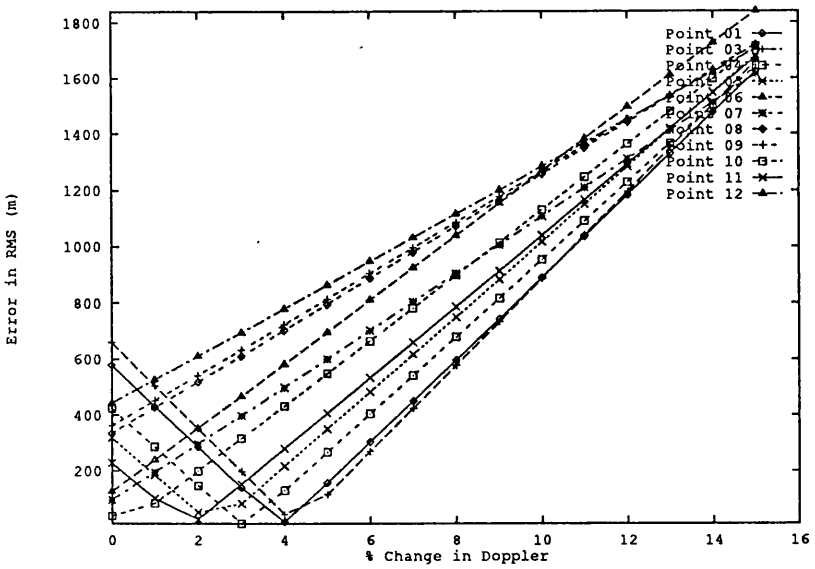

Figure 7.4: Dependence of RMS Result on Percentage Error in Doppler for Image 1

7.2.2 Image-to-Object Geocoding: Doppler Error Analysis

Figures 7.1, 7.2, 7.3 and 7.4 show the variation of component and RMS errors with the Doppler data for Image 1. Here, all the Doppler input data are increased by percentages in the range from 0–15%. All other data were kept to be the previously defined *exact* data. The start-point used was GCP 2. For all points (point 2 deliberately being excluded), it can be seen that the error components vary linearly and appear to converge.

Figures 7.5, 7.6, 7.7 and 7.8 show the results of the same procedure for Image 7. Here again, the results are linear and tend to converge; however, the gradients of the lines are steeper than those for Image 1, showing that geocoding results using Image 7 are more sensitive to Doppler mis-estimation. For both images, the ΔY component is most sensitive to the change in Doppler, while ΔX and ΔZ show similar sensitivities, the ΔZ component being slightly greater.

7.2.3 Image-to-Object Geocoding: Near-Range Error Analysis

Figures 7.9, 7.10, 7.11 and 7.12 show the component and RMS errors for Image 1 for an increase in the near-range value. As before, all other data are kept to the *exact* definition and a start-point of GCP 2 was again used. Here it can be seen that the component errors vary linearly and are parallel. Figures 7.13, 7.14, 7.15 and 7.16 show the component and RMS errors for the same procedure for Image 7, and here the results follow the same trend,

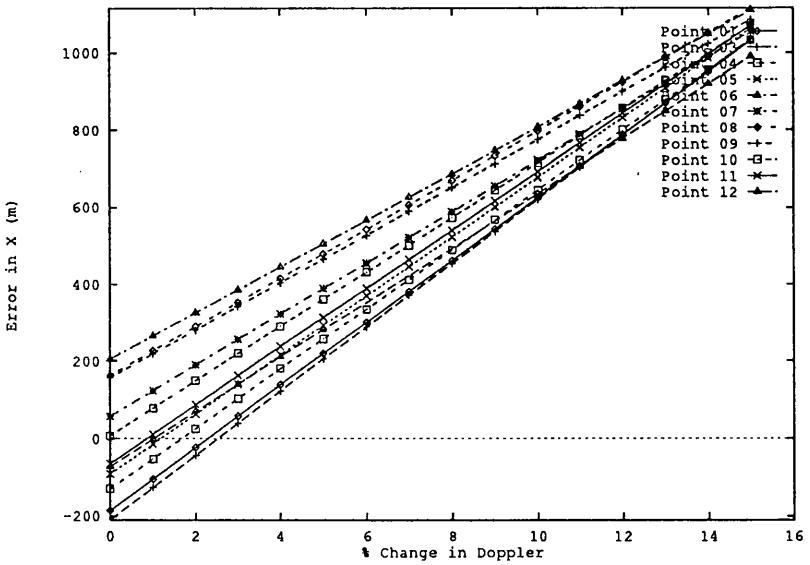

Figure 7.5: Dependence of x-Component of Result on Percentage Error in Doppler for Image 7

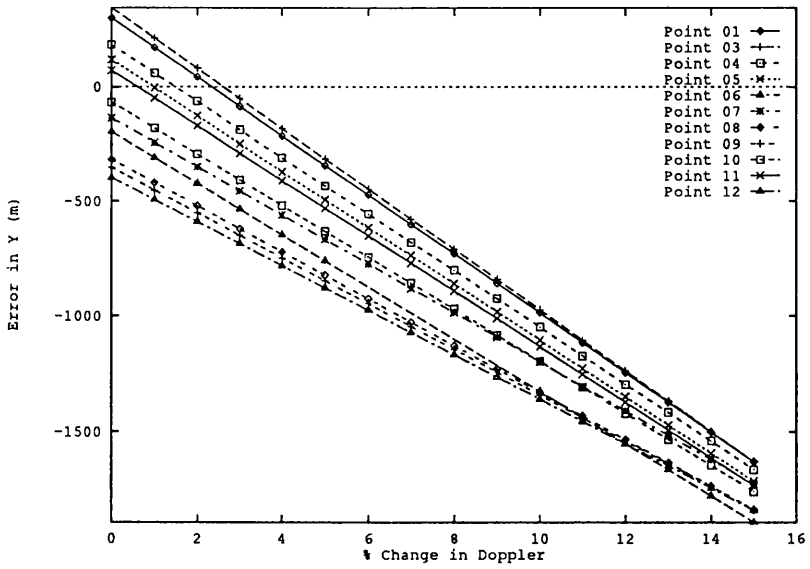

Figure 7.6: Dependence of y-Component of Result on Percentage Error in Doppler for Image 7

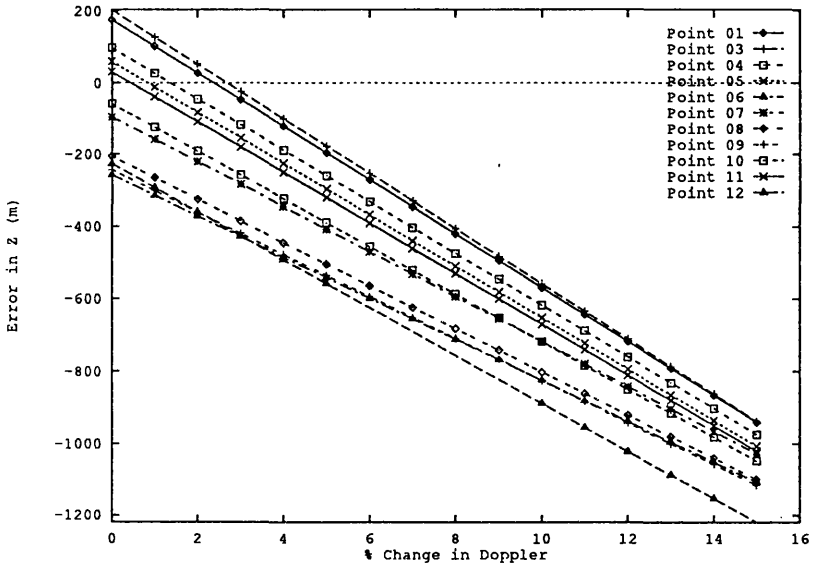

Figure 7.7: Dependence of z-Component of Result on Percentage Error in Doppler for Image 7

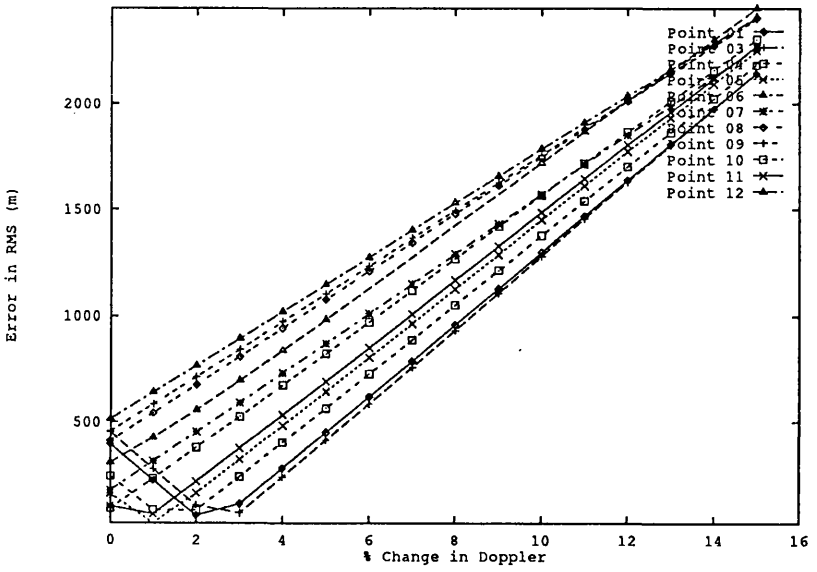

Figure 7.8: Dependence of RMS Result on Percentage Error in Doppler for Image 7

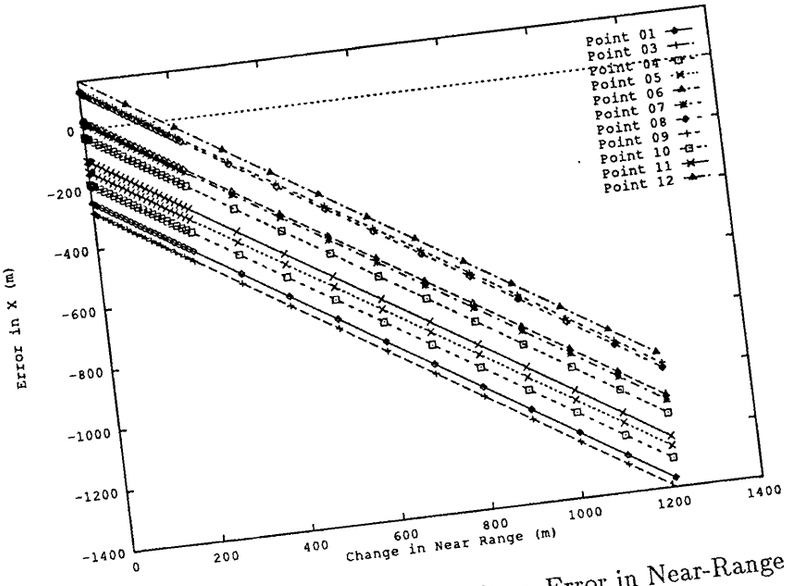

Figure 7.9: Dependence of x-Component of Result on Error in Near-Range for Image 1

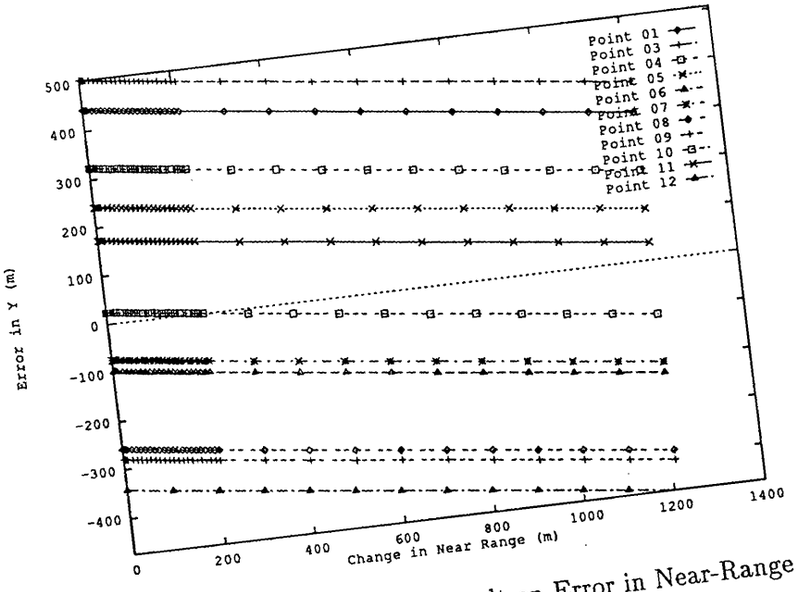

Figure 7.10: Dependence of y-Component of Result on Error in Near-Range for Image 1

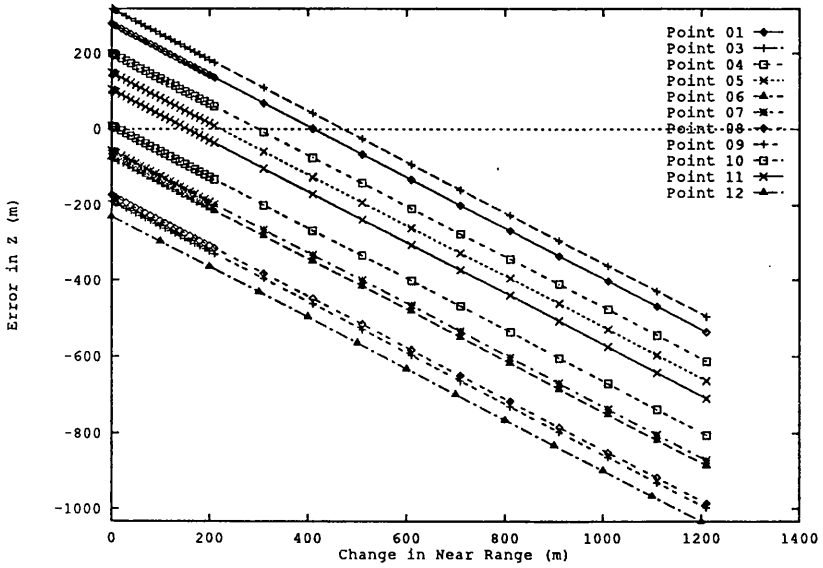

Figure 7.11: Dependence of z-Component of Result on Error in Near-Range for Image 1

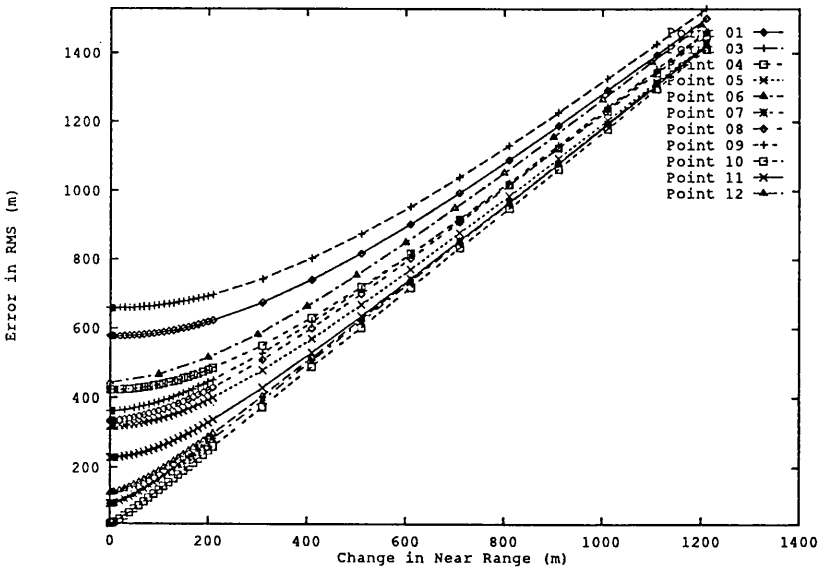

Figure 7.12: Dependence of RMS Result on Error in Near-Range for Image 1

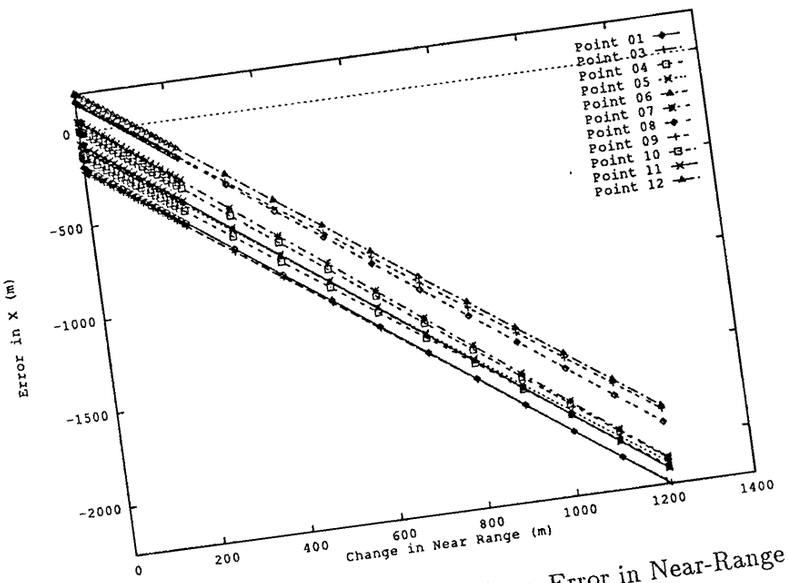

Figure 7.13: Dependence of x-Component of Result on Error in Near-Range for Image 7

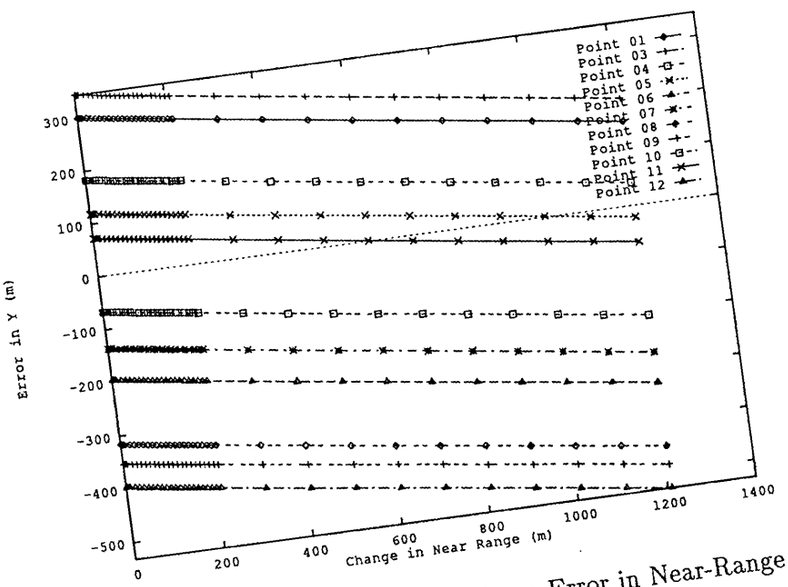

Figure 7.14: Dependence of y-Component of Result on Error in Near-Range for Image 7

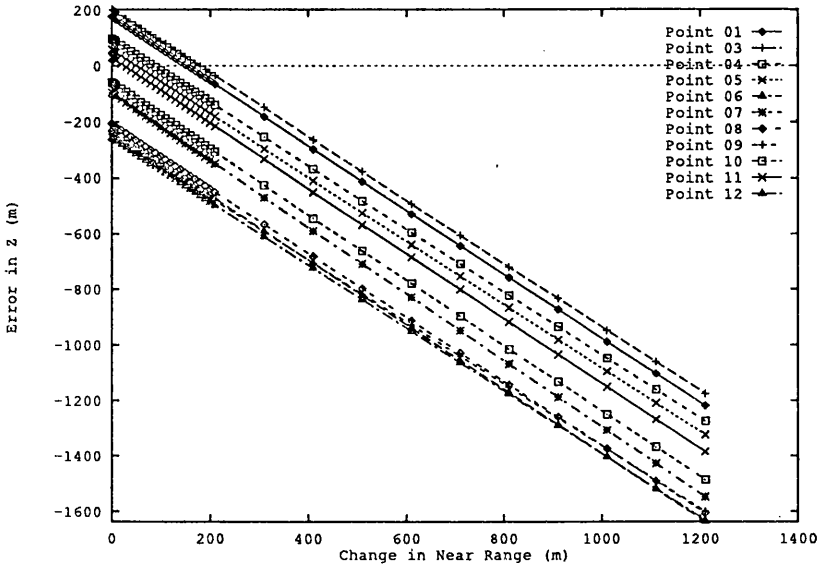

Figure 7.15: Dependence of z-Component of Result on Error in Near-Range for Image 7

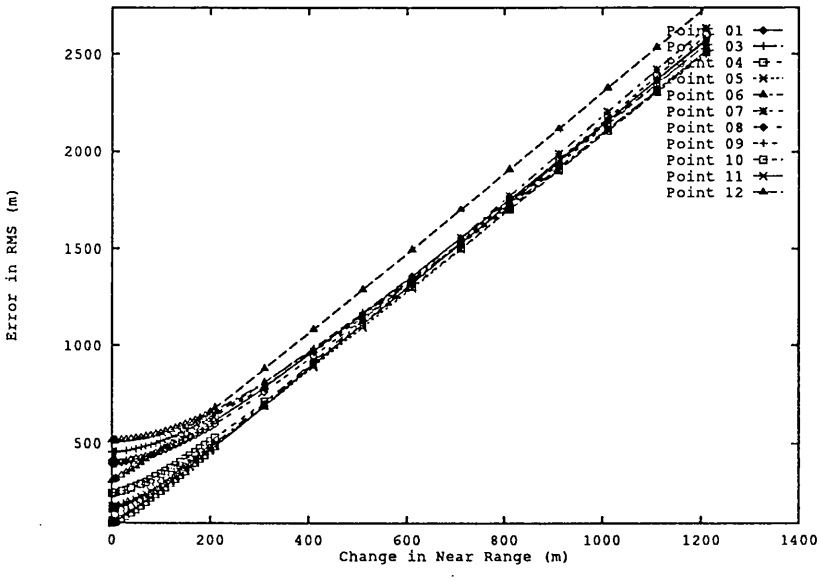

Figure 7.16: Dependence of RMS Result on Error in Near-Range for Image 7

Geocoding: Image-to-Object (m)				
Average Input: Image 1				
GCP No	Δ X	Δ Y	Δ Z	RMS Error
1	679.897	1226.434	−184.037	1414.309
2	682.063	1243.193	−19.834	1418.149
3	808.662	1281.472	19.832	1515.420
4	1385.266	1379.689	−125.404	1959.140
5	1407.015	1421.820	−403.398	2040.586
6	1501.381	936.725	−1139.720	2104.890
7	1632.263	1195.801	−704.988	2142.715
8	1875.794	1279.364	−1139.152	2540.284
9	2110.598	1411.984	−1199.806	2808.533
10	2018.192	1598.591	−749.691	2681.535
11	1503.952	1485.144	−616.307	2201.672
12	4397.970	2902.046	−1083.483	5379.402

Table 7.7: Image 1 Image-to-Object Geocoding: Average Input

i.e. the component plots are linear and parallel.

For both images, it can be seen that the ΔY component is least sensitive to change in the near-range. In fact the variation is relatively small: for a 1 Km change in near-range there is $\approx$ 100 m change in the ΔY component for each point and image. For the ΔZ component, a change of 1 Km in near-range will result in $\approx$ 0.5 Km change for Image 1 and $\approx$ 1.2 Km change for Image 7. A change of 1 Km in the near-range will result in a ΔX component change of $\approx$ 0.9 Km for Image 1 and $\approx$ 1.7 Km for Image 7.

7.2.4 Image-to-Object Geocoding: Average Data Analysis

Tables 7.7 and 7.8 show the errors obtained from geocoding on a more operational basis. Here, average pixel pixel spacings were used. An Earth model of $a = 6317.137$ Km and $e = 0.08161$ was employed; hence, large errors due to terrain effects were to be expected. The tie-point of GCP 2 was given but here the `NEXTPOINT` procedure described in Section 3.4.2 was used to give a start-point for each point.

As can be seen from the tables, the errors are large. For Image 1, the RMS error varies from 1.4 Km to 5.4 Km; for Image 7, the variation is 2.4 Km to 9.4 Km. In these cases, the error is directly correlated to point height. The correlation is almost exact for Image 1 and strong in Image 7. For Image 7 in *all* cases, the component with the largest error is ΔX, followed by ΔY; the error in the ΔZ component is, in most cases, much smaller than that in the other components. For Image 1, the size of the component error seems to be

Geocoding: Image-to-Object (m)				
Average Input: Image 7				
GCP No	Δ X	Δ Y	Δ Z	RMS Error
1	2109.630	1116.525	573.547	2454.816
2	1983.986	1111.292	640.123	2362.399
3	2104.888	1134.991	662.804	2481.545
4	3291.585	1268.708	919.722	3645.551
5	3284.934	1323.488	635.729	3598.133
6	3463.869	922.247	28.382	3584.652
7	3861.233	1176.170	614.761	4082.943
8	4348.809	1269.673	339.893	4543.098
9	4532.874	1372.969	224.502	4741.560
10	4521.237	−1541.233	701.495	4827.948
11	3706.701	1425.523	653.213	4024.728
12	8805.803	2834.729	1508.102	9372.952

Table 7.8: Image 7 Image-to-Object Geocoding: Average Input

linked to terrain height. For high points, the ΔX component gives the largest error while for lower points, the ΔY component gives the largest error. In all bar one case, point 6 (the middle height point), the ΔZ error component is the smallest and generally much smaller than the others.

7.3 Object-to-Image Geocoding

This method requires that the object (ground) positions are defined in terms of X, Y and Z; the corresponding (i, j) position in the image is then located. The term *exact* data in this type of geocoding means that the individually calculated range pixel spacings for each point were employed.

7.3.1 Object-to-Image Geocoding: Exact Data Analysis

Tables 7.9 and 7.10 show the results for *exact* data for Images 1 and 7 respectively. In both these image cases, the magnitudes of the ΔI and ΔJ are not related, i.e. a small ΔI does not necessarily correspond to a small ΔJ. Since the input azimuth pixel spacing is known to be inaccurate, it is expected that the ΔI value will be larger, and for Image 1 this is indeed the case: ΔI is always substantially larger than ΔJ. For Image 7, the results are much more variable than those of Image 1: for five points (points 5, 8, 9, 10 and 11) the ΔJ value is larger than the ΔI value.

Geocoding: Object-to-Image (pixels)			
Exact Input: Image 1			
GCP No	Δ I	Δ J	RMS Error
1	38.670	4.818	38.969
2	51.863	0.445	51.865
3	55.976	0.744	55.981
4	37.312	9.269	38.446
5	59.151	9.592	59.924
6	−31.632	7.042	32.406
7	27.610	0.612	27.617
8	−24.802	6.292	25.588
9	−32.929	2.085	32.995
10	76.625	3.273	76.695
11	58.274	9.348	59.019
12	136.152	−8.003	136.387

Table 7.9: Image 1 Object-to-Image Geocoding: Exact Input

There appears to be no correlation between the results for the two images and no apparent correlation of either sets of results with the image or ground position/height or satellite position error. However, it should be re-emphasised that, as stated previously, $\partial f_{dc}/\partial i$ cannot be assessed very accurately and $\partial f_{dc}/\partial j$ has had to be assumed to be zero. Hence, it is perhaps not surprising that these errors are so variable.

The results for using different start-points are shown in Tables 7.11 and 7.12 for Images 1 and 7 respectively. Here, it can be seen that the initial start-points have much more effect on the results than for Image-to-Object geocoding. The maximum RMS variation between start-points is ≈ 100 pixels for Image 7. For Image 1, the use of GCP 12 as a start-point is disastrous: the errors, notably in the ΔI component, are, for all bar two cases (points 7 and 12), huge compared to those of the other start-points. These two exceptions have errors which are very small. The reason for this behaviour is not evident.

For Image 1, the start-point GCP 1 gave the best results for five points (points 1, 4, 5, 10 and 11), start-point GCP 9 four points (points 2, 3, 8 and 9), start-point GCP 2 one point (point 6) and, as stated before, start-point GCP 12 gave the best result for points 7 and 12.

For Image 7, there is again no predominant best start-point. The results show that start-point GCP 1 is the best for six points (points 1, 7, 8, 9, 10 and 11), start-point GCP 2 is best for three points (points 2, 4 and 5), start-point GCP 12 is best for two points (points 3 and 12) and start-point GCP 9 is best for one point (point 6). As can be

Geocoding: Object-to-Image (pixels)			
Exact Input: Image 7			
GCP No	Δ I	Δ J	RMS Error
1	49.035	−4.659	49.256
2	41.622	−5.132	41.937
3	39.041	−4.236	39.270
4	1.962	1.621	2.545
5	0.631	4.839	4.880
6	−29.086	9.255	30.523
7	−98.023	39.116	105.539
8	−0.697	36.034	36.041
9	1.417	42.259	42.283
10	−14.564	18.447	23.503
11	−2.091	8.836	8.691
12	50.125	16.747	52.849

Table 7.10: Image 7 Object-to-Image Geocoding: Exact Input

seen, start-point GCPs 1, 2 and 12 give the best results for themselves: unlike Image-to-Object geocoding, start-point GCP 12 even produces a result of *zero* error for itself! The worst start-points are predominately GCPs 9 and 12, which give the worst results for five points each. Start-point GCP 2 gives the worst results for the remaining two points (points 7 and 12). Again, there does not appear to be any reasoning behind this spread of results, i.e. they do not seem to be related to any characteristic of the image or ground point.

As with the Image-to-Object geocoding, a study was carried out to see how the errors were affected by changes in the Doppler and near-range data. Again the *exact* definition was used with GCP 2 as the start-point.

7.3.2 Object-to-Image Geocoding: Doppler Error Analysis

Figures 7.17, 7.18 and 7.19 show the component and RMS errors for Image 1 for a percentage increase in Doppler values from 0 to 15%. Figures 7.20, 7.21 and 7.22 show the equivalent component and RMS errors for Image 7. There were problems in constructing these plots as, with increasing error, the iteration procedure tended to try to access data outside the available range of Doppler data. The program does not stop when this happens; instead, it generates a warning message and supplies the nearest point it can. However, this can upset the iteration process and erroneous results may be obtained. In this study, it was sometimes necessary to give a different start-point to various points to try to keep the iteration 'in bounds'. For Image 1, to obtain the whole plot, point 9 was given a start-

Geocoding: Object-to-Image (pixels)			
Exact Input Image 1; Various Start-Points			
GCP No	Δ I	Δ J	RMS Error
Start-Point 1			
1	41.062	0.517	41.065
2	64.123	−4.864	64.307
3	67.025	−4.398	67.169
4	19.725	7.499	21.102
5	26.351	9.971	28.174
6	−67.633	−9.082	68.240
7	−53.869	10.149	54.817
8	−43.755	−2.914	43.852
9	−52.945	−3.200	53.042
10	6.673	10.189	12.180
11	14.561	11.596	18.614
12	39.011	3.351	39.155
Start-Point 9			
1	46.339	−3.777	46.493
2	40.924	−4.851	41.211
3	45.050	−4.429	45.267
4	7.316	−89.460	89.759
5	20.745	−73.499	76.371
6	−39.370	5.142	39.704
7	−40.038	−23.534	46.442
8	−19.134	−1.531	19.195
9	−27.491	0.328	27.493
10	16.135	−35.433	38.934
11	14.039	−61.805	63.379
12	56.786	−16.518	59.140
Start-Point 12			
1	690.709	−39.924	691.862
2	784.121	−44.286	785.371
3	778.954	−43.579	780.172
4	531.190	−30.098	532.042
5	429.859	−25.165	430.595
6	−362.445	20.362	363.017
7	−1.601	−1.708	2.341
8	−244.041	13.619	244.421
9	−276.838	15.141	277.252
10	144.330	−9.187	144.622
11	337.274	−20.491	337.896
12	−2.784	0.252	2.795

Table 7.11: Image 1 Geocoding Object-to-Image: Exact Data for various Start-Points

Geocoding: Object-to-Image (pixels)			
Exact Input Image 7; Various Start-Points			
GCP No	Δ I	Δ J	RMS Error
Start-Point 1			
1	28.721	−3.730	28.962
2	44.511	−10.075	45.637
3	37.800	−8.222	38.684
4	16.972	−3.153	17.262
5	8.635	−1.571	8.777
6	−37.708	7.745	38.495
7	−7.050	−1.966	7.319
8	−32.020	6.523	32.678
9	−38.232	9.126	39.306
10	−1.449	−0.199	1.463
11	4.971	−0.493	4.995
12	−30.910	10.218	32.555
Start-Point 9			
1	50.773	−8.199	51.431
2	65.016	−20.843	68.275
3	47.586	−15.215	49.959
4	18.230	−1.489	18.291
5	30.766	10.527	32.517
6	−25.268	7.297	26.301
7	−23.618	12.114	26.544
8	−33.951	−0.007	33.951
9	−42.444	4.724	42.706
10	−20.367	9.837	22.618
11	29.958	9.039	31.292
12	−3.901	0.350	3.917
Start-Point 12			
1	28.867	−3.865	29.125
2	37.900	−7.934	38.722
3	34.272	−6.410	34.866
4	4.101	18.231	18.687
5	25.382	8.664	26.820
6	−48.740	8.481	49.472
7	−29.986	8.530	31.176
8	−49.639	11.928	51.052
9	−44.271	6.586	44.758
10	−32.336	6.857	33.055
11	10.362	4.182	11.174
12	0.000	0.000	0.000

Table 7.12: Image 7 Geocoding Object-to-Image: Exact Data for various Start-Points

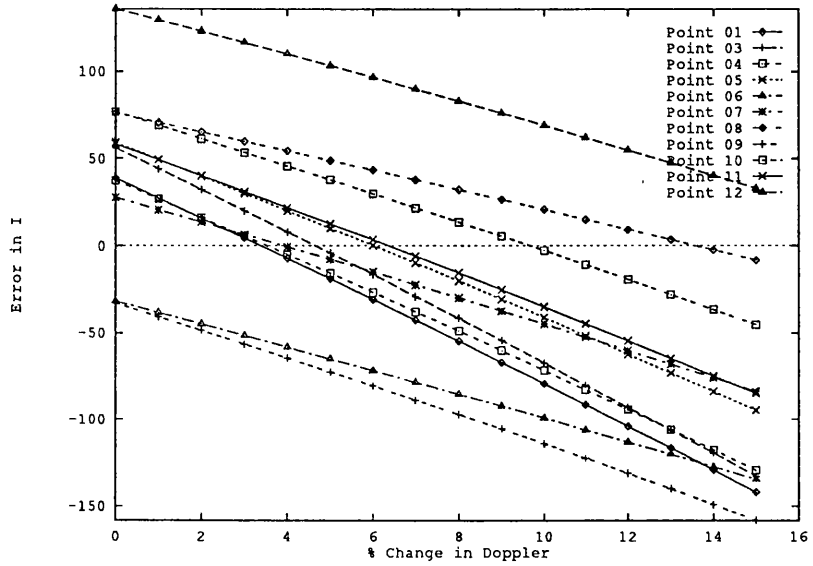

Figure 7.17: Dependence of i-Component of Result on Percentage Error in Doppler for Image 1

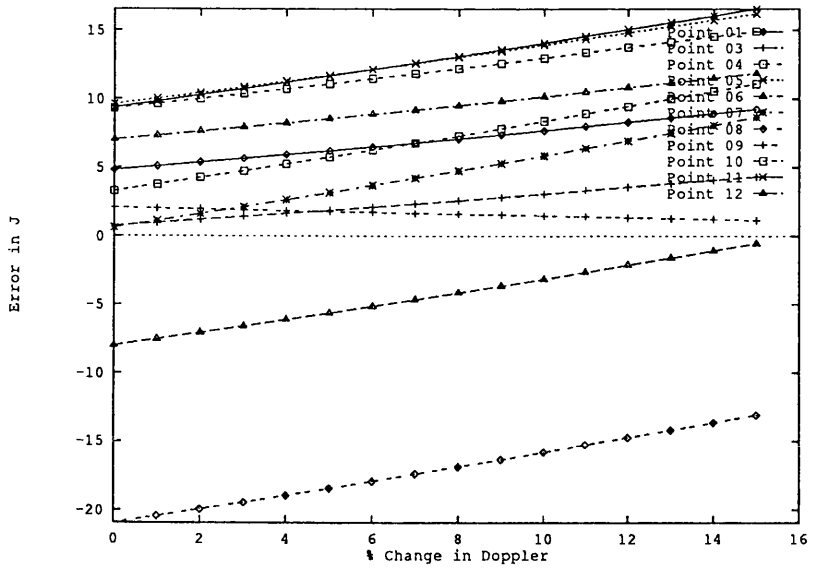

Figure 7.18: Dependence of j-Component of Result on Percentage Error in Doppler for Image 1

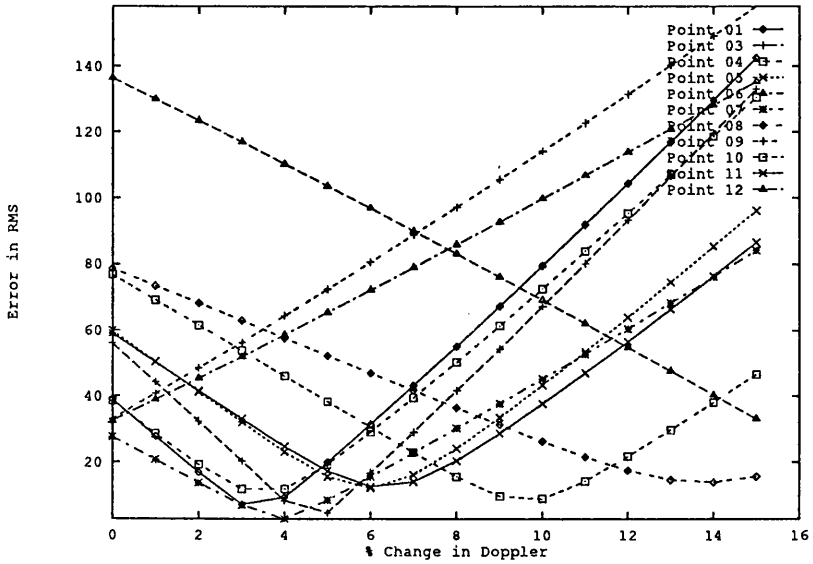

Figure 7.19: Dependence of RMS Result on Percentage Error in Doppler for Image 1

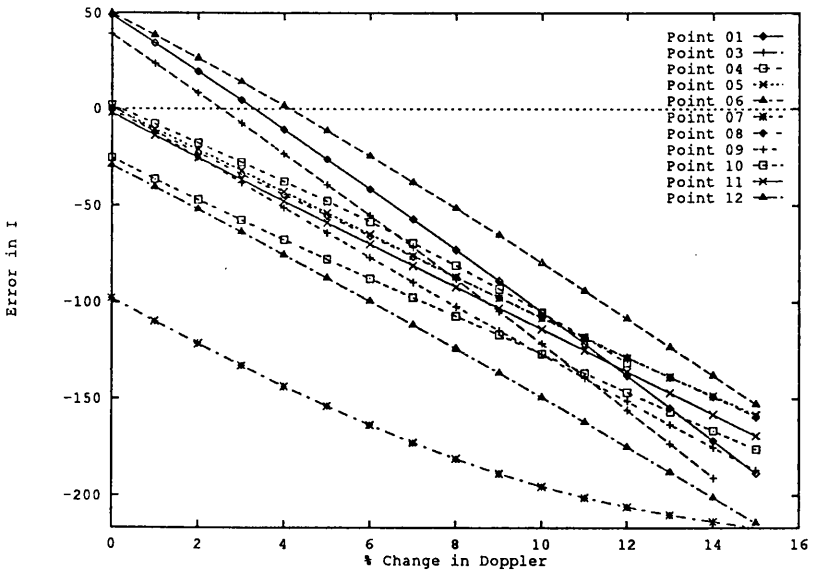

Figure 7.20: Dependence of i-Component of Result on Percentage Error in Doppler for Image 7

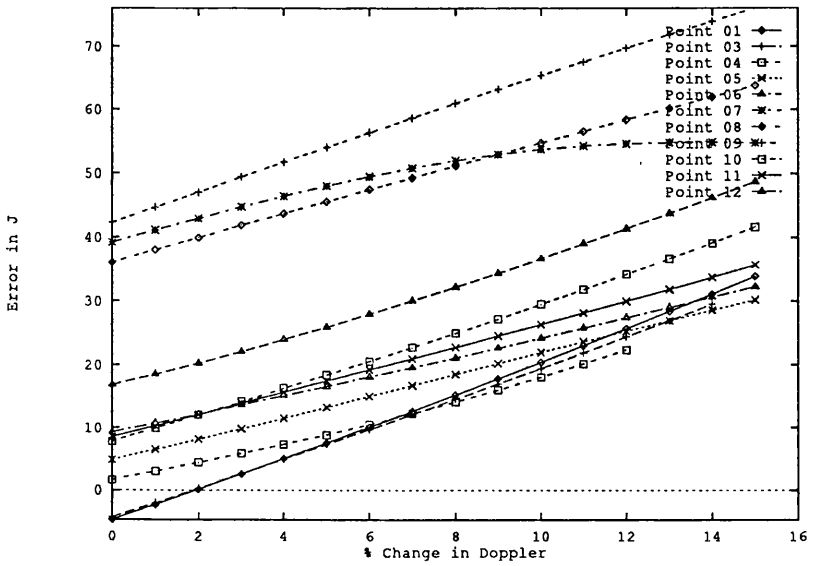

Figure 7.21: Dependence of j-Component of Result on Percentage Error in Doppler for Image 7

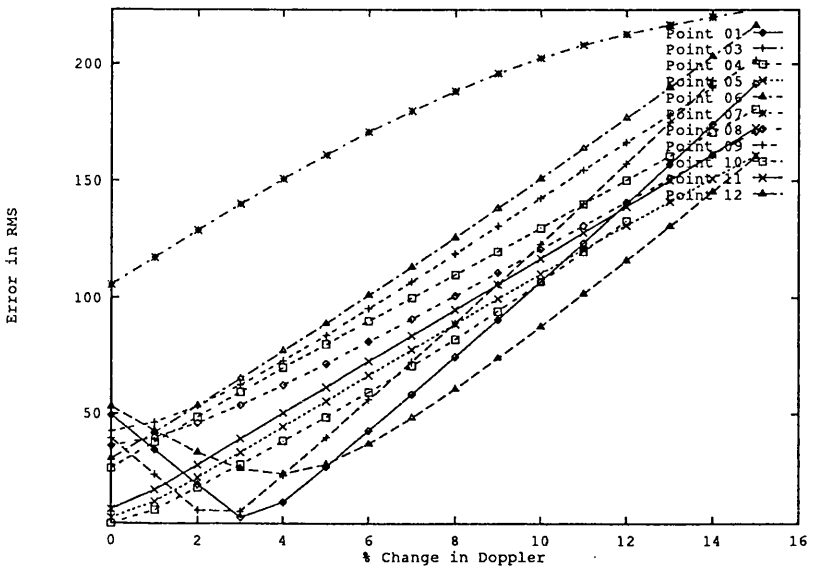

Figure 7.22: Dependence of RMS Result on Percentage Error in Doppler for Image 7

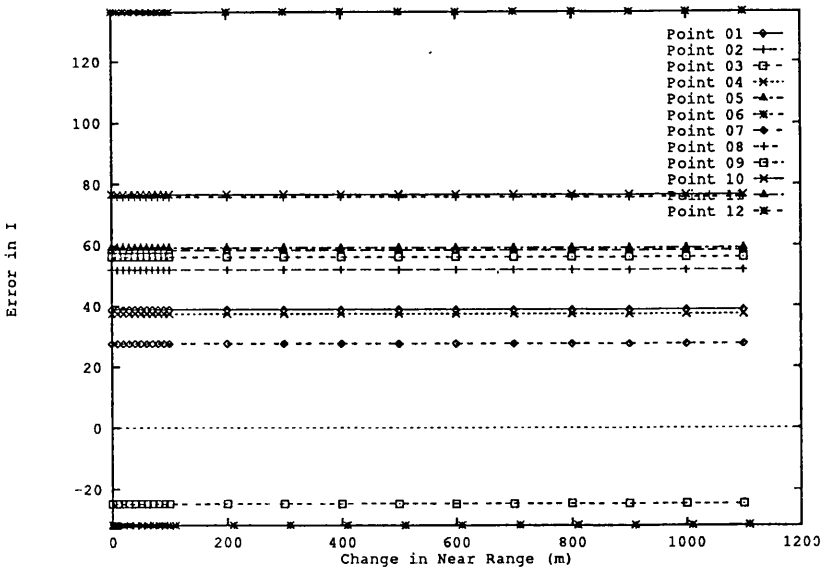

Figure 7.23: Dependence of i-Component of Result on Error in Near-Range for Image 1

point of GCP 8. For Image 7, point 4 could not be kept 'in bounds' and hence for this point the study was terminated at a Doppler error of 12%. Points 6 and 10 were also given start-points of GCP 8. For both images, the plots can be seen to be non-linear; they are not parallel and show no general sign of convergence or divergence.

7.3.3 Object-to-Image Geocoding: Near-Range Error Analysis

Figures 7.23, 7.24 and 7.25 show the component and RMS errors for Image 1 for changes in near-range. Figures 7.26, 7.27 and 7.28 show the component and RMS errors for Image 7. Here again, the near-range was increased while the other input data was kept as *exact*. A start-point of GCP 2 was again used. For Image 1, it can be seen that the ΔI error component is almost totally unaffected by a change in near-range. For Image 7, ΔI is only affected by a small amount and, as can be seen from the plots, the change can be of either sign.

For both images, the ΔJ component is, by comparison, very sensitive to changes in the near-range. The plots are linear with similar gradients (i.e., they are not exactly parallel). For Image 1, a change in near-range of ≈ 1 Km gives ≈ 90 range pixel error; for Image 7 this figure is ≈ 150 pixels.

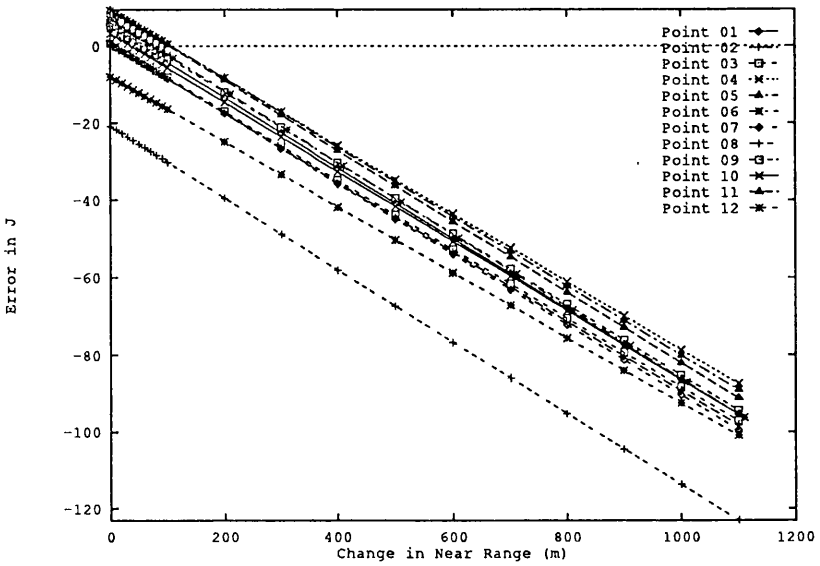

Figure 7.24: Dependence of j-Component of Result on Error in Near-Range for Image 1

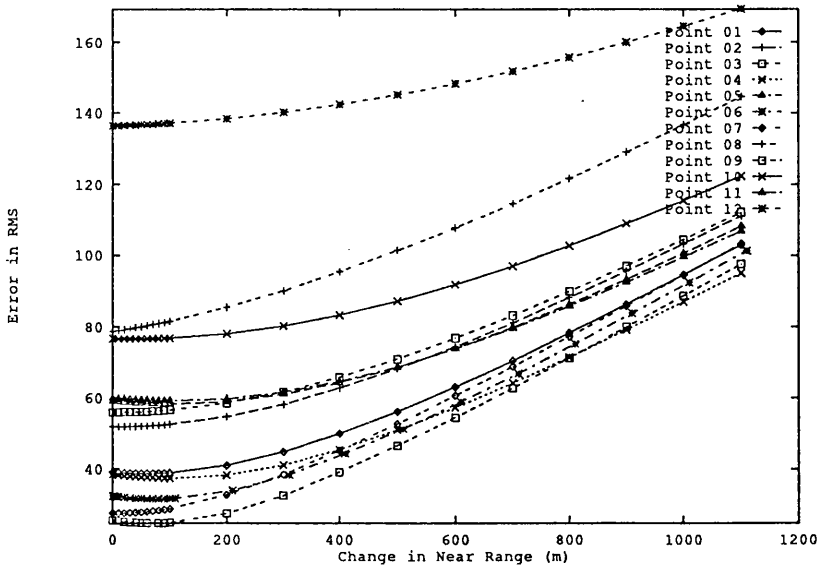

Figure 7.25: Dependence of RMS Result on Error in Near-Range for Image 1

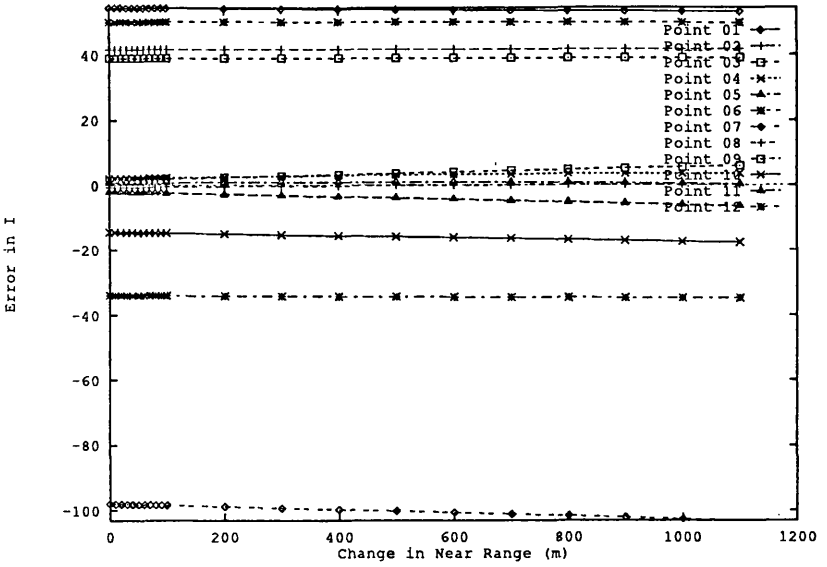

Figure 7.26: Dependence of i-Component of Result on Error in Near-Range for Image 7

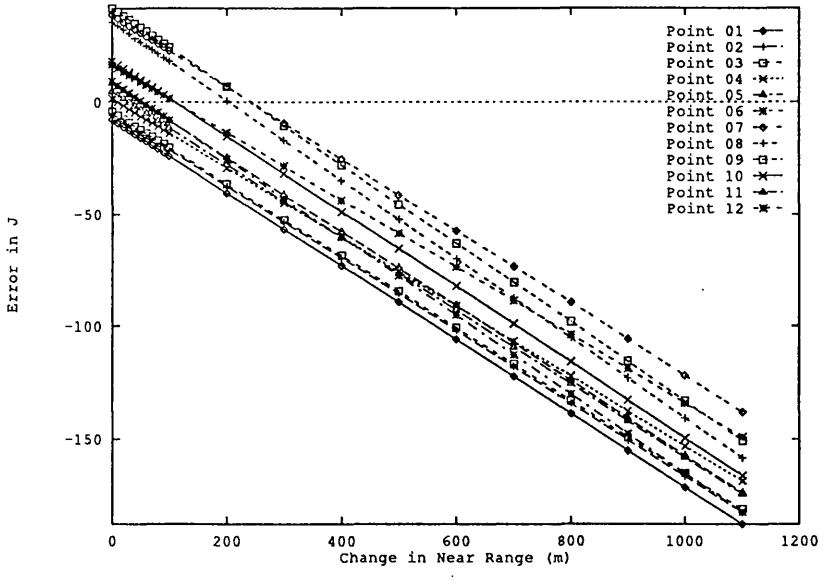

Figure 7.27: Dependence of j-Component of Result on Error in Near-Range for Image 7

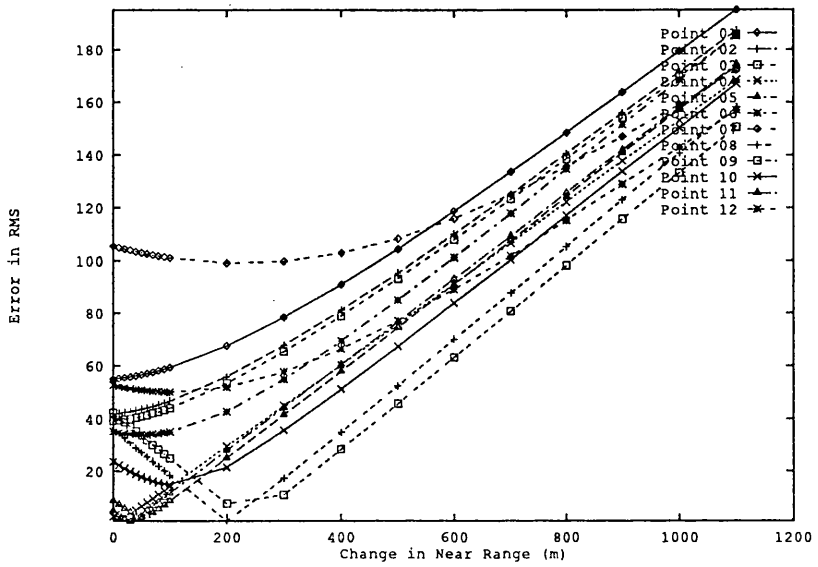

Figure 7.28: Dependence of RMS Result on Error in Near-Range for Image 7

Geocoding: Object-to-Image (pixels)			
Average Input: Image 1			
GCP No	Δ I	Δ J	RMS Error
1	38.670	−4.346	38.913
2	73.838	−3.868	73.939
3	47.924	8.957	48.754
4	41.858	33.631	53.695
5	13.906	8.729	16.419
6	−79.259	−24.132	82.851
7	−37.958	−29.666	48.176
8	177.212	−16.534	177.982
9	−21.136	−25.424	33.062
10	−48.256	−34.173	59.131
11	−0.089	−20.082	20.082
12	35.812	71.832	80.264

Table 7.13: Image 1 Object-to-Image Geocoding: Average Input

Geocoding: Object-to-Image (pixels)			
Average Input: Image 7			
GCP No	Δ I	Δ J	RMS Error
1	49.035	−1.580	49.060
2	46.938	−0.133	46.938
3	36.016	11.621	37.844
4	10.558	54.158	55.178
5	5.663	7.473	12.935
6	−59.967	−45.944	75.544
7	−12.203	1.391	12.282
8	−18.846	−24.627	31.011
9	−53.185	−28.149	60.175
10	−20.263	1.487	20.317
11	12.714	−25.490	28.485
12	−9.451	40.109	41.207

Table 7.14: Image 7 Object-to-Image Geocoding: Average Input

7.3.4 Object-to-Image Geocoding: Average Data Analysis

To investigate the spread of error obtained from Object-to-Image geocoding on a more operational basis, an average range pixel spacing was input. GCP 2 was used as a start-point for the first point (point 1, as it happens) but, subsequent to that, the start-point for the next point was taken to be the result of the last point. The results of this part of the study are shown in Tables 7.13 and 7.14. Again, for this type of geocoding, the results do not appear to show any correlation between images or with any point or data characteristic. One might have expected the errors here to be related to deviation from the 'true' range pixel spacing but this does not appear to be the case. On the whole, the average data results are not very different from the *exact* results (unlike those for Image-to-Object geocoding). Here, for Image 1, in all bar three cases (points 9, 11 and 12), the ΔI component is larger than the ΔJ component. For Image 7, there are five cases (points 4, 5, 8, 11 and 12) where the ΔJ error component is greater than the ΔI component.

7.4 Summary of Geocoding Results

SAR processor-based geocoding algorithms have been investigated in depth on real SAR imagery. Both Image-to-Object and Object-to-Image geocoding have been addressed. In each case, the satellite position was assessed from a polynomial description, and the effects of inaccuracy in the Doppler and near-range parameters were studied in detail. The effect

of differing iteration start-points has also been addressed.

7.4.1 Image-to-Object Geocoding

On an operational basis, it is known that this type of geocoding will give poor results for images of all bar flat terrain. This type of geocoding can give an RMS error of better than 700 m if the terrain height is accounted for and as exact an input dataset as was possible is used. The best result obtained here was 31.85 m (for point 10, start-point 12). The greatest problem in this part of the work was shown to be the accuracy with which the satellite position and velocity could be predicted from a curve fitted to the orbit data. The study of this type of geocoding also demonstrated the apparently unpredictable nature of satellite position and velocity errors on the final result.

The errors resulting from an increase in Doppler or near-range was shown to have an approximately linear response in each error component. The components most sensitive to these changes have been identified.

7.4.2 Object-to-Image Geocoding

This investigation was hampered somewhat by the lack of detailed Doppler data. The rate of change of Doppler with sample number was expected to be inaccurately assessed and the rate of change of Doppler with line number had to be assumed to be zero. The errors in the assessed satellite position and velocity would also affect these results. Hence, a mixture of these effects is probably responsible for the fact that the results could not be correlated together or with individual sources of error. It also explains why the results using *exact* or *average* data did not differ very much, as the only difference between these types of input datasets was the accuracy with which the range pixel spacing was defined. This obviously has a limited effect, with the other sources of error being dominant.

It has been shown that increasing the error in the near-range data has an almost negligible effect on the ΔI error component, whereas the ΔJ error component is significantly affected. An increase in the error of the Doppler data affects the errors in a less predictable manner.

With regard to the choice of start-point, the studies for both type of geocoding are rather inconclusive: no one point produces worst or best results in all cases. There appears to be no correlation, positive or negative, between points of similar or dissimilar position

or heights. On the whole — and this is very general — start-point GCPs 1 and 2 gave the best results and start-point GCPs 9 and 12 the worst. The moral seems to be: do not use start-points of extreme height (compared with the rest of the image), even for points of extreme height.

7.5 Comparison with Error Budget

In the cases where *exact* input data were used, the only sources of error were due to the satellite position and velocity, and the Doppler; all of these were assessed from curve fits. The solution of the equations should not be expected to be exact and the choice of start-point may have an effect.

In this study, for object-to-image geocoding, the Doppler was assessed very accurately, to less than 0.004 Hz (an extremely small percentage error), which Doppler error studies would indicate to have a negligible effect. The satellite position RMS error for the restituted orbit of ERS-1 is given in the error budget as 66.71 m, which is worse than those of this study. This is translated into a geocoding error of 84.86 m in the error budget.

The satellite velocity RMS error for this orbital precision is quoted as 0.05 m/s, and this is translated into a geocoding error of 3.43 m. The satellite velocity RMS error of the ERS-1 preliminary orbit is quoted to be 0.96 m/s, which is stated to result in a geocoding error of 81.76 m/s. Therefore, the velocity errors of up to 20 m/s found in this study should be expected to give large errors; however, their magnitude is unknown.

The ERS-1 error budget suggests that large errors would be expected in this study and indeed this is mostly the case. However, some fairly good results also emerge, i.e. a number of RMS geocoding errors of less than 100 m are obtained which would not be expected. Also, the study has shown that the errors are not predictable. The satellite position errors for Image 7 are less than those of Image 1. The satellite velocity errors of the two images are fairly close, with Image 7 velocity errors being, in all but one case (point 1), smaller than those of Image 1. However, Image 7 geoocoding results are not always smaller than those of Image 1.

Therefore, the error budget study can offer no assistance in understanding the satellite position and velocity error effects, as only satellite velocity errors of less than 1 m/s are considered. Conversely, the predicted results of the error budget cannot be verified by

this study, as the errors predicted for ERS-1 are not comparable with the errors in this study. However, the unpredictable nature of these results should be borne in mind: error budget studies naturally assume that the larger the satellite error, the larger the resulting geocoding error; this study does not confirm this assumption.

Chapter 8

SAR Stereo Using SIR-B Mount Shasta Imagery

8.1 Introduction

As discussed in Section 4.3, the range and Doppler equations can be used to determine the X, Y and Z co-ordinates of a ground point. The pairs of range and Doppler equations, along with their appropriate derivatives, were coded. It was decided that, since the pairs of points had to be identified in the images by eye (i.e., the study was not to include automatic matching), the satellite positions and velocities would be evaluated individually from the orbit. Hence, the input data in this study were not subject to the satellite positional error which affected the geocoding studies. (On an operational basis for full image analysis, the satellite positions would have to be assessed by a statistical fit, as with the geocoding.)

The range, Doppler, and orbit production algorithms were coded into a program STEREO. Error analyses similar to those for geocoding were then carried out. In this Chapter, the term *exact* input data means that the individually-calculated range pixel spacings were employed for each pair of points. All the other supplied input data have been constructed to be as accurate as possible. A start-point of GCP 2 was used.

8.2 SIR-B Stereo: Exact Data Analysis

Table 8.1 shows the results for this study using this *exact* data. Here it can be seen that the errors are small, the RMS error varying from 0.305 m to 16.338 m. The spread of

Stereo SAR Measurements (m)				
Exact Input				
GCP No	Δ X	Δ Y	Δ Z	RMS Error
1	−1.609	4.350	−8.854	9.995
2	0.143	−0.164	0.404	0.459
3	−2.453	6.908	−14.024	15.824
4	−0.706	2.027	−4.053	4.586
5	−0.400	0.949	−1.953	2.208
6	0.067	−0.131	0.270	0.307
7	−1.576	4.681	−9.119	10.371
8	−0.426	1.341	−2.570	2.930
9	−2.093	7.623	−14.298	16.338
10	−0.181	0.867	−1.617	1.844
11	−0.487	1.376	−2.748	3.112
12	−0.839	2.242	−4.462	5.064

Table 8.1: Stereo SAR Measurements: Exact Input

results does not seem to be correlated to any point or image characteristics. The ΔZ error component is always the largest component, followed by the ΔY error component; ΔX is invariably the smallest. The sizes of the errors in each component are correlated e.g., if the ΔZ component is relatively large, then the other components will be relatively large.

Table 8.2 shows how the SAR stereo assessment is influenced by varying start-point. As can be seen, there is very little difference. The largest RMS variation was for point 10 and was 0.172 m, and the average variation 0.03 m.

A study to see how the errors are affected by an increase in the near-range and Doppler errors was then carried out. In this case, the errors were introduced firstly into the Image 1 input data alone, then into the Image 7 input data alone, and finally into both sets of input data. All the other input data were kept to the *exact* definition with a start-point of GCP 2.

8.3 SIR-B Stereo: Doppler Error Analysis

Figures 8.1, 8.2, 8.3 and 8.4 show the error components for a percentage increase in Doppler error from 0 to 10% in the Image 1 input data alone. As can be seen from the plots, the component errors increase dramatically with increased Doppler error, showing their sensitivity to this change. The ΔZ component is most sensitive, followed by the ΔY and finally the ΔX error component.

Stereo SAR Measurements (m)				
Various Start-Points: Exact Input				
GCP No	Δ X	Δ Y	Δ Z	RMS Error
Start-Point 1				
1	−1.609	4.349	−8.851	9.992
2	0.142	−0.162	0.401	0.455
3	−2.455	6.911	−14.032	15.833
4	−0.706	2.027	−4.053	4.586
5	−0.400	0.950	−1.953	2.208
6	0.067	−0.131	0.268	0.306
7	−1.576	4.681	−9.119	10.371
8	−0.426	1.340	−2.569	2.929
9	−2.087	7.616	−14.279	16.317
10	−0.233	0.936	−1.771	2.017
11	−0.487	1.376	−2.748	3.112
12	−0.841	2.245	−4.469	5.071
Start-Point 9				
1	−1.618	4.362	−8.883	10.028
2	0.125	−0.139	0.346	0.393
3	−2.455	6.911	−14.032	15.833
4	−0.703	2.025	−4.047	4.580
5	−0.401	0.951	−1.957	2.212
6	0.063	−0.126	0.257	0.293
7	−1.573	4.677	−9.110	10.361
8	−0.426	1.340	−2.570	2.930
9	−2.093	7.623	−14.298	16.338
10	−0.233	0.935	−1.769	2.014
11	−0.489	1.378	−2.753	3.117
12	−0.839	2.242	−4.462	5.064
Start-Point 12				
1	−1.610	4.350	−8.854	9.995
2	0.143	−0.163	0.403	0.458
3	−2.455	6.911	−14.032	15.833
4	−0.705	2.027	−4.052	4.585
5	−0.400	0.949	−1.952	2.207
6	0.064	−0.127	0.259	0.295
7	−1.575	4.681	−9.120	10.371
8	−0.426	1.340	−2.570	2.930
9	−2.093	7.623	−14.298	16.338
10	−0.233	0.936	−1.770	2.016
11	−0.487	1.375	−2.747	3.110
12	−0.831	2.234	−4.442	5.041

Table 8.2: Stereo SAR Measurements: Exact Input, Various Start-Points

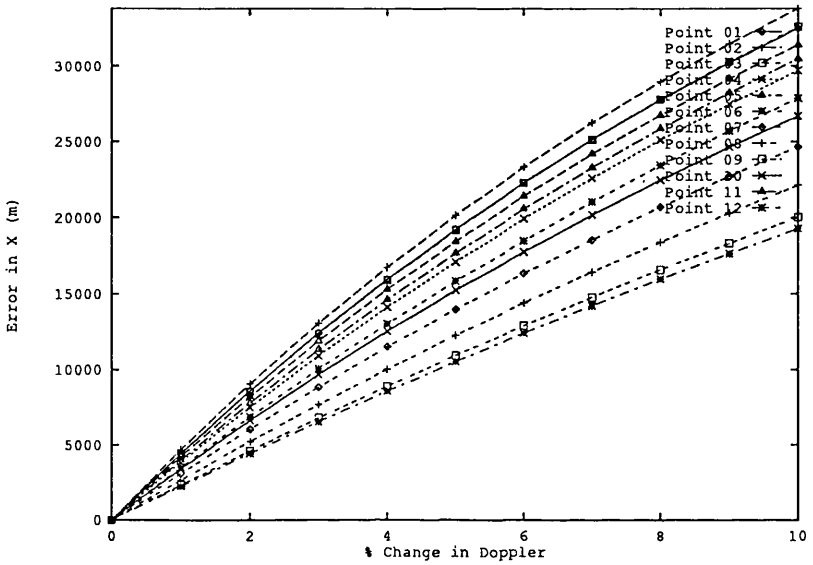

Figure 8.1: Dependence of x-Component of Result on Percentage Error in Doppler for Image 1

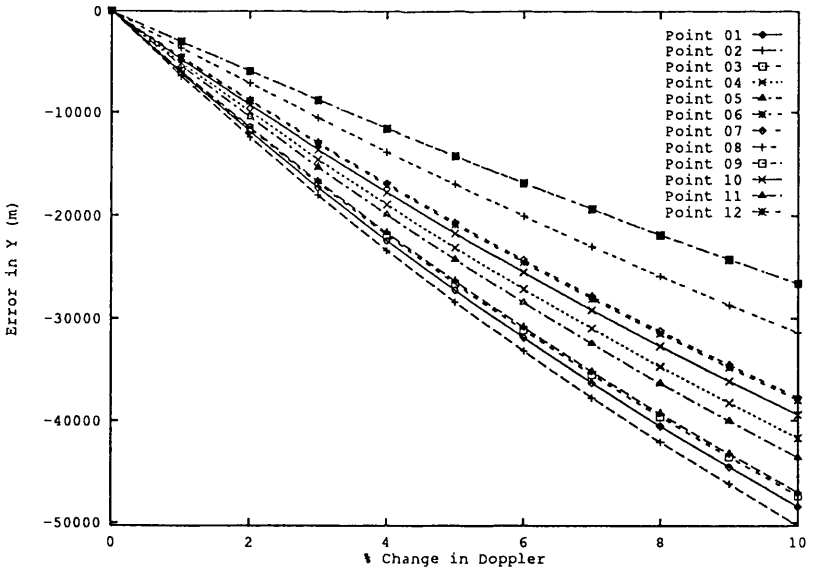

Figure 8.2: Dependence of y-Component of Result on Percentage Error in Doppler for Image 1

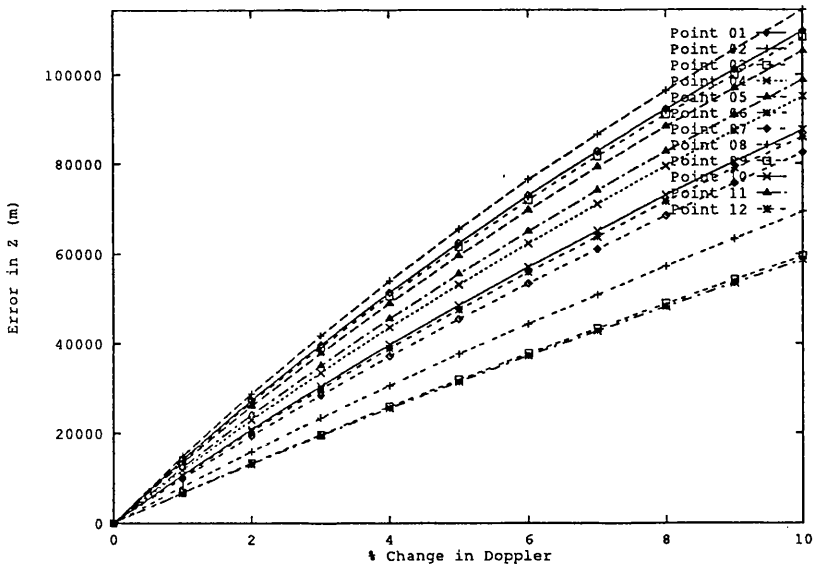

Figure 8.3: Dependence of z-Component of Result on Percentage Error in Doppler for Image 1

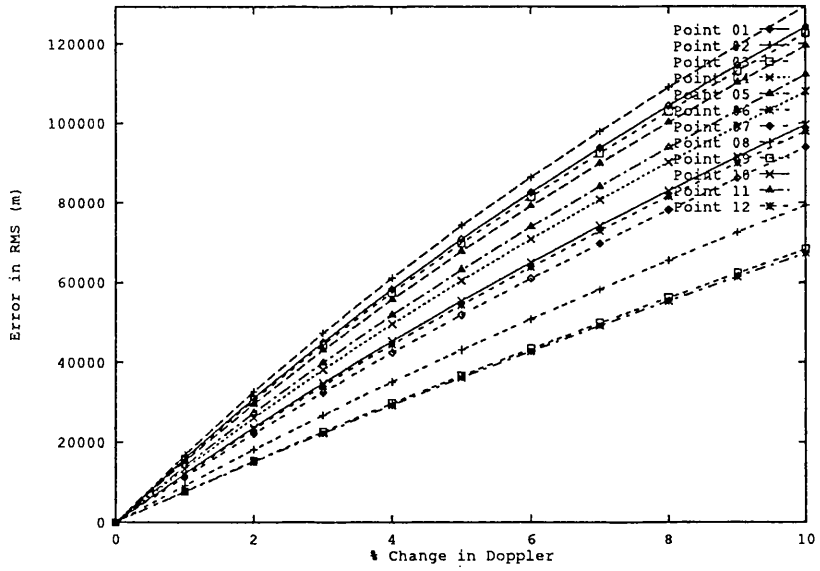

Figure 8.4: Dependence of RMS Result on Percentage Error in Doppler for Image 1

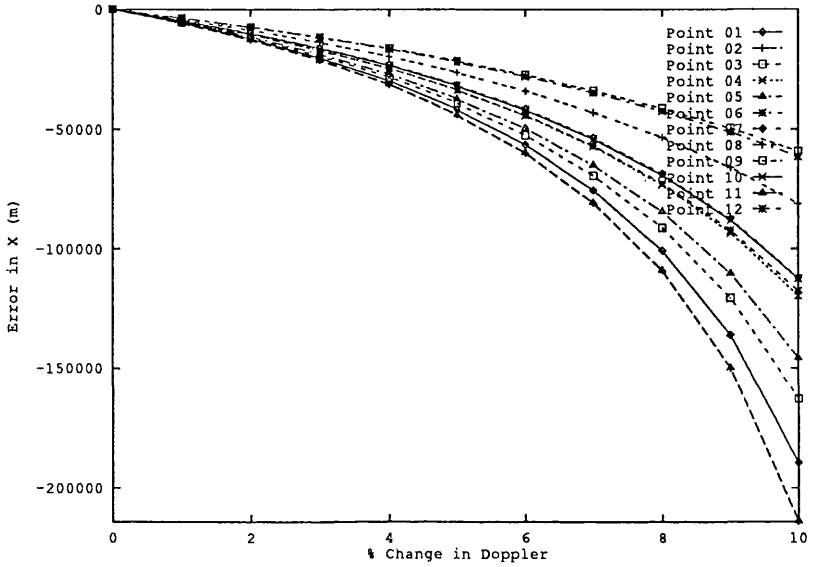

Figure 8.5: Dependence of x-Component of Result on Percentage Error in Doppler for Image 7

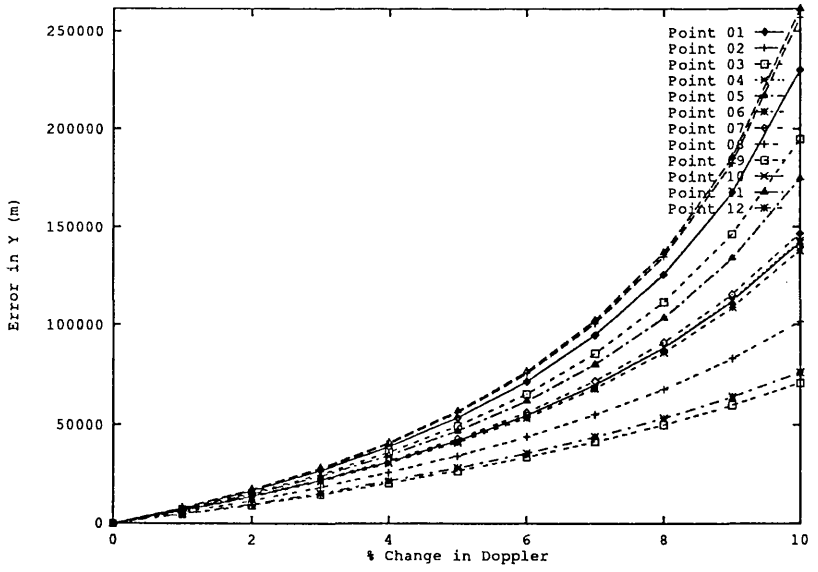

Figure 8.6: Dependence of y-Component of Result on Percentage Error in Doppler for Image 7

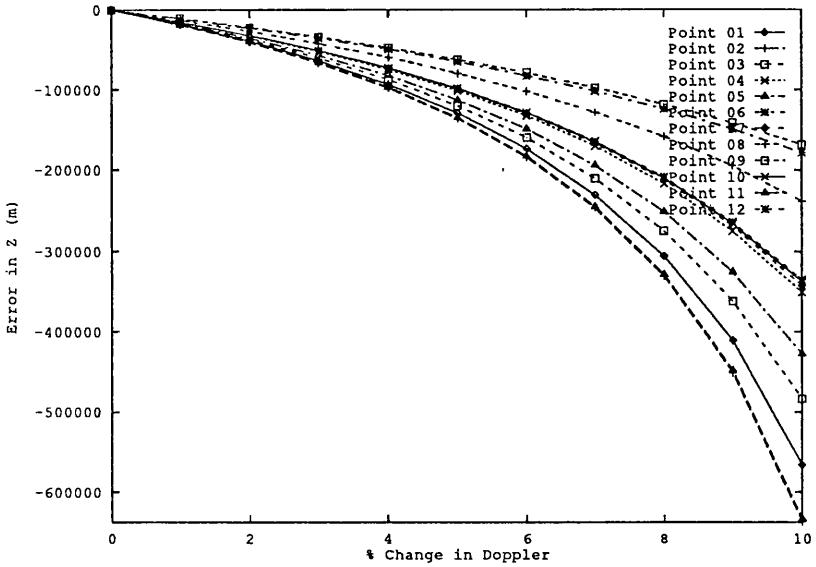

Figure 8.7: Dependence of z-Component of Result on Percentage Error in Doppler for Image 7

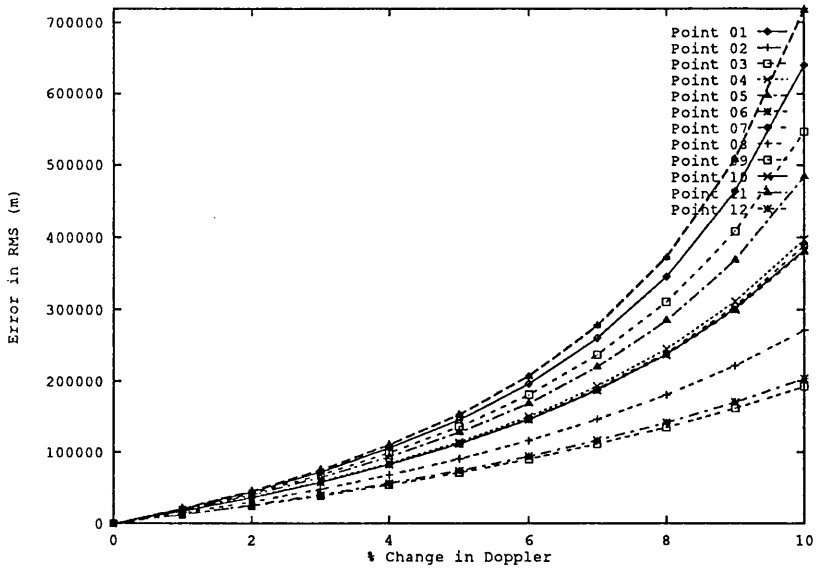

Figure 8.8: Dependence of RMS Result on Percentage Error in Doppler for Image 7

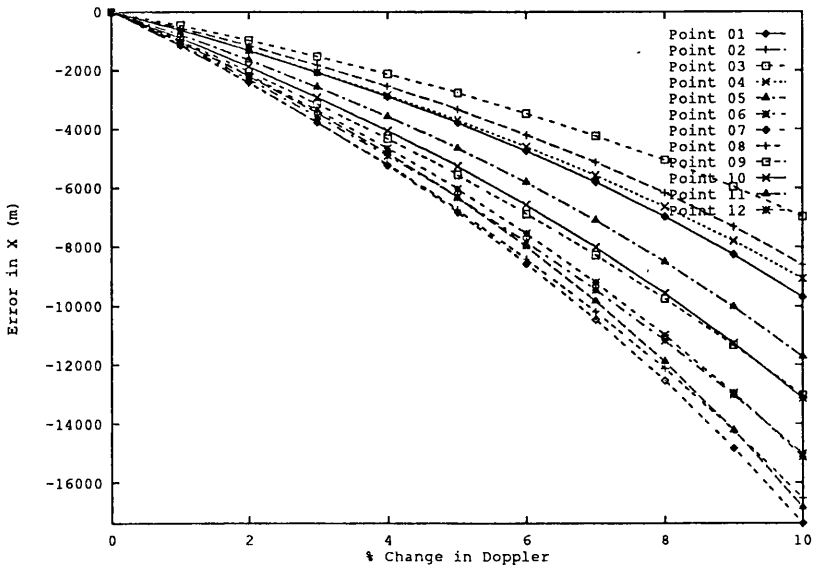

Figure 8.9: Dependence of x-Component of Result on Percentage Error in Doppler for Both Images

Figures 8.5, 8.6, 8.7 and 8.8 show the results of this part of the study for an increase in the Doppler error in the input data of Image 7. The results here are of the same form as those of Image 1, i.e. the error components are very sensitive to increased Doppler error and the relative sizes of the components of the error follow the same pattern. The plots show that a change in the Image 7 Doppler input data has a much more detrimental effect than the same change in the Image 1 data. It should be noted that the signs of the error components are reversed between images.

Figures 8.9, 8.10, 8.11 and 8.12 show the results of increasing the Doppler error in both image datasets by the same amount. It can be seen that, although the resulting errors are very large in each error component, they are not as bad as for the individual cases. The plots follow the pattern of those of increasing the error in Image 7 input alone and hence demonstrate that the errors associated with this image are dominant.

An example of changing the Doppler error in both images is shown in Table 8.3. In this case, the errors are in the opposite sense and, as can be seen from the Table, the errors combine to give much poorer accuracy.

These results indicate that the SAR stereo solutions are very sensitive to Doppler errors. If the errors occur for both images in the same sense, then the algorithm does seem to manage to compensate to some extent. If the errors are in the opposite sense, then the

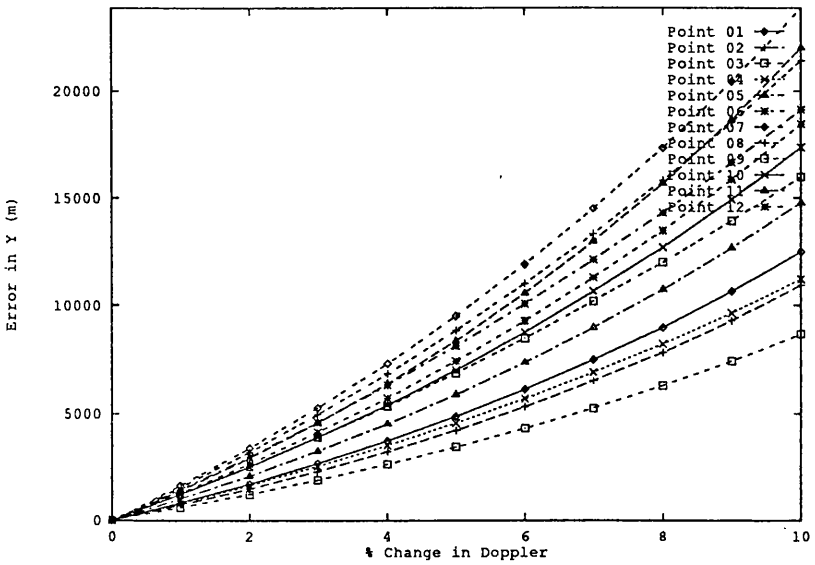

Figure 8.10: Dependence of y-Component of Result on Percentage Error in Doppler for Both Images

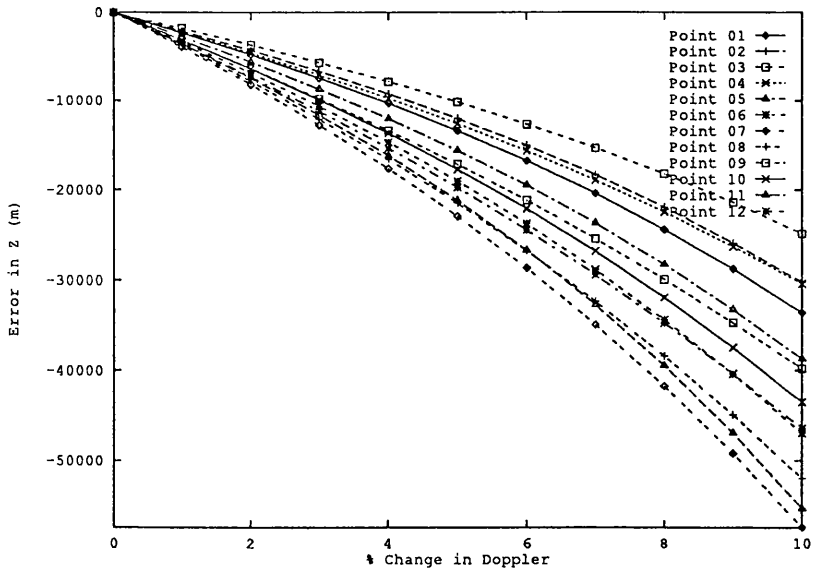

Figure 8.11: Dependence of z-Component of Result on Percentage Error in Doppler for Both Images

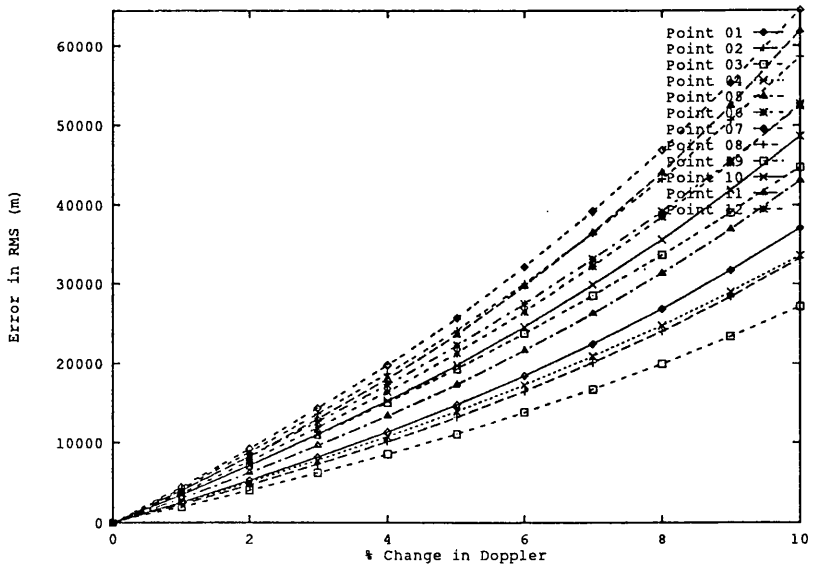

Figure 8.12: Dependence of RMS Result on Percentage Error in Doppler for Both Images

Stereo SAR Measurements (m)					
Variation of Doppler (%) for both images Exact Input, GCP 12, Opposite directions					
Doppler Change (%)		ΔX	ΔY	ΔZ	RMS
Image 1	Image 7				
0.000	−2.000	8245.302	−10613.456	25011.121	28393.426
1.000	−1.000	7579.785	−9770.885	22785.401	25924.850
2.000	0.000	6870.209	−8874.094	20427.330	23307.190

Table 8.3: Stereo SAR Measurements: Doppler Variation for both Images — Opposite Directions, GCP 12

errors are compounded. In all cases, the ΔZ error component is most sensitive to these errors, followed by the ΔY error component.

8.4 SIR-B Stereo: Near-Range Error Analysis

A study of the change in near-range error was then carried out. Here again, the error was introduced into Image 1 data alone, then Image 7 alone, and then into both images. For all these studies, the *exact* input data were used with a start-point of GCP 2. The near-range was increased each time.

Figures 8.13, 8.14, 8.15 and 8.16 show the results of this part of the study for a near-range change in Image 1 only. As can be seen, the plots show a linear response in all three error components. The Z error component was again the most sensitive to change, followed

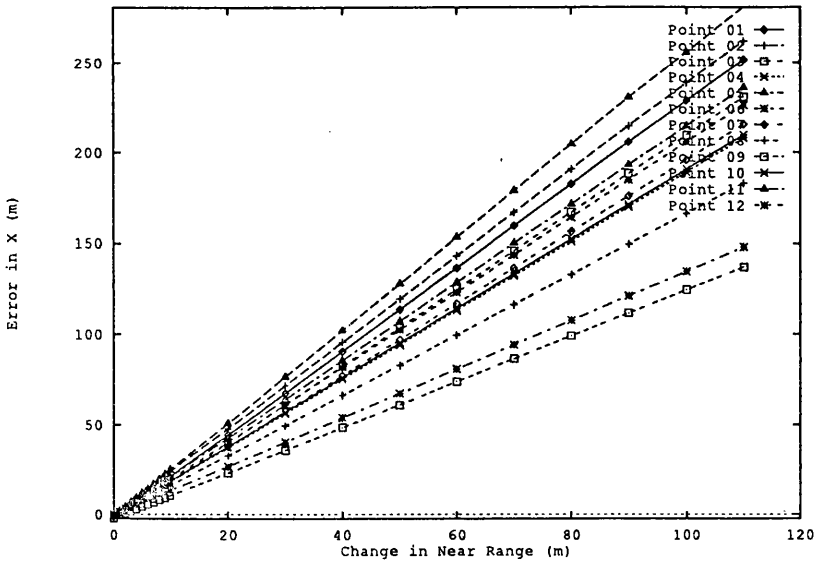

Figure 8.13: Dependence of x-Component of Result on Error in Near-Range for Image 1

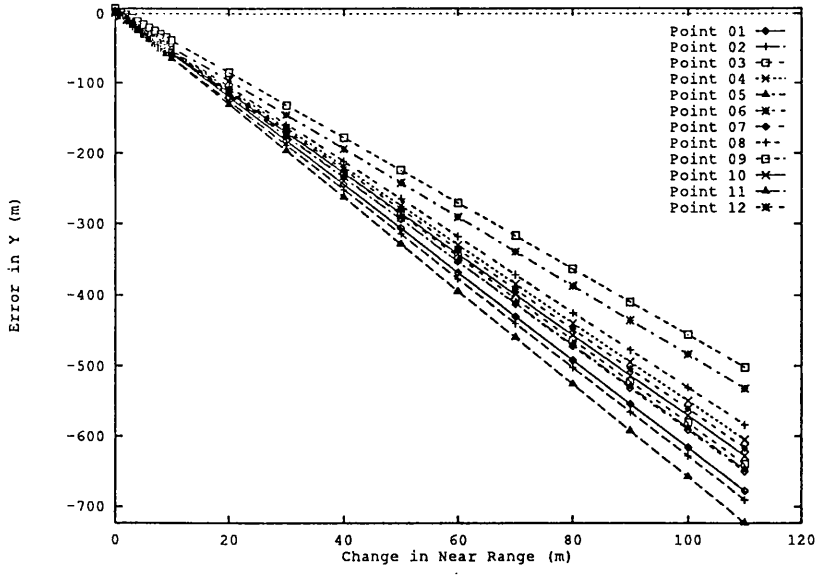

Figure 8.14: Dependence of y-Component of Result on Error in Near-Range for Image 1

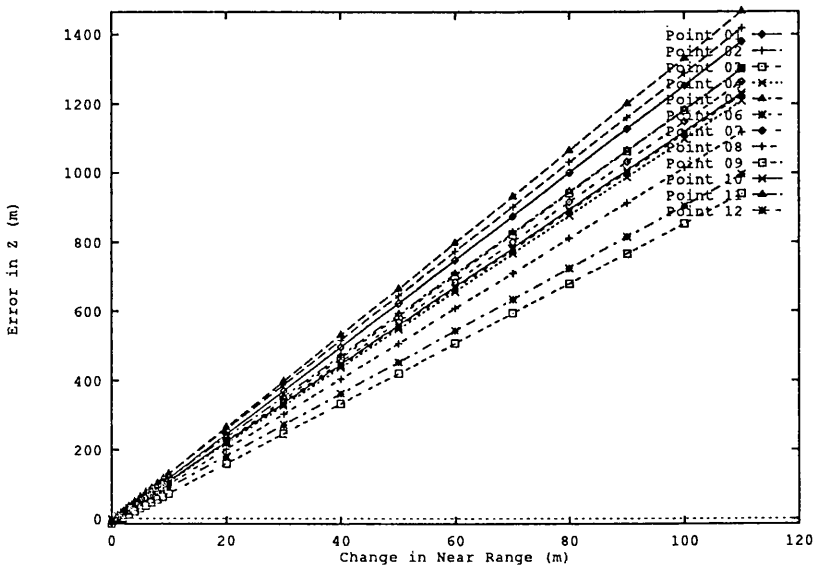

Figure 8.15: Dependence of z-Component of Result on Error in Near-Range for Image 1

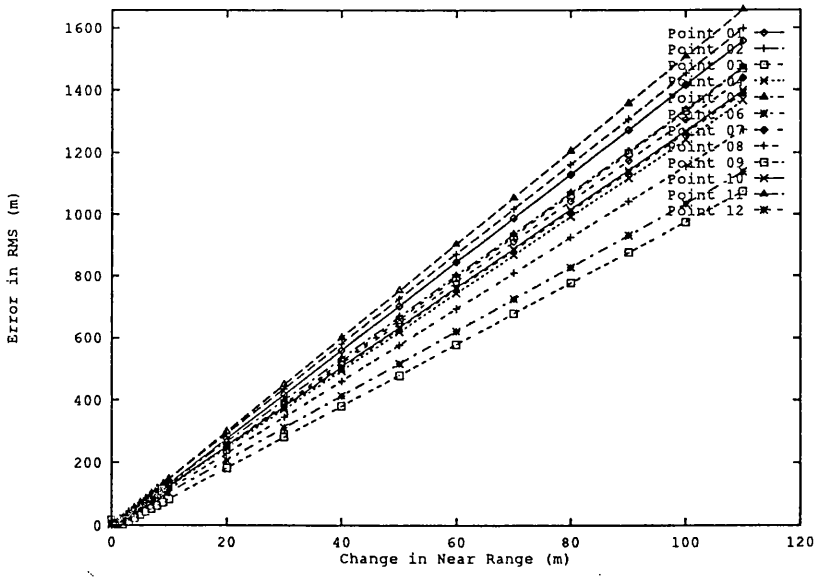

Figure 8.16: Dependence of RMS Result on Error in Near-Range for Image 1

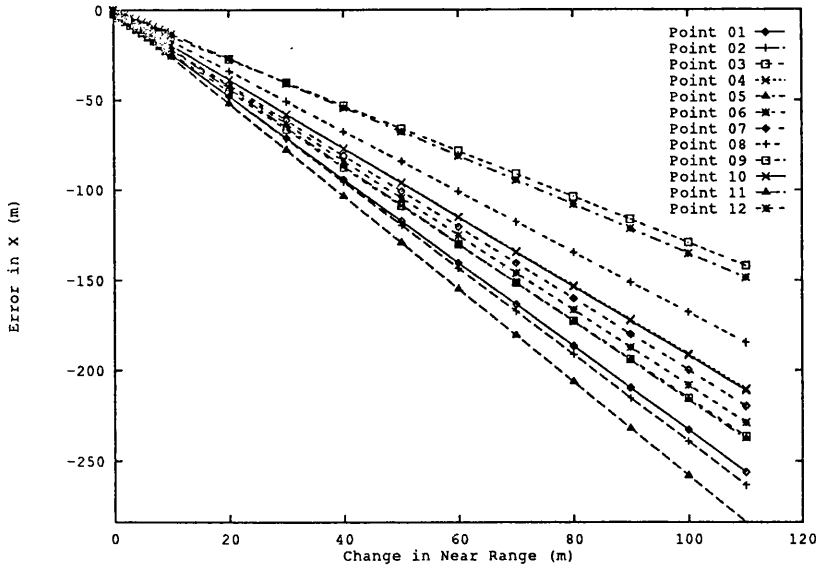

Figure 8.17: Dependence of x-Component of Result on Error in Near-Range for Image 7

by the Y error component.

Figures 8.17, 8.18, 8.19 and 8.20 show the results for a change in near-range in Image 7 only. These results follow the same pattern as those of Image 1, i.e. they are linear and the Z error component is the most sensitive to this change; this is followed by the Y error component. For each image, the magnitude of the errors are very similar but the sign is different.

Table 8.4 shows examples of results for changing the near-range error in *both* images. If the near-range error in each image is the same in both magnitude and sign, then *no* extra error is introduced: the resulting error is the sum of the 'single-image' errors shown in the previous figures. Since the magnitudes of the 'single-image' errors are very similar but of different sign, the combined effect is small. However, if the 'near-range' errors have the same magnitude but are of different sign, then larger errors result.

8.5 SIR-B Stereo: Average Data Analysis

Table 8.5 shows the results of the stereo assessment for average input data, i.e. the average range pixel spacing values for each image were used. As can be seen by comparison with Table 8.1, the errors are greatly increased. Here again, the Z error component is largest, followed by the Y error component. Throughout this stereo study, the Z error has always

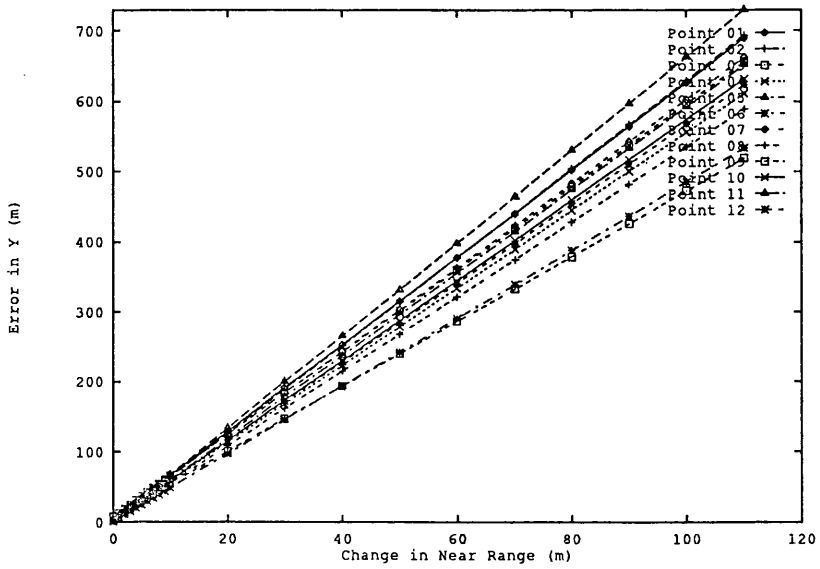

Figure 8.18: Dependence of y-Component of Result on Error in Near-Range for Image 7

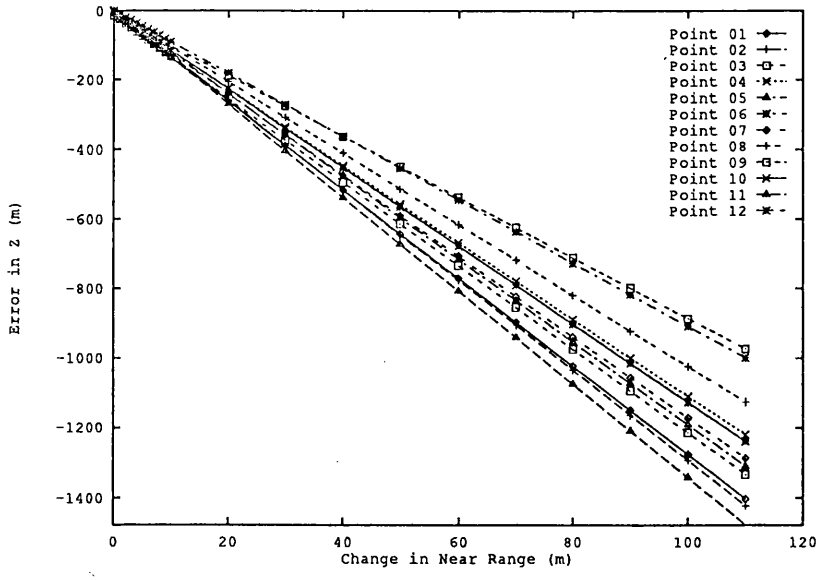

Figure 8.19: Dependence of z-Component of Result on Error in Near-Range for Image 7

Stereo SAR Measurements (m)					
Variation of Near-range (m) for both images Exact Input, GCP 8					
Near-range Change (m)		ΔX	ΔY	ΔZ	RMS
Image 1	Image 7				
0.000	0.000	−0.426	1.341	−2.570	2.930
100.000	100.000	−0.426	1.341	−2.570	2.930
200.000	200.000	−0.426	1.341	−2.570	2.930
300.000	300.000	−0.426	1.341	−2.570	2.930
400.000	400.000	−0.426	1.341	−2.570	2.930
500.000	500.000	−0.426	1.341	−2.570	2.930
600.000	600.000	−0.426	1.341	−2.570	2.930
700.000	700.000	−0.426	1.341	−2.570	2.930
800.000	800.000	−0.426	1.341	−2.570	2.930
900.000	900.000	−0.426	1.341	−2.570	2.930
1000.000	1000.000	−0.426	1.341	−2.570	2.930
0.000	0.000	−0.426	1.341	−2.570	2.930
100.000	50.000	83.086	−264.806	506.687	577.717
200.000	100.000	166.459	−530.403	1014.919	1157.193
300.000	150.000	249.689	−795.445	1522.112	1735.483
400.000	200.000	332.791	−1059.952	2028.303	2312.631
500.000	250.000	415.751	−1323.910	2533.469	2888.607
600.000	300.000	498.603	−1587.355	3037.698	3463.511
700.000	350.000	581.212	−1850.148	3540.632	4036.946
800.000	400.000	663.784	−2112.507	4042.823	4609.524
900.000	450.000	746.206	−2374.312	4543.970	5180.912
1000.000	500.000	828.488	−2635.579	5044.106	5751.145
0.000	−300.000	498.603	−1587.355	3037.698	3463.511
100.000	−200.000	498.603	−1587.355	3037.698	3463.511
200.000	−100.000	498.603	−1587.355	3037.698	3463.511
300.000	0.000	498.603	−1587.355	3037.698	3463.511
0.000	−150.000	249.689	−795.445	1522.112	1735.483
100.000	−100.000	332.791	−1059.952	2028.303	2312.631
200.000	−50.000	415.751	−1323.910	2533.469	2888.607
300.000	0.000	498.603	−1587.355	3037.698	3463.511

Table 8.4: Stereo SAR Measurements: Near-range Variation for both Images, GCP 8

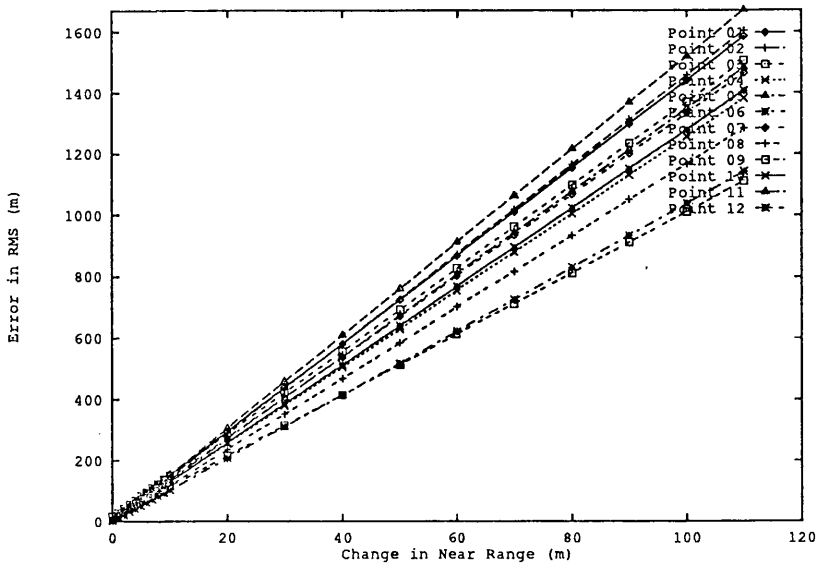

Figure 8.20: Dependence of RMS Result on Error in Near-Range for Image 7

been the greatest; as a general rule, the Y error component has been about one-half the size of the Z error component and the X error component has been about one-third of the size of the Y error component.

It has been shown here that the stereo analysis is very sensitive to error. If the input data are known accurately, then very good results can be obtained — as shown in Table 8.1. In this table, GCP 6 gave the best result. In Table 8.6 (which actually summarises results given previously) an assessment is made of the effect of changing the slant-range pixel spacing for GCP 6 of Image 1 by an amount of 1 mm. As can be seen from this table, this change has a small but noticeable effect on both the Image-to-Object and Object-to-Image geocoding. However, the effect on the stereo analysis is very marked: the Z and Y component errors are increased by a factor of ≈ 34 and the X error component by ≈ 20. The RMS error jumps from 0.307 m to 10.469 m, demonstrating how sensitive the stereo algorithm is to such variations. (It should be remembered that Leberl [Leberl, 1990] reports that the photogrammetric approach to SAR/SAR stereo is also very sensitive to error.)

GCP 6 is located at line number 1042; if there is a slant-range spacing error of 1 mm, this will result in an error of ≈ 1 m in the assessed slant-range, which is equivalent to introducing a 1 m error in the near-slant-range. Figure 7.12 indicates that an error of 1 m in the near-slant-range will result in a very small RMS error (less than 1 m) in Image-to-Object geocoding. Similarly, Figure 7.25 shows that a 1 m error in near-slant-range will also

Stereo SAR Measurements (m)				
Average Input				
GCP No	Δ X	Δ Y	Δ Z	RMS Error
1	274.722	−739.293	1505.121	1699.240
2	113.617	−298.862	613.526	691.839
3	−42.205	117.088	−238.208	268.764
4	87.008	−252.987	505.188	571.654
5	−30.249	82.746	−166.415	188.297
6	136.892	−491.545	920.227	1052.223
7	79.997	−241.369	469.113	533.597
8	144.717	−461.150	882.397	1006.095
9	−18.754	68.601	−128.575	146.933
10	−139.247	417.256	−818.581	929.283
11	158.857	−408.210	826.888	935.743
12	−912.065	2490.526	−4943.887	5610.401

Table 8.5: Stereo SAR Measurements: Average Input

result in a very small RMS error (less than 1 m) in Object-to-Image geocoding. However, Figure 8.16 shows that an error of 1 m in near-slant-range will result in an $\approx$ 10 m RMS error in the stereo assessment. Table 8.6 just highlights these results.

The question then arises as to the accuracy with which slant-range pixel spacing can be expected to be given. In Table 8.1, some GCPs have RMS errors greater than 10 m, indicating that perhaps the calculated range pixel spacings were not assessed to the required accuracy of 1 mm or better. The ERS-1 error budget discussed in Section 3.7 indicates that a range error of $\approx$ 20 m can be expected for the precise orbit. Based on the results obtained in this work, an RMS error of the order of 200 m for stereo height assessment might be expected, considering the error to be present in both images and in the opposite sense (i.e., the worst case). However, as also stated in Section 3.7, there are as yet no firm details of the UK ERS-1 SAR processor and it is possible that this error figure may be improved upon.

8.6 Summary

This research has shown the accuracy and robustness with which the algorithms can operate. Using the *exact* input, very accurate results were obtained; in some cases sub-metre accuracy was obtained. The study into the effect of differing iteration start-point demonstrated the robustness of the algorithm, as, no matter how inaccurate the start-point, the

Demonstration of Range Pixel Spacing Dependency using Image 1 GCP 6					
Process	Range Pixel Spacing (m)	ΔX (m)	ΔY (m)	ΔZ (m)	RMS (m)
Geocoding Image-to-Object	10.748	159.666	−342.461	−230.234	442.471
	10.747	160.623	−342.350	−229.538	442.373
		ΔI	ΔJ		RMS
Geocoding Object-to-Image	10.748	−31.632	7.042		32.406
	10.747	−31.632	7.140		32.428
		ΔX	ΔY	ΔZ	RMS
Stereo	10.748	0.067	−0.131	0.270	0.307
	10.747	−1.338	4.915	−9.177	10.469

Table 8.6: Demonstration of Range Pixel Spacing Dependency for Geocoding and Stereo using Image 1 GCP 6

algorithm still converged onto almost precisely the same result. For the *exact* input, the ΔX error component varied from sub-metre to less than 3 m, the ΔY error component from sub-metre to less than 8 m, and the ΔZ error component from varied here from sub-metre to less than 15 m.

In the Doppler and near-range error analysis, it was shown that the error components kept the same distribution, i.e. ΔX being the smallest and ΔZ the largest. It was shown that the algorithms are very sensitive to input inaccuracies, especially in the Doppler input. In all cases, Image 7 was the most susceptible to inaccuracy. The sign of the error in each image is an important factor: if the errors are in the same sense then the effect is much smaller than if they are in the opposite sense, when the effect is compounded.

The investigation also showed how sensitive the algorithm is to slant-range pixel spacing errors by demonstrating, for one GCP, the effect that a 1 mm change in range pixel spacing had on the overall result.

To summarise, this investigation has shown that a point can be identified to a very good accuracy providing that the input data are themselves accurate. However, as with other SAR stereo techniques, it has also shown that the algorithm is very sensitive to error, particularly in Doppler.

8.7 Comparison with Leberl's Results

As mentioned in Chapter 4, Leberl and his co-workers have studied the SIR-B imagery used in this work [Leberl *et al.*, 1986b]. A photogrammetric approach to stereo height extraction

Control Points	Intersection Angle °	Co-ordinate Errors (m)			Point
		North	East	Height	Error (m)
2	6	117	124	155	133
2	23	44	100	178	120
2	28	127	134	124	128
4	6	117	99	113	109
4	23	45	81	67	66
4	28	104	121	96	107
13	6	106	106	125	112
16	23	44	75	53	58
17	28	91	100	73	88

Table 8.7: Stereo Co-ordinate Accuracies from SIR-B Mount Shasta Imagery [Leberl *et al.*, 1986b]

was applied. There, 32 GCPs were identified by Leberl in Images 1, 3 and 7. The actual locations of these GCPs are not given. The root mean square errors they obtained for the resulting stereo models are shown in Table 8.7. It is stated that *four* orbit positions for each image, communicated from the SIR-B mission, were also used. These orbit data were not available to this author. As stated in Chapter 4, these results indicate that the theoretical belief that SAR stereo accuracy should increase with larger intersection angles does not hold.

Leberl created a DEM, of grid interval 30 m, of the Mount Shasta area from 1 : 62500 maps. This was then compared with a DEM obtained from the stereo assessment of Images 3 and 7, the latter DEM being quoted as having a grid interval of 150 m. The RMS height difference between the two DEMs is reported to be ±60 m. However, this author is a bit suspicious of the perspective view of the DEM shown in [Leberl *et al.*, 1986b], supposedly derived from the abovementioned radar images, as it appears to extend beyond the edges of the images stated to have been used.

A detailed comparison of the work of this author and that of Leberl, for the Mount Shasta imagery, would not be a fair comparison of the analytic and photogrammetric methods of terrain height assessment, since Leberl had access to important further data i.e., the four orbit positions per image. This author could not utilise Image 3; however, Leberl claims to have used this image in all his calculations. The extra orbit data were perhaps the redeeming factors.

Images 1 and 7 have an intersection angle of 28°; hence, the coordinate error shown in Table 8.7 can be compared to those obtained by this author. The best results of the

author's work are much better than those given in the table. This is, of course, to be expected, due to the way in which the required *exact* input data had to be generated. The average results of this work are much worse, which is again to be expected, as the *average* input data were known to be very inaccurate. It would not be prudent to speculate on the results that would have been obtained had the extra orbit data, used by Leberl, been available to this author.

However, from Table 8.7, it can be seen that the best height accuracy obtained from Images 1 and 7 using a photogrammetric stereo height assessment method is 73 m, and the North and East coordinate errors are larger at 91 m and 100 m respectively. It should be noted that 32 GCPs were required to achieve these results.

Chapter 9

Concluding Remarks

The aim of this research was to demonstrate object-to-image and image-to-object geocoding in practice and to investigate how the geocoding algorithms are affected by errors in the input data. This work has also shown how a ground position can be located in X, Y and Z using SAR/SAR stereo. Here, a novel technique which employs only the range and Doppler equations for each image was devised and assessed. The effect of input data error on this method was also to be studied.

The aims of the research have been met, though they have not been demonstrated as fully as the author would have liked. This was due to the lack of suitable image and header data, as discussed in Section 1.3. The work was carried out in preparation for the reception of ERS-1 imagery which will, for the first time, produce detailed ephemeris data to accompany the images. It had been hoped that some ERS-1 data would be available towards the end of this study but, as stated in Section 1.3, ERS-1 has still to be launched at this time of writing.

However, this author is not alone in being short of suitable data: many workers in the field have had to resort to image simulation in order to perform complete image study. This author preferred to use real SAR imagery but then be confined to dealing with only individual points of data.

Image-to-object and object-to-image geocoding algorithms have been described in detail in Chapter 3 and the results of their application and error analysis are recorded in Chapter 7. For this and the SAR stereo investigations, it was necessary to establish the orbit of the imaging sensor. This proved to be a surprisingly difficult task, as it required

conversion between several co-ordinate and time systems. This procedure is detailed in Chapter 5.

The study of image-to-object geocoding has shown that, provided the input data are accurate and the terrain height can be accounted for, an RMS error of better than 700 m, and down to ≈ 32 m, is achievable. The response of this type of geocoding algorithm to increased error in the near-range and Doppler data is linear in each error component, at least for the imagery used here. On an operational basis, it is known that this type of geocoding will give poor results for images of all but flat terrain. The ground covered by a whole image will operationally be described by one local ellipsoid. If no ground height data are available, and DEMs are scarce, then this type of geocoding could be used.

However, in remote sensing, an object-to-image mapping is preferable (see Section 3.8). Hence, object-to-image geocoding is important, even if no terrain height data are available. The height, even here, could be assessed from a local ellipsoid.

The study of object-to-image geocoding showed variable results, with RMS errors for accurate input data varying from 2 to, at worst, 700 pixels. However, the RMS errors generally lay in the range 20–50 pixels. This part of the research was greatly hampered by the lack of detailed Doppler data, as discussed in Section 7.3. It has been of concern to the author that, in the ERS-1 preparation studies being carried out by the various participating organisations, no-one has addressed the subject of the rate of change of Doppler with time or range. The ERS-1 SAR data will be processed to give a zero Doppler image; however, the *rate of change* of Doppler is not necessarily also zero. Doppler blocking could also produce a rate-of-change error. The author has not received a satisfactory answer to her queries to the relevant organisations regarding this topic.

The error study for this type of geocoding has shown that increasing the error in the near-range data has an almost negligible affect on the ΔI error component, whereas the ΔJ component is greatly affected. An increase in the error of the Doppler data affects the errors in a less predictable manner than that of near-range errors. The responses to the error could be described, on the whole, as near-linear.

The results of the image-to-object geocoding demonstrated the direct correlation between errors in the satellite position and velocity and the resulting geocoding errors. However, the results also showed that the effects of these errors were not predictable. The satellite position and velocity errors would also affect the object-to-image geocoding but,

due to the iterative nature of the solution of this type of geocoding, it is not possible to quantify these effects. It would not really be prudent to comment on the theoretical error analysis given in the error budget (Section 3.7) with regard to the satellite position and velocity errors predicted for ERS-1, as these errors are not comparable with those of this study. The errors of the error budget were also 'stand-alone', i.e. only one source of error was considered at a time. The errors of this study at best contain effects due to satellite position and velocity, as well as effects due to the choice of start point and iteration method; it is worth re-emphasising that this study has shown that the magnitude of the geocoding errors are not predictable from the satellite position and velocity errors. Since most operational geocoding systems employ a polynomial description of the satellite trajectory, it must be remembered that the position and velocity error of the polynomial will be worse than the individually-quoted errors.

Studies into the selection of iteration start point for each type of geocoding were rather inconclusive. In these studies it was shown that even giving the 'answer' as a start point (and you cannot get any more accurate than that), the resulting geocoding accuracy was not necessarily better than using a more inaccurate start point. The presence of other errors obviously has a noticeable but unpredictable effect.

In operational geocoding, resampling the image data will be necessary. Although not demonstrated here, an investigation into the effect of resampling on simulated single-look, detected data [Clark *et al.*, 1989] showed that the original image statistics were not conserved following resampling. The image statistics were distorted and negative values were generated (for wholly positive data). This could have serious consequences for further analysis of this resampled imagery and should always be considered when handling this type of SAR imagery.

It should be borne in mind that SAR imagery is affected by a number of radiometric and geometric distortions which, in many applications, complicate or even prevent effective utilisation of the imagery. While geocoding can correct the location of a feature on the Earth surface, provided that a DEM of sufficient accuracy is available, it cannot reconstruct radiometric properties without further information. For example, objects that would be detectable in a flat area may not be detectable in a foreshortened region, even after terrain correction. It should also be noted that geocoding will degrade radiometric image quality due to the additional resampling of the image. Hence, great care must be taken in the

analysis of a geocoded product.

The study of SAR/SAR stereo has shown that the ground location, including particularly height, can be found accurately using a technique, thought to be novel, that employs the solution of the range and Doppler equations for points in both images. If the input data can be given to a sufficient accuracy, results obtained using this method can rival those obtained from interferometry. The method described in Section 4.3 is simple to understand and implement, whereas interferometry is very complicated and can only be used for very specific stereo cases. The SAR/SAR stereo method described herein can be used for all stereo cases provided the data to describe the range and Doppler are available. However, it has also been shown that the algorithm is very sensitive to error, and especially to error in the Doppler. It has been shown that, for a particular GCP, an error in the range pixel spacing of 1 mm in one of the images, which results in a slant-range error of ≈ 1 m, caused a change in the RMS error of the point location from 0.307 m to 10.469 m. (It should be remembered that Leberl [Leberl, 1990] reports that the photogrammetric approach to SAR/SAR stereo is also very sensitive to error.) It was unfortunate that no precise image data were available to test this method further with accurate input data; this method could give accurate results with little effort.

If accurate SAR/SAR automatic image matching methods were available (and work is being carried out on this topic at UCL and other institutions), then this method could be applied without the need for operator intervention, or perhaps only in a checking rôle, and a DEM could be constructed automatically.

In both geocoding and SAR/SAR stereo studies, the results are dependent on the accuracy obtained in solving the non-linear equations inherent in this work. Again, the author is concerned that other workers in the field are not giving this problem sufficient importance. Some establishments engaged in geocoding studies are not using standardised, well-tested, routines such as those described in Section 3.4.5, but are coding their own. This author has seen forecasts of ERS-1 geocoding errors, none of which include any error due to the solution of these non-linear equations (all expect an exact solution!).

Geocoding has been carried out at various establishments e.g., the American Jet Propulsion Laboratory and the German DLR, using Seasat and other SAR data, with a good deal of success despite the lack of accurate ephemeris data. The limiting factor is the pixel size of the DEM: it does not matter how good the SAR image or header data are if the DEM

has a relatively large pixel size, is inaccurate or (at worst) not available—the geocoded product will be deficient. ERS-1, with its anticipated accurate ephemeris data, should, using the algorithms described and assessed in this work, provide accurate geocoded products provided that a suitable DEM is available. The ERS-1 error budget study (see Section 3.7) indicates that geocoding accuracies of ≈ 200 m can be expected. This work indicates that this figure is unlikely to be optimistic as a number of GCPs had geocoding accuracies of less than this figure despite the known deficiencies in the data used in this study. As also stated in Section 3.7, it is expected that the geocoding error budget for ERS-1 will be improved upon once the details of the UK ERS-1 SAR processor are known precisely. Current geocoding work at the German DLR also indicates that better accuracies than these can be anticipated.

ERS-1 SAR data should be an excellent test for the SAR/SAR stereo height assessment work. If image matching can be carried out, DEMs could be constructed easily using the algorithm developed in this study. The DEM pixel spacing will depend on the accuracy with which the required data are known. However, a DEM with a pixel spacing of 200 m or worse would be preferable to no DEM at all, which is the current status for many parts of the world.

Despite the previously discussed limitations of SAR imagery and the problems encountered with the SIR-B data used in this work, it can still be appreciated that, with ERS-1 and the other SAR-carrying platforms to be launched in the 1990s, we are moving towards a time when a useful definition of global topography is a good possibility.

The aims at the outset of this research work have been met, though the application of the algorithms developed here need to be applied to better datasets. ERS-1 should provide these and, since this study was in preparation of the reception of ERS-1 data: we are ready — where's the data?

Bibliography

[Barber, 1985] B. C. Barber. Review article. Theory of digital imaging from orbital synthetic aperture radar. *International Journal of Remote Sensing*, 6(7):1009–1057, 1985.

[Blom, 1988] R. G. Blom. Effects of variation in look angle and wavelength in radar images of volcanic and aeolian terrains, or now you see it, now you don't. *International Journal of Remote Sensing*, 9(5):945–965, 1988.

[Bloom *et al.*, 1988] A. L. Bloom, E. J. Fielding, and X. Fu. A demonstration of stereophotogrammetry with combined SIR-B and Landsat TM images. *International Journal of Remote Sensing*, 9(5):1023–1038, 1988.

[Bracewell, 1978] R. N. Bracewell. *The Fourier Transform and its Applications.* McGraw-Hill, 1978.

[Brill, 1987] M. H. Brill. Triangulation from optical and SAR images using direct linear transformations. *Photogrammetric Engineering and Remote Sensing*, 53(8):1097–1102, August 1987.

[Buchroithner, 1987] M. F. Buchroithner. User requirements for geocoded sar imagery experiences form radargrammetric application studies. In *Proceedings of the First International Workshop on Image Rectification Techniques for Spaceborne Synthetic Aperture Radar*, pages 89–91. GEOSAR Working Group, Institute for Image Processing and Computer Graphics, Graz, Austria, January 1987.

[Chang and Curlander, 1989] C Y Chang and J. C. Curlander. Doppler centriod estimation ambiguity for synthetic aperture radars. *IGARSS'89 12th Canadian Symposium on Remote Sensing.*, pages 2567–2571, July 1989.

[Chew, 1990] S. C. Chew. Validation of geocoded ERS-1 SAR data. Technical report, University College London, 1990.

[Clark *et al.*, 1989] C. Clark, A. Hendry, and A. Sowter. Resampling and SAR image statistics. In *Proceedings of the Second International Workshop on Image Rectification Techniques for Spaceborne Synthetic Aperture Radar*, pages 19–22. GEOSAR Working Group, Institute for Image Processing and Computer Graphics, Graz, Austria, January 1989.

[Craubner, 1989] A. Craubner. Mapping of a rectangular grid, defined within a SAR slant range image to specified cartographic projections. In *Proceedings of the Second International Workshop on Image Rectification Techniques for Spaceborne Synthetic Aperture Radar*, pages 11–14. GEOSAR Working Group, Institute for Image Processing and Computer Graphics, Graz, Austria, January 1989.

[Curlander *et al.*, 1987] J. C. Curlander, R. Kwok, and S. S. Pang. A post-processing system for automated rectification and registration of spaceborne SAR imagery. *International Journal of Remote Sensing*, 8(4):621–638, 1987.

[Curlander *et al.*, 1989] J. Curlander, W. Kober, and F. Leberl. SAR Image – Terrain Database Registration. *IGARSS'89 12th Canadian Symposium on Remote Sensing.*, pages 2487–2490, July 1989.

[Curlander, 1982] J. C. Curlander. Location of spaceborne SAR imagery. *IEEE Transactions on Geoscience and Remote Sensing*, GE-20(3):359–364, July 1982.

[Curlander, 1984] J. C. Curlander. Utilization of spaceborne SAR data for mapping. *IEEE Transactions on Geoscience and Remote Sensing*, GE-22(2):106–112, March 1984.

[Diefallah, 1988] M. A. Diefallah. A proposed polynomial for geometric rectification of orbital SAR imagery. *The 16th International Congress of Photogrammetry and Remote Sensing. Comm III.*, 27(B3):160–169, 1988.

[Domik *et al.*, 1984] G. Domik, F. Leberl, and J. Raggam. Differential rectification of SLR-images using map-derived and radar-generated digital elevation models. Technical Report DIBAG Report Number 17, Institute for Image Processing and Computer Graphics, Graz, Austria, February 1984.

[Dowman, 1984] I. J. Dowman. Cartographic and geometric correction. In *Proceedings of the SAR-580 Investigators' Workshop*, pages 125–129. JRC, May 1984.

[Elachi, 1988] C. Elachi. *Spaceborne Radar Remote Sensing: Applications and Techniques.* IEEE Press, 345 East 47th Street, New York, NY 10017-2394, 1988.

[Foley *et al.*, 1990] J. D. Foley, A. van Dam, S. K. Feiner, and J. Hughes. *Computer Graphics Principles and Practice.* Addison-Wesley, 1990.

[Freeman, 1986] A. Freeman. An introduction to SAR theory. Technical Report ITM 86/70, Marconi Research Centre, MSDS Research Laboratory, West Hanningfield Rd, Great Baddow, Chelmsford, Essex, October 1986.

[Friedmann, 1981] D. E. Friedmann. Operational resampling for correcting images to a geocoded format. *Fifteenth International Symposium on Remote Sensing of Environment*, pages 195–212, May 1981.

[Fullerton *et al.*, 1986] J. K. Fullerton, F. Leberl, and R. E. Marque. Opposite-side SAR image processing for stereo viewing. *Photogrammetric Engineering and Remote Sensing*, 52(9):1487–1498, September 1986.

[Gabriel and Goldstein, 1988] A. K. Gabriel and R. M. Goldstein. Crossed orbit interferometry: Theory and experimental results from SIR-B. *International Journal of Remote Sensing*, 9(5):857–872, May 1988.

[GEC-Marconi Research Centre and DIBAG, 1989] GEC-Marconi Research Centre and DIBAG. Study of an error budget for ERS-1 SAR imagery. Technical report, GEC-Marconi Research Centre, UK, and Institute for Image Processing and Computer Graphics, Austria, November 1989.

[Glassner, 1989] A. S. Glassner. *An Introduction to Ray Tracing.* Academic Press, 1989.

[Green, 1985] R. M. Green. *Spherical Astronomy.* Cambridge Unviersity Press, 1985.

[Guindon and Maruyama, 1986] B. Guindon and H. Maruyama. Automated matching of real and simulated SAR imagery as a tool for ground control point acquisition. *Canadian Journal of Remote Sensing*, 12(2):149–158, 1986.

[Guindon, 1985] B. Guindon. Automatic control point acquisition in radar-optical image registration. *Canadian Journal of Remote Sensing*, 11(1):103–112, 1985.

[Hatcher, 1984] D. A. Hatcher. Simple formulae for Julian day numbers and calender dates. *Quarterly Journal Royal Astromonical Society*, 25:53–55, 1984.

[Herland, 1989] Einar-Arne Herland. ERS-1 SAR processing with CESAR. *IGARSS'89 12th Canadian Symposium on Remote Sensing.*, pages 191–199, July 1989.

[Hovanessian, 1980] S. A. Hovanessian. *Introduction To Synthetic Array and Imaging Radars.* Artech House, 1980.

[Howard, 1987] P. D. Howard. The impact of SAR processing algorithms on geocoding of SAR imagery. In *Workshop on Image Rectification Techniques for Spaceborne SAR*, pages 51–55, January 1987.

[Kaupp *et al.*, 1982] V. H. Kaupp, L. C. Bridges, M. A. Pisaruck, H. C. MacDonald, and W. P. Waite. Comparison of simulated stereo radar imagery. *IGARSS'82*, 2:2.1–2.5, 1982.

[Kaupp *et al.*, 1983] V. H. Kaupp, L. C. Bridges, M. A. Pisaruck, H. C. MacDonald, and W. P. Waite. Simulation of spaceborne stereo radar imagery: Experimental results. *IEEE Transactions on Geoscience and Remote Sensing*, GE-21(3):400–404, July 1983.

[Kavanagh *et al.*, 1989] P. F. Kavanagh, I. H. Wong, B. Guindon, and G. J. Princz. Canada's fast operational ERS-1 SAR precision processing and geocoding system. *IGARSS'89 12th Canadian Symposium on Remote Sensing.*, pages 1795–1798, July 1989.

[Kiremidjian, 1981] G. K. Kiremidjian. Radar image to map registration. *Optical Engineering*, 20(6):899–906, 1981.

[Kwok *et al.*, 1987] R. Kwok, J. C. Curlander, and S. S. Pang. Rectification of terrain-induced distortions in radar imagery. *Photogrammetric Engineering and Remote Sensing*, 53(5):507–513, May 1987.

[LaPrade, 1963] G. LaPrade. An analytical and experimental study of stereo for radar. *Photogrammetric Engineering*, XXIX:294–300, 1963.

[LaPrade, 1972] G. L. LaPrade. Stereoscopy — a more general theory. *Photogrammetric Engineering*, pages 1177–1187, 1972.

[Laycock, 1990] J. Laycock. Resampling algorithms for geocoding. *Third International Workshop on Image Rectification of Spaceborne SAR*, October 1990.

[Leberl and Raggam, 1982] F. Leberl and J. Raggam. Stereo side-looking radar experiments. *IGARSS'82*, pages 597–611, 1982.

[Leberl *et al.*, 1986a] F. W. Leberl, G. Domik, J. Raggam, J. Cimino, and M. Kobrick. Multiple incidence angle SIR-B experiment over Argentina: Stereo-radargrammetric analysis. *IEEE Transactions on Geoscience and Remote Sensing*, GE-24(4):482–491, July 1986.

[Leberl *et al.*, 1986b] F. W. Leberl, G. Domik, J. Raggam, and M. Kobrick. Radar stereomapping techniques and application to SIR-B images of Mt. Shasta. *IEEE Transactions on Geoscience and Remote Sensing*, GE-24(4):473–481, July 1986.

[Leberl *et al.*, 1988] F. Leberl, W. Mayr, and G. Domik. SIR-B stereo-radargrammetry of Australia. *International Journal of Remote Sensing*, 9(5):997–1011, May 1988.

[Leberl, 1979] F. Leberl. Accuracy analysis of stereo side-looking radar. *Photogrammetric Engineering and Remote Sensing*, 45(8):1083–1096, August 1979.

[Leberl, 1990] F. W. Leberl. *Radargrammetric Image Processing.* Artech House Inc, Norwood USA, 1990.

[Lewis and Wilson, 1989] D. J. Lewis and C. Wilson. Description of the EODC SAR processor. *Proceedings of the 15th Annual Conference of The Remote Sensing Society.*, pages 249–254, September 1989.

[Massonnet, 1987] D. Massonnet. State of radar processing at C.N.E.S. with respect to ERS-1 and its geocoding. In *Workshop on Image Rectification Techniques for Spaceborne SAR*, pages 23–25, January 1987.

[Meier and Nuesch, 1985] E. H. Meier and D. R. Nuesch. Registration of spaceborne SAR data to large scale topographical maps. In *19th International Symposium on Remote Sensing of Environment, Ann Arbor*, pages 581–594, 1985.

[Meier *et al.*, 1989] E. Meier, C. Graf, and D. Nuesch. Generation of geocoded spaceborne SAR image products. *IGARSS'89*, pages 2473–2477, 1989.

[Naraghi *et al.*, 1983] M. Naraghi, W. Stromberg, and M. Daily. Geometric rectification of radar imagery using digital terrain models. *Photogrammetric Engineering and Remote Sensing*, 49(2):195–199, 1983.

[Noack *et al.*, 1987] W. Noack, A. Popella, and G. Schreier. Knowledge-based SAR processing and geocoding in the elementary components of the German processing and archiving facility for high throughput and precision processing of ERS-1 SAR data. *IEEE Transactions on Geoscience and Remote Sensing*, GE-25(6):758–768, 1987.

[Perkins *et al.*, 1988] D. C. Perkins, D. R. Howell, and M. R. Szczur. *Digital Image Processing in Remote Sensing*, chapter The Transportable Applications Environment — an Interactive Design-to-Production Development System. Taylor and Francis, 1988.

[Pisaruck *et al.*, 1984] M. A. Pisaruck, V. H. Kaupp, H. C. MacDonald, and W. P. Waite. Model for optimal parallax in stereo radar imagery. *IEEE Transactions on Geoscience and Remote Sensing*, GE-22(6):564–569, November 1984.

[Powell, 1970] M. J. D. Powell. *Numerical Methods for Nonlinear Algebraic Equations*, chapter A Hybrid Method for Nonlinear Algebraic Equations. Gordon and Breach, 1970.

[Press *et al.*, 1986] W. H. Press, B. P. Flannery, S. A. Teukolsky, and W. T. Vetterling. *Numerical Recipes.* Cambridge University Press, 1986.

[Quegan *et al.*, 1991] S. Quegan, C. Yanasse, H. de Groof, P. N. Churchill, and A. J. Sieber. The radiometric quality of AgriSAR data. *International Journal of Remote Sensing*, 12(2):277–302, February 1991.

[Quegan, 1990] S. Quegan. Interpolation and sampling in SAR images. *IEEE Transaction on Geoscience and Remote Sensing*, 28(4):641–646, July 1990.

[Raggam and Leberl, 1984] J. Raggam and F. Leberl. SMART — a program for radar stereo mapping on the KERN DSR-1. In *Proceedings of the 50th Annual Convention American Society of Photogrammetry*, pages 765–773, 1984.

[Raggam, 1987] J. Raggam. Relevant parameters in the reconstruction of the analytical SAR sensor model. In *Workshop on Image Rectification Techniques for Spaceborne SAR*, pages 33–39, January 1987.

[Ramapriyan *et al.*, 1986] H. K. Ramapriyan, J. P. Strong, Y. Hung, and C. W. Murray. Automated matching of pairs of SIR-B images for elevation mapping. *IEEE Transactions on Geoscience and Remote Sensing*, GE-24(4):462–472, July 1986.

[Rosenfield, 1968] G. H. Rosenfield. Stereo radar techniques. *Photogrammetric Engineering*, XXXIV:586–594, 1968.

[Runge and Bamler, 1989] H. Runge and R. Bamler. PRF ambiguity resolving for SAR. *IGARSS'89 12th Canadian Symposium on Remote Sensing.*, pages 2572–2575, July 1989.

[Sack *et al.*, 1989] M. Sack, J. Ward, and G. J. Princz. Overview of Canada's ERS-1 SAR data processing facility. *IGARSS'89 12th Canadian Symposium on Remote Sensing*, pages 1791–1794, July 1989.

[Schreier *et al.*, 1988] G. Schreier, D. Kosmann, and A. Roth. Design aspects of a system for geocoding satellite SAR images. *The 16th International Congress of Photogrammetry and Remote Sensing. Comm I.*, 27(B10):I–135 – I–143, 1988.

[Slama *et al.*, 1980] Chester C. Slama, Charles Theurer, and Soren W. Henriksen, editors. *Manual of Photogrammetry.* American Society of Photogrammetry, 4 edition, 1980.

[Sowter and Smith, 1989] A. Sowter and D. J. Smith. SAR image geometry errors related to Doppler frequency assumptions. In *Workshop on Geocoded and Value Added Products of SAR*, January 1989.

[Strobl, 1987] D. Strobl. A new procedure of SAR geocoding based on image simulation. In *Workshop on Image Rectification Techniques for Spaceborne SAR*, pages 57–65, January 1987.

[Thomas *et al.*, 1986] J. Thomas, V. Kaupp, W. Waite, and H. MacDonald. Computer derived height from SIR-B stereo radar images. In *Proceedings IGARSS'86*, pages 639–643, 1986.

[Tsilibaris and Tribnig, 1988] X. Tsilibaris and G. Tribnig. The potential of spaceborne synthetic aperture radar for topographic mapping with particular reference to the European ERS-1 AMI. Technical report, Institute for Image processing and Computer graphics, Wastiangasse 6, A-8010 Graz, Austria, September 1988.

[Welch and Papacharalampos, 1990] R. Welch and D. Papacharalampos. 3-D computation and display of terrain models from stereo imaging radar data. In *IGARSS'90*, volume 3, pages 1967–1969, May 1990.

[Whelan and Hodgson, 1971] P. M. Whelan and M. J. Hodgson. *Essential Pre-University Physics.* John Murray, 1971.

[Wolberg, 1990] G. Wolberg. *Digital Image Warping.* IEEE Computer Society Press, 1990.

[Wu and Lin, 1989] J. Wu and D. C. Lin. Accuracy in positioning with stereoscopic SLAR imagery for topographic mapping. *IGARSS'89 12th Canadian Symposium on Remote Sensing*, pages 2479–2482, July 1989.

[Zebker and Goldstein, 1986] H. A. Zebker and R. M. Goldstein. Topographic mapping from interferometric synthetic aperture radar observation. *Journal of Geophysical Research*, 91(B5):4993–4999, April 1986.